Doctoral thesis

Characterization of the HIV-1 membrane and its interactions with anti-viral compounds using advanced microscopy techniques

Pablo Carravilla

December 2017

Supervisors
José L. Nieva Escandón
Nerea Huarte Arrayago

eman ta zabal zazu

Universidad del País Vasco
Euskal Herriko Unibertsitatea

Department of Biochemistry and Molecular Biology
Biofisika Institute

(c)2017 PABLO CARRAVILLA PALOMANES

Doctoral thesis

Characterization of the HIV-1 membrane and its interactions with anti-viral compounds using advanced microscopy techniques

Pablo Carravilla

December 2017

Supervisors
José L. Nieva Escandón
Nerea Huarte Arrayago

eman ta zabal zazu

Universidad del País Vasco
Euskal Herriko Unibertsitatea

Department of Biochemistry and Molecular Biology
Biofisika Institute

A ti Ama,
que me has traído hasta aquí.

Declaration

I, Pablo Carravilla Palomanes, declare that this thesis has been composed solely by myself and that it has not been submitted, in whole or in part, in any previous application for a degree. The work presented is entirely my own, if not stated otherwise by reference or acknowledgment, with the following exceptions:

- The *genpol* and FCS analysis programs used in chapters 3-6 were developed by Jose Requejo-Isidro and Unai Lorenzo.
- Imaging experiments in chapter 4 were performed in collaboration with Nerea Huarte.
- HIV lipids used in chapter 4 were extracted by Maier Lorizate and Jon Ander Nieto-Garai.
- Lipid mixing experiments in chapter 5 were performed by Johana Torralba with assistance from Beatriz Apellániz.
- 4E10 and 10E8 Fabs in chapter 6 were designed and purified by Edurne Rujas and Sara Insausti, who also performed vesicle flotation assays.
- FCS experiments in chapter 6 were performed in collaboration with Itziar R. Oar-Arteta.
- The STED image analysis program in chapter 6 was developed by Dominic White and further improved by Eneko Largo.
- Some of the pseudovirus purifications in chapter 5 and 6 were performed by Miguel García-Porras.
- Writing assistance was received from José Luis Nieva, Nerea Huarte and Jose Requejo-Isidro.

Contributions

Journal publications

- Serrano S.*, Araujo, A.*, Apellaniz, B., Bryson, S., Carravilla, P., De La Arada, I., Huarte N., Rujas E., Pai, E. F., Arrondo, J. L. R., Domene, C., Jimnez, M. A., & Nieva, J. L. (2014). Structure and immunogenicity of a peptide vaccine, including the complete HIV-1 gp41 2F5 epitope: Implications for antibody recognition mechanism and immunogen design. Journal of Biological Chemistry, 289(10), 65656580.

- Apellaniz, B., Rujas, E., Carravilla, P., Requejo-Isidro, J., Huarte, N., Domene, C., & Nieva, J. L. (2014). Cholesterol-Dependent Membrane Fusion Induced by the gp41 Membrane-Proximal External Region-Transmembrane Domain Connection Suggests a Mechanism for Broad HIV-1 Neutralization. Journal of Virology, 88(22), 1336713377.

- Carravilla, P., Nieva, J. L., Goi, F. M., Requejo-Isidro, J., & Huarte, N. (2015). Two-Photon Laurdan Studies of the Ternary Lipid Mixture DOPC:SM:Cholesterol Reveal a Single Liquid Phase at Sphingomyelin:Cholesterol Ratios Lower Than 1. Langmuir, 31(9), 28082817.

- Huarte, N.*, Carravilla, P.*, Cruz, A., Lorizate, M., Nieto-Garai, J. A., Krusslich, H., Perez-Gil J., Requejo-Isidro J., & Nieva, J. L. (2016). Functional organization of the HIV lipid envelope. Scientific Reports, 6, 34190.

- Carravilla, P., Cruz, A., Martin-Ugarte, I., Oar-Arteta, I. R., Torralba, J., Apellniz, B., Perez-Gil J., Requejo-Isidro J., Huarte N., & Nieva, J. L. (2017). Effects of HIV-1 gp41-Derived Virucidal Peptides on Virus-like Lipid Membranes. Biophysical Journal, 3495(17), 307476.

- Chojnacki, J., Waithe, D., Carravilla, P., Huarte, N., Galiani, S., Enderlein, J., & Eggeling, C. (2017). Envelope glycoprotein mobility on HIV-1 particles depends on the virus maturation state. Nature Communications, 8(1), 545.

*These authors contributed equally to this work.

Congress contributions

- 19th IUPAB congress and 11th EBSA congress (Edinburgh, United Kingdom, 16-20 July 2017). Research Poster (P1021): MPER-derived virucidal peptides diruspt the HIV-1 lipid envelope functional organization (Carravilla P., Cruz A., Martin-Ugarte I., Oar-Arteta I. R., Torralba J., Apellaniz B., Perez-Gil J., Requejo-Isidro J., Huarte N., & Nieva J.L.)

- Spanish-Portuguese Meeting for Advanced Optical Microscopy (Bilbao, 5-7 October 2016). Research Poster (P22): Membrane interactions of HIV-1 neutralizing antibodies assessed by scanning fluorescence correlation spectroscopy (Oar-Arteta I.R., Carravilla P., Rujas E., Huarte N., Nieva J. L., & Requejo-Isidro J.)

- Liposomes, Exosomes and Virosomes: From Modelling Complex Membrane Processes to Medical Diagnostics and Drug Delivery (Ascona, Switzerland, 11-16 September 2016). Research Poster (20-POS) Imaging the Packing State and Lateral Organization of the HIV-1 Membrane Lipids by Two-Photon and Atomic Force Microscopy (Carravilla P., Cruz A., Lorizate M., Krusslich H. G., Perez-Gil J., Nieva J. L., Requejo-Isidro J., & Huarte N.)

- Biophysics of Proteins at Surfaces: Assembly, Activation, Signalling (Madrid, Spain, 13-15 October 2015) Biophysical Society Thematic Meeting. Research Poster (7-POS) Cholesterol-dependent membrane fusion induced by the HIV-1 gp41 MPER-TMD and blocking by antibodies functioning at membrane surfaces (Carravilla P., Rujas E., Apellaniz B., Araujo A., Huarte N., Largo E., Serrano S., Domene C., Jimnez M. A., & Nieva J. L.)

- XXXVII Congress of the Spanish Society of Biochemistry and Molecular Biology (SEBBM) (Granada, Spain, 10-12 September 2014). Research Poster (P05-14): Two photon fluorescence microscopy of GUV discloses unprecedented liquid domain segregation behavior in cholesterol-enriched lipid bilayers (Carravilla P., Goi F. M., Nieva J. L., Requejo-Isidro J., Huarte N.)

- Membrane, Morphology and Function (Fara San Martino, Italia, 5-8 May 2014) Biochemical Society Meeting. Research Poster 1 (P050): Phase behavior of lipid mixtures that emulate the HIV-1 membrane (Carravilla P., Requejo-Isidro J., Cruz A., Perez-Gil J., Huarte N., & Nieva J. L.). Research Poster 2 (P051): Two photon fluorescence microscopy of GUV discloses unprecedented liquid domain segregation behavior in cholesterol-enriched lipid bilayers (Huarte N., Carravilla P., Goi F. M., Nieva J. L., & Requejo-Isidro J.)

- XIIIth Meeting of the Spanish Biophysical Society (Valencia, Spain, 19-21 June 2013). Research Poster (30): Phase Behavior of Lipid Mixtures That Emulate the HIV-1 Membrane (Carravilla P., Requejo-Isidro J., Cruz A., Perez-Gil J., Huarte N. and Nieva J. L.)

Resumen

El virus de la inmunodeficiencia humana (VIH) es un retrovirus perteneciente al género *Lentivirus* que infecta principalmente linfocitos T CD4+. El síndrome de inmunodeficiencia adquirida (SIDA) es un espectro de enfermedades causado por la infección por VIH, que interfiere con el correcto funcionamiento del sistema inmune y aumenta el riesgo de infecciones oportunistas que acaban causando la muerte del paciente. En 2016, alrededor de 36.7 millones de personas vivían infectadas por el VIH tipo 1 (VIH-1) y se produjeron cerca de 1 millón de muertes relacionadas con el SIDA.

El VIH está recubierto de una bicapa lipídica adquirida de las células huésped durante la gemación. La proteína de envuelta (Env) es la única de origen viral que se expone en esta membrana. Env es responsable del reconocimiento del receptor CD4 y los correceptores CCR5 o CXCR4 en la membrana plasmática de la célula objetivo mediante la subunidad gp120 y la subsecuente fusión de las membranas celular y viral, mediada por la subunidad transmembrana gp41 (Fig. 1). Este proceso da lugar al poro de fusión por el que la cápside del virus se libera al citosol de la célula huésped.

A pesar de que la envuelta lipídica es adquirida de la membrana plasmática de la célula infectada, la composición química de ambas es muy diferente, ya que la membrana del virus se encuentra enriquecida en ciertos lípidos como el colesterol (hasta un 50% del contenido lipídico total). Por ello se ha propuesto que el virus adquiera su membrana de balsas lipídicas o *lipid rafts* en la membrana celular. Los *rafts* son nanodominios temporales enriquecidos en colesterol, esfingolípidos y ciertas proteínas a los que se les adjudica diferentes funciones gracias a la compartimentalización de elementos de la membrana plasmática. Se desconoce la razón por la que la gemación del VIH ocurre a través de estos dominios, sin embargo diferentes estudios han demostrado que la composición de la membrana viral es crítica para la infección, es decir, que la membrana juega un papel activo durante la fusión.

En esta tesis se han estudiado diferentes características y procesos que ocurren a nivel de la envuelta del VIH-1 mediante técnicas de microscopía avanzada, que han permitido la cuantificación de diferentes parámetros biofísicos.

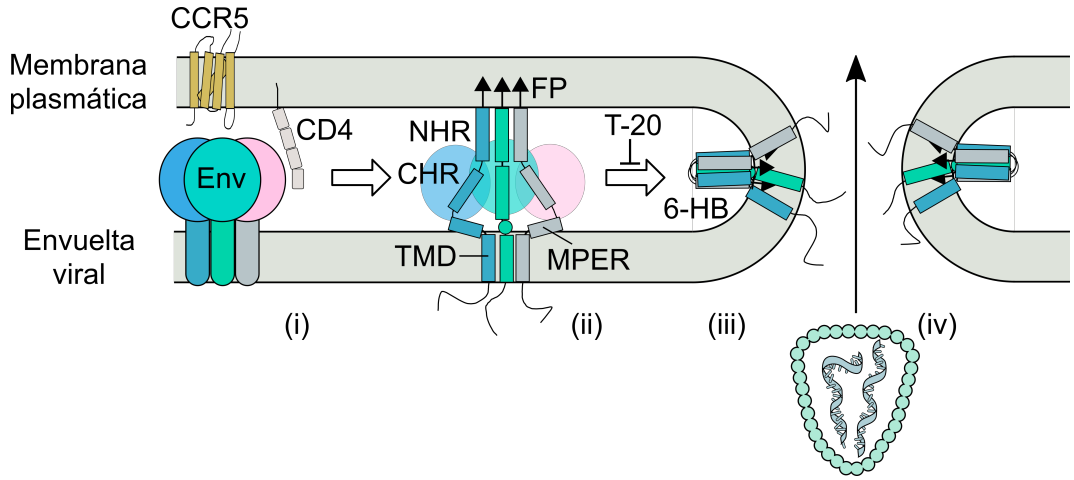

Figure 1: Fusion mediada por Env. (i) gp120 reconoce el receptor CD4 y el correceptor CCR5 (o CXCR4) que se traduce en un cambio conformacional de toda la proteína. (ii) En la nueva conformación el domimio FP de gp41 se inserta en la membrana plasmática celular. (iii) Por último los dominios NHR y CHR se pliegan sobre si mismos formando un manojo de seis hélices (6-HB, del inglés *six helix bundle*) que da lugar al poro de fusión (iv).

En primer lugar, se ha analizado el grado de empaquetamiento de bicapas lipídicas en vesículas unilamelares gigantes (GUVs, del inglés *Giant Unilamellar Vesicles*) utilizando microscopía de dos fotones de la sonda fluorescente Laurdan. Laurdan es un fluroforo que se reparte en la membrana independientemente de la fase de esta y que sufre un desplazamiento en su espectro de emisión dependiente de la polaridad del medio. Esto permite, mediante la función GP, cuantificar el grado de hidratación del la interfase de una bicapa lipídica, que es proporcional a su orden molecular. Durante la implementación de esta técnica e inicialmente como método de validación de la misma, se ha construido un diagrama de fases de GP de la mezcla lipídica DOPC:colesterol:esfingomielina (Fig. 2). La región correspondiente a las mezclas en las que existe coexistencia de fases se mantiene siempre por debajo de la relación colesterol:esfingomielina 1:1 y es menor que la descrita por otros autores en estudios similares. Esto puede deberse a la existencia de ciertas fuentes de segregación artefactual que han sido identificadas y se pueden evitar mediante la excitación por dos fotones, por ejemplo, la fotooxidación. El diagrama de fases puede ser utilizado como herramienta para definir mezclas lipídicas que emulen una membrana biológica deseada.

Para definir la organización y función de la membrana viral, se ha extraído el contenido lipídico de virus infectivos. Estas mezclas lipídicas han sido reconstituidas en GUVs y monocapas Langmuir-Blodgett para analizar su grado de orden molecular y comportamiento de fases. La determinación del nivel de empaquetamiento ha permitido el desarrollo de mezclas lipídicas que emulan la membrana viral y han

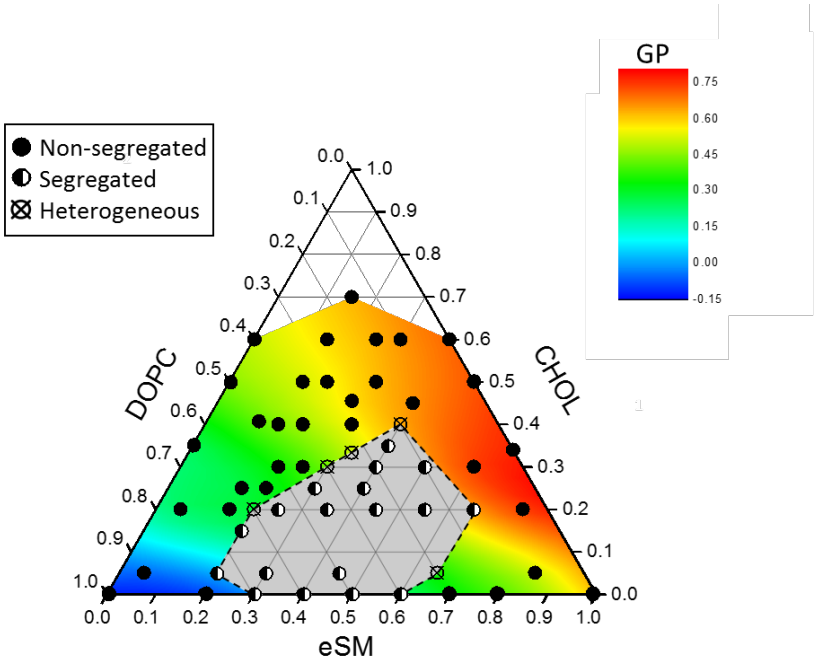

Figure 2: Diagrama de fases GP de la mezcla DOPC:colesterol:esfingomielina. La escala de colores corresponde a la función GP calculada a partir de la cuantificación de la intensidad de la emisión de fluorescencia del Laurdan en GUVs. *Non-segregated*: población homogénea. *Segregated*: segragación de fases. *Heterogeneous*: mezcla en la que se observan tanto vesículas segregadas como uniformes.

sido utilizadas en los capítulos posteriores como modelo de la envuelta lipídica. Mediante microscopía de fuerza atómica se ha demostrado que la membrana viral puede organizarse en nanodominios (Fig. 3, izquierda). También se ha analizado el efecto de compuestos virucidas que actúan a nivel de membrana en los citados parámetros biofísicos. Los resultados obtenidos sugieren que un agente capaz de interferir con la nanoorganización de la membrana viral podría inhibir la infección (Fig. 3, derecha).

Basado en estas evidencias se ha procedido al estudio del mecanismo de inhibición mediada por péptidos derivados de los dominios MPER y TMD de la proteína gp41 del VIH-1. Únicamente un péptido cuya secuencia comprende el dominio MPER y la secuencia N-terminal dominio TMD ha presentado actividad virucida ($MPER_{671-693}$). A pesar de que otros péptidos son también capaces de alterar la nanoorganización de membranas modelo, sólo $MPER_{671-693}$ parece estructurarse en los límites de los dominios lipídicos y presentar la capacidad de inducir permeabilización de membranas modelo, dos procesos que pueden estar relacionados con su actividad virucida.

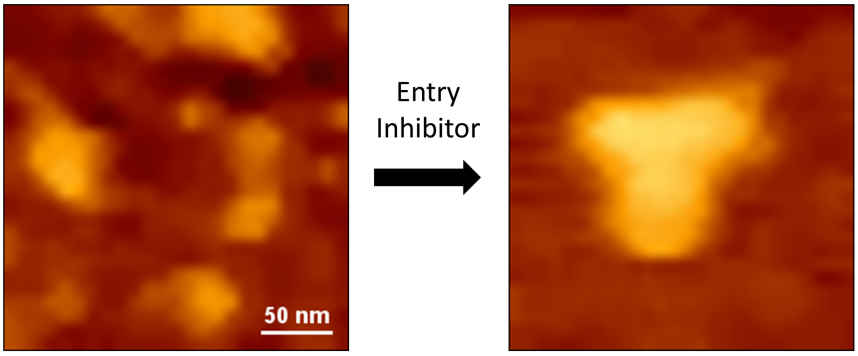

Figure 3: Modelo de la organización de la envuelta lipídica del VIH-1. Izquierda, membrana funcional, organizada en nanodominios. Derecha, algunos inhibidores de la infección (*Entry inhibitor*) pueden interferir con la organización de la membrana.

Por último, se ha estudiado el mecanismo de unión de anticuerpos de amplio espectro anti-MPER directamente a viriones utilizando microscopía de fluorescencia de superresolución STED (del inglés *Stimulated Emission Depletion*). De este modo, se ha determinado que los anticuerpos anti-MPER y anti-gp120 reconocen el mismo tipo de agrupaciones de Env en la membrana viral. Además se ha establecido una correlación entre la unión y la neutralización en el caso de los anticuerpos anti-MPER 4E10 y 10E8, que parece depender de la capacidad de establecer interacciones con lípidos a traves del lazo HCDR3 (Fig. 4) o de la superficie MAPA (del inglés *membrane-associated paratope area*), aunque en ningún caso se ha observado una interacción directa entre 4E10 o 10E8 y la membrana viral. Experimentos de espectroscopía de correlación de fluorescencia realizados utilizando membranas modelo sugieren que la interacción entre 4E10 y la membrana es superficial e inespecífica, además de estar impedida debido al alto empaquetamiento de la envuelta lipídica.

En conclusión, los estudios de microscopía avanzada realizados durante esta tesis han permitido la caracterización y mayor comprensión de la membrana del VIH-1 y del mecanismo de inhibición y neutralización de compuestos y anticuerpos anti-VIH en el contexto de la membrana viral. Estas son las conclusiones generales de este trabajo:

1. Las mezclas DOPC:colesterol:esfingomielina se organizan a nivel microscópico en una fase homogénea cuando la relación colesterol:esfingomielina es mayor que 1. El diagrama de fases GP construido a permitido determinar que la relación entre colesterol y esfingomielina es la que determina el grado de orden de estas mezclas lípidicas.

2. Los lípidos de la membrana del VIH-1 forman bicapas altamente empaquetadas

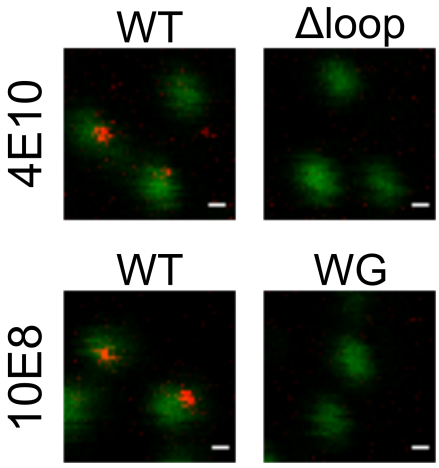

Figure 4: Los anticuerpos 4E10 y 10E8 (señal STED, rojo) se unen a viriones de VIH-1 (verde). La ablación de la punta del lazo HCDR3 (mutantes Δloop y WG) afecta a esa unión.

y son capaces de organizarse en nanodominios. Compuestos antivirales que se insertan en la membrana interfieren con esta nanoorganización.

3. El péptido $\text{MPER}_{671-693}$ derivado de la región MPER-TMD de la proteína gp41 del VIH-1 es capaz de inhibir la infección de viruses envueltos. Los estudios realizados utilizando membranas modelo sugieren que este péptido se acumula en los límites de los dominios lipídicos e induce la permeabilización de la bicapa.

4. Los anticuerpos de amplio espectro 4E10 y 10E8 reconocen Env en la membrana viral pero no se unen a esta directamente. Aumentar la interacción de 4E10 o 10E8 con lípidos mediante mutaciones en el lazo HCDR3 o en la región MAPA mejoran la capacidad neutralizante de estos.

Contents

1 Introduction **1**
1.1 HIV-1 . . . 1
1.1.1 AIDS and HIV . . . 1
1.1.2 HIV-1 . . . 2
1.1.3 Envelope glycoprotein mediated membrane fusion . . . 3
1.1.4 The viral lipid envelope . . . 6
1.1.5 Membrane-active compounds displaying virucidal activity against HIV-1 . . . 9
1.1.6 Broadly neutralizing antibodies . . . 15
1.2 Quantitative fluorescence microscopy . . . 17
1.2.1 Fluorescence . . . 17
1.2.2 Fluorescence microscopy . . . 19
1.2.3 Environmental sensitive probes . . . 21
1.2.4 Fluorescence correlation spectroscopy . . . 24
1.2.5 Super-resolution fluorescence microscopy . . . 28
1.3 Goals . . . 31

2 Experimental techniques **33**
2.1 Model membranes . . . 33
2.1.1 Multilamellar vesicles . . . 33
2.1.2 Giant unilamellar vesicles . . . 34
2.1.3 Large unilamellar vesicles . . . 35
2.1.4 Lipid concentration determination . . . 36
2.1.5 Langmuir-Blodgett monolayers . . . 37
2.2 Fluorescence spectroscopy . . . 38
2.2.1 Leakage assay . . . 38
2.2.2 Lipid mixing assay . . . 39
2.3 Advanced fluorescence microscopy . . . 40
2.3.1 Laurdan GP measurements . . . 41
2.3.2 Fluorescence correlation spectroscopy . . . 45
2.3.3 Super-resolution STED microscopy . . . 46

2.4 Atomic force microscopy 47
2.5 Virus and cell biology 50
2.5.1 Virus production 50
2.5.2 Infectivity assay 51

3 Building a DOPC:SM:cholesterol molecular order phase diagram based on Laurdan GP measurements 53
3.1 Introduction 55
3.2 Experimental Techniques 56
3.3 Results 57
3.3.1 Cholesterol:sphingomyelin molar ratios modulate macroscopic lateral separation 57
3.3.2 Two-photon microscopy avoids light-induced artifactual domains 60
3.3.3 Cholesterol and sphingomyelin effect on membrane lipid order 62
3.3.4 Generalized Polarization ternary phase diagram 63
3.4 Discussion 66
3.4.1 Two-photon excitation does not photoinduce domains in model membranes 66
3.4.2 Traveling along the phase diagram 68
3.4.3 Comparison with previous data 70
3.5 Conclusions 71

4 Imaging the packing state and lateral organization of the HIV lipid envelope 75
4.1 Introduction 77
4.2 Experimental Techniques 78
4.3 Results 82
4.3.1 Membrane lipid packing in HIV-1 mixtures and surrogates . 82
4.3.2 Miscibility of the HIV membrane lipids 87
4.3.3 Alteration of HIV membrane lipid packing and miscibility by membrane-active agents 88
4.4 Discussion 94
4.5 Conclusions 98

5 Effects of HIV-1 gp41-derived virucidal peptides on virus-like lipid membranes 101
5.1 Introduction 103
5.2 Experimental Techniques 104
5.3 Results 106
5.3.1 Virucidal activity of gp41-derived peptides 106

5.3.2 Role of cholesterol in the membrane activity of virucidal peptides . . . 109
5.3.3 Membrane activity of gp41-derived peptides . . . 113
5.4 Discussion . . . 115
5.5 Conclusions . . . 118

6 Single virion super-resolution microscopy studies of the mechanistic details of Env glycoprotein recognition by broadly neutralizing hiv-1 antibodies 119
6.1 Introduction . . . 121
6.2 Materials and methods . . . 123
6.3 Results . . . 128
6.4 Discussion . . . 141
6.5 Conclusions . . . 143

7 Conclusions 145

Chapter 1

Introduction

1.1 HIV-1

1.1.1 AIDS and HIV

The human immunodeficiency virus (HIV) is the causative agent of the acquired immunodeficiency syndrome (AIDS). AIDS is a spectrum of conditions that starts with an infection that may remain asymptomatic, followed typically by a long period with no manifestations and that finally, results fatal in most cases after the virus interferes with the immune system and an opportunistic infection that cannot be combated by host defense mechanisms leads to death of the patient. Tuberculosis (caused by the bacterium *Mycobacterium tuberculosis*) remains the leading cause of death among people living with HIV, accounting for around one in three AIDS-related deaths.

AIDS was first observed in 1981 and the virus isolated for the first time in 1983 (Barre-Sinoussi et al., 1983; Gallo et al., 1983). According to the Joint United Nations Programme on HIV and AIDS (UNAIDS) in 2016 there were around 36.7 million people living with HIV, 1.8 million people newly infected with the virus and 1 million AIDS-related deads. Moreover, 35 million people have died because of AIDS since the pandemic started. Around 25.5 million people (69% of the infected individuals) live in Africa (Fig. 1.1), a region where accessibility to prevention means and antiviral medication is highly limited.

Progress has been significant but not enough during the last years. Around 30% of people living with HIV still do not know their HIV status, 17.1 million of the infected individuals do not have access to antiretroviral therapy and more than half of all people living with HIV are not virally suppressed. Still if we analyze the same data from an optimistic perspective we can notice that prevention-treatment efforts are yielding results: more than half of HIV positive people (53%) now have access to treatment and AIDS-related deaths have fallen from 1.9 million in 2005

to 1 million in 2016.

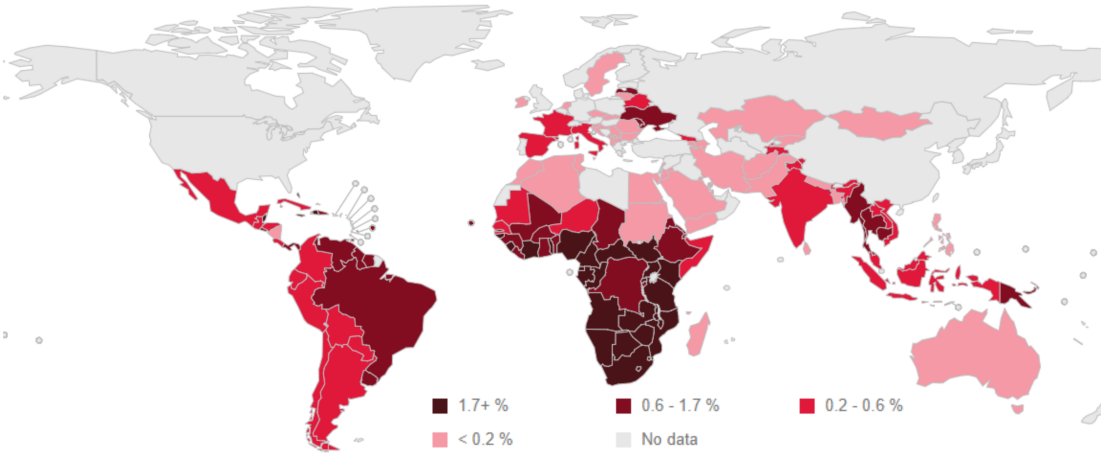

Figure 1.1: HIV prevalence in 2016 according to UNAIDS.

AIDS is managed with the so-called Highly Active AntiRetroviral Treatment (HAART), that relies on the combination of a number of antiviral compounds that inhibit different steps of the HIV replication cycle. The treatment decreases the patient's viral load, maintains function of the immune system and prevents opportunistic infections. Where accessible and affordable for the patients, HAART has proven extremely successful since it has drastically reduced the number of AIDS-related deaths and HIV is considered just a chronic infection.

Although not so serious, the situation is far from perfect in Europe. In the particular case of the Basque Autonomous Community, in 2016 there were 5661 patients receiving antiviral treatment, 39 new AIDS cases (value that peaked in 1994 with 533 new cases) and 38 AIDS related deaths (428 in 1996) according to Osakidetza (Basque health agency).

The necessity of a worldwide available prophylactic vaccine that would prevent HIV-1 infection arises upon this alarming epidemiological status and the lack of an efficient and accessible treatment.

1.1.2 HIV-1

HIV can be divided in two major classes. HIV type 1 (the class studied in this thesis work and henceforth HIV-1) is the most common and pathogenic strain and it is responsible for the world pandemic. HIV type 2 is a less virulent and infectious class, although it is also known to cause AIDS. It is contained in West Africa, but still a few cases have been reported in Europe, America or Asia.

HIV-1, together with other immunodeficiency viruses, belongs to the *Retroviridae* family. This group is characterized by the use of reverse transcriptase to convert their genomic RNA into DNA, which a virus-born integrase enzyme will subsequently help integrating into the host cell genome. This cell will assume the viral genetic material as part of its own, leading to the translation of proteins required for assembly of new viral copies.

Members of the *Lentivirus* genus such as HIV-1, exhibit an especially long incubation period, i.e. the time it takes for immunodeficiency symptoms to appear after the initial exposure to the pathogen. Their genome comprises three main genes, namely: (i) *gag*, which codifies for proteins that form the matrix (MA), the capsid (CA) and the nucleocapsid (NC); (ii) *pol*, responsible for the translation of the protease, the reverse transcriptase and the integrase and (iii) *env*, a gene that codifies for gp160, a 160 kDa membrane glycoprotein that is post-translationally cleaved into two subunits: surface gp120 subunit (SU) and transmembrane gp41 subunit (TM), that upon oligomerization form the Env protein, a trimer of non-covalently attached gp120-gp41 heterodimers. Env is responsible for receptor/co-repetor recognition (gp120) and membrane fusion (gp41). The lentiviral genome further includes a set of accessory genes that vary across different lentivirus, which in particular for HIV-1 are *vif*, *vpr*, *vpu*, *tat*, *rev* and *nef*.

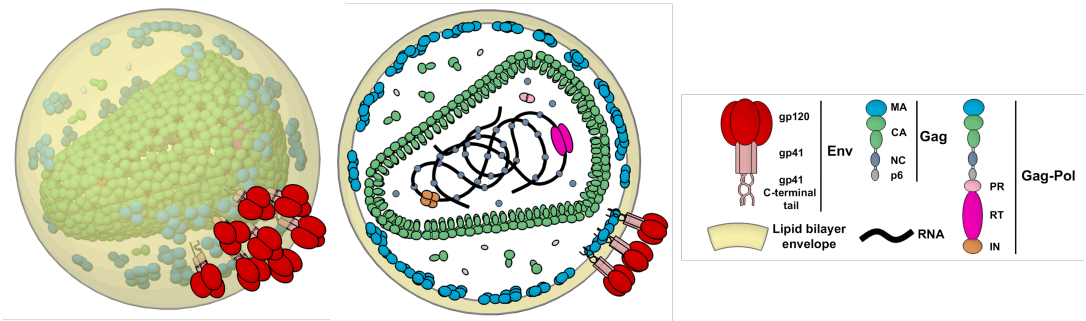

Figure 1.2: Diagram of a mature HIV-1 viral particle. Note the low ammount and clustering of spikes and the scattered matrix proteins underneath the envelope surface. Image by Dr. Jakub Chojnacki.

1.1.3 Envelope glycoprotein mediated membrane fusion

HIV-1 fuses its membrane to access and activate the replication cycle within the cytoplasm of host cells, typically CD4+ T cells and cells of the monocyte/macrophage lineage (Checkley et al., 2011; Wilen et al., 2012). The Env glycoprotein, which embodies the fusion machinery, is considered to be an archetype of Class I viral fusion protein (White et al., 2008). In the order of 10-15 Env peplomers project

from the virion surface (Checkley et al., 2011) (Fi.g 1.2), such a low number of exposed proteins is supposed to hamper B cell activation. The number of Env proteins necessary to overcome the membrane fusion energetic barrier is unclear and seems to depend on the virus strain, i.e. on the Env protein sequence and glycosilation pattern (Brandenberg et al., 2015). Super-resolution microscopy studies have shown that in mature HIV-1 virions Env is clustered in a single focus (note Env clustering in Fig. 1.2), suggesting that in order for HIV-1 to be infective all Env molecules must be in close proximity, which would favor a coordinated Env action (Chojnacki et al., 2012).

Env function depends on both protein-protein and protein-lipid interactions. Gp120 not only interacts with cell receptors, but also has been shown to bind lipids such as GalCer or GM3 in the host cell plasma membrane (Nehete et al., 2002). However, gp41 is the main player in membrane-protein interactions. Gp41 is a 338 residue transmembrane glycoprotein. It is divided in 3 major domains: the ectodomain, the transmembrane domain and the cytoplasmic domain; and can be further divided in at least seven domains (Fig. 1.3). All of them have been proposed to interact with membranes. A review about gp41-membrane interactions was recently published by Klug et al. (2017).

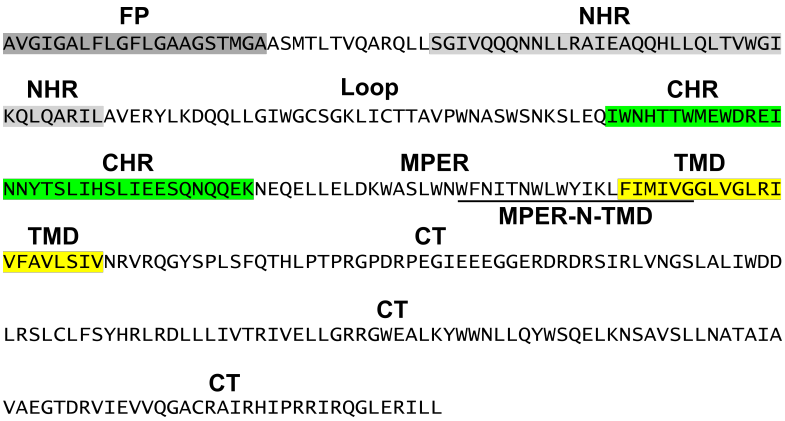

Figure 1.3: Gp41 amino acid sequence with functional domains.

The fusion peptide (FP) is the most N-terminal domain of gp41. It is highly hydrophobic and thus, it partitions to the cell membrane once fusion is activated and acts both as a membrane destabilizing domain and as a membrane anchor. The N- and C-terminal heptad repeats (NHR and CHR respectively), which are linked with a flexible loop, are two helical domains responsible for major conformational rearrangements that occur during fusion.

The CHR is followed by the membrane-proximal external region (MPER), a hydrophobic-at-interface domain (Lorizate et al., 2008) that partitions into the viral lipid envelope and is responsible for HIV membrane perturbation during

fusion. It is highly conserved among different HIV-1 strains, suggesting that its function is highly relevant to the viral fusion mechanism. Moreover, some naturally occurring MPER-targeting antibodies are able to inhibit Env-mediated fusion, which is further explained in the 1.1.6 section. The MPER sequence contains a highly conserved cholesterol recognition amino acid consensus (CRAC) motif (LWYIK) that interacts with cholesterol in the viral membrane (Vincent et al., 2002). The functional role of the CRAC motif is still unclear. Mutations in the CRAC do not totally impair infectivity (Epand et al., 2006), suggesting that the CRAC motif may not be involved in fusion, but rather in Env trafficking. On the contrary, other authors have reported highly reduced viral fusion ability upon CRAC depletion (Chen et al., 2009), even if Env properly incorporated into virions.

The transmembrane domain (TMD) has also been proposed to actively take part in the fusion process. Indeed, substituting the full domain with that of other viruses results in impaired Env-mediated fusion (Miyauchi et al., 2005). Moreover, structural studies show that the C-terminal segment of the MPER domain and the TMD may form an uninterrupted α-helix (Apellániz et al., 2015), suggesting that both domains act coordinately during the fusion process (MPER-N-TMD, Fig. 1.3). Finally, the cytoplasmatic tail constitutes the C-terminal end of gp41. It interacts with the Gag MA domain and also with other CT domains to sustain Env clustering (Chojnacki et al., 2012). Aditionally, it has been also linked to destabilization of the viral membrane during fusion (reviewed in Klug et al. (2017)).

Insights into the structural organization of the Env native state have been recently obtained from crystallographic studies of soluble cleaved Env trimers (reviewed in Ward and Wilson (2015)). Together with previous information on the low-energy, post-fusion structures (Eckert and Kim, 2001), the high-resolution structural data suggest an activation pathway that starts with gp120 interaction with receptor/co-receptor, follows with insertion of the gp41 fusion peptide (FP) into the cell target membrane, and reaches completion with the refolding of gp41 ectodomain trimers into low-energy six helix bundles 6-HBs (Fig. 1.4). In the 6-HB structure the three C-terminal helices (CHR region of gp41) are packaged in a direction opposite to the N-terminal helices (NHR region of gp41) (Eckert and Kim, 2001). Thus, the formation of this structure pulls cell and virus membranes into close contact, a movement that ultimately generates the fusion pore allowing the capsid passage to the host cell cytosol (Fig. 1.4).

This model predicts blocking 6-HB formation at any stage of the process will inhibit the fusion activity of gp41 and, hence, viral entry. Accordingly, the conformational transition undergone by gp41 trimers to form the 6-HB constitutes the target for the clinically approved fusion inhibitor Enfuvirtide (Eckert and Kim, 2001; Lalezari et al., 2003). However, the high overall cost, arising from the drug production complexity (Enfuvirtide is based on T-20, a 36-mer peptide), the

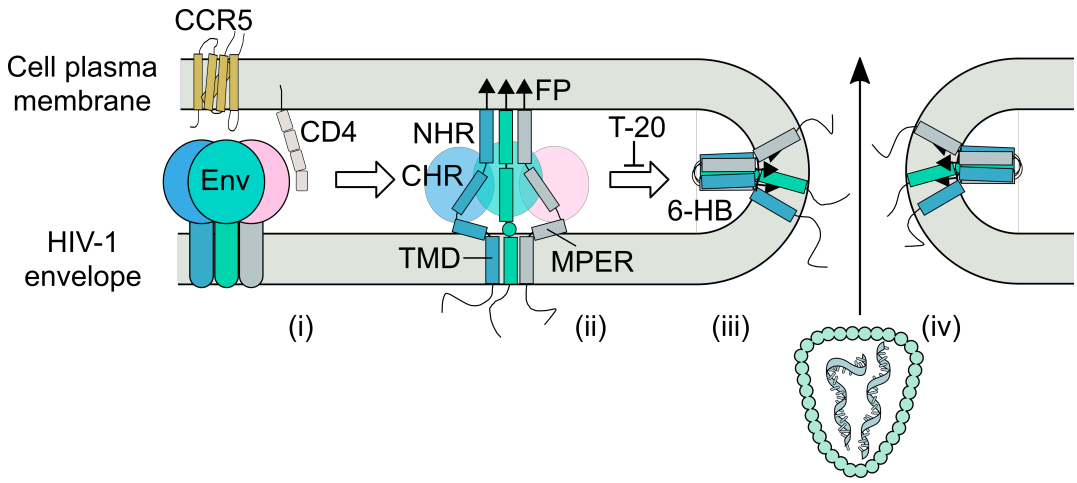

Figure 1.4: Role of the Env protein during HIV-1 fusion. After CD4 receptor and CCR5 coreceptor recognition (i) the gp120 subunit of Env suffers a conformational rearrangement and the FP in gp41 is propelled towards the plasma membrane of the target cell (ii). In that extended conformation, the FPs insert into the cell membrane and the three NHR domains adopt a coiled coil structure. Subsequent packing in the opposite direction of the CHR domains causes gp41 to refold adopting a structure known as the 6-helix bundle (6-HB), which brings both membranes into close proximity (iii). During this process, the FP and the MPER domains can also perturb the cell and viral membranes, respectively, thereby promoting membrane merger. The coordinated activity of several trimers opens a fusion pore allowing passage of the capsid (iv). T-20 prevents transition from (ii) to (iii).

appearance of resistance in long lasting treatments, and the extremely high dosage required to attain effectiveness have limited the clinical application of Enfuvirtide to salvage therapies (Haqqani and Tilton, 2013). Thus, development of new fusion inhibitors displaying broad and sustained antiretroviral activity against HIV-1 remains a pursued goal to date (Flexner and Saag, 2013; Wisskirchen et al., 2014).

1.1.4 The viral lipid envelope

For membrane merger to occur, lipid bilayers must be brought into close apposition, a process that requires overcoming the highly repulsive hydration and electrostatic forces operating at the membrane surface. It has been argued that repulsion would be minimal within point-like membrane protrusions created by focal application of curvature/tension stress (Chernomordik and Kozlov, 2008; Kozlov et al., 2010). From a *lipidcentric* point of view then (Fig. 1.5), generation of these structures represents the limiting step of the overall viral membrane fusion. Thus, in analogy to enzyme catalysis, the fusogenic Env glycoprotein would actively promote and/or stabilize a transition state along the fusion pathway, which minimizes repulsion between lipid bilayers. It has been proposed that the FP and MPER domains

of gp41, would be in charge of inducing this kind of lipid intermediate structures (reviewed by Apellaniz et al. (2014a)).

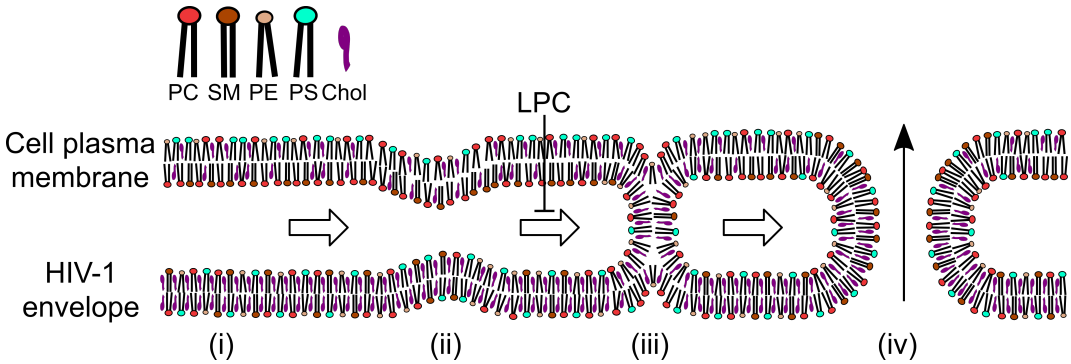

Figure 1.5: Lipid organization during HIV-1 membrane fusion. Having both membranes in close proximity (i) is not enough to induce fusion. In order to decrease the energy barrier preventing the initiation of the process lipid bilayers must form point-like protrusions (ii) that minimize hydration repulsion forces. The outer monolayers form the first connecting structure, known as the hemifusion stalk (iii) that evolves until the inner leaflets fuse and the formation of a fusion pore takes place (iv), the final lipid structure allowing diffusion of the capsid. LPC increases positive curvature and blocks the transition from (ii) to (iii). For the sake of simplicity lipid domains are not represented.

Membrane curvature play a pivotal role during fusion. Curvature depends, among others, on lipid geometry, that arises from lipid molecular structure. Polar headgroups fill the membrane interface and thus, bigger groups tend to form inverted cone shaped lipids that favor positive curvature, e.g. phosphatidylserine; and smaller headgroups, i.e. those in cone shaped lipids, are related to negative curvature, such as phosphatydilethanolamine or cholesterol.

Hydrophobic tails also contribute to geometry. Unsaturations fix the angle of lipid hydrocarbon chain bonds increasing the volume occupied in the hydrophobic section (inverted cone shape) and favoring negative curvature. Acyl chain number also contributes to lipid geometry: single acyl chains promote inverted coned geometry, such as in the case of lysophospholipids, and lipids with multiple hydrocarbon chains, e.g. cardiolipin, form coned shaped lipids. In conclusion, geometry ultimately depends on the volume difference between the headgroup and the hydrophobic tail.

In the most widely accepted fusion model, an hourglass-shaped lipid structure termed stalk, with mean negative curvature, is postulated to emerge as an intermediate common to all fusion processes (Fig. 1.5) (Chernomordik and Kozlov, 2008; Kozlov et al., 2010). The stalk finally expands to form a fusion pore that connects the aqueous compartments previously isolated by the fusing membranes. FPs are believed to also promote formation of lipid structures compatible with stalk formation (Apellaniz et al., 2014a; Kozlov et al., 2010). Thus, FPs would not

behave as inert membrane anchors that insert into the cell membrane, but would take active part in the fusion process as catalytic agents by promoting formation of small hydrophobic patches, lipid tail protrusions, curvature stress and/or softening of the lipid bilayer at membrane-membrane contacts. Consistent with occurrence of stalk-like intermediates along the viral fusion process, agents that insert into the lipid envelope promoting positive curvature can block membrane merger and viral infection by a variety of unrelated enveloped viruses (St.Vincent et al., 2010). These findings have led to the proposal that compounds opposing the formation of lipid stalks can comprise broad-spectrum entry inhibitors.

Molecular composition of the HIV membrane

Pioneering work by Aloia and coworkers demonstrated that high levels of cholesterol (Chol) and sphingomyelin (SM) correlate with the low fluidity of the HIV membrane (Aloia et al., 1988, 1993). Mass spectrometry studies by Brügger et al. (2006) subsequently indicated that lipids promoting membrane order accumulate in the HIV membrane at concentrations found in detergent-resistant membranes, with Chol being the most abundant molecular species, as it accounts for 40-50 mol % of the total lipid content (Table 1.1). Consistent with those early findings, measurements of lipid packing demonstrate that the HIV membrane is highly ordered (Lorizate et al., 2009). Supporting a functional role for the high Chol concentration, depletion of this compound by several agents results in HIV infectivity inhibition (reviewed by Wojcechowskyj and Doms (2010)).

The high Chol and SM concentrations (among other raft-related lipids) found in the viral envelope also supports the hypothesis of HIV-1 budding from lipid rafts (Nguyen and Hildreth, 2000). The Chol molecule is amphipathic, containing a small polar head group and a large hydrophobic moiety formed by a hydroxyl group and an acylated sterol ring, respectively. Due to its chemical nature, Chol (i) intercalates between phospholipid hydrophobic tails in the core of the membrane and (ii) preferentially interacts with sphingolipids through hydrogen bonding of hydroxyl and amide groups at the membrane interface level (reviewed by Slotte (2016)). The former property accounts for the ordering effect induced by Chol, whereas the latter one constitutes the most important basis for the formation of lipid rafts. These entities can be defined as small, transient and ordered membrane domains, enriched in Chol, sphingolipids and proteins that preferentially partition to these lipid environments (recently reviewed by Sezgin et al. (2017a)). The properties and functions of lipid rafts are highly relevant for HIV biology as it will be further elaborated along this thesis work.

In addition to increase lipid packing and sustain lipid domain formation, the size imbalance of polar headgroup vs. hydrophobic core makes Chol a negative-curvature inducing lipid, which has important implications for fusion (Aeffner et al., 2012).

Consequently, this compound is also thought to stabilize non-bilayer membrane structures, such as the previously mentioned stalk, facilitating the outbreak of fusion, that otherwise would be energetically sequestered (Yang et al., 2016b). However, its role during the process does not appear to be strictly limited to the alteration of the physical chemistry of the lipid envelope. As mentioned before, the MPER domain of gp41 includes a Chol recognition amino acid consensus (CRAC) motif, that appears to interact with Chol (Epand et al., 2006) and modulate fusion and postfusion events (Chen et al., 2009). The MPER also displays fusogenic activity *in vitro* that is seemingly dependent on the Chol content of the viral membrane (Apellaniz et al., 2014b).

Besides the main raft-type lipids, the viral envelope may be enriched in aminophospholipids, dihydrosphingomyelin, plasmenyl phosphoethanolamine, phosphoinositides, or ceramide (Table 1.1), distributed with small variations that depend on the producer cell lines (Brügger et al., 2006; Chan et al., 2008; Lorizate et al., 2013). Furthermore, the aminophospholipids phosphatidylserine (PS) and phosphatidylethanolamine (PE) are accessible at the external membrane leaflet of mature virions (Callahan et al., 2003; Henriques et al., 2012; Li et al., 2014; Phoenix et al., 2015; Soares et al., 2008). This observation is consistent with the loss in the static viral particles of the asymmetric lipid distribution generated at the plasma membrane by ATP-dependent aminophospholipid translocases.

PE, is the most abundant glycerophospholipid exposed on the viral envelope. It is greatly enriched upon viral budding, mostly in its plasmalogen form (Brügger et al., 2006). Plasmalogens have been related to formation of lipid rafts, promotion of non-lamellar membrane structures occurring in fusion and protection against lipid oxidation (Dean and Lodhi, 2017). These three effects of plasmalogens perfectly fit the pivotal function ascribed to the lipid envelope during HIV infection, even if their exact role on the process has not been elucidated yet.

In summary, the HIV envelope is enriched in Chol and other raft lipids, therefore constitutes an ordered environment, and contains PE and PS accessible at the external monolayer.

1.1.5 Membrane-active compounds displaying virucidal activity against HIV-1

The tightly-packed/highly-solvated glycoprotein layer covering the vast majority of enveloped viruses (i.e., Influenza virus (Katz et al., 2014)), is expected to hinder to some extent, the accessibility of membrane-partitioning compounds to the lipid bilayer. In stark contrast, only 10-15 peplomers incorporate per HIV particle and a bare lipid envelope covers most of its solvent-accessible surface (Zhu et al., 2006) (Fig. 1.2). Thus, the unrestrained accessibility from solvent, combined with the

Table 1.1: Lipid composition of the HIV-1 envelope according to Brügger et al. (2006). Only lipid species that account for more than 1 mole % of the total lipid content are listed.

Lipid	%
PC	8.8
Chol	45.2
SM	12.5
DHSM	5.7
PE	4.4
pl-PE	14.8
PS	8.4

distinct chemical composition and physicochemical properties described above, make the HIV membrane a suitable target for membrane-active virucides. An additional factor, shared with other enveloped viruses, is that static HIV particles lack the membrane-repairing mechanisms existing in metabolically active host cells, and therefore cannot escape the damage induced by the potential virucide activity displayed by those compounds (Vigant et al., 2015; Wojcechowskyj and Doms, 2010).

The set of compounds described to intercalate between the lipids of the HIV envelope may alter its physical chemistry, and thereby interfere with the entry function. These compounds appear to incorporate into the viral membrane following two distinct mechanisms, namely: (i) recognition and binding to specific viral lipid species; and (ii) capacity for partitioning effectively from water into the Chol-enriched, highly packed lipid envelope. These pathways of interaction also define different degrees of specificity with respect to the cell membranes. In this section, the membrane-active anti-HIV compounds described in the literature are summarized using their membrane-insertion mechanism as the primary criterion for their classification.

Compounds that target Chol

As mentioned before, the functional requirement of Chol for entry, makes this compound an attractive anti-HIV target. Cyclodextrins (CD) are perhaps the compounds most widely used to block HIV infection by targeting Chol. CDs are cyclic oligosaccharides that are used to deplete or incorporate this molecule into membranes. In the early 00s, several research groups investigated the effect of CD-induced Chol extraction from HIV virions (Campbell et al., 2002; Guyader et al., 2002; Liao et al., 2003) and HIV-producing cell lines (Liao et al., 2001; Ono and Freed, 2001) and determined that this lipid is essential for HIV infection.

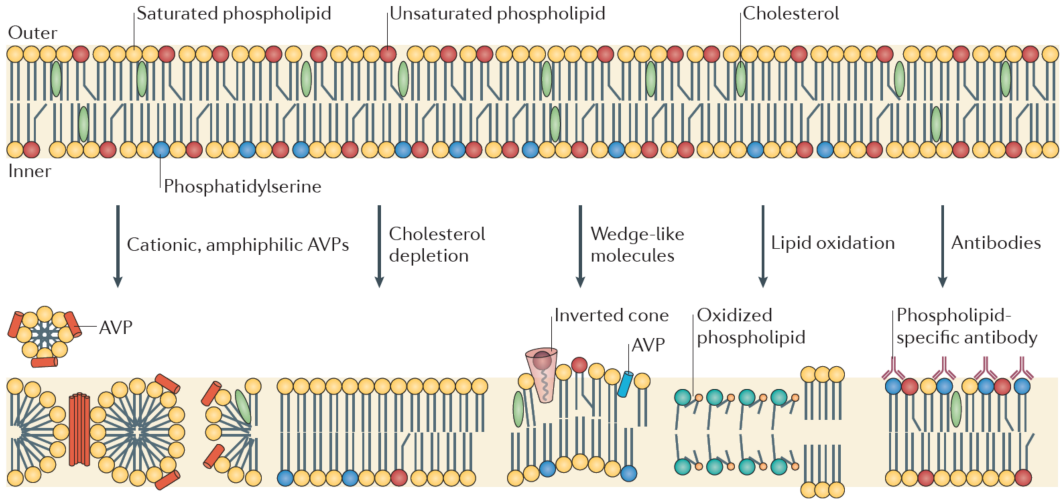

Figure 1.6: Schematic diagram of different membrane-targeting anti-viral mechanisms. AVP stands for anti-viral peptides. Taken from Vigant et al. (2015), who have not taken into account the loss of lipid asymmetry.

Specifically, Chol seems to be required only during the fusion step, since Chol-depleted viruses remain intact, are able to bind to receptors on target cells, and CD-mediated Chol replenishment restores their infectivity (Campbell et al., 2002).

Yet, the exact mechanism that explains why Chol depletion inhibits HIV fusion is still to be determined. Its negatively curved nature is known to facilitate fusion (Aeffner et al., 2012) but other models have arisen. The influenza virus, which also includes around 50% Chol in its envelope (Gerl et al., 2012), loses infectivity upon its depletion too (Sun and Whittaker, 2003). In fact, a moderated reduction of envelope Chol accelerates fusion kinetics (Domanska et al., 2013) and brings hemagglutinin molecules closer to each other as described in Domanska et al. (2015). In that work, the authors propose a model where lipid domains in the viral membrane rule the distribution of hemagglutinin, and Chol depletion alters the organization of such domains. CD treatment induced first coalescence and then disappearance of ordered domains. An active role in fusion of Chol-dependent lipid domains has also been noted in recent studies, in which it is proposed that the process starts at boundaries between ordered and disordered domains (Yang et al., 2016a, 2017). The putative role of lipid nanodomains in HIV fusion is studied in chapters 4 and 5 of this thesis.

Other methods to reduce the membrane Chol level, such as the use of liposomes including polyunsaturated fatty acids, have proven efficient in inhibiting hepatitis B virus, hepatitis C virus (HCV) and HIV infection (Pollock et al., 2010). Phenothiazines have been also described to interact with this compound and inhibit HCV infectivity, an effect that correlated with the increase of viral membrane fluidity

(Chamoun-Emanuelli et al., 2013). Finally the antifungal antibiotic Amphotericin B also binds to Chol in the viral envelope and inhibits HIV infection (Schaffner et al., 1986). Its methyl ester form (AME) is a modified version with reduced cytotoxicity (Waheed et al., 2006). AME disrupts membrane morphology (Waheed et al., 2008) and inhibits infection of HIV-1 isolates with an intact version of the cytoplasmic tail (CT) of gp41 (Waheed et al., 2007). HIV has been able to develop AME resistance via cleavage of the CT of gp41 by the viral protease, upon incorporation of the P203L and S205L mutations.

Compounds that target aminophospholipids

Transbilayer asymmetry is lost in the viral membrane, thus the aminophospholipids PE and PS localize also in the outer leaflet of the HIV-1 envelope (Callahan et al., 2003; Henriques et al., 2012). In human cells aminophospholipid exposure is related to a number of conditions, such as apoptosis or blood coagulation (Zwaal et al., 2005). Aminophospholipid exposure is not common in healthy cells, making PE and PS interesting targets against HIV (Soares et al., 2008). In fact, some human proteins interact with aminophospholipids accessible on the lipid envelope to block virus spread. Most notably, TIM proteins capture virions immediately after budding from the plasma membrane by binding PS with their conserved PS-binding IgV domain, thus inhibiting HIV-1 release (Li et al., 2014).

PS is not only accessible on the surface, but also overall enriched in the viral envelope (Lorizate et al., 2013). Whether the virus requires PS and actively selects it from the plasma membrane or it only constitutes remains of lipid rafts is still unknown. Some enveloped viruses have been reported to use PS-binding proteins that participate in apoptotic cell recognition as an alternative mechanism to bind target cells (Morizono and Chen, 2014). HIV-1 is able to take advantage of PS in some circumstances too. Indeed, annexin V binding to PS in virions inhibits macrophage infection (Callahan et al., 2003). In contrast, macrophage infection by vesicular stomatitis virus (VSV) or Abelson murine leukaemia virus (aMLV) pseudotyped particles is not inhibited by annexin V, suggesting the process is HIV Env specific, even if the treatment does not alter HIV-1 binding to target cells. Recent studies have reported that HIV induces cell plasma membrane PS exposure, which acts as a cofactor for Env mediated fusion (Zaitseva et al., 2017).

Anti-PS antibodies have been show to target virus-infected cells and even enveloped virus themselves. Bavituximab is a chimeric PS-targeting antibody that is able to clear Pichinde infectious viruses from blood (Soares et al., 2008) or bind Ebola virions (Dowall et al., 2015). It can be effective in anti-cancer therapies and is in clinical trial for treatment of different tumors (He et al., 2009; Vasiljevic et al., 2015). Antibodies naturally occurring during HIV infection, such as the anti-MPER 4E10 broadly neutralizing antibody (bNAb), also recognize PS in

the viral membrane to enhance affinity for the membrane-inserted protein epitope (Irimia et al., 2016; Rujas et al., 2017a). This mechanism was also recently extended to the anti-MPER 10E8 bNAb (Irimia et al., 2017).

The other aminophospholipid, PE, constitutes also a major target for host defense antimicrobial peptides (Phoenix et al., 2015). Cyclotides, cyclic peptides from some angiosperm families, are defense peptides that target bacterial and viral membranes among others. Kalata B1 is a cyclotide that inhibits HIV-1 infection. This activity has been linked to the ability to bind to PE in the context of biological membranes, since kalata B1 membrane association is receptor independent (Sando et al., 2011). Kalata B1 membrane interaction is favored in raft-like lipid environments and appears to follow this sequential mechanism: PE binding, membrane insertion, induction of PE flip-flop to the outer leaflet, binding of more kalata B1 monomers, permeabilization and subsequent membrane disruption, which seems to result in the infection inhibition (Henriques et al., 2011). Other cyclotides that bind PE possess anti-HIV properties as well (Henriques et al., 2012).

Non-specific, curvature-modifying and lipid-oxidizing agents

Targeting specific lipids presents some major drawbacks for virucidal efficacy. Since the exact mechanism for membrane composition selection during budding has not been clarified yet, it cannot be discarded that the targeted lipids are not totally essential for infection. If that were the case, resistant viral mutants not exposing those species would be expected to emerge. Thus, instead of targeting a single chemical compound (lipid or protein), interest in the development of virucides inserting non-specifically into the viral membrane has grown in the last few years. However, this approach presents an enormous challenge: to target the viral membrane, avoiding damage to the plasma membrane of cells or other extracellular vesicles. Nonetheless, there are some physicochemical specificities of viral membranes that can be exploited. A better understanding of the role of the viral lipid envelope during the infection cycle will for sure help in this effort and has been one of the goals of this thesis work.

As mentioned above, the stalk intermediate has a mean negative curvature (Fig. 1.5). In this regard membrane curvature is a targetable physical property of viral envelopes. Thus, whereas cone-shaped lipids, such as Chol or PE, promote negatively curved membrane structures, helping to overcome the energetic barrier for fusion; inverted-cone compounds, such as lysophosphatidylcholine (LPC), confer positive curvatures to biological membranes and have been shown to inhibit viral fusion (Güther-Ausborn et al., 1995; Martin and Ruysschaert, 1995). However, lipids are not suitable pharmaceutical compounds, because they are cytotoxic and rapidly metabolized or degraded. Thus, non-cytotoxic and more stable compounds

have been recently developed to target viral membrane curvature.

For instance, rigid amphipathic fusion inhibitors (RAFIs) are wedge-shaped (inverted cone-shaped, favoring positive curvature) small molecules that insert into lipid membranes and inhibit infection of enveloped viruses blocking a step prior to viral entry (Colpitts et al., 2013; Guyader et al., 2002). Importantly, the IC_{50} of a number of RAFIs is greatly lower than their CC_{50}, i.e. they are inhibitory at non-toxic concentrations.

Amphiphilic thiazolidine derivatives, another set of broad-spectrum antiviral compounds targeting membranes were reported almost at the same time than RAFIs (Wolf et al., 2010). LJ001 and more effectively LJ130 (Vigant et al., 2013) are type II photosensitizers that partition into the membrane of different enveloped viruses and upon light irradiation produce $^1O_2$ that oxidizes phospholipid double bounds, altering the physical properties of the membrane and inhibiting membrane fusion (Hollmann et al., 2014; Vigant et al., 2013). Phospholipid C=C double bound oxidation may fix acyl chain position preventing the membrane reorganization necessary for fusion (Hollmann et al., 2015). Interestingly, RAFIs where also proposed to exert their virucidal effect through photooxidation of the viral envelope (Vigant et al., 2014).

Non-specific, membrane-active peptides

A plethora of small peptides, including antimicrobial peptides as the human neutrophil peptide 1 (HNP-1), has been described to display anti-HIV activity (Vancompernolle et al., 2005; Wang et al., 2010; Zhang et al., 2002). However, the mechanism of action of these compounds is poorly understood and appears to rely mostly on their lectin-like properties (Demirkhanyan et al., 2012). Some aromatic-rich short peptides have been reported to block viral entry by changing directly the physical chemistry of the viral membrane upon partitioning (Badani et al., 2014; Galdiero et al., 2015). A series of works support the possibility that peptides derived from hydrophobic-at-interface envelope glycoprotein sequences, such as C5A from HCV or CpreTM from HIV, both showing antiviral activity against HIV (Apellaniz et al., 2011; Bobardt et al., 2008), may comprise new generic antivirals (Galdiero et al., 2008; Giannecchini et al., 2003; Hrobowski et al., 2005; Sainz Jr. et al., 2006; Spence et al., 2014). In the particular case of HIV-1, the gp41 MPER-TMD region (Fig. 1.3) encompasses sequences enriched in aromatic residues with the potential of inserting into the lipid envelope (Lorizate et al., 2008), which provides a template for virucidal peptides (see chapter 5 of this thesis).

1.1.6 Broadly neutralizing antibodies

Env is the only viral protein accessible on the viral envelope and thus, it is the main target of the immune response. However, despite the accessible location, elicitation of a protective response occurs only in 10-25 % of HIV-infected individuals (Doria-Rose et al., 2009; Stamatatos et al., 2009). Usually, neutralization arises from the combined action of different Env-targeting antibodies. Still, a small number of patients (ca. 1%) develop broadly high neutralization breadth and potency responses (Simek et al., 2009), that sometimes arise from the activity of a single antibody, i.e. a broadly neutralizing antibody (bnAb). bnAbs have attracted great interest because understanding their molecular neutralization mechanism can help in the development of immunogens that could be used in the design of anti-HIV-1 vaccines.

HIV-1 presents different immune evasion mechanisms that prevent highly neutralizing responses. The high mutational rate that arises from the HIV error-prone reverse transcriptase (Roberts et al., 1988), leads to an estimated 35 % sequence variability between virus subtypes known as clades (Gaschen, 2002). Env is also a higly glycosylated protein, with 24 possible glycosilation sites distributed along gp120 and gp41, which hinders epitope accesibility. Also, due to the low oligomer stability, the protein is presented in different forms on the viral surface. Apart from the functional trimeric structure, the poor stability of the gp120/gp41 complex promotes oligomer disassociation leaving non-functional gp41 stumps on the surface of the virus, that are recognized by non-neutralizing antibodies (Cavacini et al., 1998; Gohain et al., 2016). Non-functional gp160 aggregates are also present in the viral membrane and deviate the humoral response(Moore et al., 2006). In addition, the viral membrane also plays a role in masking the conserved MPER segment possibly by interfering with the generation of an immune response against this region.

Env-targeting bnAbs bind to different regions (*vulnerability sites*) of gp120 and gp41: CD4-binding site (CD4bs), the trimer apex and the high-manose patch on gp120; gp120-gp41 interface and MPER on gp41. The most widely studied anti-Env bnAbs (summarized in Fig. 1.7) were recently reviewed by Burton and Hangartner (2016). This thesis work has been focused on anti-MPER antibodies and the role played by antibody-viral membrane interactions in the neutralization process (see chapter 6 of this thesis).

Anti-MPER antibodies

MPER constitutes a conserved tryptophan-rich domain on the Env glycoprotein (Fig. 1.3) that represents a site of vulnerability targeted by neutralizing antibodies, some of them, e.g. 4E10 and 10E8, with remarkably high breadth (Stiegler et al.,

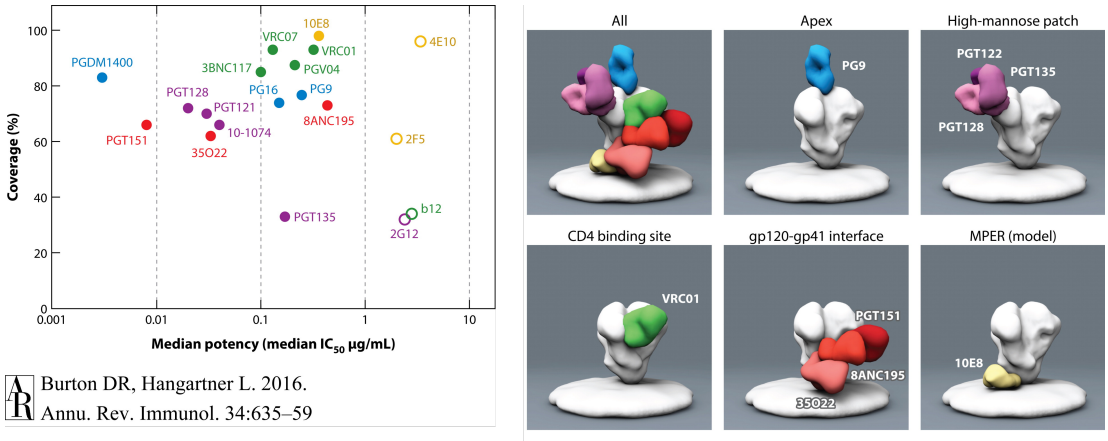

Figure 1.7: Anti-Env broadly neutralizing antibodies. (Left) Breadth (coverage) and potency (IC_{50}) of the most neutralizing anti-HIV antibodies. (Right) bnAbs bound to different interaction sites on the Env spike. Both images taken from Burton and Hangartner (2016).

2001; Huang et al., 2012) (Fig. 1.7). Due to the conserved nature of this region and the high effectiveness of anti-MPER antibodies, multiple studies have tried to shed light on the neutralization and elicitation mechanisms of these antibodies.

MPER is embedded into the membrane interface hindering recognition and, thus, engagement by antibodies (Nieva et al., 2011). However, bNAbs targeting this conserved region have evolved to incorporate structural elements to both recognize and engage the epitope in a membrane environment. The hydrophobic residues at the apex of the long CDR-H3 loop of anti-MPER antibodies are involved in mediating epitope recognition in biological membranes and, therefore, they are required for viral blocking ((Alam et al., 2007; Huang et al., 2012; Scherer et al., 2010)). In addition, several studies have shown the capacity of 4E10 to directly bind lipids (Alam et al., 2009; Irimia et al., 2016; Rujas et al., 2017a), although the nature of the lipid-4E10 interaction is still a matter of controversy. On the other hand, despite multiple similarities encountered between 4E10 and 10E8 antibodies, such as binding overlapping epitopes within MPER, 10E8 lacks the overall membrane binding tendency of 4E10 (Huang et al., 2012; Kwon et al., 2016), although some authors have reported 10E8-lipid interactions (Chen et al., 2014; Irimia et al., 2017).

Lipid interaction has been proposed as a strategy employed by anti-MPER antibodies to increase their neutralization potency either by acquisition of a second binding site and thus, increasing antibody avidity (heteroligation) (Klein et al., 2013) and/or by providing an opportunity window to capture gp41 fusion intermediates from a membrane pre-concentrated state (Alam et al., 2009)). Heteroligation, i.e., to combine strong binding to gp41 and weak binding to viral membrane, might be of special importance for HIV blocking due to its low spike density (Zanetti et al.,

2006). Interestingly, although 10E8 antibody does not display strong interactions with membranes, it exhibits higher potency than any anti-MPER reported to date with an IC_{50} mean value of 0.35 μg/mL (Huang et al., 2012).

Due to the critical role adscribed to the region targeted by the 4E10 and 10E8 antibodies in HIV infection, a phenomenon at the origin of their exceptional neutralization breadth, these antibodies serve as models of broad protection against HIV infection, particularly for the purpose of vaccine design.

1.2 Quantitative fluorescence microscopy

1.2.1 Fluorescence

Light absorption is a process by which energy is transferred from a photon to a molecule. Photons have an energy proportional to their frequency as indicated in eq. 1.1:

$$E = h\nu = \frac{hc}{\lambda} \tag{1.1}$$

Where h is the Planck constant and ν is the photon frequency that is inversely proportional to the wavelength (λ) and related to the speed of light (c). In common absorption events (represented in Fig. 1.8) a molecule gets energy from one (or more) photons and is excited from the ground state (S_0) to a higher electronic state (S_1 or S_2) (10^{-15} s). Excited molecules can loss this excess of energy through radiative and non-radiative electronic transitions. At room temperature thermal energy is not sufficient to populate excited vibrational states so after excitation, electrons relax to the lowest energy vibrational state (10^{-12}-10^{-10} s) (wavy lines in Fig. 1.8). Electrons can also undergo internal conversion (10^{-12} s), i.e. a non-radiative transition where the electrons relax to the lowest vibrational state within S_1 (dashed line in Fig. 1.8). Complete electronic relaxation to the ground state can occur through different paths. If it involves spontaneous emission of light the phenomenon is known as luminescence.

Luminescence is the emission of a photon by a molecule. If the electronic transition to one of the vibrational levels of the ground state occurs between states with the same spin (10^{-9} s) the phenomenon is known as fluorescence. Excited electrons can also undergo a spin conversion to the first triplet state (T_1), known as intersystem crossing. Since the electron pair spins are no longer paired relaxation from S_1 to S_0 is a classically forbidden mechanism and thus, with low probability, excited states involving unpaired electrons present longer lifetimes. Either relaxation mechanism involves photon emission. The emitted photon wavelength is proportional to the energy gap between electronic states and

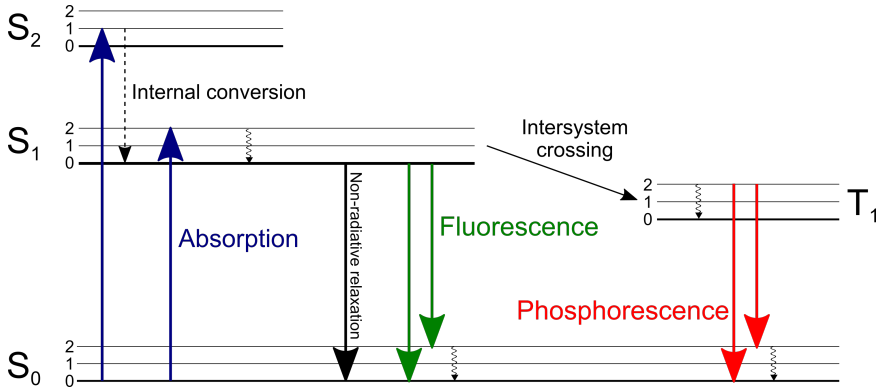

Figure 1.8: Simplified Jablonski diagram for two luminescence events: fluorescence and phosphorescence. S_0, S_1 and S_2 represent the ground, first and second singlet electronic states respectively. T_1 is the triplet electronic state. Different vibrational energy levels are depicted as 0, 1 and 2. Colored lines indicate events involving photon absorption (blue) or emission (green and red). Black lines correspond to non-radiative events. Wavy lines indicate vibrational relaxation.

independent from the excitation wavelength, although it is generally longer (lower energy). This photon frequency difference is known as the Stokes shift. Energy differences arise from non-radiative relaxation events, such as internal conversion or interactions with the solvent (solvatochroism, see next section 1.2.3).

There are exceptions to the Stokes shift. Under some circumstances such as multiphoton excitation, the emission wavelength is shorter than that of the excitation, i.e. emitted photons are more energetic than those absorbed. A molecule can be excited by simultaneously absorbing two or more photons (Fig. 1.9) if the sum of their energy matches the energy difference between the ground and first singlet electronic states. Photon absorption occurs at very short times (10^{-15} s), so absorbed photons must coincide in time (within 10^{-16} and 10^{-15} s) and space. High photon densities are achieved using mode-locked lasers that generate femtosecond optical pulses.

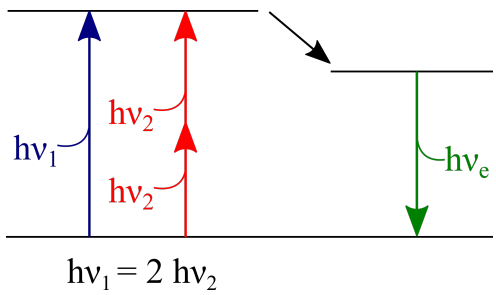

Figure 1.9: Simplified Jablonski diagram for one and two photon absorption and subsequent emission. $h\nu_1$ and $h\nu_2$ are the absorbed photons by single or two-photon excitation respectively. $h\nu_e$ is the emitted photon.

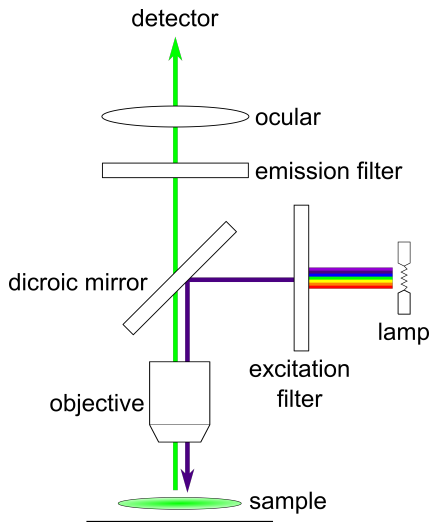

Figure 1.10: Schematic of a epifluorescence microscope.

Fluorescent molecules cannot undergo an infinite number of excitation and emission cycles. Photobleaching is the irreversible photon-induced damage that results in the inability of a fluorophore to emit light. Molecules in their excited state are highly reactive and can interact with themselves or surrounding molecules, which turns into isomerization, destruction of covalent bonds or formation of new bonds with other molecules. The excited triplet state is involved in most photoinduced reactions, because it is long-lived compared to the singlet state and thus, molecules in their triple state are more prone to react with neighbor molecules and triplet oxygen. .

1.2.2 Fluorescence microscopy

Fluorescence microscopy is a widely exploited field in life sciences. It is used to obtain high contrast magnified images of a sample of interest. Widefield epifluorescence microscopes are the most common piece of equipment used for fluorescence imaging because of high usability and relative low price. In a common widefield epifluorescence microscope (schematic in Fig. 1.10) lamps are used as light sources. Illumination light passes through an excitation filter located before the objective that selects an excitation wavelength. Fluorescence emission is collected through the same objective and separated from excitation light by a dichroic filter. Unwanted light is rejected by the emission filter just before reaching the detector (which converts light in an electric signal) or the eye pieces that allow direct viewing.

This set-up presents some disadvantages such as the inability for optical sectioning, i.e. the capability of an optical system to create resolved images of focal planes.

In widefield fluorescence microscopy all planes in the sample are excited, collected and imaged at the same time, which can lead to loss of contrast and photodamage of fluorophores out of the focal plane. Different fluorescence microscopy techniques permit optical sectioning, such as confocal, multiphoton or total internal reflection microscopies.

Confocal microscopy

Confocal microscopy allows optical sectioning by rejecting out-of-focus light through spatial filtering. A pinhole (an optical aperture) that rejects out-of-focus light is introduced in the emission path before the detector. Light coming from planes below or above the focus plane cannot pass through the pinhole and thus it is not collected by the detector, dramatically enhancing contrast. In confocal microscopy instead of a lamp, a laser is used as an excitation light source, greatly reducing the focal volume. The excitation beam is scanned across the sample by two oscillating mirrors (scanner) and the emitted light is collected by the same objective and reflected by the mirrors of the scanner (de-scanned detection). In some cases detectors are placed before the scanner to enhance sensitivity and they are referred to as non-descanned detectors (NDD-s). Once the emitted light travels across the pinhole aperture, it is detected and converted into an electric signal by a point detector, such as a photomultiplier tube (PMT) or an avalanche photodiode (APD). This signal is translated into pixels, which are used to generate a reconstructed digital image.

As noted, single-photon optical sectioning is introduced after the sample is excited, i.e. molecules outside the focal plane are also excited but their emission is not collected. This can represent a major drawback when using labile probes. Labile fluorophores are imaged by set-ups that allow excitation sectioning, reducing photobleaching of the sample out of the focal plane. This is achieved by using high numerical aperture lens and pulsed illumination sources.

Multiphoton microscopy

As stated before, two-photon excitation is a process in which a molecule is excited by simultaneous absorption of two photons of half the energy gap between the ground and the excited state (Fig. 1.9), where each photon provides half of the energy required for excitation. Pulsed lasers allow two-photon excitation because they emit light pulses of extremely high photon densities instead of continuous waves, favoring simultaneous multiphoton excitation at the laser beam focus (where highest photon densities are achieved) but not in the areas above or below the focal plane.

Advantages of multiphoton microscopy are multiple, such as excitation sectioning

(without using pinhole apertures), which turns into higher contrast images, or the use of infrared light to excite UV fluorophores, reducing photodamage and facilitating long term imaging of the sample. Also infrared light present higher penetrability, due to reduced scattering and lower absorption by the medium. Multiphoton microscopy presents some disadvantages too, e.g. the use of longer excitation wavelengths that turns into reduced resolution because of the use of longer emission wavelengths or the need of more expensive and complicated instrumentation.

1.2.3 Environmental sensitive probes

Typically fluorophores have a large dipole moment that arises from charge separation within the molecule. When the dipole moment (μ) is much larger in the excited state (μ_E) than in the ground state (μ_G), the excited molecule can be stabilized by the solvent molecules through reorientation (relaxation) of solvent dipoles around μ_E. This effect is enhanced with solvent polarity, giving rise to longer emission wavelengths in polar environments (Fig. 1.12. Solvent relaxation mainly affects the emission spectra rather than the absorption spectra. Solvatochroism can be explained with the Lippert-Mataga equation:

$$\nu_A - \nu_F = \frac{2}{hc}\left(\frac{\epsilon - 1}{2\epsilon + 1} - \frac{n^2 - 1}{2n^2 + 1}\right)\frac{(\mu_E - \mu_G)}{a^3} + \text{constant} \tag{1.2}$$

Where $\nu_A - \nu_F$ is the wavenumber difference between the absorbed and the emitted photons (Stokes shift), ϵ and n are the dielectric constant and the refractive index of the solvent respectively and a^3 is the volume of the cavity occupied by the fluorophore. The constant represents the Stokes shift in the gas phase. The whole term in the parentheses is termed orientation polarizability (Δf) and accounts for properties of the solvent. The first term in the parentheses depends on both the redistribution of electrons and the reorientation of solvent molecules around the fluorophore and is thought to be the only solvent property affecting the Stokes shift significantly. In fact, the second term only depends on the redistribution of electrons, which happens roughly on the time scale of absorption and hence affect equally both the excited and the ground state. In conclusion, high Stokes shifts arising from large differences between the dipole moment in the excited and the ground state ($\mu_E - \mu_G$) are explained by the Lippert-Mataga equation and mainly depend on the polarity of the solvent.

Solvent relaxation is a phenomenon that can be exploited to study membrane biophysics. Fluorescent dyes that present (i) a big difference between the ground and excited state dipoles, (ii) partition to the membrane and (iii) have their fluorescent moieties around the bilayer interface are suitable to quantify membrane molecular order. In tighlty packed lipid bilayers water accessibility to the membrane is limited and so, the membrane interface constitutes an apolar environment. On

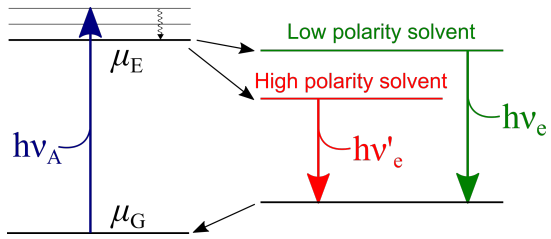

Figure 1.11: Simplified Jablonski diagram for solvent relaxation (black arrows) effects. $h\nu_A$ is the absorbed photon. $h\nu_e$ and $h\nu'_e$ are the photons emitted in low and high polarity solvents respectively. μ_E and μ_G are the dipole moments in the ground and excited states.

the contrary, in fluid membranes the interface is highly hydrated/polar and emission is redshifted in comparison with rigid membranes (Fig. 1.11). The spectral shift for these fluorophores is thus, a function of the hydration and viscosity of the membrane, reflecting its phase state.

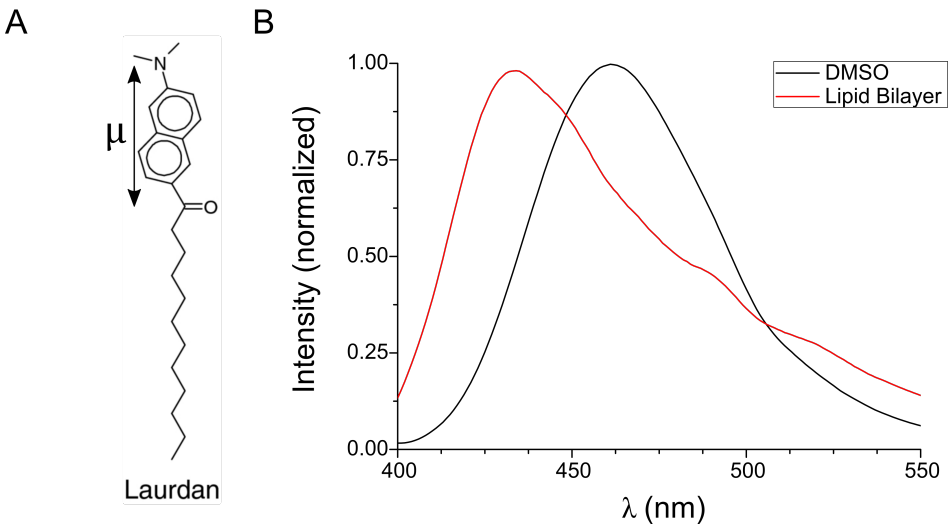

Figure 1.12: (A) Molecular structure of Laurdan. The double arrow (μ) represents the dipole moment. Fluorescence properties arise from the 2-dimethylaminonaphtalene group and the 6-lauroyl group is responsible for membrane partition. (B) The Stokes shift derived from environmental polarity changes: DMSO dissolved Laurdan emission spectrum is compared with that one of Laurdan incorporated into lipid vesicles at 25° C. Excitation wavelength was 374 nm.

6-lauoryl-2-dimethylaminonaphtalene (Laurdan) resembles all the properties enumerated above. Laurdan is a naphthalene derivative first synthesized by Weber and Farris (1979). The fluorescent moiety of Laurdan has a significant dipole moment (μ) because of partial charge separation between 2-dimethylamine and 6-carbonyl groups (Fig. 1.12 A). The dipole moment increases upon excitation and causes the reorientation of solvent molecules, decreasing the energy level of excited

molecules and causing a solvent polarity dependent Stokes shift (Parasassi et al., 1998) (exemplified in Fig. 1.12 B). Due to the presence of the 6-lauroyl group, Laurdan partitions into lipid bilayers in a phase independent manner (Krasnowska et al., 1998). It has been demonstrated that the chemical nature of the polar head-group or the net charge of phospholipids do not affect water accessibility to the interface, which rather depends on the molecular order of a given membrane phase state (Parasassi et al., 1998; Amaro et al., 2017).

A wavelength ratiometric parameter called Generalized Polarization (GP) quantifies Laurdan's emission spectral shift from tightly packed bilayers (hardly hydrated) to loosely packed (highly hydrated) membranes, thus providing an indirect measurement of membrane order through lipid packing:

$$GP = \frac{I_B - G \times I_R}{I_B + G \times I_R} \tag{1.3}$$

.

Where I_B and I_R are the emission intensities in the blue and red edges of the emission spectrum and G is the calibration factor. This G factor was introduced by Gaus et al. (2003) to normalize GP values obtained in different equipment/conditions and is calculated by the following equation:

$$G = \frac{GP_{ref} + GP_{ref}GP_{mes} - GP_{mes} - 1}{GP_{mes} + GP_{ref}GP_{mes} - GP_{ref} - 1} \tag{1.4}$$

GP_{mes} is the GP value of pure Laurdan dissolved in dimethyl sulfoxide (DMSO) measured in the same experimental conditions of all samples. GP_{ref} is a reference that has been established as the convention value ($GP_{ref} = 0.207$) (Gaus et al., 2006).

The GP function has been used to measure lipid order of model membranes (Parasassi et al., 1998), cells (Kaiser et al., 2009), viruses (Lorizate et al., 2009) and even whole organisms (Owen et al., 2011). Bulk spectroscopic studies of Laurdan labeled membranes give information about membrane molecular order, but they are not able to detect phase coexistence. In fact, when lateral segregation exists, the GP value obtained by spectroscopic measurements is an average value of the GP values corresponding to each phase.

Multiphoton fluorescence microscopy is normally used to study membrane lateral structure and phase segregation behavior in model and biological membranes labeled with Laurdan (Kaiser et al., 2009) reviewed by Bagatolli (2006). Laurdan is excited around 400 nm, which makes it compatible with multiphoton microscopy (800 nm). As detailed in the previous 1.2.2 section, multiphoton excitement minimizes photobleaching of the sample by restricting the process to the focal plane (excitation sectioning). Lateral resolution is the main drawback of this technique since resolution achieved by an optical microscope set-up is proportional

to the numerical aperture of the lens and inversely proportional to the wavelength (equation 1.11). It has been predicted for lipid rafts to comprise an area of 50-200 nm (Lingwood and Simons, 2010; Sezgin et al., 2017a), making them not detectable by fluorescence microscopy. Instead each pixel would contain information of different phases coexisting in the corresponding area. Recently, several works combine super-resolution microscopy (see next section 1.2.5) with polarity sensitive probes and have reported membrane compositional heterogeneity (Moon et al., 2017; Sezgin et al., 2017b). Phase behavior can also be studied in giant vesicle model membranes, because lipid domains (not to be confused with rafts) comprise greater areas in these models, which are visible by conventional microscopy.

Some modern microscopes are equipped with detection systems that divide the emission in 32 channels, allowing to collect the whole emission spectra of a fluorophore for each pixel, instead of the common two channel detection methods (Sezgin et al., 2015a). This approach, known as spectral imaging, combines the benefits of spectroscopic and microscopic measurements.

Other polarity-sensitive probes that report on membrane molecular order have been developed too. C-Laurdan is a Laurdan derivative with improved photostability, allowing for single photon excitation (Dodes Traian et al., 2012). Di-4-ANEPPDHQ is an environmental sensitive probe that was first developed as a membrane potential sensor (Obaid et al., 2004). Compared to Laurdan, di-4-ANEPPDHQ's excitation spectrum is red-shifted and the molecule can be excited using a 488 nm laser line, available in most comercial confocal microscopes. Interestingly, Laurdan and di-4-ANEPPDHQ do not report on the same membrane properties, as the latter presents complex relaxation kinetics greatly influenced by cholesterol (Amaro et al., 2017). A number of di-4-ANEPPDHQ derivatives with improved photostability or different excitation/emission spectra have been developed. A systematic study of the properties and behavior of the most widely used polarity sensitive probes was published by Sezgin et al. (2014).

1.2.4 Fluorescence correlation spectroscopy

Fluorescence correlation spectroscopy (FCS) is a methodology based on the statistical analysis of fluorescence intensity fluctuations that offers high-resolution (temporal and spatial) analysis. FCS allows for accurate determination, among others, of local concentrations, mobility coefficients or characteristic rate constants of reactions of fluorescently labeled biomolecules.

The fluorescent emission of a diffraction limited spot (Fig. 1.13 A) is detected and used to construct the fluctuating intensity trace (Fig. 1.13 B). The deviations from the mean intensity arise from the temporal spontaneous variation of the number or brightness of fluorescent particles in the illuminated focal volume. The mean number of fluorescent molecules that are simultaneously at the illuminated

focal volume (N) is determined by the concentration of molecules; but the frequency with which that number changes causing a fluctuation of the fluorescence intensity is conditioned mainly by the mobility of the molecules in and out of the focal volume. Thus, the main source of fluctuations is the diffusion of the molecules. In addition, photophysical fluctuations such as the triplet state affect the brightness of the molecules, producing fluctuations that are also reflected on the intensity trace.

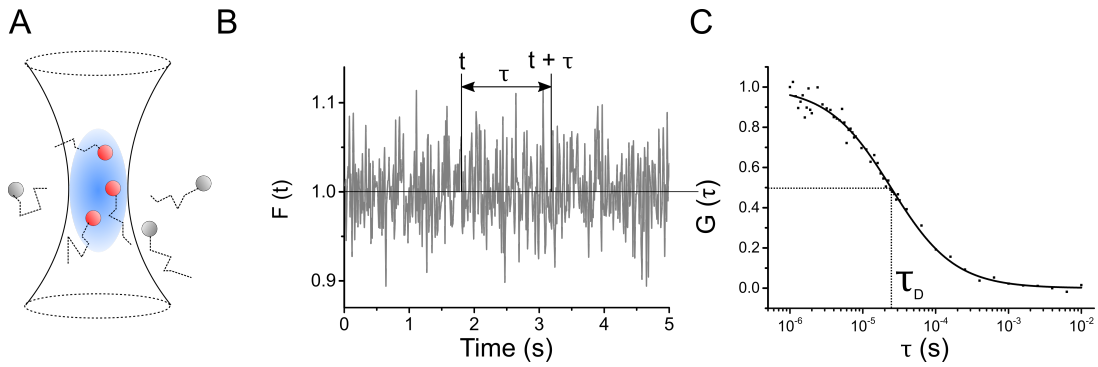

Figure 1.13: Basis of an FCS experiment. (A) Fluorescent emission of molecules diffusing inside the focal volume is measured. (B) The fluctuating intensity (F (t)) trace contains the information about the processes that affect the fluorescence. (C) From the trace, the autocorrelation function is calculated, from which the concentration and diffusion-coefficients of the molecules can be determinated.

Obtaining the information about the sources of the fluctuations contained on the intensity traces requires being able to differentiate those fluctuations from the mean intensity value, i.e. having a high signal to noise ratio. Therefore, to obtain accurate measurements FCS must be performed with very low number of molecules (N ≈ 1-100) simultaneously at the focal volume, so that each of them contributes substantially to the measured signal. This is achieved using very low sample concentrations (in the nanomolar range) and reducing the observation volume (V_{eff}) to ≈ 1 fL. This detection volume is created by focusing a laser light to a diffraction-limited spot with a high numerical aperture objective (NA > 0.9). The effective volume has an ellipsoid shape and is defined by the sizes of its radius (ω_0) and height (z_0):

$$V_{eff} = \pi^{3/2}\omega_0^2 z_0 \tag{1.5}$$

The eccentricity parameter defines the shape of the focal volume:

$$S = z_0/\omega_0 \tag{1.6}$$

Reduction of N must be accompanied by a high-enough photon count rate per detected molecules per time unit to obtain enough data for a strong statistical

analysis of the fluctuations. This requires bright fluorescent dyes, i.e. dyes with high extinction coefficients (absorption efficiency) and high quantum yields (emission event rate) ; stable and powerful light sources like lasers; and ultrasensitive detectors, e.g. APDs with single-photon sensitivity. FCS is often referred to as single-molecules technique, because it is based on the measurement of fluctuations of the fluorescence caused by changes in the number or brightness of single molecules. However, it does not analyze each molecule individually, but it obtains the information through the statistical analysis of the signal of many molecules.

Access to the information contained on the intensity trace is possible by calculation of the autocorrelation function (ACF). The ACF provides a measure of the self-similarity of the signal at points separated by different lag times (τ), and is used to identify characteristics of a signal that are repeated in time. The ACF describing a single species freely-diffusing in 3 dimensions is:

$$G(\tau) = \frac{1}{V_{eff}\langle C\rangle}\frac{1}{\left(1+\frac{\tau}{\tau_D}\right)}\frac{1}{\sqrt{1+\left(\frac{\omega_0}{z_0}\right)^2\frac{\tau}{\tau_D}}} \tag{1.7}$$

The various sources of fluctuation that affect the fluorescent signal have different characteristic frequencies, so they are represented at different temporal regions of the ACF. In this thesis, FCS has been used to study the characteristics of diffusion, which are reflected at intermediate lag times: 10^{-5} - 10^{-2} (Fig. 1.13 C). The time necessary for the ACF to decay to the half of its maximal value at that interval (τ_D) characterizes the mean time molecules spend inside the detection volume. It is directly related with the diffusion coefficient of molecules (D) and the radius of the focal volume, allowing the determination of those parameters:

$$\tau_D = \frac{{\omega_0}^2}{4\ D} \tag{1.8}$$

The amplitude of the ACF at $\tau = 0$ ($G(0)$) is inversely proportional to the number of fluorescent molecules at the focal volume, so it provides the possibility to measure the concentration:

$$G(0) = \frac{1}{N} = \frac{1}{C\ V_{eff}} \tag{1.9}$$

Scanning FCS

The determination of the concentration and diffusion coefficients of proteins in solution by conventional FCS may be useful for the study of different processes, e.g. the binding kinetics of antibodies to viruses (Ray et al., 2014). However, FCS in this thesis has been used to study the interaction of the antibodies with

membranes and membrane-inserted epitopes, which requires the adaptation of the technique to overcome two major limitations that arise from the application of FCS on membranes. One is that the slow thermal movements of the membrane may put it partially or totally out of the focal volume at some moments of the measurements, introducing artefacts on the ACF. The other one is that membrane bound molecules diffuse much slower than in solution, so they would stay longer inside the illuminated focal volume, making them more prone to photodegradation as consequence of a prolonged excitation.

Scanning FCS is the modality of this technique applied to the membrane in which the laser is scanned through a line perpendicular to the membrane plane instead of focusing it on a single point (Fig. 1.14 A). This way, the membrane will always be measured along the scanned line, while data analysis will allow to choose the pixels corresponding to the membrane (Fig. 1.14 B) for the calculation of the ACF. In addition, scanning the focus reduces the exposition of the fluorophores to light, and consequently their susceptibility to photodegradation.

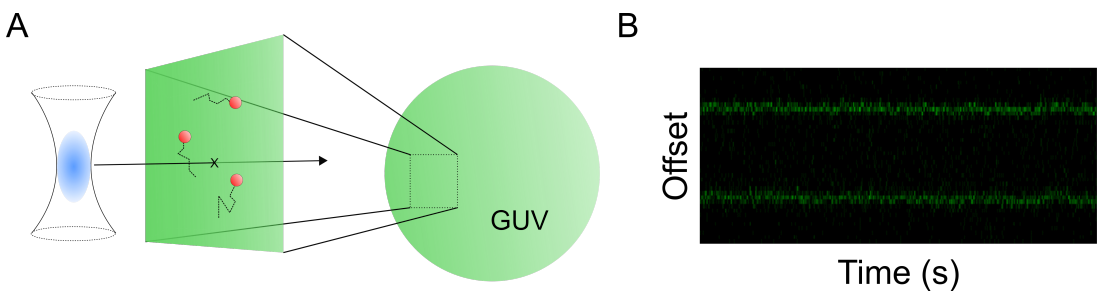

Figure 1.14: Description of the scanning modality of FCS. The laser is repeatedly scanned through a line crossing the membrane of a giant unilamellar vesicle (GUV).(B) Emissionn is collected across all points of the scanning line, that crosses the vesicle membrane twice, so two signals can be distinguished.

Scanning FCS is a modality adapted to membrane-bound molecules, which usually diffuse quite slowly, but the frequency of the scanner poses a limitation to the maximal diffusion coefficient that can be determined. In the set-up used in this thesis, the focus was scanned though a 64 pixel line with a 1400 Hz scan rate, so that each pixel was measured every 714 μs. In consequence for the molecules that spend less than 714 μs on the pixel corresponding to the membrane a precise τ_D cannot be assigned.

Diffusion in a lipid membrane occurs in a single plane rather than in 3D, so the ACF of scanning FCS experiments is fitted to the following model for 2D diffusion:

$$G(\tau) = \frac{1}{N}\left(1+\frac{\tau}{\tau_D}\right)^{-1/2}\left(1+\frac{\tau}{S^2\ \tau_D}\right)^{-1/2} \tag{1.10}$$

1.2.5 Super-resolution fluorescence microscopy

Fluorescence microscopy does not come without limitations. Microscopes are diffraction-limited systems, in other words the spatial resolution of optical microscopy is limited due to the diffraction of light. Resolution is the ability of a system to distinguish closely located features and it is defined as the minimum distance between two discernible objects. In conventional optical microscopy experiments the resolution in the lateral dimension is around 0.25 μm, depending on the wavelength (λ) and the objective numerical aperture (NA):

$$R = \frac{0.61\lambda}{NA} \tag{1.11}$$

This is the Rayleigh criterion for resolution (R); if two objects are further than that distance they can be visualized as two separate objects. Although diffraction-limited resolution is sometimes enough to study biochemical processes, the scale of most biological elements (some organelles, viruses, proteins, lipids, membrane domains...) is well below the resolution limit of optical microscopy and therefore it is difficult to visualize and fully understand most biological processes. There are microscopy techniques that increase resolution by reducing the illumination wavelength, such as electron microscopy. However, it requires extensive sample processing and thus it is not readily applicable to live cells, making it difficult to visualize dynamic processes.

Great efforts have been made during the last two decades to overcome these limitations and the so-called super-resolution fluorescence microscopy or optical nanoscopy techniques that offer sub-diffraction resolution have been (and still are being) developed. In this thesis work the organization of the HIV-1 (ca. 120 nm size) membrane and the interaction of neutralizing antibodies and virucidal compounds with the lipid envelope has been the studied, thus optical nanoscopy techniques have proven very useful.

Sub-difraction resolution has been achieved through different approaches. Stochastic optical reconstruction microscopy (STORM) and photoactivation localization microscopy (PALM) are single molecule stochastic localization microscopy techniques and rely on the photo-activation or photo-switching property of fluorophores to compile the point spread function for each molecule. They offer up to 10 nm resolution (Xu et al., 2012) if the proper deconvolution algorithms are used. PALM and STORM have been used to detect lipid-driven ordered membrane nanodomains (Owen et al., 2012; Moon et al., 2017). Unfortunately, due to the high number of frames needed to successfully reconstruct an image, the time resolution of these techniques is below the time scale of most biological processes. Among nanoscopy techniques structured illumination microscopy (SIM) and near-field scanning optical microscopy (NSOM) should be mentioned as well. Super-resolution fluorescence

microscopy was reviewed by Requejo-Isidro (2013) or more recently by Sahl et al. (2017) and Sezgin (2017)).

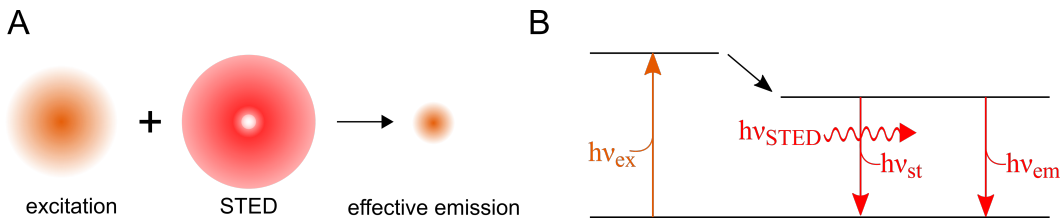

Figure 1.15: STED microscopy. (A) After excitation (orange) molecules are irradiated with a doughnut shaped depletion (STED) beam (red) that switches off excited molecules, reducing the effective emission volume. (B) Simplified Jablonski diagram for stimulated (STED) and spontaneous (em, fluorescence) relaxation.

Stimulated emission depletion microscopy (STED) is a nanoscopy technique that relies on depletion of fluorophores around the focal spot to achieve sub-diffraction resolution (Klar et al., 2000). In a typical absorption/emission cycle an electron is excited to a higher electronic state and afterwards spontaneously relaxes to the ground state emitting a photon. Stimulated depletion is a process whereby non-destructively an excited molecule interacts with a photon and drops to a lower energy level emitting a second photon of identical wavelength. In a STED experiment the molecules are switched off using a depletion laser (STED beam) that stimulates relaxation (Fig. 1.15 A). In STED microscopes the excitation beam is overlapped with a doughnut-shaped red-shifted STED beam that depletes the fluorophores only in the periphery of the excitation spot (but not in the center) (Fig. 1.15 A), giving rise to a smaller effective emission volume. Resolutions down to $\approx$ 20 nm have been reported using STED.

Light induced bleaching and toxicity are among the major drawbacks of STED microscopy. Even if stimulated depletion (transition from S_1 to S_0) is a non-destructive process, excitation and STED beams can induce other photophysical transitions that are detrimental for fluorophores. The STED beam can excite electrons to higher electronic states (S_n) from S_0, S_1 or T_1, which ends up in the formation of a cation dye molecule and a solvated electron and results in bleaching of the fluorophore.

There are some fluorophores that perform well in STED experiments, such as Atto and Abberior dyes. Since most popular fluorescent proteins in molecular and cell biology (e.g. GFP or YFP) are not stable enough and offer lower resolution with STED, new organic dyes are constantly being developed.

STED has been used to study HIV-1 virions (Chojnacki et al., 2012) or membrane organization (for a recent review see Sezgin (2017)). Moreover, STED can be combined with other microscopy tehcniques, such as the use of polarity-sensitive probes to measure membrane molecular order (Sezgin et al., 2017a) or FCS, that

has been applied to study membrane dynamics (Eggeling et al., 2009) and HIV-1 protein mobility (Chojnacki et al., 2017) among others. An extensive review of STED microcopy was recently published by Blom and Widengren (2017).

1.3 Goals

Main goal

To investigate features relevant for HIV-1 biology, such as membrane molecular order, phase behavior, molecule mobility on membrane surfaces or observation of sub-diffraction structures, using advanced microscopy techniques.

Specific goals

- To infer the role of the viral-enriched raft-lipids cholesterol and sphingomyelin in the membrane order and organization of simple lipid mixtures.
- To characterize the HIV-1 lipid envelope organization using the above mentioned microscopy techniques.
- To define a model lipid mixture that resembles the properties of the HIV-1 lipid envelope.
- To study the effect of membrane-targeting anti-viral peptides on the HIV-1 membrane organization.
- To study the binding of broadly neutralizing anti-MPER antibodies to HIV-1 virions and determine the contribution of antibody-membrane interactions to the process.

Chapter 2

Experimental techniques

In this chapter a general overview and protocol of the experiments performed during this thesis work are given. For more specific details of each experiment check the *Materials and methods* section of each chapter.

2.1 Model membranes

Cell membranes are highly complex systems as they are composed of many different molecules: proteins, phospholipids, sterols Thus, it is not easy to assess the properties and behavior of each component. That is the reason why many membrane studies rely on model membranes. These can be moderately complex as membrane extracts (with or without proteins) or as simple as a pure lipid monolayer. Their main disadvantage is that these model systems are a very simplified version of a natural membrane, so the conclusions obtained may not be directly applicable to more complex systems. However, they allow a reasonably good control of membrane composition under the desired conditions, so they are still extremely useful tools for studying membrane components and their interactions.

2.1.1 Multilamellar vesicles

A lipid structure in a bilayer conguration enclosing an aqueous solution is called a liposome. Liposomes are spontaneously generated when diluting cylindrical-shaped lipids in aqueous solutions, and thus, represent a fast source of lipid model membranes. Depending on the treatment, liposomes can be prepared to have a unique or several bilayers or lamellas. Multilamellar vesicles (MLVs) have been used in this thesis as a previous step to giant unilamellar vesicle production. The following protocol was used to produce MLVs:

1. Pure lipid stocks are prepared by diluting commercially available lipids in powder into a chloroform solution to the desired concentration.

2. The desired amount of lipid is pipetted from the stock in organic solution into a glass pear-shaped flask.

3. The organic solvent is evaporated by putting the solution under a N_2 gas flow.

4. To completely remove any traces of organic solvent, the sample is introduced into a vacuum desiccator for 1 hour. A dried lipid film at the bottom of the test tube is obtained.

5. The lipid is prehydrated during 30 minutes under a gentle flow of ultrapure H_2O saturated N_2 stream using a bubbler.

6. Then, MLVs are obtained after the lipid is totally hydrated by incubating the desired amount of aqueous or buffer solution for 30 minutes at a temperature higher than the mixture transtition temperature, tipically 50 °C. For giant unilamellar vesicle production lipids are hydrated to a final concentration of 0.5 g/L in 250 μL of ultrapure H_2O.

7. Finally, vesicle size is adjusted by 30 times extrusion of the hydrated vesicles across two 0.4 μm pore size filters in an Avanti Mini Extruder at 55 °C.

2.1.2 Giant unilamellar vesicles

Giant unilamellar vesicles (GUVs) were produced by spontaneous swelling as described by Shnyrova et al. (2013):

1. Observation dishes (MatTek) are BSA-blocked for at least 15 minutes with 125 μL 0.5 g/L BSA. Dishes are gently rinsed 5 times with 200 μL of ultrapure H_2O.

2. MLVs produced following the protocol in the previous section is mixed with 40 μm diameter silica microspheres (beads). 20 μL of MLVs are mixed with 5 μL of beads on a polytetrafluoroethylene (also known as Teflon) surface. The mixture is homogenized and separated in 2-3 μL droplets that are vacuum dried for 45-90 min.

3. The dried lipid/beads are scrapped with a pippete tip and soaked in a second tip with a sucrose (3 g/L) containing buffer that will constitute the inner buffer of GUVs and will ensure deposition of the vesicles to the bottom of

the dish due to higher density of the inner buffer compared to the isosmotic 5 mM HEPES 150 mM KCl pH 7.4 outer buffer. The tip is placed for 5 min in a sealed container saturated with water vapor obtained upon heating ultrapure water at 55 °C.

4. Rehydrated lipid vesicles are transferred to the observation dish containing the outer buffer.

5. If antibodies or peptides have to be incubated with the GUVs, sometimes it is convenient to add and homogenize them before adding the vesicles. This way, GUV exposure to high local concentrations of a putative perturbing agent is avoided.

2.1.3 Large unilamellar vesicles

Large unilamellar vesicles (100 nm) used in leakage and lipid mixing studies are generally prepared by mechanical extrusion of MLV suspensions through polycarbonate porous filters of the desired size according to the following protocol:

1. Pure lipid stocks are prepared by diluting commercially available lipids in powder into a chloroform solution to the desired concentration.

2. The desired amount of lipid is pipetted from the stock in organic solution into a glass pear-shaped flask.

3. The organic solvent is evaporated by putting the solution under a N_2 gas flow.

4. To completely remove any traces of organic solvent, the sample is introduced into a vacuum desiccator for 1 hour. A dried lipid film at the bottom of the test tube is obtained.

5. In order to reduce the size and amount of lamellas within the MLVs, the sample is subjected to 10 freeze/thaw cycles. The sample tube is immersed in liquid N_2 for 1 minute. Once frozen, the sample is transferred into a water bath at a temperature above that of the mixture transition temperature until total defreezing and sample equilibrium is achieved. The sample is vortexed and the same procedure is repeated for 10 times.

6. To obtain unilamellar vesicles of a specific size, vesicles are finally extruded 10 times through polycarbonate filters (Nucleopore, Cambridge, MA, EEUU) with the desired pore diameter and with the help of a nitrogen gas flow of 200 psi. By using a water bath, the extruder is maintained at a temperature above that of the mixture transition temperature.

7. The final concentration is checked in terms of lipid phosphorous as will be explained below.

2.1.4 Lipid concentration determination

The phospholipid concentration determination is based on the quantification of inorganic phosphorous. Briefly, the approach consists in hydrolyzing the phospholipids until the lipid phosphate group is free to interact with specific reagents that will color the solution in a concentration-dependent manner.

1. 0, 25, 50, 75 and 100 nmol phosphorous are pipetted into separate test tubes from a NaH_2PO_4 solution, which will be used to construct a calibration curve from which the exact lipid concentration of the sample will be determined.

2. A small volume of the LUV sample containing approximately 50 nmol lipid phosphorous is then pipetted into separate tubes.

3. 500 μL of a 70 % perchloric acid ($HClO_4$) solution are pipetted into each tube. The tubes are vortexed and placed in a heating block at 200 °C for 45 min. Phospholipid hydrolysis is achieved leaving free inorganic phosphate.

4. After cooling down to room temperature the following solutions are added:

   (a) 4 ml of an ammonium heptamolybdate based solution (2.2 g/L ammonium heptamolybdate $(NH_4)_6Mo_7O_{24}.4H_2O$ and 14.3 mL/L sulphuric acid (H_2SO_4) 95-98%).

   (b) 500 μl of a 10 % ascorbic acid solution (added while vortexing).

5. The tubes are boiled in a water bath for 5 min. The inorganic phosphate reacts with the molybdate which subsequently reacts with the ascorbic acid giving a yellow-colored solution. The solution color is blue-shifted depending on the amount of phosphorous.

6. The tubes are cooled down and absorbance at 812 nm is measured. 7) To obtain the phospholipid concentration of the sample, the absorbance of the standards is plotted against the phosphorous concentration and adjusted to a straight line. The slope of the curve and the sample absorbance are used to calculate the sample concentration.

2.1.5 Langmuir-Blodgett monolayers

.

Another model system for the study of lipid-lipid and/or lipid-protein interactions are monomolecular films at the air-water interface, the so-called lipid monolayers. An important advantage of this system compared to vesicles is that no curvature nor fluctuation effects are present, and furthermore, there is a complete control of the surface pressure, lipid composition and molecular packing at every time. Its main drawback, shared with most *in vitro* techniques, is the transference of the obtained conclusions to complex biological membrane bilayers. However, very precise information about lipid-lipid interaction behavior can be obtained, a much more difficult task when performing *in vivo* measurements.

Lipid monolayers can be prepared in a fast and easy way. Spreading a lipid solution on top of an aqueous solution a monolayer is generated in the air-water interface. Due to their amphipathic nature, lipids self-organize by putting their hydrophilic headgroups in close contact with the water environment while moving their acyl chains towards the air. This is usually achieved by diluting lipids in highly volatile organic solutions, such as pure chloroform or chloroform/methanol mixtures. Once generated, different properties of the monolayer can be studied based on the accurate control of its surface pressure by the use of a Langmuir balance. This is commonly done by the Wilhelmy method, using a suspended probe immersed in the air-water interface that measures any deviation from water surface tension, i.e. induced by the presence of the monolayer.

Langmuir-Blodgett (LB) films are formed when monolayers at the air-water interface are transferred to solid supports, such as glass or mica. In the context of the present work, supported planar monolayers (SPMs) have been prepared and transfered onto solid supports to analyze lipid phase behavior of viral and virus-like lipid mixtures by fluorescence and atomic force microscopy according to the following protocol:

1. The PTFE trough is cleaned with choloroform and methanol to remove lipid traces from previous experiments.

2. The trough is further cleaned after 5 compression/expansion cycles carried out with ultrapure water.

3. A clean paper flag is attached to the force transducer and the balance zeroed to measure 0 mN/m. Cleanliness is checked after closing the barriers to the minimum area. If the trough is clean, i.e. no increase in surface pressure is measured, water can be removed. If impurities are detected the interface is cleaned by absorbing the surface with a pipette connected to a vaccum pump.

4. The trough is filled with the subphase buffer (5 mM Tris/HCl 150 NaCl pH 7.4, prepared in ultrapure water).
5. Solid supports are prepared. Typically, two rectangular glass covers are cleaned with chloroform and methanol and let dry for 10 minutes. Afterwards, a mica sheet is cleaved and placed on top of one of the glass cover. The supports are mounted in the dipper and immersed in the subphase.
6. 5 extra compression/expansion cycles are performed. Cleanliness is checked again.
7. Once the subphase is thoroughly clean, the desired lipid mixture is prepared in chloroform:methanol (9:1) at 1 mM.
8. Using a microsyringe the lipid mixture is deposited drop by drop until the surface pressure reaches and stabilizes at 0.2-0.3 mN/m. To avoid destabilizing the monolayer the tip is placed very close to the interface while adding lipid drops.
9. Wait 10 minutes to allow for organic solvent evaporation.
10. Activate the feedback program (a value of 0.2 has yielded the best results in this work).
11. To reach the desired lateral pressure, the monolayer is compressed at a constant barrier speed of 25 mm/min. Wait 10 minutes for the monolayer to stabilize.
12. Transfer the monolayer to the solid supports by lifting them at a constant 5 mm/min speed.
13. If the monolayer is going to be transferred at more than one pressure, repeat the compression and transference steps until all the desired pressures have been transferred.
14. Store the LB monolayers. In this work, atomic force microscopy measurements have been performed within the next 5 days.

2.2 Fluorescence spectroscopy

2.2.1 Leakage assay

A simple way to study bilayer perturbations generated by membrane active peptides and proteins relies on the measurement of the fluorescence changes of vesicle

encapsulated fluorescent probes. In this assay, the fluorescent probe ANTS (8-aminonaphtalene-1,3,6-trisulfonic acid sodium salt) and its quencher DPX (p-xylenebis(pyridinium)bromide), are co-encapsulated in the aqueous compartment of the liposomes. By entrapping both ANTS and DPX inside the vesicles, their close proximity allows DPX to quench ANTS fluorescence. Upon membrane perturbation, both molecules leak out and are diluted into the external medium where interaction probability decreases, inducing an increase of ANTS fluorescence. By monitoring ANTS fluorescence, vesicle permeabilization can be followed in time.

1. LUVs are prepared as previously in 2.1.3 a buffer containing both ANTS and DPX (20 mM ANTS, 70 mM DPX, 40 mM NaCl, 10 mM HEPES (pH 7.4)). A high DPX:ANTS ratio is used to ensure complete quenching inside vesicles.

2. The vesicle suspension is passed through a Sephadex G-75 column to remove non-entrapped ANTS and DPX molecules. A previously adjusted isosmotic buffer solution (150 mM NaCl, 10 mM HEPES (pH 7.4)) is used during filtration.

3. Lipid concentration is determined as described in 2.1.4.

4. 1 mL (100 μM) LUV is placed in a quartz cuvette under continuous stirring. A cut-off filter of 470 nm is placed between the sample and the emission monochromator to avoid vesicle-derived light scattering distortions in the emission signal. The sample is excited at 355 nm and the fluorescence emission is measured at 520 nm. After the fluorescence is stabilized (F_0, typically 1 min) a certain amount of peptide is added and the fluorescence increase is followed (F_i). After a certain period of time, tipically 5 minutes, 10 μL of Triton X-100 10% (v/v) are added to ensure complete permeabilization of the vesicles (F_{max}).

5. The percentage of leakage induced by the membrane-perturbing agent is calculated following equation 2.1:

$$\text{Leakage } \% = \frac{F_i - F_0}{F_{max} - F_0} \times 100\% \tag{2.1}$$

2.2.2 Lipid mixing assay

Membrane fusion occurs when two initially separate and apposed membranes merge into one by undergoing a sequence of intermediate transformations as explained in section 1.1.3. One of the key steps is the mixing of the membrane lipids. Lipid mixing studies in this thesis are based on the resonance energy

transfer (RET) between the fluorescent lipids N-(7-nitro-benz-2-oxa-1,3-diazol-4-yl) phosphatidylethanolamine (NBD-PE) and N-(lissamine Rhodamine B sulfonyl) phosphatidylethanolamine (Rho-PE) (Molecular Probes (Eugene, OR, USA)). The emission spectra of NBD-PE ($\lambda_{ex}/\lambda_{em}$ = 460/534 nm) overlaps with the excitation spectra of Rho-PE ($\lambda_{ex}/\lambda_{em}$ = 550/590 nm), meaning that if both probes are sufficiently close, the energy gained upon excitation of NBD will be transferred to Rho which will then be excited and will emit a red-shifted photon. To study lipid mixing, both probes are incorporated in the vesicles to a concentration that ensures a small distance between the probes. Consequently, excitation of NBD leads to a fluorescence emission signal at λ_{em} of Rho. If this vesicle population is mixed with non-labeled vesicles and fusion takes place, the distance between the probes after the fusion will increase (probes get diluted) and the emission signal at the wavelength of Rho will decrease, increasing that of the NBD. Lipid mixing is quantified according to the following protocol:

1. Two LUVs populations are prepared:

   (a) LUVs including 0.6 mol % of each probe.

   (b) LUVs including 0.12 mol % of each probe.

   (c) Unlabeled LUVs

   Fluorescent dyes in chloroform are mixed with the desired lipids in step 2 of the LUV generation protocol.

2. 1 mL of a mixture of 20 μM of fluorescent vesicles (A) and 80 μM of unlabeled vesicles (C) (1:4) are placed in a quartz cuvette with a cut-off filter of 515 nm between the sample and the emission monochromator. The sample is excited at 460 nm and fluorescence emission is measured at 530 nm. After fluorescence stabilized (F_0, typically 1 min) a certain amount of peptide is added and the fluorescence increase of NBD is followed (F_i).

3. The fluorescence in the above conditions of 100 μM of the diluted-probe vesicles (B) was recorded and used as the 100% fusion signal (F_{max}).

4. The % of fusion is calculated as follows:

$$\text{Fusion } \% = \frac{F_i - F_0}{F_{max} - F_0} \times 100\% \tag{2.2}$$

2.3 Advanced fluorescence microscopy

Experimental procedures following the photophysical phenomena explained in section 1.2 are explained in the following sections. Laurdan GP and antibody

mobility measurements were performed in a Leica TCS SP5 II confocal microscope. Besides the internal excitation sources, the microscope used during this thesis work was equipped with a Mode-Locked Ti:Sapphire pulsed laser (Deep See Mait-Tai (HP DS), Spectra Physics) with a repetition rate of 80 MHz and a pulse width of less than 100 fs. It has an average peak power of ca. 3 W and a tuneable range of near-infrared wavelengths (690-1040 nm).

Extra emission detection units were also added to the microscope. Besides the internal detection PMT units, the set-up was equipped with two NDD HyD Hybrid PMTs (Leica/Hamamatsu) (for Laurdan measurements); and two SPCM-AQR-13 FCS APDs (Leica/Percin-Elmer) (for FCS measurements).

2.3.1 Laurdan GP measurements

1. Prepare Laurdan labeled (1 % mol/mol) GUVs according to the protocol in section 2.1.2.

2. In the microscope, Laurdan emission from GUVs is directly visualized through the oculars using a xenon-arc lamp with an excitation bandpass filter of 340-380 nm. A 400 nm dichroic mirror is placed in the optical path to isolate excitation and emission light. Emitted light is directly visualized after passing through a 425 nm filter.

3. Multiphoton excitation of Laurdan is achieved upon illuminated with a pulsed 780 nm beam from the femtosecond-pulsed Ti:Sapphire laser. Set transmission to 10% (increase if emission signal is low), gain to 15% and offset to 54% (optimal for 780 nm excitation).

4. GUVs are imaged using a ×63/1.2 NA (numerical aperture) water immersion objective. Collect the emission with the NDD hybrid detectors at 435 ± 20 nm and 500 ± 10 nm.

5. Capture images in 512×512 pixel format at a 400 Hz scan speed and save them in TIFF format for subsequent analysis.

6. GP values from microscopy images are calculated using *genpol*, a MATLAB (MathWorks, Natick, MA, USA) based home-developed software:

   (a) Set the G factor (calculated measuring the GP of 5 μM Laurdan in DMSO), a 2-pixel circular smoothing and an intensity threshold around 30% of the maximal intensity signal.

   (b) The software calculates the GP value for each pixel of an image.

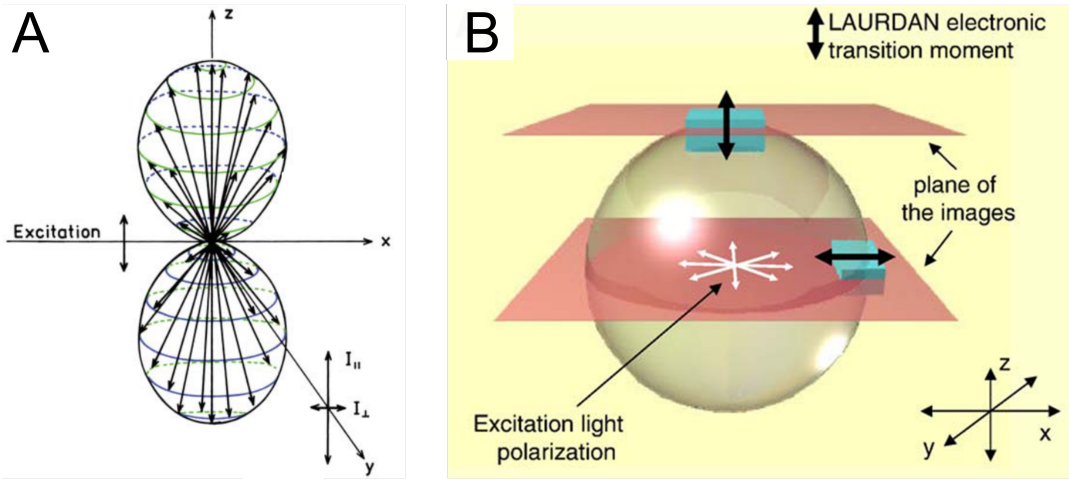

Figure 2.1: (A) Excitation efficiency is proportional to the squared cosine of the angle between the excitation polarization and the molecule absorption dipole. (B) In GUVs (spherical vesicles) Laurdan electronic transition moment is aligned parallel to the polarization only at the equatorial plane (taken from Bagatolli (2006)).

(c) The mean GP value and the standard deviation are calculated for each image. In cases of lateral segregation the software can distinguish between both phases and calculate all parameters for each of them.

(d) Calculate the mean GP value for each lipid mixture after imaging and processing at least 30 GUVs.

Photoselection

One of the objectives of this work has been to accurately measure changes in the molecular order of a bilayer caused by small changes in the lipid composition. For instance, the effect of the reduction of an unsaturation in a lipid species that accounted for 5% of all the lipid content was calculated and found to significantly reduce the GP value of that lipid composition ($p < 0.001$). These minute changes can only be detected if the acquisition and the analysis are finely controlled, adjusted and understood. In particular photoselection must be avoided to prevent systematic bias of the GP value.

In absorption events, those molecules with their absorption transitions moment aligned parallel to the electric vector of the excitation wave have the highest probability of being excited (Fig. 2.1 A). The excitation efficiency (probability) is proportional to $\cos^2\Theta$, where Θ is the angle between the light polarization plane and the electronic transition moment of the molecule, i.e. no excitation occurs when the absorption dipole is perpendicular to the electric vector of light.

In lipid bilayer the dipole moment of Laurdan is aligned perpendicular to the

bilayer plane (Fig. 1.12). GUVs are spherical, hence when imaging with linearly polarized light only molecules that in the equatorial plane have their electronic transition moment parallel to the electric vector of polarized light are excited (Fig. 2.1 B). Circularly polarized light allows equal excitation of all the molecules in the equatorial plane, because the electric field of the wave changes its direction in a rotatory manner (but not its amplitude). Circular polarization is obtained upon addition of the electromagnetic fields of two perpendicularly polarized waves delayed 1/4 λ one from the other.

In preliminary imaging assays, a position dependent excitation of Laurdan molecules in the equatorial plane of GUVs was observed (Fig. 2.2 B, right). The particular emission pattern observed in all the vesicles (maximal and minimal excitation in perpendicular axis) suggested that Laurdan molecules were undergoing photoselection. This photoselection pattern is typically derived from elliptically polarized excitation (Fig. 2.2 B, left). Elliptical polarization differs from circular polarization in that in the former, not only the direction of its electric vector but its amplitude changes too.

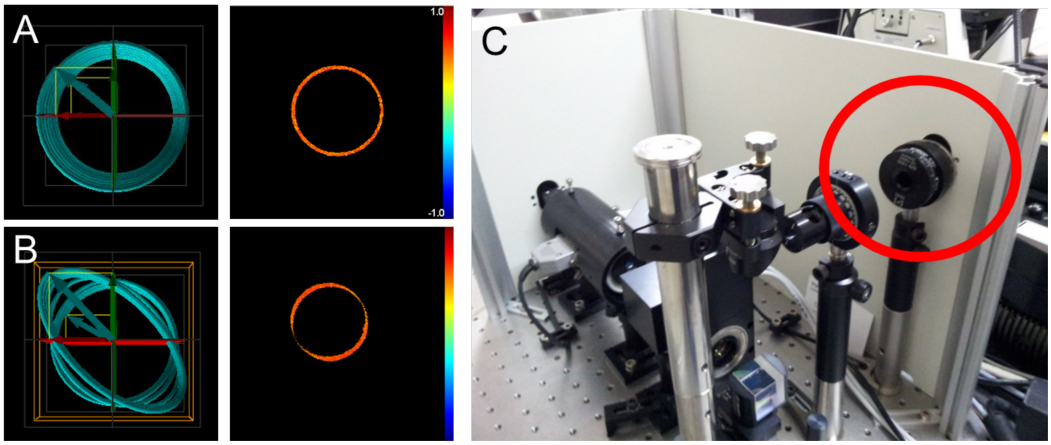

Figure 2.2: (A) The electric vector of circularly polarized light only changes its direction in a rotational manner; instead its amplitude is constant thus equally exciting all the fluorophores in the equatorial plane of GUVs independent of their orientation. (B) Elliptical polarization is produced by the delay of one of the components in the optical path. The vector suffers an amplitude variation giving rise to a characteristic pattern of excitation. (C) This was corrected by the introduction of a variable compensator in the optical path (circled in red).

This is not just a cosmetic issue; in fact photoselection introduces a systematic error in GP measurements (Fig. 2.3 A). In a lipid bilayer environment Laurdan mobility depends on the membrane phase state. In rigid bilayers Laurdan wobbling movements are restricted due to the high packing degree; as opposed to fluid phase membranes were Laurdan molecules have a higher freedom. This phenomenon turns into preferential excitation of Laurdan molecules associated with lower GP

values, i.e. molecules that present higher mobility because of relatively low lipid order give rise to an underestimated value.

Inside the microscope, the polarization of light may be altered by the internal optics. Hence, circularly polarized light at the input of the microscope may turn into elliptically polarized at the sample plane, inducing photoselection. A variable compensator, known as Berek compensator was introduced in at the entrance of the microscope (Fig. 2.2 C). The variable compensator is an optical device that introduces an arbitrary delay to the optical components. Adjustment of the exact plane and degree of retardation is an arduous task that requires trial and error changes of both parameters since the exact initial retardation introduced in the optical path is difficult to measure. Circular polarization was achieved at the angle at which the average GP for the whole GUV is maximal (Fig. 2.3) and the standard deviation of the GP pixel distribution is minimal, indicating negligible effect of photoselection on the GP. A GP variation of 2.5% was detected even at small departures from the optimal (e.g. ± 2°, Fig. 2.3 B), which may result in the increase of the overall uncertainty of the experiment.

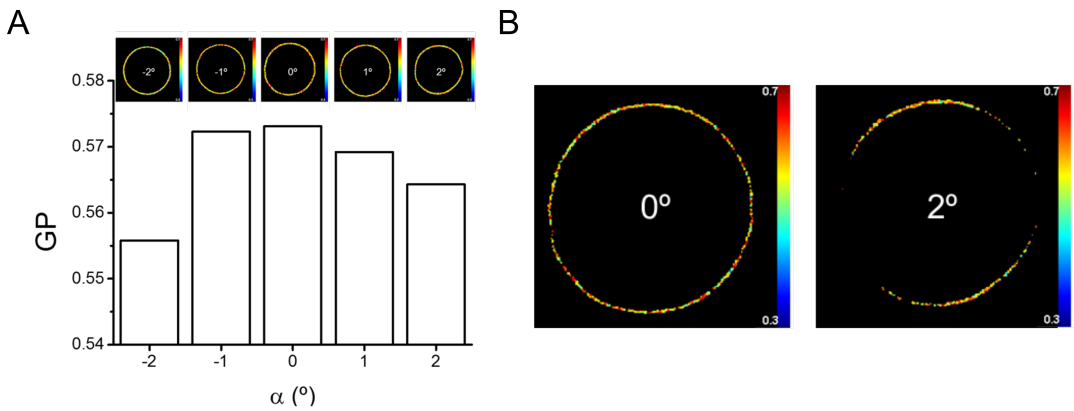

Figure 2.3: Quantification of the generalized polarization is very sensitive to small polarization mismatches. (A) Small departures from circular polarization result in artifactual GP quantification. To adjust the variable wave plate, the GP values of a virus-like (see chapter 4 GUV labeled with 1% Laurdan at small incremental retardance angles were calculated. (B) Photoselection at 2° was not noticeable in GP images at standard analysis conditions, but it became apparent when raw images were threshold to 75% of the maximal intensity. Under these conditions no photoselection can be observed for the GP image on the left, which was therefore chosen as optimal for accurate GP calculation. GP color scale: 0.3 to 0.7.

In conclusion, emission collected after the introduction and fine adjustment of the Berek compensator no longer showed photoselection-derived patterns (Fig 2.3), allowing precise quantification of light emitted by all fluorophores located at the equatorial plane of imaged GUVs.

2.3.2 Fluorescence correlation spectroscopy

FCS was applied to study the diffusion behavior of fluorescently-labeled antibodies in solution or bound to lipid membranes. The basis of the technique is explained in section 1.2.4.

Focal volume calibration

Before performing a FCS experiment, the size of the focal volume must be calculated, as it may vary slightly from day to day. Exact dimensions of the focal volume are required for the accurate calculation of the parameters obtained by FCS.

1. Switch on the microscope and let the lasers stabilize for 1 h.
2. Prepare different concentrations (10-30 nM) of a fluorescent dye (Abberior STAR RED in this thesis work) in observation dishes in the GUV outer buffer.
3. Select a fixed region of interest (ROI) at the center of the dish in the x and y axes; and at the optimal focal distance of the objective in the Z axis (150 μm in this case).
4. Abberior STAR RED is excited using the He/Ne 633 nm laser Alexa 633 and emission recorded for 90-120 s with FCS APDs after passing through a BP647-703 nm filter.
5. The signal is decoded and the autocorrelation curves are calculated using a MATLAB based home-developed software.
6. The curves are fitted to a 3D diffusion autocorrelation function (equation 1.7, from which ω_0 and z_0 are estimated.

Scanning FCS

The diffusion coefficient of membrane bound antibodies was quantified using scanning FCS according to the following protocol.

1. Prepare Laurdan labeled (1 % mol/mol) GUVs according to the protocol in section 2.1.2.
2. Incubate GUVs with Abberior STAR RED (KK114) labeled antibodies (Fabs). Fab concentration must be kept low (10-50 nM) to avoid saturation of the focal volume.

3. Set the image size to 64×8192 pixels, the scan rate to the maximum (1400 Hz) and the acquisition mode to xt, which consists on the continuous scan of the same line in time.

4. Select an appropriate GUV. Choose a GUV which shows (i) reduced drifting to prevent large membrane movements during the acquisition and (ii) minimum protein concentration to give a good signal to noise ratio. Select a section of the GUV around its equatorial plane.

5. Focus the membrane of the GUV in the middle of the field of view using 15× zoom and 64 pixels in the x axis direction, which results in a pixel size of 260 nm.

6. Choose an appropriate excitation power. In this work, a value of 10,000 photon counts per second has yielded good autocorrelation curves.

7. Acquire the emission signal for 3-5 minutes to ensure enough statistical power.

8. Using the FCS analysis software, decode the signal, select the membrane and calculate the autocorrelation function.

9. Fit the curve to a 2D diffusion autocorrelation function (equation 1.10) and calculate the diffusion coefficient.

2.3.3 Super-resolution STED microscopy

Antibodies bound to HIV-1 viral particles have been imaged on a home-built STED microscope installed in a biosafety level 3 environment. The samples were prepared according to the following protocol:

1. Incubate glass coverslips with poly-L-lysine for 5 min. Let them dry for 15 min.

2. Adhere purified virus particles to poly-L-lysine coated glass coverslips for 15 min.

3. Block coverslips using 2% fatty acid free bovine serum albumin (BSA) (Sigma)/PBS for 15 min. Gently wash with PBS.

4. Only for colocalization experiments: Incubate unlabeled anti-HIV antibodies (100 ng/μL) in blocking buffer for 1 h. Gently wash with PBS 3 times.

5. Only for colocalization experiments: Incubate with Abberior STAR 600 labeled anti-human Fab for 1 h in blocking buffer. Gently wash with PBS 5 times.

6. Incubate Abberior STAR RED (KK114) conjugated Fabs (20-100 ng/μL) 1 h in blocking buffer. Gently wash with PBS 3 times.

7. Mount the coverslip in PBS.

STED imaging was performed on a modified Abberior Instrument RESOLFT QUAD-P super-resolution microscope (Abberior Instruments GmbH) according to the following protocol:

1. Place the sample in a 100× (1.40 NA) oil immersion objective. Only samples prepared within 24 hours were imaged for emission intensity quantification.

2. Set the 485, 594 (only for dual color experiments) and 640 nm excitation powers to 5, 15 and 15 μW, respectively (measured in the back aperture of the microscope).

3. Set the STED laser wavelength to 755 nm and power 2.5-3.5 V. To check resolution image 20 nm Crimson beads and calculate the full-width at half maximum (FWHM) of the emission intensity signal.

4. Acquire the STED signal from antibodies and the confocal GFP signal to localize viral particles. To avoid photobleaching of the STED dyes it is convenient to image first in super-resolution mode. In dual color colocalization experiments it is recommended to scan each channel line by line. This way biased colocalization coefficients that may arise from molecules moving during both channel acquisition are avoided.

5. Image at least 10 different areas for each sample. Typically 100-200 viral particles will be visible in each image.

6. Analyze all the images. In this thesis work a home-developed Python-based software has been used to analyze viral particle localization, intensity, numer of foci and colocalization, among others.

2.4 Atomic force microscopy

Atomic force microscopy (AFM) is a high-resolution imaging technique. It is not based on optical methods and relies in scanning probe microscopy, a method where a physical probe is scanned over a surface to form a topographic image of the sample. It offers nanoscopic resolution in the xy axes and subnanometer resolution in z.

In atomic force microscopy measurements, a laser beam is focused onto the top-end of a flexible cantilever where a small tip is attached to scan the desired

surface (Fig. 2.4). The cantilever reflects the laser beam, which is focused into a position-sensitive four quadrant photodetector by the use of a mirror. When measuring a sample, the tip is scanned across the xy axes within the selected area in which, as the tip finds height differences, it translates into a deflection of the cantilever in the z axis, which is detected by the photodetector. In this way, the movement of the laser through the different quadrants is controlled and correlated to offer subnanometric resolution topographic images where forces between tip and sample as low as 50 pN can be properly maintained.

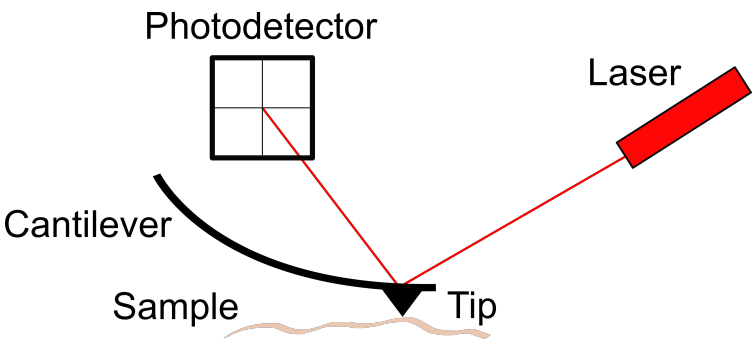

Figure 2.4: Simplified schematic of an atomic force microscope.

Biological membranes are very soft samples to measure by AFM, thus they require a very precise control of the scanning conditions. Choosing a suitable cantilever and tip is one of the most critical steps. Different features of the tip and the cantilever have to be specifically selected, such as the material, shape, coating, spring constant and resonance frequency among others. Due to easy machining, cantilevers are typically made of nitride or silicon nitride. They can be rectangular or triangular, and usually have a metal coating for increased reflectivity.

The use of proper solid supports is also critical when measuring ca. 5 nm-thin soft small structures such as lipid bilayers. For this reason, atomically flat supports are needed. Hydrophilic negatively-charged muscovite mica is the most widely used support for AFM measurements of membrane structures. Mica sheets are very easily prepared upon cleavage of the upper sheets prior to sample incubation, presenting a clean flat surface. Glass supports are also used when a precise combination of AFM and fluorescent microscopy techniques is to be performed, but these supports do not present an atomically flat surface. Furthermore, the scan speed, scanning angle and/ or the force applied by the tip on the sample must be properly controlled. The measurement of a biological membrane can be performed typically under two different methods: contact mode or intermittent contact mode, also known as tapping mode.

Contact mode

In this scanning mode the tip is physically in contact with the sample. A constant force is maintained and the topography of the sample is followed in terms of changes of the vertical deflection of the cantilever, that is converted to units of length to build the height image. It is a common scanning mode, but due to constant contact, samples can be damaged if too high forces are applied. In biological sample measurements, cantilevers with spring constants between 0.05 and 0.5 N/m and resonance frequencies between 5 and 50 KHz in vacuum are typically used. Contact mode has been used in most of the experiments performed for this thesis work.

Intermittent contact mode

Also known as dynamic or tapping mode, this scanning procedure is less aggressive than contact mode. It is based on the oscillation of a cantilever at its resonance frequency close to the sample surface. During the cantilever oscillation, the tip contacts the surface just once, and then retracts to the neighboring position for the next oscillation cycle. The topographic image can then be obtained by following variations of the resonance frequency or the signal amplitude. An important parameter that can be obtained from this scanning mode is the phase of the oscillation signal, which can provide information about stiffness or adhesion of the sample. In this case, the lateral forces are smaller than in contact mode and softer samples can be scanned. Tapping cantilevers are usually stiffer than those used in contact mode.

All the AFM experiments in this thesis work were performed in a JPK Nanowizard II (JPK Instruments, Berlin, Germany). The settings typically used to measure a lipid monolayer were the following:

- Probe: C and D cantilevers in a MLCT probe (Bruker, Billerica MA, USA)
- Image size: 512×512 pixel^2
- Scan area: Max. 100×100 μm^2. Min. 500×500 nm^2.
- Scanner frequency (line rate): 1-4 Hz
- Scan mode: Contact mode
- Setpoint: 0.1 N/m (ca. 0.15 V for E cantilevers and ca. 0.4 V for D cantilevers)
- Integral gain: 150-1000 Hz (Increase for smaller scan areas)
- Proportional gain: 0.002 (default)
- Z range: 3 μm

2.5 Virus and cell biology

2.5.1 Virus production

Human embryonic kidney 293 cells, also referred to as HEK293 cells, are derived from human embryonic kidney grown in tissue culture. A variant of this cell line is the 293T cell that contains the SV40 Large T-antigen allowing episomal replication of transfected plasmids containing the SV40 origin of replication. HEK293T cells are maintained at 37 °C and 5% CO_2 in M medium (maintenance) consisting of Dulbecco's Modified Eagle's Medium, 10% FBS and supplemented with 1:100 dilution of non-essential amino acids, 1:100 dilution of sodium pyruvate and 1:100 dilution of penicillin/streptomycin (stocks at 100×). The cells are passaged when they reach ca. 80-90% confluence (typically twice a week). All cell-culture reagents are from Gibco (Invitrogen).

To produce HIV-1 and VSV-G pseudotyped viruses, HEK293T cells are transfected with a full-length env clone (pIII-Env or JR-CSF) (pIIenv: AIDS Research and Reference Reagent Program, Division of AIDS, NIAID, NIH, contributed by K. Page and D. Littman; JR-CSF: kindly provided by Jamie K. Scott and Naveed Gulzar, Simon Fraser University, Burnaby, Canada), or VSV-G encoding pMD2.G plasmid (envelope glycoprotein of the vesicular stomatitis virus), using the calcium phosphate or the polyethylenimine method. For infectivity assays each plasmid is co-transfected with the vectors pWPXL-GFP and pCMV8.91, encoding respectively a green fluorescent protein and an env-deficient HIV-1 genome (kindly provided by Dr. Patricia Villace, CSIC, Madrid). The GFP containing plasmid, bears LTR and Ψ sequences necessary to be integrated in the host cell genome. pCMV8.91, in contrast, lacks these sequences and the virulence factors Vpu, Vpr, and Vif are mutated to avoid generation of infectious viruses. For imaging experiments, cells are co-transfected with pCHIV and peGFP.Vpr or pmCherry.Vpr. To produce JR-CSF pseudotyped particles cells are co-transfected with an Env-deficient pCHIV, peGPP.Vpr and the JR-CSF Env expression plasmid. The following procedure was followed for $CaCl_2$ transfection:

1. Seed 4.5×10^6 HEK293T cells in a 100 mm culture disc in M medium. Quantities in this protocol are for 1 dish.

2. After 20h replace the medium with new M medium.

3. Prepare transfection solutions:

   (a) Solution A: $CaCl_2$ 250 mM (the stock solution at 2.5 M is stored at -20C).

(b) Solution B: NaCl 140 mM, $Na_2HPO_4.2H_2O$ 1.5 mM, Hepes 50 mM (stock at 1 M from Gibco), MiliQ H_2O, pH 7.05. Filter all the solutions through 0.22 μm filters (Millex HV, Millipore NV, Brussels, Belgium) and store them at RT.

4. Transfect the cells:

   (a) Mix 3 μg of pHXB2 or pMD2.G, 10 μg of pWPXL and 18 μg of pCMV 8.91 with 1.3 mL of solution A. Vortex the mixture.

   (b) While gently vortexing the tube with solution A + DNA, 1.3 mL of solution B is added drop by drop. Let aggregates form for one minute.

   (c) Add the mixture to the dish drop by drop covering the entire surface.

5. 18 h after transfection the medium is replaced by M medium without FBS.

6. After 48h viral particles are harvested from culture supernatants by collecting the medium from the flask using a pipette. Centrifuge for 5 min at 3,000 rpm to discard cell debris. Filter the virus-containing supernatant through a 0.45 μm filter.

7. Centrifuge at 70,000 g (avg.) for 2 hours at 4 °C in a swinging-bucket rotor. At the bottom of the centrifuge tube a cushion of 3 mL of 0.22 μm-filtered solution of 20% (w/v) sucrose is placed and will act as a filter to finally obtain pure concentrated viral particles.

8. Discard the supernatant and add 50 μL of cold PBS to the pellet. Let the pellet resuspend gently for 30 min in a shaker at 4 °C.

9. Collect the samples and store them for up to 6 months at -80 °C.

2.5.2 Infectivity assay

Infectivity of the pseudotyped viral particles, antibody neutralization potency and anti-viral virucide activity were determined using the TZM-bl target cell line (AIDS Research and Reference Reagent Program, Division of AIDS, NIAID, NIH, and contributed by J. Kappes). TZM-bl, previously designated the JC53-bl (clone 13) is a HeLa cell line derived from JC.53 cell line that stably expresses large amounts of the CD4 receptor and CCR5 co-receptor. The TZM-bl cell line was generated from JC.53 cells by introducing separate integrated copies of the luciferase and β-galactosidase genes under control of the HIV-1 promoter and it is highly sensitive to infection with diverse isolates of HIV-1. TZM-bl cells are maintained at 37 °C and 5% CO_2 in M* medium consisting of Dulbeccos Modified Eagles Medium, 10%

heat-inactivated FBS (30 min at 56 °C) and supplemented with 1:100 dilution of non-essential amino acids, sodium pyruvate and penicillin/streptomycin at 100×. The cells are passaged when they reach ca. 80-90% confluence (typically twice a week). After pseudovirus production, serial dilutions of the stock are incubated with TZM-bl cells to titrate the viral infectivity. A detailed protocol follows for Fab neutralization activity determination:

1. In a 96-well plate, 50 μL of PBS with or without antibodies, are incubated for 1 h with 50 μL of pseudoviruses in M* medium without antibiotics.

2. Harvest TZM-bl cells and centrifuge to eliminate trypsin. Resuspend in M* medium with 20% antibiotics and 30 μg/mL of DEAE-dextran (Sigma-Aldrich, St-Louis, MO). Plate 11,000 cells/well in 100 μL. Incubate for 48 h.

3. Replace the medium with M* medium after 48 h.

4. After 24 h harvest the cells with 100 μL/well trypsin, add 200 μL/well of PBS and quantitate infected cells by flow cytometry.

If due to possible cytotoxicity, contact between the inhibitor and the cells wants to be avoided, viruses can be attached to the plate and inhibitors washed away according to the following protocol:

1. Wells in a 96-well plated are incubated for 15 min with 100 μL of 50 μg/mL poly-L-lysine. Wash with 200 μL PBS.

2. HIV pseudoviruses diluted to a 10-15% tissue culture infectious dose in PBS are deposited onto poly-L-lysine-coated wells and incubated at 4 °C for 40 min. After washing, free poly-lysine is blocked for 20 min by medium addition (90% DMEM; 10% FBS) at 37 °C.

3. Several dilutions of a given peptide in PBS are subsequently applied for 90 min at 37 °C. Wash three times with 200 μL PBS.

4. 11,000 TZM-bl target cells are layered on top of immobilized virions in the presence of 30 mg/mL DEAE-dextran.

5. Incubate for 48 h and replace the medium with M* medium.

6. After 24 h harvest the cells with 100 μL/well trypsin, add 200 L/well of PBS and quantitate infected cells by flow cytometry.

Chapter 3

Building a DOPC:SM:cholesterol molecular order phase diagram based on Laurdan GP measurements

Abstract

The ternary lipid mixture DOPC:eggSM:cholesterol in excess water has been studied in the form of giant unilamellar vesicles using two-photon fluorescence microscopy. Publications based on single-photon fluorescence microscopy have reported heterogeneous phase behavior (phase coexistence) in the region of the triangular phase diagram corresponding to SM:cholesterol molar ratios < 1. This region has been examined by two-photon microscopy of Laurdan-labeled mixtures and it has been found that only a single liquid phase exists. It is shown that macroscopic phase separation in the above region can be artifactually induced by one-photon excitation of the fluorescent probes and ensuing photooxidation, and is prevented using two-photon excitation. The main effect of increasing the concentration of cholesterol in mixtures containing 30 mol % SM was to increase the rigidity of the disordered domains. Increasing the concentration of SM in mixtures containing 20 mol % cholesterol gradually augmented the rigidity of the ordered domains, while the disordered domains reached minimal order at a SM:cholesterol 2.25:1 molar ratio, which then increased again. Moreover, the detailed measurement of Laurdan generalized polarization across the whole phase diagram allowed the representation, for both the single- and two-phase regions, of the gradual variation of membrane lateral packing along the diagram, which is found to be governed largely by SM:cholesterol interactions.

3.1 Introduction

The properties of cell plasma membranes are often mimicked by pure lipid bilayers. An important new concept introduced in the field in the last two decades is that lipids are not homogeneously distributed along the plane of the membrane, but rather organized into laterally-separated domains (Sankaram and Thompson, 1990; Simons and Ikonen, 1997; Goñi et al., 2008; Almeida, 2014; Shlomovitz et al., 2014). Plasma membrane lipids are often described by ternary models of the kind unsaturated-PC:DPPC (or SM):cholesterol (Chol). A review of these models can be found in (Goñi et al., 2008). Ternary lipid systems in excess water have been studied by a variety of techniques; the most relevant in this context are those reports based on fluorescence microscopy (Veatch and Keller, 2003a, 2005a) and spectroscopic techniques, e.g. fluorescence (de Almeida et al., 2003) or EPR (Ionova et al., 2012). In particular, DOPC:(egg or N-palmitoyl)SM:Chol has been studied using single-photon fluorescence microscopy (Veatch and Keller, 2003a, 2005a; Kahya et al., 2003), NMR (Oradd et al., 2002) or EPR (Smith and Freed, 2009).

This thesis work is focused on the study of the cholesterol-enriched HIV-1 lipid envelope (Brügger et al., 2006). This directed the interest of this chapter to the analysis of the region of the triangular phase diagram with SM:cholesterol molar ratio < 1. Fluorescence microscopy studies show extensive L_o/L_d phase separation in this area. However, several data pointed to the problems associated to light-induced photooxidation and the subsequent flawed detection of phase boundaries (Feigenson, 2007; Ayuyan and Cohen, 2006). For this reason, the DOPC:eggSM:cholesterol system in excess water is studied using two-photon excited Laurdan fluorescence. Laurdan has been used to report on the phase state of the membrane as its fluorescent emission undergoes a large spectral shift that is sensitive to the reorientation of polar molecules in the fluorophore environment. Imaging the phase state of Laurdan-labeled membranes is commonly performed using non-linear two-photon excitation rather than single-photon excitation as scattering at longer wavelengths is reduced and photobleaching outside the focal plane is minimized. The use of Laurdan with two-photon excitation should not cause artifactual induction of phase separation. Indeed, the results presented here show that, throughout the SM:cholesterol < 1 region, a single fluid phase is observed.

3.2 Experimental Techniques

Materials

1,2-dioleoyl-sn-glycero-3-phosphocholine (DOPC), 1-palmitoyl-2-oleoylphosphatidylcholine (POPC), cholesterol (Chol), egg sphingomyelin (eSM, containing ≈ 86% N-palmitoyl SM), brain sphingomyelin (bSM, containing ≈ 50% N-stearoyl SM), 23-(dipyrrometheneboron difluoride)-24- norcholesterol (TopFlour Cholesterol or BODIPY-cholesterol) and N-(lissamine rhodamine B sulfonyl)-1,2-dioleoyl-sn-glycero-3-phosphoethanolamine (Rho-DOPE) were purchased from Avanti Polar Lipids (Birmingham, AL, USA). 6-dodecanoyl-2-dimethylaminonaphthalene (Laurdan) was obtained from Molecular Probes (Eugene, OR, USA). Phospholipid stock concentrations were determined by phosphate assay. Propyl gallate (nPG) was purchased from Sigma-Aldrich.

Preparation of Vesicles

Giant unilamellar vesicles (GUVs) were produced by spontaneous swelling as described by (Shnyrova et al., 2013). Large unilamellar vesicles (LUV) were first prepared according to the extrusion method in pure H_2O. 0.125 mg lipid was co-dissolved in 100 μL $CHCl_3$:CH_3OH (9:1) with the fluorescent probes (either 1% Laurdan or a 0.5% Top Fluor Chol / 0.5% Rho-DOPE mixture). The probe-containing lipid mixture was introduced in a vacuum desiccator for 1 h to remove the organic solvent. The desiccated lipid was hydrated for 1 h at temperatures above the transition temperature of the mixture (typically 55 °C or 65 °C for the mixtures with highest SM content) and subsequently subjected to 30 cycles of extrusion through two 0.4 μm pore size polycarbonate filters in an Avanti Mini Extruder at 65 °C.

5 μL silica beads (40 μm) were then mixed with 20 μL of the LUV suspension, separated in ≈ 3 μL drops on a teflon film and vacuum dried for 45 min. Dried beads covered with lipid were collected and transferred to a 3 g/L sucrose buffer in order to induce spontaneous swelling of GUVs. Finally vesicles were transferred to the observation dish in an isosmotic 10 mM Hepes, 150 mM KCl (pH 7.4) buffer.

When needed to test the effect of an antioxidant on light-induced phase separation, GUVs were incubated in 10 mM nPG for 15 minutes before imaging.

Multiphoton and Confocal Fluorescence Microscopy

Images were acquired on a Leica TCS SP5 II microscope (Leica Microsystems GmbH, Wetzlar, Germany). GUVs were imaged through a ×63 water-immersion objective (numerical aperture, NA=1.2) and 512×512 pixel images were acquired at 400 Hz per scanning line. Unilamellar GUVs were selected and imaged at the

equatorial plane to avoid photoselection. A pulsed titanium-sapphire (Mai-Tai Deepsee, Spectra-Physics) laser tuned at 780 nm was used for two-photon imaging of Laurdan-labeled samples. Fluorescence emission was collected by non-descanned (NDD) hybrid detectors, as they offer higher sensitivity compared to descanned photomultipliers. The blue edge of the emission spectrum was collected by NDD 1 at 415-455 nm and the red edge by NDD 2 at 490-510 nm. GUVs co-labeled with TopFluor and Rhodamine were excited with a CW laser at 488 nm or 543 nm, respectively (one-photon excitation) or with the Ti:sapphire laser at 890 nm (two-photon excitation). The corresponding fluorescent emission was collected at 495-530 nm or 620-685 nm, respectively, using a pinhole aperture of 1 (Airy units) for one-photon imaging. Irradiance at the sample plane was $\approx$ 500 GWcm^{-2} for two-photon excitation and $\approx$ 104 Wcm^{-2} for CW one-photon excitation.

Data and Image Analysis

Generalized polarization (GP) images were calculated using in-house developed software based on MATLAB (MathWorks, MA, USA). After smoothing the images in each channel with a 2-pixel averaging circular filter and thresholding the intensity, we calculated the GP value for every pixel in the image following equation 3.1, where I_B is the intensity collected by NDD 1, I_R the intensity collected by NDD 2 and G is the factor that accounts for the relative sensitivity of the two channels, calibrated with 5 μM Laurdan solution in pure DMSO (Gaus et al., 2003):

$$GP = \frac{I_B - G \times I_R}{I_B + G \times I_R} \tag{3.1}$$

The mean GP value for each lipid mixture was calculated after imaging and processing at least 30 GUVs. Two or more independent experiments were routinely carried out and averaged. In the case of co-existing phases in the same vesicle, the software allows the GP to be calculated for each domain separately.

3.3 Results

3.3.1 Cholesterol:sphingomyelin molar ratios modulate macroscopic lateral separation

The present work is based on the use of the well-characterized fluorescent dye Laurdan and describes the lateral separation behavior of bilayers composed of DOPC:eSM:Chol and DOPC:bSM:Chol under a new light. These mixtures have often been used as models for membrane raft nanodomains. Excitation of Laurdan increases its dipole and may cause the reorientation of water molecules associated

to the lipid membrane, hence decreasing Laurdan's excited state energy and shifting its emission to a higher wavelength. Laurdan is therefore a valuable tool to monitor membrane lateral separation into liquid-ordered (L_o) (less hydrated) and liquid-disordered (L_d) (more hydrated) domains as a redder emission is observed in polar solvents and a bluer in apolar ones. Here, two-photon fluorescence microscopy has been used to image single GUVs labelled with Laurdan and to characterize the lateral separation behavior and lipid packing of a mixture consisting of the low melting temperature (T_m) lipid DOPC, Chol and the high T_m sphingolipid eSM. In order to check the validity of our findings for other SM species, the most conspicuous experiments were repeated replacing egg SM for brain SM. From here on, DOPC:SM:Chol in mol % notation will be used to designate lipid mixture compositions.

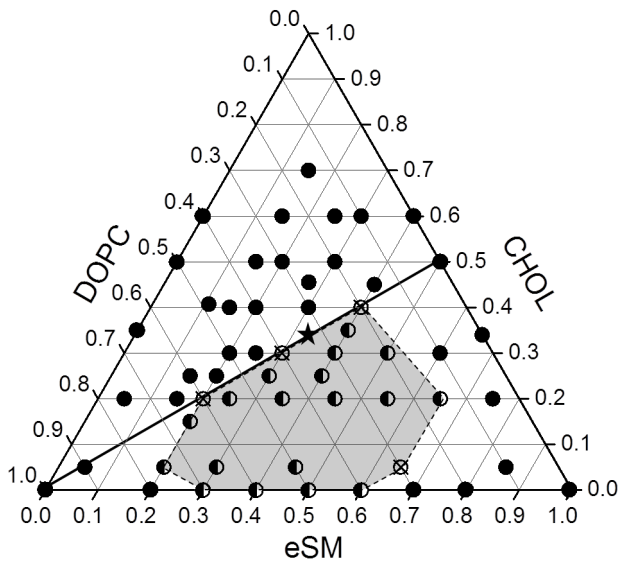

Figure 3.1: DOPC:eSM:Chol ternary mixture phase diagram at 23 °C. All measured lipid compositions (lipid ratios expressed as mole fractions) are shown on a Gibbs triangle. Single phase and phase-separated mixtures are depicted as solid and half-solid circles, respectively. Compositions showing heterogeneous vesicle populations are marked with a cross. The star indicates the 1:1:1 molar ratio mixture.

Fig. 3.1 shows the lipid mixtures that have been measured in the form of a Gibbs triangle for the DOPC:eSM:Chol mixture. Phase-separated and single-phase membranes are depicted as half-solid and solid circles, respectively. Please note that this methodology does not allow distinction between gel (s_o) and L_o domains. Gel phase, or solid domains, would only be expected for 100 mol % eSM and nearby

regions in the diagram (de Almeida et al., 2003; Pokorny et al., 2006). As seen in this ternary plot, no macroscopic lipid separation could be observed for eSM:Chol molar ratios lower than 1: single-phase membranes were observed for all mixtures above the 1:1 bisectrix. In order to rule out that these observations are specific to egg SM, several mixtures of DOPC:bSM:Chol were prepared with analogous result to DOPC:eSM:Chol: when the bSM:Chol ratio was lower than 1 (e.g. 40:20:40 and 30:30:40), vesicles were found to be homogenous too; when the bSM:Chol ratio was higher than one (e.g. 50:30:20 and 40:20:20) phase-separated vesicles were observed. These results do not agree with previously published fluorescence-based phase diagrams of the same mixture (Kahya et al., 2003; Bezlyepkina et al., 2013; Tian et al., 2007; Lindblom et al., 2006) or mixtures containing the closely related palmitoyl-SM (Veatch and Keller, 2005a; Zhao et al., 2007; Nyholm et al., 2011; Veatch and Keller, 2005b). In order to facilitate comparison with previously published data, the observations presented in this chapter have been plotted against available data as compiled in (Bezlyepkina et al., 2013) in Fig. 3.2.

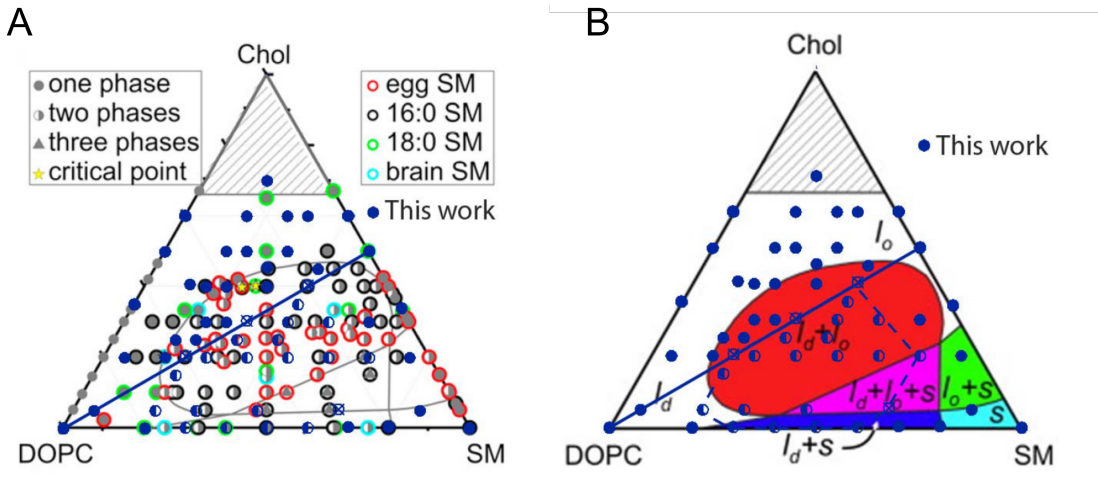

Figure 3.2: Comparison of previously published data of the DOPC:eSM:Chol ternary mixture at 23 °C plotted against this work. (A) Previously published data (as compiled in Bezlyepkina et al. (2013)) plotted against the data in this chapter (blue dots) and grouped according to the number of coexisting phases. Single-phase and phase-separated mixtures are shown as solid and half-solid circles, respectively. (B) Tentative phase region boundaries. The boundaries empirically found for the data reported in this thesis work are shown in blue. Adapted from (Bezlyepkina et al., 2013). The main observation in this work is the absence of phase separation at SM:Chol ratios lower than one, which has never been reported before and affects the previously accepted boundaries of phase-coexisting regions.

Mixtures containing equimolar SM:Chol quantities, that is, lipid compositions represented with a cross and located at the 1:1 molar ratio boundary (thick line in the diagram), formed heterogeneous vesicle populations. This result was also

reproduced for an equimolar bSM:Chol mixture (40:30:30). Heterogeneity in samples containing equimolar SM:Chol mixtures had been previously described by Veatch and Keller (Veatch and Keller, 2003b). In the DOPC:SM:Chol 1:1:1 mixture (star in the diagram in Fig. 3.1) both single-phase and vesicles with separated domains were observed, suggesting that the SM:Chol ratio could be a critical factor in liquid phase separation.

3.3.2 Two-photon microscopy avoids light-induced artifactual domains

Laurdan-labeled DOPC:eSM:Chol vesicles with Chol content that exceeded by only 5 mol % that of eSM (e.g. 45:25:30) showed a spatially homogeneously distributed intensity on both the blue and red edges of the spectrum, consistent with the existence of a single macroscopic domain. This result is against observations commonly described in the literature (Veatch and Keller, 2005a; Kahya et al., 2003; Smith and Freed, 2009). In order to rule out effects specific to Laurdan, similar samples were prepared adding standard TopFluor-Chol (TF-Chol) and Rhodamine-DOPE (Rho-DOPE) fluorescent probes (de Almeida et al., 2003; Pinto et al., 2013; Ariola et al., 2009). TF-Chol is a green-emitting cholesterol analog known to preferentially partition in the L_o phase (Sezgin et al., 2012); Rho-DOPE is a red-emitting DOPE analog that partitions in the L_d phase in PC:SM:Chol mixtures (Pinto et al., 2013). Confocal imaging showed that these probes distribute homogeneously within vesicles of the above composition, thus confirming the existence of a single domain (Fig. 3.3 A). However, upon continuous excitation of TF-Chol and Rho-DOPE with visible light (one-photon excitation) for very few seconds, the evenly distributed fluorescence emission in the green and red channels separated in bright green-only fluorescent domains and green and red fluorescent domains (Fig. 3.3 B). The green-only domains have been identified as L_o regions where TF-Chol preferentially partitions, whereas the red-green ones would correspond to L_d regions where the remaining TF-Chol and Rho-DOPE would coexist. Initially homogeneous (45:25:30) GUVs with either 0.5% TF-Chol and no Rho-DOPE, or 0.5% Rho-DOPE and no TF-Chol, also showed light-induded domain separation upon excitation at 488 and 543 nm, respectively. The on-set of domain formation took significantly longer in the former case than in the latter (few seconds and several minutes, respectively), indicating that TF-Chol is a major precursor (albeit not the only one) of light-induced lateral separation. The addition of the free-radical scavenger nPG to either mixture prevented the formation of domains (Fig. 3.4), although caution must be exercised as this antioxidant has also been shown to become a bilayer component and alter the equilibrium phase boundary of DSPC:DOPC:Chol mixtures (Zhao et al., 2007).

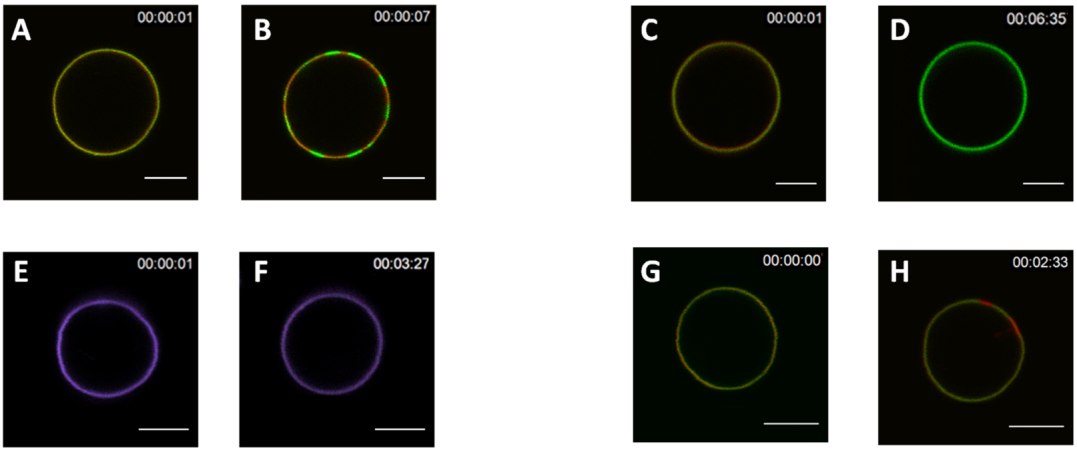

Figure 3.3: Photoinduction of laterally separated membranes. (A and B) GUVs made of DOPC:eSM:Chol (45:25:30, 0.5% TF-Chol and 0.5% Rho-DOPE) after one-photon continuous excitation for 1 s (A) and 7 s (B). Lateral separation is seen in B. (C and D) Vesicles as in A and B, after two-photon excitation for 1 s (C) and for more than 6 min (D). No domain formation is observed. (E and F) Vesicles as in A and B but with Laurdan (1%, no TF-Chol or Rho-DOPE) after continuous two-photon laser excitation for 1 s (E) and more than 3 min (F). (G and H) DOPC:eSM:Chol mixture (15:25:60, 0.5% TF-Chol and 0.5% Rho-DOPE) after one-photon excitation for 1 s (G) and 2 min (H). Lateral separation is seen in H. Scale bars, 5 μm.

In contrast, imaging TF-Chol at 890 nm (two-photon microscopy) at a comparable photon-emission yield did not result in formation of domains even upon continuous irradiation for several minutes (Figs. 3.3 C and D), suggesting that two-photon excitation opens up an excitation and relaxation pathway alternate to that of single-photon excitation. Similarly, light-induced domain-formation was not observed in Laurdan-labeled GUVs upon two-photon excitation at 780 nm, even when vesicles were continuously imaged for more than three minutes (Figs. 3.3 E and F). Previous studies have suggested that light-induced phase coexistence could occur for ternary compositions near miscibility transition boundaries (Veatch and Keller, 2003a). The same effect was achieved upon one-photon excitation even at 60% cholesterol (Fig. 3.3 G and H), although it required longer than for mixtures with lower cholesterol concentration (over 2 min). Again, this effect could not be reproduced using two-photon microscopy.

Photoinduced microscopic phase separation, as well as the efforts to minimize it using antioxidants, reducing agents and oxygen scavengers, has been previously described (Ayuyan and Cohen, 2006; Zhao et al., 2007; Sezgin et al., 2013). The results presented here show, however, successful prevention of photoinduced, artefactual phase separation by means of two-photon excitation of the fluorescent lipid analogues (as opposed to single-photon excitation).

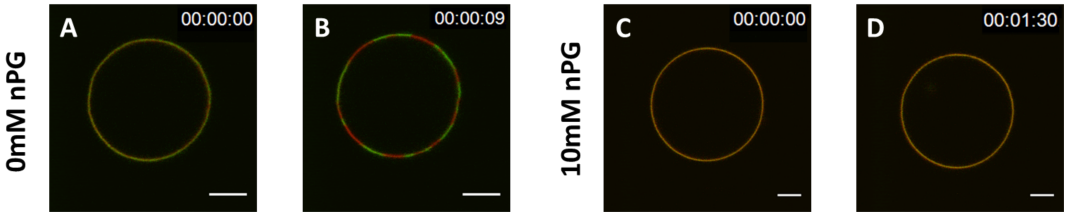

Figure 3.4: Photoinduced phase separation is prevented by antioxidant nPG. (A and B) GUVs made of DOPC:eSM:CHOL (30:30:4, 0.5% TF-Chol and 0.5% Rho-DOPE) upon simultaneous 488 and 543 nm illumination for 0 s and 9 s, respectively. Lateral separation is seen in B. (C and D) GUVs as in A and B after incubation with the free-radical scavenger nPG for 15 minutes. No phase separation is observed after 90 s irradiation. Scale bars, 5 μm.

3.3.3 Cholesterol and sphingomyelin effect on membrane lipid order

The findings described above evidence that artifactual, light-induced microscopic domain formation is avoided using two-photon fluorescence microscopy. Membrane lateral packing can therefore be accurately quantified throughout the ternary diagram using this imaging technique and the polarity probe Laurdan. The Generalized Polarization (GP) quantity (Parasassi et al., 1991; Bagatolli and Gratton, 2000) (described above) was used to determine membrane lateral packing depending on lipid composition (Fig. 3.5). Several GP measurements of GUVs with increasing concentrations of Chol and eSM were carried out to directly quantify their contribution to membrane packing and lateral separation. This approach also allowed assessment of the lateral packing within individual domains upon increasing concentrations of these compounds.

Fig. 3.5 A and B show GP values as a function of Chol content in mixtures with fixed eSM mole percentages. For both cases, mixing of the initially separated domains was clearly observed as soon as Chol:eSM molecular ratio exceeded 1 (thick lines). Besides, increasing Chol concentration mainly raised the rigidity of the fluid domains (sets of low GP values), while the ordered domains (sets of high GP values) were barely altered.

GP measurement of mixtures with increasing eSM concentration at fixed Chol mole percentages provided further insights into the domain coexistence behavior of the ternary mixture (Figs. 3.5 C and D): increasing the eSM content for the 20 mol % Chol mixture resulted in an increase of the L_o order (Fig. 3.5 C), while the fluidity of the L_d domain showed a bimodal behavior, first decreasing with increasing SM concentration, reaching a minimum at the eSM:Chol 2.25:1 ratio, and increasing afterwards. At 30 mol % fixed Chol concentration, all measured compositions lied below the eSM:Chol 2.25:1 ratio limit (Fig. 3.5 D). Under these conditions, increasing the eSM concentration induced disordering of the L_d phase while the

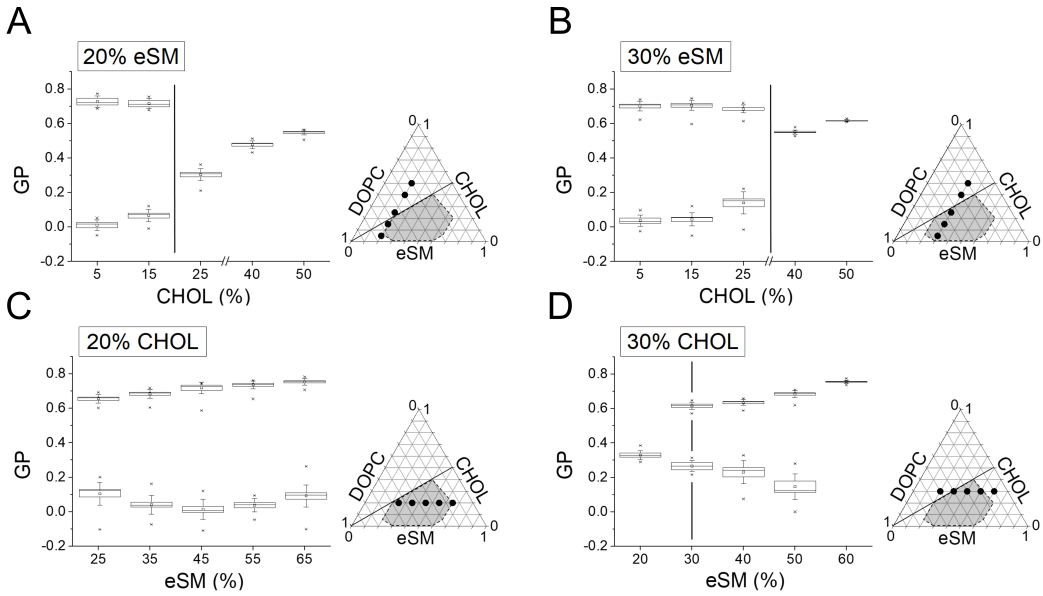

Figure 3.5: Membrane lateral packing dependence on cholesterol and sphingomyelin. A and B) Average GP determination with increasing amounts of Chol in vesicles containing fixed 20 or 30 mol % eSM, respectively. (Two GP values are defined for the laterally separated lipid compositions, the upper one corresponds to the more rigid domain and the lower one to the more fluid domain). High Chol ratios mainly induce more packed L_d domains. C and D) Average GP determination with increasing amounts of eSM in vesicles containing fixed 20 or 30 mol % Chol, respectively. Higher eSM concentrations lead to more rigid membranes. However, while eSM always rigidifies the ordered domain, its effect on the co-existing fluid domain depends on the eSM:Chol molar ratio. In all panels the Gibbs triangles at the right-hand side show the compositions measured in each case. The ends of the whiskers represent standard deviations.

L_o phase became more rigid. Both domains merged into a single highly-ordered domain at 60 mol % eSM.

3.3.4 Generalized Polarization ternary phase diagram

GP quantification for the domains in each lipid mixture also allowed the Gibbs triangle to be rendered in false color scale, where red denotes maximal rigidity and blue maximal fluidity (Fig. 3.6). Fig. 3.6 A corresponds to single-phase vesicle compositions, while Fig. 3.6 B and C show the GP for rigid and fluid domains of the phase-separated vesicles (left and right, respectively). For a better perception of the GP differences occurring in the domain-coexisting region, contour lines have been plotted in Fig. 3.6 B and C.

The GP of single-phase DOPC:eSM:Chol mixtures at low eSM content increased as a function of Chol concentration as expected, showing highest fluidity for DOPC-enriched mixtures (maximal fluidity, GP $\approx$ -0.12, was measured for pure DOPC

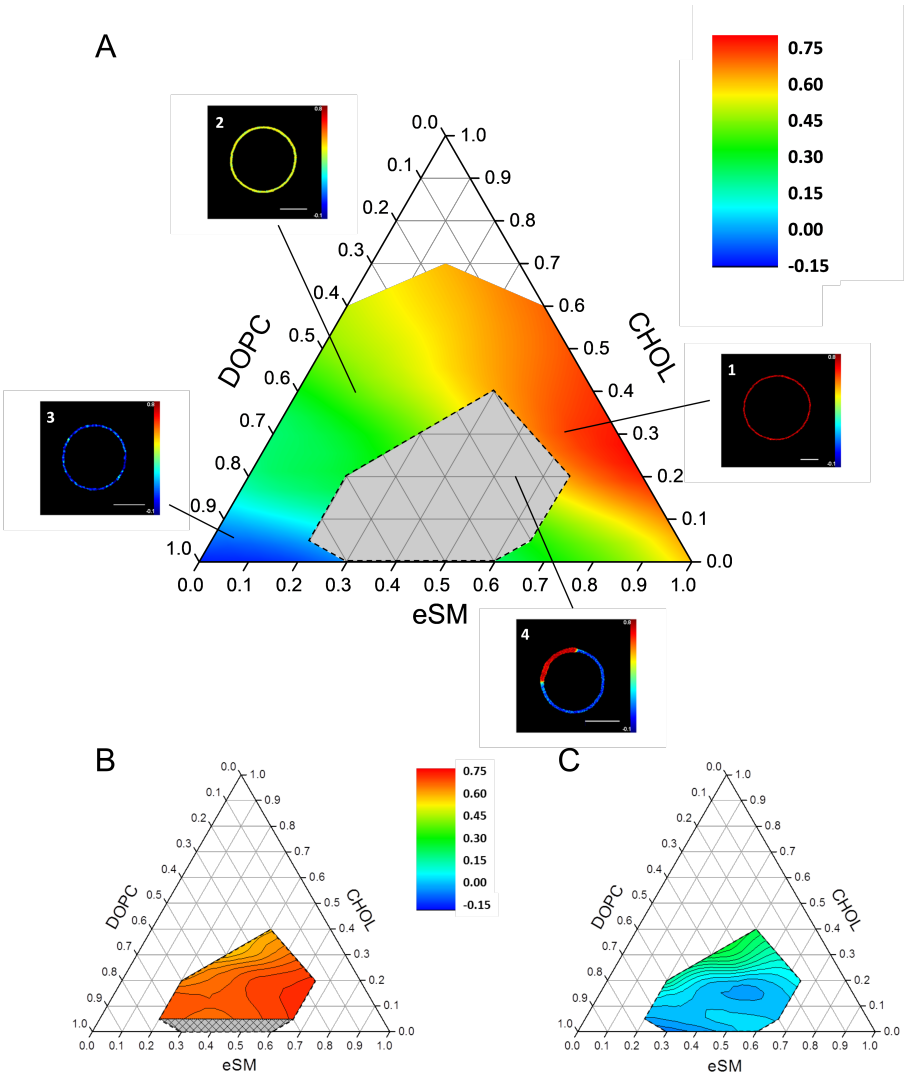

Figure 3.6: GP phase diagram of the DOPC:eSM:Chol ternary mixture at 23 °C. (A) GP values of lipid mixtures that do not undergo lateral separation are plotted in false color, red for the most compact lipid packing and blue for the less compact. Vesicle GP images illustrate several phase states. Compositions of the vesicles shown are: 1), 10:60:30; 2), 50:10:40; 3), 90:5:5; and 4), 25:55:20. (B and C) GP values of the rigid and fluid domains coexisting in laterally separated lipid mixtures (rigid domains in B, fluid domains in C) shown in the same false color scale as in A. Phase-separated mixtures containing very low cholesterol (5%) exhibit very small rigid domains floating on a fluid membrane. The GP for these minuscule, highly mobile rigid domains is hardly quantifiable (gray area in B) as opposed to the large fluid area. The sharp, straight boundaries are a reflection of the compositions that were selected to prepare the diagram (shown in Fig. 3.1).

vesicles). For fixed Chol mole percentages, and outside the phase-coexisting region, the GP increased with the eSM content of the mixture. In these regions of the

phase diagram the GP increased monotonically with increasing amounts of either Chol or SM.

Maximal membrane rigidity (GP $\approx$ 0.76) was scored for membranes that did not undergo domain separation and contained low DOPC and high eSM concentrations (e.g. 5:75:20). Interestingly, pure eSM GUVs showed a lower GP value of 0.61 and, for fixed low DOPC mole percentages and no lateral separation, the GP followed a bimodal behavior, reaching its maximum at eSM:Chol ratios ranging between 4:1 and 2:1. Mixtures with eSM:Chol ratio in this region were actually the most compact in the diagram (GP $\approx$ 0.76). This finding suggests that in these conditions (single-phase mixtures with low DOPC content) the membrane fluidity (as reported by Laurdan) is modulated by the eSM:Chol ratio rather than by the individual lipid content. These results would be in line with recent X-ray diffraction observations of the structure of SM:Chol bilayers that suggest that, at low Chol concentrations, the presence of this compound favors intermolecular interactions between SM molecules, increasing the rigidity, that would otherwise form intramolecular hydrogen bonds or hydrogen bonds with water and would result in a more fluid structure (Quinn, 2013). Notwithstanding the appeal of this explanation, it cannot be ruled out an unpredicted behaviour of Laurdan inside the gel matrix, which might account for the lower GP of pure SM vesicles.

When considering the region corresponding to laterally heterogeneous compositions (Fig. 3.6 B and C), and taking into account the impossibility to determine the GP value of gel domains in the absence of Chol due to their small size (gray area in 3.6 B), maximal rigidity (GP $\approx$ 0.75) was scored for L_o domains separated at low DOPC concentration and high eSM content (e.g.15:65:20) (Fig. 3.6 B). This value was close to the maximal rigidity measured in the single-phase vesicles made of eSM and Chol. In contrast, the fluid L_d domain of this mixture had an average GP value of 0.09 (Fig. 3.6 C), which was significantly higher than the minimal GP measured in pure DOPC vesicles, indicating that, while enriched in DOPC, the L_d phase in this mixture must also contain a fraction of the other lipids.

The lowest order for separated fluid domains (GP $\approx$ 0.01) was scored for the DOPC:eSM:Chol 35:45:20 mixture (Fig. 3.6 C). The average GP value for the coexisting L_o domain was 0.73 (Fig. 3.6 B), again comparable to the maximal rigidity scored for single-phase vesicles enriched in eSM and Chol, indicating that almost all Chol and eSM appear to separate into the ordered domain, while the fluid L_d shows features close to pure DOPC membranes. This high fluidity of a separated domain is also measured in mixtures with high DOPC content and low sphingomyelin concentration (75:20:5) (Fig. 3.6 C), where almost all eSM is expected to separate into a different domain.

3.4 Discussion

The main observation in this chapter is that, when the different regions of the triangular phase diagram for DOPC:eSM:Chol are examined using Laurdan-labeled GUVs and two-photon microscopy, a single, homogeneous phase is observed for all the mixtures containing eSM:Chol at molar ratios lower than 1. This is not in agreement with many previous studies on this subject, and the discrepancy could arise due to photoinduced artifacts.

There is an ample literature on phase diagrams of lipid mixtures relevant to the study of membrane rafts. A review of methods and results can be found in (Goñi et al., 2008). Phase diagrams of these mixtures have been built using one or more of these techniques: fluorescence spectroscopy (de Almeida et al., 2007; De Almeida et al., 2005; Frazier et al., 2007), fluorescence microscopy (Veatch and Keller, 2005a; Kahya et al., 2003; Veatch and Keller, 2005b; Bagatolli and Gratton, 2000), atomic force spectroscopy (Connell and Smith, 2006; Rinia et al., 2001), Langmuir balance (Smaby et al., 1994; Keller et al., 1998), calorimetry (Mannock et al., 2003; Nyholm et al., 2003), X-ray scattering (Chachaty et al., 2005; Mills et al., 2008), NMR spectroscopy (Oradd et al., 2002; Aussenac et al., 2003; Thewalt and Bloom, 1992) or ESR spectroscopy (Ionova et al., 2012; Smith and Freed, 2009). While overlapping on the whole, the results obtained using different techniques are not fully coincident, particularly in the regions of the phase diagram that are close to the phase boundaries. This can be explained in some cases by the difficulty of reproducibly preparing and studying samples whose properties are intrinsically fluctuating or depending on small differential lipid-lipid interaction (Almeida, 2009). In other cases, the various techniques may be reporting on different aspects of the same reality. Lipid composition is obviously important, e.g. DOPC facilitates L_o/L_d phase separation in PC:SM:Chol mixtures easier than POPC (Filippov et al., 2004).

The data reported here point to yet another possibility, namely that technical imperfections may sometimes lead to flawed results. The observed divergence between previous results and those in this chapter at SM:Chol molar ratios < 1, i.e. the lack of phase separation (Fig. 3.1) may be due, to satisfactory prevention of photochemically induced effects in the experiments performed for this thesis work.

3.4.1 Two-photon excitation does not photoinduce domains in model membranes

Unsaturated lipids and cholesterol are susceptible to free radical- and singlet oxygen-mediated oxidative degradation, with the corresponding formation and breakdown of lipid peroxides with different physical and chemical properties (Girotti, 1990). Lipid peroxidation can be photoinduced, which may result in artifactual domain

formation (Ayuyan and Cohen, 2006; Zhao et al., 2007; Jacob and Mason, 2005). Lipid peroxidation is a process that depends on the lipid environment (and, thus, membrane composition), dye concentration and excitation power. The data in (Fig. 3.3) show that it is also affected by the way the probe is excited (single or two-photon excitation) and that advantage of this dependence can be taken to prevent the formation of light-induced artifactual lipid domains.

Sezgin et al. (2013) had observed that, upon irradiation, TF-Chol readily changed its partitioning behavior in DOPC/SM/Chol GUVs and ascribed this effect to photoconversion of TF-Chol into a different green-fluorescent molecule. Light-induced lipid domains have been observed upon excitation of TF-Chol at 488 nm and of Rho-DOPE at 543 nm (Fig. 3.3), but no photoconversion or domain photoinduction could be observed when either TF-Chol, Rho-DOPE or Laurdan were excited taking advantage of a two-photon transition at 890 nm (TF-Chol and Rho-DOPE) or 780 nm (Laurdan) using a high repetition rate (80 MHz), 100 fs IR pulsed laser.

Single-photon excitation of a fluorescent dye can in most cases be described by a three-level energy model that involves excitation from the singlet ground state (S_0) to the singlet excited state S_1) and intersystem crossing to a long-lived lower energy triplet (T_1). Lipid-peroxidation may now majorly occur through two pathways: Charge transfer from a methylene group at the site of the unsaturation to the dye molecule in its triplet state results in a free radical that rapidly combines with molecular oxygen to form lipid peroxidates; alternatively, energy transfer from the dye's T_1 level to the triplet ground state of molecular oxygen may occur resulting in highly reactive singlet oxygen that leads to ensuing lipid peroxidation (Girotti, 1990). In either case the dye molecule returns to the ground state and is available for a new round of photoionization until it is eventually bleached following dye-destructive reactions, while the newly formed lipid peroxides readily reacts with neighboring molecules, setting-off a chain reaction that propagates through the membrane.

Two-photon excitation and subsequent dye relaxation on a two-photon microscope are not, however, properly described by this model: in line with our observations that two-photon microscopy does not induce photooxidation, formation of triplet states upon high repetition rate (MHz) femtosecond two-photon excitation has been found to be negligible at the required irradiances for microscopy experiments (Mütze et al., 2012; Eggeling et al., 2005; Dittrich and Schwille, 2001). In a typical two-photon microscope operating at 80 MHz and scanning with a pixel dwell time of 5 μs, a molecule is hit by 400 pulses in a row every 12.5 ns, every pulse containing roughly 10^8 photons. Due to the short interpulse period, much shorter than the μs-long triplet lifetime, whenever a long-lived triplet state is reached, photons from consecutive pulses may be absorbed and even saturate

the transition into higher excited T_n states (Sánchez et al., 1997), ending up in the rapid formation of a cation dye molecule and a solvated electron. Additionally, the high peak irradiance per pulse may lead to excitation into high electronic singlet levels (S_n) when a single extra photon is absorbed by the molecule already in its excited state or by higher-order resonance absorption (Dittrich and Schwille, 2001; Patterson and Piston, 2000), resulting too in a cation/solvated electron pair. Both mechanisms are in principle possible, although favoring the former is the observation that reducing the excitation repetition rate below 1 MHz results in an increased fluorescence yield, possibly because the longer interpulse break (longer than 1 μs) allows the triplet states to relax to the ground state before the next excitation cycle, preventing, this way, further excitation into higher excited triplet states (Donnert et al., 2007). These processes do result in bleaching of the dye molecule, but, as there is either no involvement of the excited triplet state of the dye, or the triplet states are only populated for a very short time (in the ns scale), there is no efficient precursor for photooxidation reactions, which majorly follow the two pathways described above.

In agreement with this explanation it is observed that, although two-photon microscopy of TF-Chol and Rho-DOPE did not induce domain formation, the two-photon excitation photobleaching rates of both dyes were significantly enhanced with respect to one-photon excitation at comparable photon-emission yields. Light-induced domain formation would thus involve a triplet state of the dye molecules that results in peroxidation of neighboring lipids through energy- or charge-transfer (not necessarily resulting in singlet oxygen creation in the latter case) and is avoided by the use of two-photon excitation.

Additionally, it is observed that, after light-induced phase separation of TF-Chol and Rho-DOPE in DOPC:eSM:Chol GUVs, the L_o phase shows fluorescence emission from TF-Chol only (no fluorescence from Rho-DOPE can be detected) that fades at a much faster rate than the TF-Chol coexisting with Rho-DOPE in the L_d phase (Fig 3.3 B). This observation hints at photoconversion of TF-Chol into a green emitting probe that preferentially partitions into the L_d phase, as previously reported (Sezgin et al., 2013), but its underlying reason could not be unequivocally identified.

3.4.2 Traveling along the phase diagram

The studies summarized in Figs. 3.5 and 3.6 provide additional interesting information on the DOPC:eSM:Chol mixture under conditions in which photooxidation artifacts do not occur. The experiments with increasing Chol concentration (Fig. 3.5 A, B) reveal that, when phase separation occurs, Chol addition increases the order of L_d domains. This is not mirrored by an equivalent disordering of the L_o domains, indicating a preferential partition of Chol into SM-rich domains. Sepa-

ration of a SM:Chol L_o phase in ternary systems with unsaturated-PC has been repeatedly observed (Veatch and Keller, 2005a; de Almeida et al., 2003; Filippov et al., 2004), and attributed to a direct interaction, via H-bonding (Patra et al., 1999; Slotte, 2016). Other studies, however, deny specific binding of Chol with SM over PC (Holopainen et al., 2004).

The data on mixtures with increasing SM concentration at constant Chol percentage (Fig. 3.5 C, D) complement previous observations. At 20 mol % Chol, SM-driven lateral separation processes widen the order gap between Ld and Lo domains up to 45 mol % SM (eSM:Chol molar ratio 2.25:1). The data in Fig. 3.5 C can be explained by the model proposed by Smith and Freed (Smith and Freed, 2009) at high DOPC concentrations repulsion between unsaturated chains and Chol favors accumulation of the latter lipid in the more ordered phase, while at SM:Chol ratios > 2.25 the high degree of chain alignment in these areas rich in saturated lipid may induce Chol repulsion from these domains. At 30 mol % Chol (Fig. 3.5 D) all samples are below the 2.25 SM:Chol molar ratio. Travel along this region of the phase diagram begins and ends with a single phase, although the GP values at 20 and 60 mol % are very different, 0.33 and 0.76 respectively. Between these two extreme SM concentrations L_o and L_d phase coexist, of which L_o is progressively incorporating more Chol until no further L_d domains are detected under the microscope. The equimolar SM:Chol ratio is important as it has been shown using a variety of techniques (Goñi et al., 2008; Patra et al., 1999; Holopainen et al., 2004) that this composition corresponds to a homogeneous liquid-ordered phase.

The ensemble of the data has been collected in Fig. 3.6. The measured GP values can be seen in the Table 3.1. Fig. 3.6 can be used as a tool to formulate DOPC:eSM:Chol ternary mixtures with a desired phase behavior and degree of lipid order. The similarities and differences of the phase diagram in Fig. 3.6 as compared to those published previously are discussed below.

The study of the GP for individual vesicles has allowed to gain insights into the region where L_d-L_o phases coexist. Inside this region, the composition of each domain and, hence, the GP, is defined by tie-lines. In a phase diagram, a tie-line is a line that crosses the phase separation region, the ends of the segment defined by the separation boundaries correspond to the composition of each of the phases in the separation region. The data reported here have been matched against previously described tie-lines and found that the GP values measured for each type of domain in the phase-coexisting region agree well with the GP values for the mixtures at the tie-line end points in the coexisting region described, which, according to the results reported in this chapter, is smaller than previously described ones. As an example, the mixture DOPC:eSM:Chol (35:45:20) has been studied, which forms domains with GP ≈ 0.73 and 0.01 for the L_o and L_d domains, respectively. According to

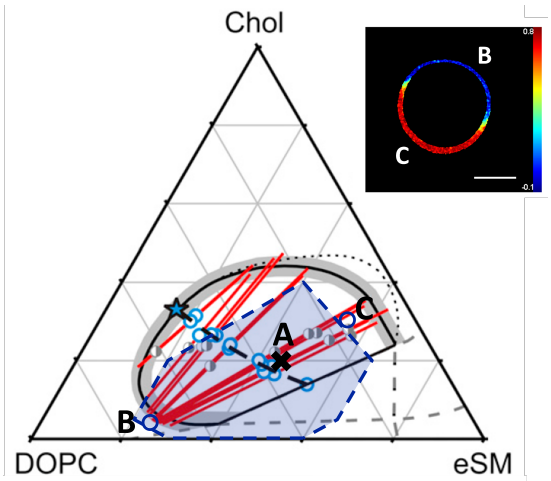

Figure 3.7: Traveling along the tie-lines of the DOPC:eSM:Chol phase-diagram. The GP values of each domain in the L_d-L_o phase-coexisting region agree well with the GP of the mixtures at the tie-line end points. The coexisting region found in this work using two-photon microscopy of Laurdan is smaller (dashed line) than that previously described (solid black curve). The inset shows a 35:45:20 DOPC:eSM:Chol representative GUV. Adapted from Bezlyepkina et al. (2013).

the expected tie-lines (Bezlyepkina et al., 2013), shown in Fig. 3.7, the mixture DOPC:eSM:Chol 35:45:20 (point A in Fig. 3.7) should form vesicles with domains with compositions 72:25:3 (B) and 15:55:30 (C). These compositions correspond to GP values 0.71 and 0.00, as read on Fig. 3.6, which match the GP measured for each domain within ± 0.02 uncertainty (0.73 and 0.01 respectively).

3.4.3 Comparison with previous data

There are several studies of ternary mixtures of the kind unsaturated-PC:DPPC or SM:cholesterol, some of them reviewed in (Goñi et al., 2008). Considering only the data at room temperature (as in the present chapter) there is a discrepancy in the region of SM (or DPPC):cholesterol < 1: in some cases a single liquid phase is observed along this region of the phase diagram, whilst in others phase separation is observed. A single liquid phase has been reported, besides the observations in this chapter (Fig. 3.1), at least by Veatch and Keller (Veatch and Keller, 2005a) for the POPC:PSM:Chol system (but not for the equivalent DOPC containing one) using single-photon fluorescence microscopy and more recently by Ionova et al. (Ionova et al., 2012), also for POPC:PSM:Chol, on the basis of EPR spectroscopy. Phase separation in the same region has been revealed in POPC:SM:Chol using either fluorescence microscopy (de Almeida et al., 2003) or δ-lysin-induced carboxyfluorescein efflux (Pokorny et al., 2006), and with DOPC:SM:Chol using EPR spectroscopy (Smith and Freed, 2009) and fluorescence

microscopy, as mentioned above (Veatch and Keller, 2005a; Kahya et al., 2003). The reason why different techniques provide inhomogeneous results was discussed in detail in (Goñi et al., 2008). In particular, microscopy lacks the resolution to observe nanodomains that are otherwise detected by spectroscopic techniques. However, the main issue in this chapter deals with the presence or absence of macroscopic (i.e. at the micrometer scale) domains under the fluorescence microscope in a given region of the ternary phase diagram. These data, obtained with two-photon Laurdan fluorescence microscopy support the absence of macroscopic phase separation at SM:Chol < 1, and explain other results showing phase coexistence as an artifact due to photo-induced phase separation. Studies by Thewalt and co-workers (Veatch et al., 2007) have experimentally addressed this problem, comparing data obtained with ^{2}H-NMR and with fluorescence microscopy. They conclude that probes like DiIC12 or Texas Red alter phase coexistence behavior in DOPC:DPPC:Chol bilayers whilst Laurdan does not. In line with these results, Laurdan concentration did not affect the GP value for those concentrations most commonly reported in the literature, ranging from 0.2% to 1% (see previous chapter *Experimental section*). In addition this probe partitions equally well into ordered and disordered fluid phases and displays a phase-dependent emission spectral shift. These studies provide strong support to the observations reported here.

3.5 Conclusions

Results in this chapter support that, in DOPC:eggSM:Chol and DOPC:brainSM:Chol mixtures in excess water, a single liquid phase exists for SM:Chol molar ratios < 1. They also support that light-induced photooxidation can induce macroscopic phase separation in this region, which may account for conflicting reports published previously based on single-photon microscopy. Experimental data also demonstrate that this artifact can be avoided using appropriate probes and imaging conditions, such as Laurdan and two-photon fluorescence excitation and allow ascribing the conflicting results to the different photo-physics of single and two-photon excitation and subsequent dye relaxation. In addition, they suggest that the variation of lipid order in single and two-phase regions corresponding to different mixtures of DOPC:eggSM:Chol is largely due to SM:Chol interactions.

Table 3.1: Laurdan GP values for different DOPC:eSM:Chol mixtures measured at 23 °C, for vesicles exhibiting lateral phase separation, and single-phase (homogeneous) vesicles.

DOPC	*eSM*	*Chol*	$\mathbf{GP}_{Lo}$	$\mathbf{GP}_{Ld}$	**GP**
1	0	0	-	-	-0.12
0.8	0.2	0	-	-	-0.11
0.7	0.3	0	x	-0.04	-
0.6	0.4	0	x	-0.01	-
0.5	0.5	0	x	0.01	-
0.4	0.6	0	x	0.08	-
0.3	0.7	0	-	-	0.33
0.2	0.8	0	-	-	0.40
0	1	0	-	-	0.61
0.9	0.05	0.05	-	-	-0.07
0.75	0.2	0.05	0.72	0.01	-
0.65	0.3	0.05	0.70	0.04	-
0.5	0.45	0.05	0.70	0.06	-
0.3	0.65	0.05	0.76	0.03	0.33
0.1	0.85	0.05	-	-	0.49
0.65	0.2	0.15	0.71	0.06	-
0.75	0.05	0.2	-	-	0.26
0.65	0.15	0.2	-	-	0.27
0.6	0.2	0.2	0.66	0.21	0.30
0.55	0.25	0.2	0.68	0.10	-
0.45	0.35	0.2	0.69	0.04	-
0.35	0.45	0.2	0.73	0.01	-
0.25	0.55	0.2	0.73	0.04	-
0.15	0.65	0.2	0.75	0.09	-
0.05	0.75	0.2	-	-	0.75
0.6	0.15	0.25	-	-	0.23
0.55	0.2	0.25	-	-	0.30
0.45	0.3	0.25	0.68	0.14	-
0.35	0.4	0.25	0.70	0.17	-
0.5	0.2	0.3	-	-	0.33
0.45	0.25	0.3	-	-	0.39
0.4	0.3	0.3	0.61	0.26	0.42
0.3	0.4	0.3	0.63	0.23	-
0.2	0.5	0.3	0.68	0.14	-
0.1	0.6	0.3	-	-	0.75
0.33	0.33	0.33	0.621	0.275	0.46

Table 3.1: Laurdan GP values for different DOPC:eSM:Chol mixtures measured at 23 °C, for vesicles exhibiting lateral phase separation, and single-phase (homogeneous) vesicles.

DOPC	*eSM*	*Chol*	$\mathbf{GP}_{Lo}$	$\mathbf{GP}_{Ld}$	**GP**
0	0.66	0.34	-	-	0.75
0.65	0	0.35	-	-	0.23
0.25	0.4	0.35	0.65	0.23	-
0.45	0.15	0.4	-	-	0.46
0.4	0.2	0.4	-	-	0.48
0.3	0.3	0.4	-	-	0.55
0.2	0.4	0.4	0.62	0.25	0.64
0.49	0.11	0.40	-	-	0.42
0.15	0.4	0.45	-	-	0.65
0.27	0.27	0.46	-	-	0.59
0.5	0	0.5	-	-	0.46
0.35	0.15	0.5	-	-	0.52
0.3	0.2	0.5	-	-	0.55
0.2	0.3	0.5	-	-	0.62
0	0.5	0.5	-	-	0.71
0.4	0	0.6	-	-	0.51
0.25	0.15	0.6	-	-	0.59
0.15	0.25	0.6	-	-	0.62
0.1	0.3	0.6	-	-	0.66
0	0.4	0.6	-	-	0.70
0.15	0.15	0.7	-	-	0.62

Chapter 4

Imaging the packing state and lateral organization of the HIV lipid envelope

Abstract

The chemical composition of the human immunodeficiency virus type 1 (HIV-1) membrane is critical for fusion and entry into target cells, suggesting that preservation of a functional lipid bilayer organization may be required for efficient infection. HIV-1 acquires its envelope from the host cell plasma membrane at sites enriched in raft-type lipids. Furthermore, infectious particles display aminophospholipids on their surface, indicative of dissipation of the inter-leaflet lipid asymmetry metabolically generated at cellular membranes. In this chapter, two-photon excited Laurdan fluorescence imaging and atomic force microscopy are combined to obtain insights into the phase state of membranes reconstituted from viral lipids (i.e., extracted from infectious HIV-1 particles), establish the role played by the different specimens in the mixtures, and characterize the effects of membrane-active virucidal agents on membrane organization. In determining the molecular basis underlying lipid packing and lateral heterogeneity of the HIV-1 membrane, these results may help develop compounds with antiviral activity acting by perturbing the functional organization of the lipid envelope.

4.1 Introduction

The human immunodeficiency virus type 1 (HIV-1) is an enveloped virus that follows a membrane fusion strategy to access and activate the replication cycle within the cytoplasm of host cells, typically CD4+ T cells and cells of the monocyte/macrophage lineage (Wilen et al., 2012). Host cell recognition and fusion with its plasma membrane is mediated by the viral envelope glycoprotein (Env) (Checkley et al., 2011). Furthermore, the physical properties and chemical composition of the HIV membrane play a key role in the entry process (Waheed and Freed, 2010; Lorizate et al., 2011). While much is known about the mechanistic and structural details of Env-mediated fusion (Eckert and Kim, 2001; Ward and Wilson, 2015), the functional organization of membrane lipids is less well understood.

HIV-1 acquires its lipid envelope and Env proteins by assembly and budding at the plasma membrane of the infected cell (Sundquist and Kräusslich, 2012; Freed, 2015). Assembly is driven by the viral Gag polyproteins, and appears to occur in specific membrane microdomains (Sundquist and Kräusslich, 2012; Freed, 2015). Advanced mass spectrometry combined with protocols optimized for the isolation of viral lipids enabled the determination of the HIV-1 membrane composition (Brügger et al., 2006; Chan et al., 2008; Lorizate et al., 2013). These studies showed that cholesterol (Chol) and sphingomyelin (SM) are enriched in the virus at concentrations similar to those in detergent-resistant membranes (Brügger et al., 2006). Quantitative analyses also revealed that, as compared to the bulk plasma membrane, the viral membrane appears to be enriched in specific lipids, including aminophospholipids, dihydrosphingomyelin (DHSM), plasmenyl phosphoethanolamine (or plasmalogen phosphatidylethanolamine, pl-PE), phosphoinositides, or ceramide, and this composition varied depending on the producer cell lines (Chan et al., 2008; Lorizate et al., 2013, 2009).

In addition, mature virions have been reported to expose phosphatidylserine (PS) and phosphatidylethanolamine (PE) on their external surface (Callahan et al., 2003; Soares et al., 2008; Li et al., 2014; Henriques et al., 2012; Phoenix et al., 2015) (see also section 1.1.4). Thus, the membrane acquired by HIV from infected cells appears to have lost the asymmetric lipid distribution generated at the plasma membrane by ATP-dependent aminophospholipid translocases. It has been suggested that PS exposure on virions and virally infected cells may enable viruses to evade immune recognition and diminish inflammatory responses to infection (Soares et al., 2008; Hoffmann et al., 2005). Aminophospholipids may also act as cofactors for HIV-1 infection of macrophages (Callahan et al., 2003), a phenomenon possibly related to the functional modulation of viral membrane lipid packing and lateral organization

(Waheed and Freed, 2010; Lorizate et al., 2011).

To gain insight into the molecular basis governing packing order and lateral heterogeneity in the complex HIV membrane, Giant Unilamellar Vesicles (GUVs) and monolayers made of lipids extracted from infectious HIV-1 (Lorizate et al., 2009) have been studied. HIV-membrane GUV and virion lipid packing has been quantified by applying two-photon Laurdan fluorescence microscopy, as detailed in the previous chapter 3. The topographic features of HIV-1 lipid monolayers have been analyzed by Atomic Force Microscopy (AFM). These complex membranes have been compared with compositionally simple models, identifying individual species that are critical for the maintenance of high order and lateral demixing. The functional relevance of lipid order and miscibility has been assessed by subsequent characterization of the perturbing effects exerted by membrane-active agents on membranes made from virus-derived lipids and their virucidal activity.

The results presented in this chapter indicate that the complex HIV membrane is highly packed, but less ordered than the rigid domains segregated in DOPC:SM:Chol-based models, and may display de-mixed nanoscopic lipid assemblies modulated by the lipid composition. Fluidification and induction of nanodomain coalescence by membrane-active compounds appear to be detrimental for viral entry, and changing membrane order may thus represent an alternative target for antiviral development.

4.2 Experimental Techniques

Materials

1,2-dioleoyl-sn-glycero-3-phosphatidylcholine (DOPC), 1-palmitoyl-2-oleoylphosphatidylcholine (POPC), 1,2-dioleoyl-sn-glycero-3-phosphatidylethanolamine (DOPE), 1-palmitoyl-2-oleoylphosphatidylethanolamine (POPE), 1,2-dioleoyl-sn-glycero-3-phosphatidylserine (DOPS), 1-palmitoyl-2-oleoylphosphatidylserine (POPS), cholesterol (Chol), egg sphingomyelin (SM, containing $\approx$ 86% N-palmitoyl SM), dodecanoyl dihydrosphingomyelin (DHSM), 1-(1Z-octadecenyl)-2-oleoyl-sn-glycero-3-phosphatidylethanolamine (pl-PE), 23-(dipyrrometheneboron difluoride)-24-norcholesterol (Topflour-Chol) and N-(lissamine rhodamine B sulfonyl)-1,2-dioleoyl-sn-glycero-3-phosphoethanolamine (Rho-DOPE) were purchased from Avanti Polar Lipids (Birmingham, AL, USA). 6-dodecanoyl-2-dimethylaminonaphthalene (Laurdan) was obtained from Molecular Probes (Eugene, OR, USA). Phospholipid stock concentrations were determined by phosphate assay. 2,2-Azobis(2-methyl-propionamidine) dihydrochloride (AAPH) and methyl-β-cyclodextrin (MβCD) were purchased from Sigma-Aldrich (St. Louis, MO). The MPER(671-693) peptide used in this study was synthesized

in C-terminal carboxamide form by solid-phase methods using Fmoc chemistry, purified by reverse-phase high-performance liquid chromatography (HPLC), and characterized by matrix-assisted laser desorption ionizationtime-of-flight (MALDI-TOF) mass spectrometry (purity > 95%).

Preparation of giant unilamellar vesicles

Giant unilamellar vesicles (GUVs) were produced by spontaneous swelling of lipid films deposited on 40 μm silica beads as described (Mattila et al., 2015). Briefly, lipid-Laurdan mixtures (0.125 mg total lipid) in $CHCl_3$:CH_3OH (9:1) were dried in a vacuum desiccator for 1 h to remove the organic solvent. The desiccated lipid was hydrated for 1 h at temperatures above the transition temperature of the mixture (typically 55 or 65 °C for the mixtures with highest SM content) and subsequently subjected to 30 cycles of extrusion through two 0.4 μm pore size polycarbonate filters in an Avanti Mini Extruder at 65 °C. Five microliters of silica beads was then mixed with 20 μL of the LUV suspension, separated in $\approx$ 3 μL drops on a teflon film, and vacuum-dried for 45 min. Dried beads covered with lipid were collected and transferred to a 3 g/L sucrose buffer to induce spontaneous swelling of GUVs. Finally vesicles were transferred to the observation dish in an isosmotic 10 mM HEPES, 150 mM KCl (pH 7.4) buffer.

HIV-1 Laurdan loading

For virion GP measurements Optiprep purified NL4-3 virus particles expressing mCherry.Vpr were incubated with 20 μM Laurdan for 20 min at room temperature. Unbound C-Laurdan was removed by ultracentrifugation through 20% (w/w) sucrose cushion at 70,000 g (avg.) for 2 h at 4 °C. Purified Laurdan labelled HIV-1 was adhered to Poly-L-Lysine coated coverslips for 15 min and washed with PBS.

Multiphoton fluorescence microscopy

GUV images were acquired on a Leica TCS SP5 II microscope (Leica Microsystems GmbH, Wetzlar, Germany). For multiphoton imaging the sample was excited at 780 nm using a femtosecond-pulsed titanium-sapphire Mai-Tai Deepsee laser (Spectra-Physics, Berlin, Germany). To avoid photoselection, GUVs must be excited with a circularly polarized beam at the sample plane and imaged at their equatorial plane. A variable wave plate (Newport 5540) located at the input IR port of the microscope was used to compensate for the any polarization effect induced by the microscope optics and this way obtain a circularly polarized beam in the centre of the field of view at the sample plane. GUVs were imaged through a $\times$63 water-immersion objective (numerical aperture, NA=1.2) and 512$\times$512 pixel images were acquired at 400 Hz per scan-line. The fluorescence emission was

collected by non-descanned (NDD) hybrid detectors, as they offer higher sensitivity compared to descanned photomultipliers. The blue edge of the emission spectrum was collected by NDD 1 at 415-455 nm and the red edge by NDD 2 at 490-510 nm. Generalized Polarization (GP) measurements were carried out on unilamellar GUVs.

HIV-1 virion images were acquired by spectral imaging on a Zeiss upright LSM 780 confocal microscope equipped with a 32-channel GaAsP spectral imaging detector and a femtosecond-pulsed titanium-sapphire Mai-Tai Deepsee laser (Spectra-Physics, Berlin, Germany. Laurdan was excited at 780 nm and the emission spectrum was collected between 415 nm and 549 nm in 8.9 nm wide intervals.

Data and image analysis

GP images of GUVs were calculated using in-house developed software based on MATLAB (MathWorks, MA, USA). After smoothing the images with a 2-pixel averaging circular filter and thresholding the intensity, the GP value for every pixel on the image was calculated following equation 4.1, where I_B is the intensity collected by NDD 1, I_R the intensity collected by NDD 2 and G is the factor that accounts for the relative sensitivity of the two channels, calibrated with 5 μM Laurdan solution in pure DMSO (Gaus et al., 2003):

$$GP = \frac{I_B - G \times I_R}{I_B + G \times I_R} \tag{4.1}$$

The mean GP value for each lipid mixture was calculated after imaging and analyzing at least 30 GUVs. Two or more independent experiments were carried out and averaged. In the case of co-existing phases in the same vesicle, the software allows the GP to be calculated for each domain separately.

HIV-1 virion GP analysis was performed using a Java Fiji plug-in developed for an efficient analysis of the acquired spectral data (Sezgin et al., 2015b). To obtain comparable results the same wavelenght ranges were used for GUVs and virions.

Planar supported phospholipid monolayers

Phospholipid monolayers were spread from chloroform/methanol 9:1 (v/v) solutions onto a 5 mM Tris (pH 7.4), 150 mM NaCl subphase, in a thermostated Langmuir–Blodgett trough (NIMA Technologies, Coventry, United Kingdom) as previously described (Bobardt et al., 2008; Badani et al., 2014). After 10 min to allow for solvent evaporation, monolayers were compressed at 25 cm^2/min up to the desired pressure and then transferred onto a glass coverslip at 5 mm/min. Specific labeling of fluid disordered phase was attained by including head-group labeled Rho-DOPE (0.5 mol %) in the monolayer composition. Fluorescence microscopy

Table 4.1: Synthetic virus-like (VL) lipid mixtures used in this chapter

	PC	CHOL	SM	DHSM	PE	pl-PE	PS
VL-0	15 % (DOPC)	45 %	40 %				
VL-1	37 % (DOPC)	46 %	17 %				
VL-2	14 % (DOPC)	46 %	17 %		16 % (DOPE)		7 % (DOPS)
VL-3	14 % (POPC)	46 %	17 %		16 % (POPE)		7 % (POPS)
VL-4	14 % (POPC)	46 %	12 %	5 %	3 % (POPE)	13 %	7 % (POPS)

observation of the planar supported monolayers was performed with a Leica DMI 4000b fluorescence microscope (Leica Microsystems GmbH, Wetzlar, Germany) and a Hamamatsu Orca R-2 digital CCD camera (Hamamatsu Photonics, Japan). AFM images were obtained from the mica-supported films using a JPK Nanowizard II atomic force microscope (JPK Instruments, Germany) operated in contact mode, using silicon nitride tips with a spring constant of 0.1 N/m.

Cell entry assays

HIV-1 pseudoviruses were produced by transfection of human kidney HEK293T cells with the full-length env clone JR-CSF using calcium phosphate. Cells were co-transfected with vectors pWXLP-GFP and pCMV8.91, encoding a green fluorescent protein and an env-deficient HIV-1 genome, respectively. After 24 h, the medium was replaced with Optimem-Glutamax II (Invitrogen Ltd, Paisley, UK) without serum. Two days after transfection, the pseudovirus particles were harvested, passed through 0.45 μm pore sterile filters (Millex HV, Millipore NV, Brussels, Belgium) and finally concentrated by ultracentrifugation in a sucrose gradient. HIV entry was determined using TZM-bl target cells, a HeLa cell line that stably expresses large amounts of CD4 and CCR5, as described in Markosyan et al. (2005). HIV pseudoviruses diluted to a 10-15% tissue culture infectious dose in PBS were deposited onto Poly-L-Lysine-coated 96-well plates, and incubated at 4 °C for 40 minutes. After washing, free poly-lysine was blocked for 20 minutes by medium addition (90% DMEM, 10% FBS) at 37 °C. Several dilutions of a given virucide in PBS were subsequently applied for 90 min at 37 °C. After three gentle washing steps, 1,1 x 10^4 TZM-bl target cells were layered on top of immobilized virions in the presence of 30 μg/mL DEAE-dextran (Sigma-Aldrich, St-Louis, MO). Infection levels after 72 hours were inferred from the number of GFP-positive cells as determined by flow cytometry using a BD FACSCalibur Flow Cytometer (Becton Dickinson Immunocytometry Systems, Mountain View, CA).

4.3 Results

4.3.1 Membrane lipid packing in HIV-1 mixtures and surrogates

To quantitatively determine HIV membrane packing, Laurdan-stained GUVs made from a complex mixture of lipids extracted from purified, infectious HIV-1 analized by two-photon imaging (Fig. 4.1). Fig. 4.1 A displays a ratiometric GP image of a GUV made of HIV lipids (micrograph on the left) and the average GP values determined for 4 different preparations (right panel). All reconstituted HIV membranes displayed a single ordered phase with mean average GP values ranging between 0.64 ± 0.01 and 0.68 ± 0.01. The mean value measured for the complete population (n = 228) was 0.66 ± 0.02. By comparison, the DOPC:SM:Chol (2:2:1) mixture (traditionally used as a separated lipid raft model (Kaiser et al., 2009) and henceforth L_d/L_o phase-separated model) laterally separated in two domains: one with a GP value of 0.70 ± 0.02, corresponding to a liquid-ordered (L_o) phase, defined as enriched in saturated sphingolipids and cholesterol in a highly condensed state, and the other with a GP value 0.06 ± 0.06, corresponding to a liquid-disordered (L_d) phase, enriched in unsaturated glycerophospholipids in a disordered state (Fig. 4.1 C). These observations were consistent with an overall high degree of lipid packing in the viral envelope. However, the significant differences in the distribution of the collected GP values (Fig. 4.1 D) further suggest that the lipid packing level of the viral membrane is below that measured in the L_o domain of the phase-separated model, or in the two-component SM:Chol (1:1) mixture (0.71 ± 0.01, Fig. 4.1 D).

To identify the HIV lipid species responsible for sustaining lipid packing, Laurdan GP values were further determined for GUVs made from synthetic virus-like (VL) mixtures (Fig. 4.1 B and Table 4.1). Models combining 5 lipids (VL-2 and VL-3) have been derived from the HIV lipidome established by Brügger et al. (Brügger et al., 2006), and are commonly employed as surrogates of the viral membrane (Scherer et al., 2010; Alam et al., 2009; Yang et al., 2015). Similarly to the HIV-1 mixture, all VL mixtures displayed a single phase (GP images on top). However, quantification of the GP values revealed significant differences in lipid packing (bottom panel).

The simpler models VL-0 and VL-1 combine a single glycerophospholipid, DOPC with SM and Chol. VL-0 matches the GP value of the HIV membrane using a similar Chol content (ca. 45%), and DOPC and SM content as determined from the GP-phase diagram of the DOPC:SM:Chol ternary mixture described in the previous chapter 3 (Fig. 4.2). Thus, VL-0 embodies a simplified model of the HIV membrane displaying a comparable level of lipid packing. In contrast, the VL-1 mixture combines DOPC with the mole fractions of SM and Chol found in the

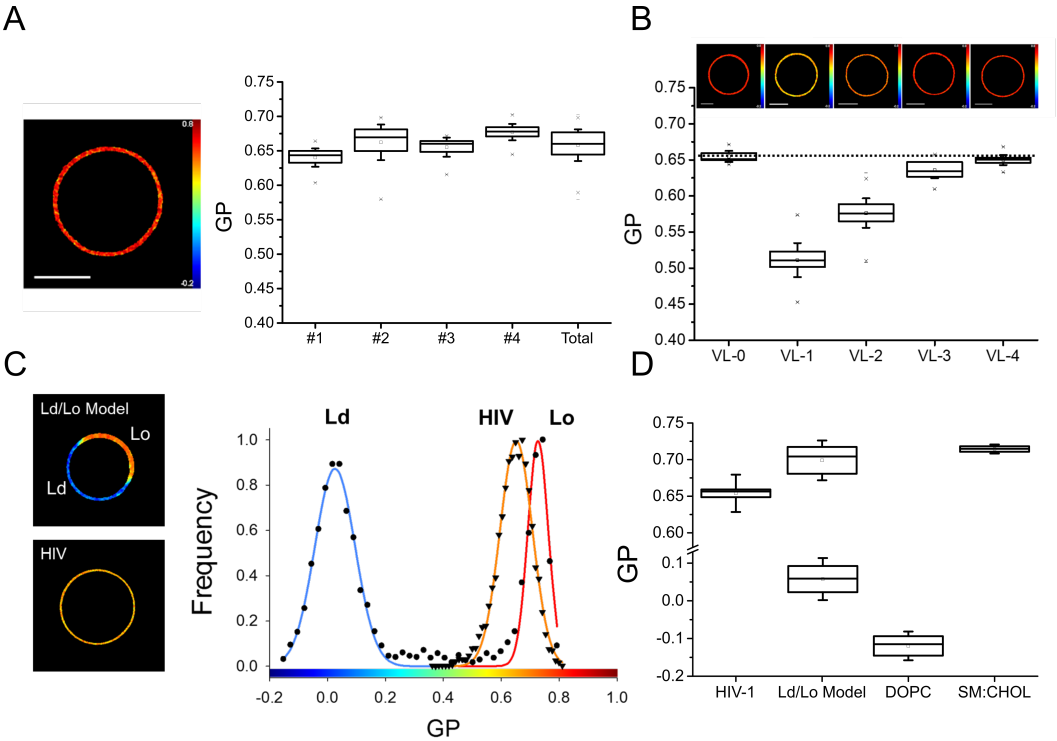

Figure 4.1: Lateral packing of HIV and model membranes using two-photon excitation fluorescence microscopy of Laurdan-labeled GUVs. (A) Laurdan GP imaging of a single HIV-reconstituted GUV (left), and GP quantification for 4 different HIV-reconstituted GUV preparations (right, # 1-4). Total corresponds to the grouping of all data measured in the 4 preparations. GP mean values depicted as box-and-whisker plots (the ends of the whiskers represent standard deviations). (B) GP images and average values determined for virus-like membrane surrogates (top and bottom, respectively). The dotted line shows the mean GP value calculated for the HIV membrane (Total in the previous panel). Lipid-compositions are summarized in Table 4.1 (C) GP pixel distribution of a representative GUV of the L_d/L_o phase-separated model (DOPC:SM:Chol 2:2:1) (image on the left, top) and a representative GUV reconstituted from HIV membranes (image on the left, bottom). (D) Mean GP values of GUVs reconstituted from HIV membranes, L_d/L_o phase-separated model, L_d (DOPC) and L_o (SM:CHOL 1:1) models. Scale bars are 5 μm in all micrographs; GP color scale limits: -0.2, 0.8 in A and B and -0.2, 1.0 in C.

viral lipidome (Brügger et al., 2006; Chan et al., 2008; Lorizate et al., 2013). The Laurdan GP value determined for the VL-1 mixture was much lower than for GUVs made from virus-extracted lipids or VL-0. The lipid mole ratios reveal similar Chol content in VL-0 and VL-1 mixtures, but higher SM content in the more ordered mimic. Thus, SM sustains the higher GP value of VL-0 in comparison to the VL-1 mixture. The GP values displayed in Fig. 4.1 B demonstrate that an increase of mixture complexity to render VL-2, VL-3 and VL-4 surrogates, may emulate the ordering effect of SM.

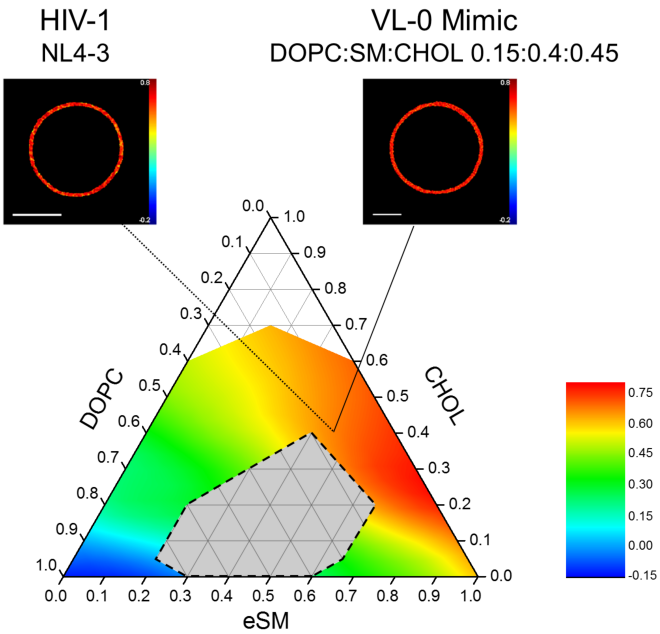

Figure 4.2: GP phase diagram of the DOPC:SM:Chol ternary mixture as determined in the previous chapter 3. GP values are plotted in false color, red representing the most compact lipid packing and blue the less compact. Lipid composition of the VL-0 packing mimic has been extrapolated from the GP value corresponding to the HIV-reconstituted GUVs.

The GP value of the VL-1 mixture increased significantly when replacing a fraction of DOPC by the aminophospholipids DOPE and DOPS (VL-2 model used in(Scherer et al., 2010)). A further increase of the GP value was observed for the VL-3 mixture containing 1-palmitoyl-2-oleoyl phospholipids (POPC; POPE; POPS) instead of the respective di-oleyl lipids. A subtle increase of the Laurdan GP value was finally observed for GUVs made of the VL-4 mixture. In this case, fractions of POPE and SM were replaced with pl-PE and DHSM, respectively, two species that are enriched and account for a significant mole percentage of virion lipids

(Brügger et al., 2006). GUVs made of this 7-lipid mixture exhibited a membrane order degree comparable to that measured for GUVs made of HIV-1 lipid extracts (Fig. 4.1 B, dotted reference line).

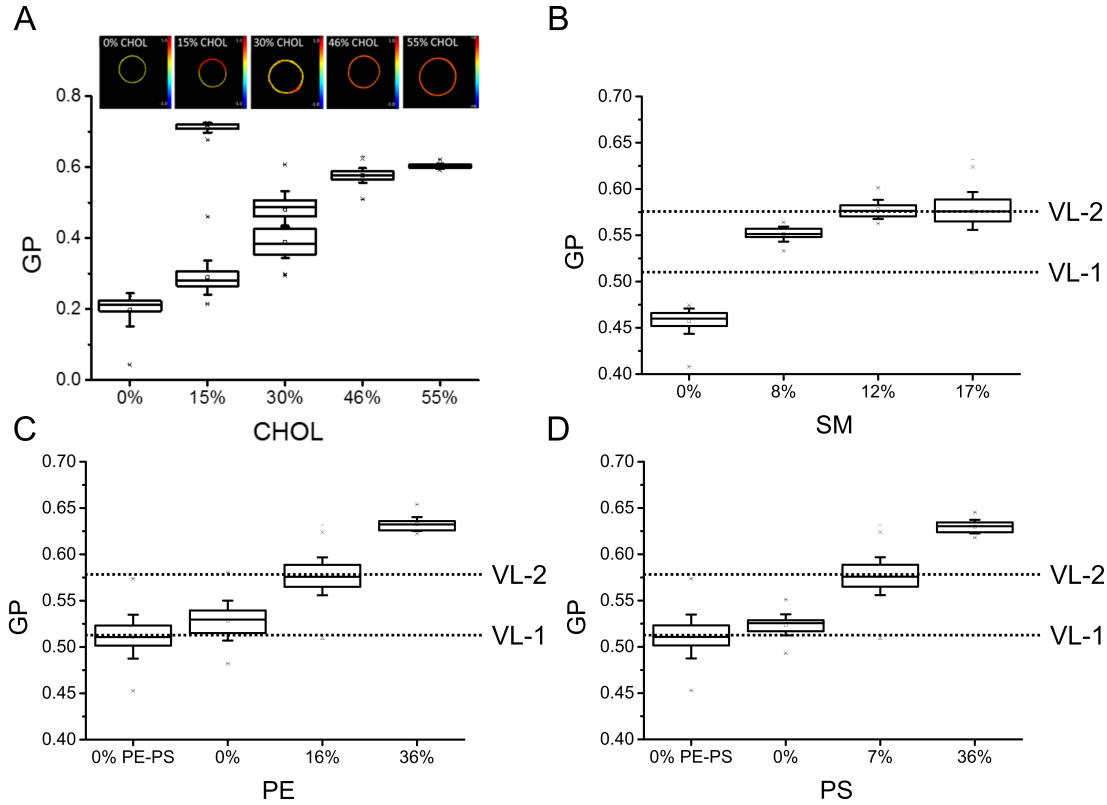

Figure 4.3: Membrane lateral packing dependence on the lipid components of viral mimic VL-2. (A) GP images (top) and average determination (bottom) with increasing amounts of Chol. Two GP values are defined for the laterally separated lipid compositions containing 15 and 30 mol % Chol, the upper one corresponds to the more ordered/dehydrated domain and the lower one to the more disordered/hydrated domain. GP color scale limits: -1.0, 1.0. (B-D) Membrane order dependence on phospholipid species, SM (B) PE (C) and PS (D). Chol content was 46 mol % in all cases. The dotted lines indicate the average GP for VL-1 and VL-2 mixtures.

The higher Laurdan GP values of increasingly complex mixtures indicated that HIV lipid packing primarily depends on polar head-group identity and acyl-chain saturation degree, while the presence of DHSM and pl-PE may also contribute to increase the order level as previously suggested (Brügger et al., 2006). Laurdan GP values displayed in Fig. 4.3 further illustrate the contribution to the lipid packing of single components in the generally used VL-2 model. As expected, Chol is the main determinant of membrane order (Fig. 4.3 A). The VL-2 mixture devoid of Chol displayed GP values consistent with a single fluid phase. Inclusion of 15-30 mole % of Chol induced microscopic L_o-L_d domain separation, while increasing

its content to reach the levels existing in the viral envelope generated a single, highly ordered phase. With 15 mol % Chol the lipid packing difference between the ordered and disordered phases (ΔGP) was less pronounced than in the L_o-L_d separation model (ΔGPs of 0.42 and 0.64, respectively, compare Fig. 4.3 A and Fig. 4.1 D), while this difference became even smaller with 30 mol % Chol (ΔGP = 0.09). These findings are consistent with recent reports indicating that subtle compositional variations may lead to a variety of lipid packing states in model and natural membranes (Levental et al., 2011; Sezgin et al., 2015a).

Figs. 4.3 B-D show the effects of the three phospholipids SM, PE and PS, when PC was used as reference. SM enhanced the order level in a dose-dependent way, and above that measured for the VL-1 ternary mixture (Fig. 4.3 B). Interestingly, SM levels below those existing in the mixture were sufficient to attain maximal order. In line with the composition-dependent lipid packing, both, PE and PS, increased GP (Figs. 4.3 C and D). These observations suggest that aminophospholipids may take part in regulating the ordered vs. disordered balance in de-mixed fluid domains (Bakht et al., 2007). They also imply that the loss of inter-leaflet asymmetry in virions emerging from infected cells does not necessarily result into more loosely packed lipid bilayers as previously suggested (Callahan et al., 2003).

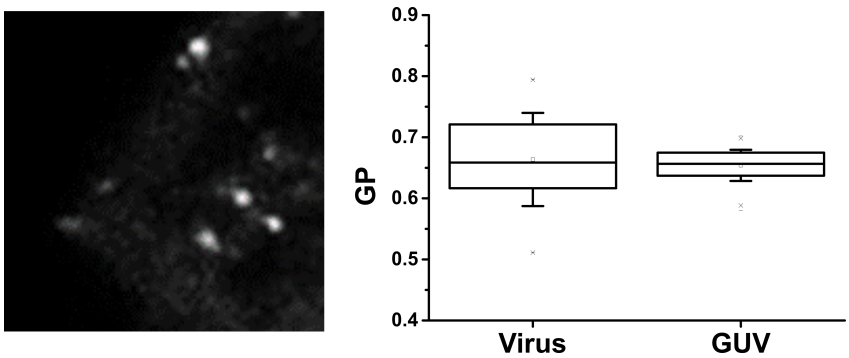

Figure 4.4: GP measurment on intact ultrapure HIV-1 virions labeled with Laurdan. (Left) Laurdan emission from HIV- virions. (Right) GP mean values determined in HIV-1 particles and GUVs made from HIV-1 lipids.

In the context of a different research project (see reference (Chojnacki et al., 2017)), the molecular order of the HIV-1 lipid envelope was also directly measured on intact HIV-1 virions (Fig. 4.4, left). Despite difficulties in GP quantification because of the subdiffraction size of HIV-1 particles, the GP value was successfully quantified. The average GP value measured for intact ultrapure virions was the same than that measured for HIV extracted lipids in reconstituted GUVs (Fig. 4.4, right). This suggests that viral matrix or the Env and cell proteins present in the HIV-1 envelope do not significantly affect the molecular order of the HIV-1 membrane.

4.3.2 Miscibility of the HIV membrane lipids

To determine the liquid-liquid immiscibility of the HIV membrane (resulting from the differences in packing and dynamics of lipids in different liquid phases), Langmuir–Blodgett films compressed to defined surface pressures (Π) were transferred onto mica and analyzed by combining fluorescence imaging and AFM as described in (Cruz and Pérez-Gil, 2007). Fig. 4.5 shows the miscibility transitions and topographic information of HIV-1 lipid films as a function of Π at both the microscopic (fluorescence microscopy) and the nanoscopic (AFM) lengthscales (top and bottom panels, respectively). At the lowest pressure examined (5 mN/m) phase separation was observed in fluorescence microscopy images (dark (ordered) domains in a fluorescent (disordered) background). At the slightly higher 8 mN/m pressure fluorescence micrographs display homogeneous films, while the AFM analysis reveals a coarse texture and the presence of de-mixed nanoscopic domains, which decreased in size at Π values of 10 and 20 mN/m. Thus, the 5-8 mN/m threshold seems to represent a miscibility transition pressure for the HIV mixture, in accordance with similar values reported for ternary mixtures containing Chol (Veatch and Keller, 2002). The monolayer colapsed at 30 mN/m, as evidenced by the partial exclusion of some material away from the interface (arrowheads). This behavior contrasts with the widespread belief that 30 mN/m represents the lateral pressure of biological membranes. According to the results in this chapter the lateral pressure that resembles the phase state of a certain lipid composition is different for each lipid mixture.

Finally, the miscibility of the virus-like lipid monolayers defined in Table 4.1 were compared. Unlike the HIV extracted lipids, the 3-lipid mixtures VL-0 and VL-1 and the 5-lipid VL-3 mixture displayed microscopic phase separation at Π values higher than 5 mN/m (Fig. 4.6). Only the 5-lipid VL-2 and the 7-lipid VL-4 mixtures showed the same phase behavior as the HIV monolayers (i.e. microscopic domain separation at 5 mN/m and homogeneous fluorescence emission at higher pressures). Further nanoscopic AFM analysis of the lipid monolayers at the controversial Π of 8 mN/m (Fig. 4.7) show that, even if none of the samples exhibit the exact same appearance as the HIV extracted lipid monolayers, the complex VL-4 mixture displays the most similar phase organization. Note that, unlike the HIV monolayers, VL-4 membranes consisted of a continuous rigid phase bearing fluid domains.

The very small size and rough morphology of the boundaries in rigid clusters of the HIV mixture are consistent with the low line tension at domain interfaces that characterize lipid systems undergoing fluctuations in phase composition (Honerkamp-Smith et al., 2009). This coarse pattern is maintained at surface pressures below collapse of the monolayer, which emphasizes its relevance for the envelope organization. In contrast, the simple VL-0 and VL-1 surrogates displays an ordered background that contains laterally separated large platforms with smooth

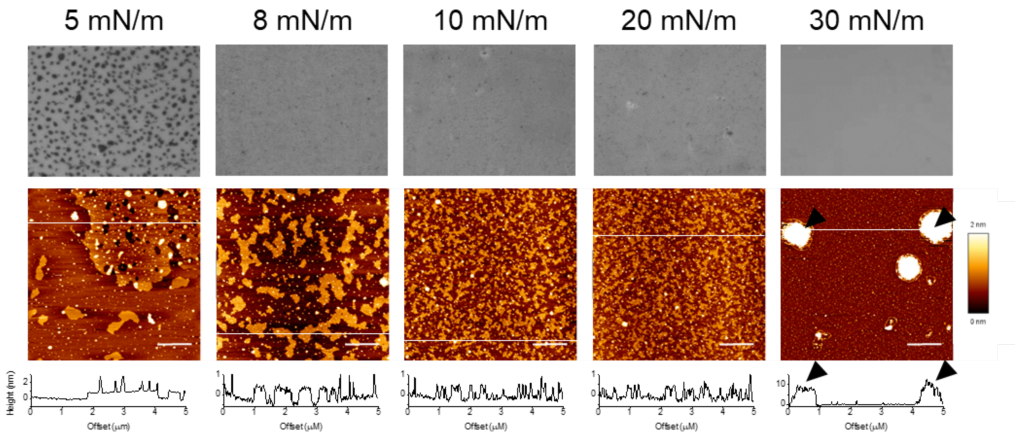

Figure 4.5: Liquid-liquid immiscibility of the HIV membrane. (A) Fluorescence microscopy (top) and AFM (bottom) images taken from a HIV mixture film compressed at the indicated surface pressures. In fluorescence images, the bright background (liquid-disordered) corresponds to the fluorescence emission of the Rho-DOPE probe that gets excluded from the ordered domains (dark spots only observable at $\Pi = 5$ mN/m). Plots below AFM images display the height profiles for the trajectories indicated by the white lines. Monolayer collapse at $\Pi = 30$ mN/m is evidenced from the accumulation of material excluded from the interface (arrowheads mark white spots with heights of ca. 10 nm). Scale bars are 100 and 1 μm in fluorescence and AFM images, respectively.

shapes. Thus, for comparable lipid packing degrees (identical GP values), the HIV lipid membrane and the simple VL-0 surrogate display different degrees of complexity regarding the lateral organization at the nanoscopic level. This suggests that model membranes based on 3-lipid combinations are not optimal surrogates of the HIV membrane. The 5- and 7-lipid mixtures VL-3 and VL-4 show coarsed domains, indicating that complex mixtures are necessary to resemble the features of biological membranes.

Altogether, GP and monolayer results show that the complex VL-4 mixture best mirrors the biophysical properties of the HIV-1 lipid envelope. Therefore, it will be used as a HIV membrane model in further experiments (see next chapter 5).

4.3.3 Alteration of HIV membrane lipid packing and miscibility by membrane-active agents

To establish the functional relevance of the lipid packing and miscibility states accessible to the natural HIV membrane, reconstituted GUVs and lipid monolayers were treated with membrane-active compounds displaying virucidal activity (Figs. 4.8-4.17). Fig. 4.8 (top panels) compiles the effects exerted on HIV lipid packing by three different compounds, namely: the Chol-extracting compound methyl-β-cyclodextrin (MβCD) (Campbell et al., 2002; Guyader et al., 2002), the gp41-

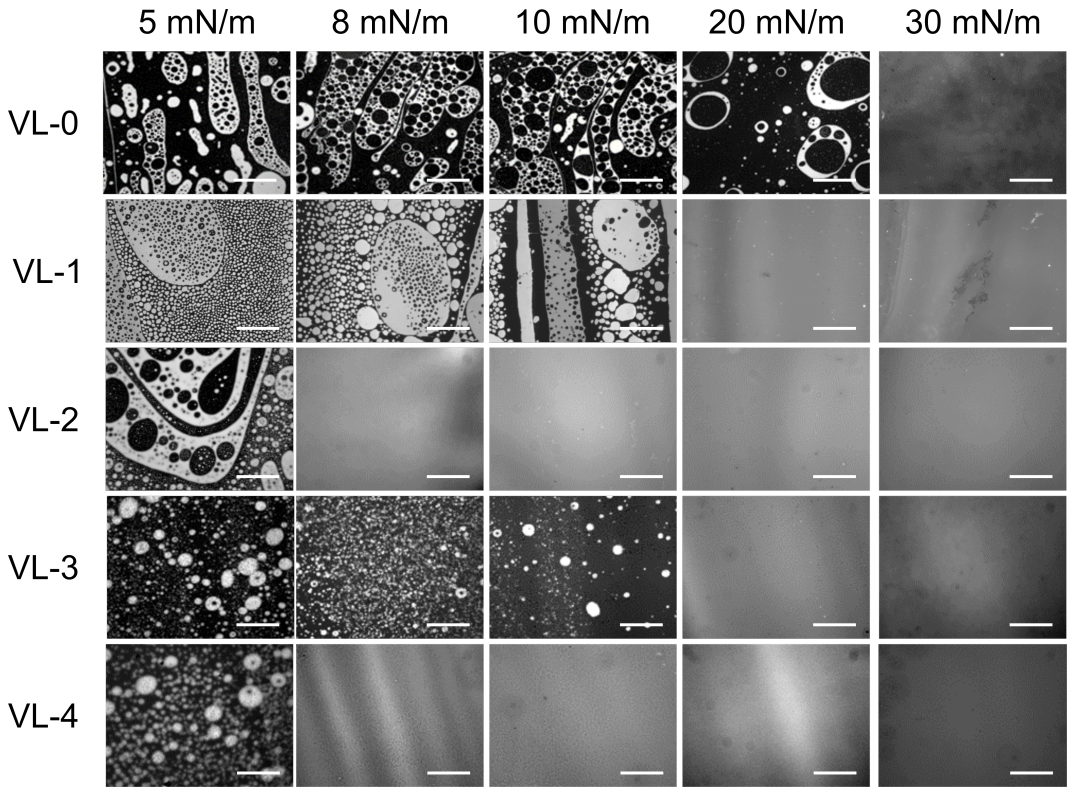

Figure 4.6: Liquid-liquid immiscibility of the virus-like model mixtures. Fluorescence images of Rho-DOPE labeled lipid monolayers compressed at different lateral pressures. Scale bars are 100 μm.

derived membranolytic peptide MPER(671-693) (also known as CpreTM) (Apellaniz et al., 2011) and the peroxyl radical generator 2,2-Azobis(2-methyl-propionamidine) dihydrochloride (AAPH)(Khaselev and Murphy, 2000). Cell entry assays were carried out in parallel to confirm the efficacy of these compounds as virucides (bottom panels).

Laurdan-labeled HIV GUVs treated for at least 15 minutes with MβCD exhibited lower Laurdan GP values than untreated controls, indicating a decrease in lipid packing induced by this compound (Fig. 4.8 A, top), which was consistent with the effect observed in Laurdan-stained virus particles (Lorizate et al., 2009). At the end time-points of incubation, homogeneous phase GUVs with a low GP value co-existed with vesicles displaying lateral separation(see Fig. 4.9 for an example of the latter). These findings give further support to the intrinsic capacity of the complex HIV membrane to access a variety of lipid packing states, which evolve modulated by the Chol content as in the surrogate mixtures (see previous Fig. 4.3 A). Emphasizing the functional relevance of this capacity, Chol extraction by MβCD blocks virus-cell entry (Campbell et al., 2002; Guyader et al., 2002; Liao

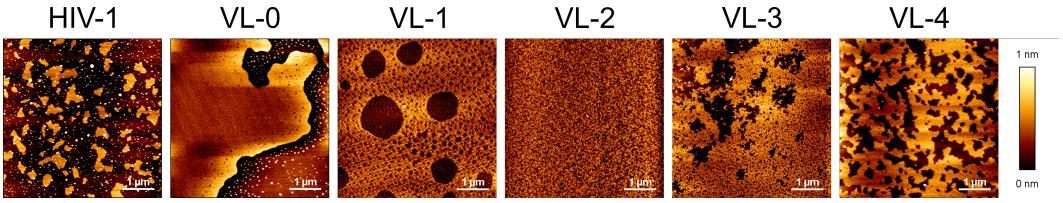

Figure 4.7: Nanoscopic AFM analysis of the phase organization of HIV and VL lipid monolayers compressed at 8 mN/m.

et al., 2003) (see also experiment in Fig. 4.8 A, bottom).

Membranolytic, aromatic-rich, short peptides such as C5A from hepatitis C virus or MPER(671-693) from HIV, both showing antiviral activity against HIV (Apellaniz et al., 2011; Bobardt et al., 2008), encompass an additional class of membrane-active virucidal agents (Badani et al., 2014) (see also next chapter 5). As shown in Fig. 4.8 B (top), Laurdan-labeled HIV GUVs treated with this peptide displayed a subtle, but significant reduction of the GP values. In these samples, the lowest GP values were measured for aggregated vesicles displaying a contact diaphragm, consistent with a correlation between membrane-perturbing and fluidifying effects induced by the peptide. Again, the membrane-fluidifying MPER(671-693) was virucidal for HIV (Fig. 4.8 B, bottom).

Lipid oxidative damage also perturbs the HIV membrane and suppresses infectivity (Lenard et al., 1993; Vigant et al., 2015). The effects of HIV lipid oxidation on lipid packing and cell entry were studied after exposure of HIV GUVs and pseudovirus particles to the free radical initiator AAPH (Khaselev and Murphy, 2000). Reduction of the Laurdan GP value indicated an overall fluidification of the membrane as a consequence of its oxidative action (Fig. 4.8 C, top), while the pseudovirus exposure to AAPH inhibited cell entry (Fig. 4.8 C, bottom). Contrasting these findings, the oxidative action of some compounds has previously been correlated with increased lipid packing and reduced membrane fluidity (Hollmann et al., 2014), effects postulated to impair viral fusion (Vigant et al., 2015). To ensure that the fluidification effect observed in 4.8 (top panels) did not pertain uniquely to the complex HIV mixture, Laurdan GP values were also calculated and averaged in AAPH-treated VL-2 and VL-4 single GUVs. As shown in Fig. 4.10, the GP values of VL-2 GUVs decreased readily upon incubation with AAPH, while more stringent conditions were required to observe the same fluidifying effect in the case of the more packed VL-4 surrogate, probably because of impaired accessibility to the lipid bilayer core, due to higher lipid packing. To prove that lipids following AAPH treatment were subject to similar degradative processes, Laurdan GP values for vesicles made of the same lipid composition used in previous studies (i.e., POPC) (Hollmann et al., 2014) were also determined (Fig. 4.10, right panel). In this case the apparent discrepancy disappears as higher GP values were

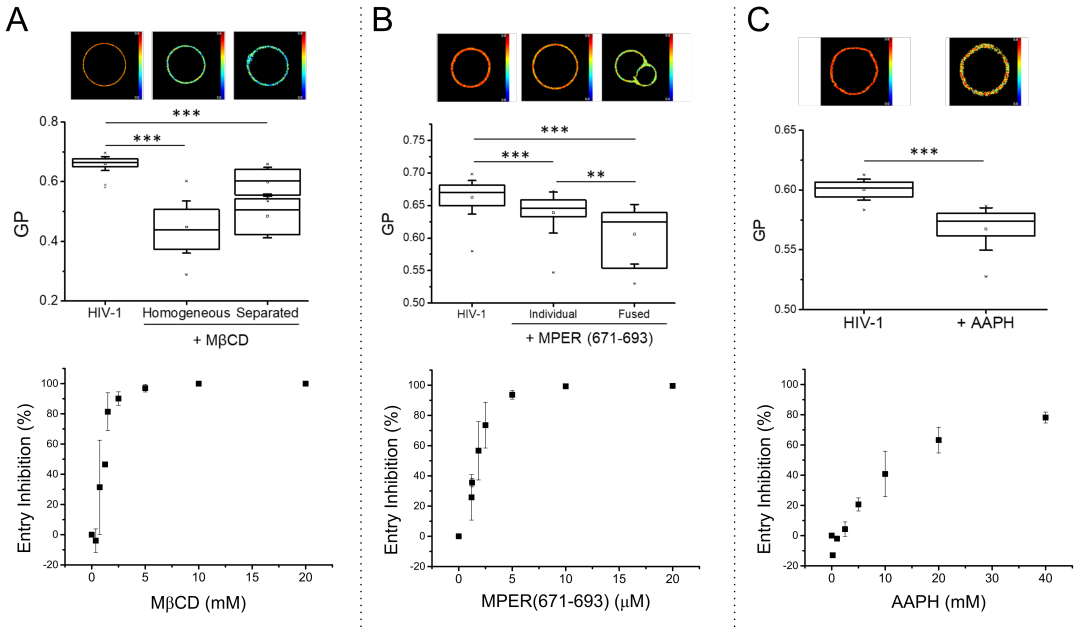

Figure 4.8: Effect of membrane-active compounds on HIV membrane lateral packing after 15 min incubation with HIV GUVs (top panels) and pseudovirus cell entry (bottom panels). (A) Top: Samples were incubated with MβCD (1 mM). The group of vesicles that displayed better fitting to two-component distributions is plotted using two boxes, the upper one corresponding to the more ordered domains and the lower one to the more disordered regions. Bottom: HIV-1 pseudoviruses were treated with increasing concentrations of MβCD. Entry was inferred from the number of total TZM-bl cells expressing GFP. Values represent means ± SD of three independent assays. (B) Samples were treated with MPER(671-693) peptide. Average GP values were determined for GUVs treated for at least 15 minutes with 1 μM peptide (top). The population of GUVs displaying membrane diaphragms were sorted out and measured separately. (C) Samples incubated with AAPH. GP values were determined after incubation with 20 mM AAPH (top). Conditions otherwise as in the previous panels. (***p $<$ 0.0001; **p $<$ 0.001). GP color scale limits: 0, 0.9.

observed, consistent with an increase in lipid packing of AAPH-treated POPC vesicles. It can be surmised that the single-lipid POPC model does not reproduce the variety of lipid packing states inherent to the complex HIV membrane.

Together, the observed changes in mean Laurdan GP values induced by the virucidal agents underpin the correlation between decrease in HIV lipid packing (related to membrane fluidification) and antiviral activity. In other words, keeping a high level of envelope lipid packing seems to be crucial for the virus entry function.

The effects of the membrane-perturbing compounds on the in-plane organization of the HIV mixture were evaluated next. Fluorescence images of monolayers treated with these compounds exhibited lateral de-mixing into micron-size domains (Fig. 4.11), which were not observed in parallel, untreated controls. The morphological

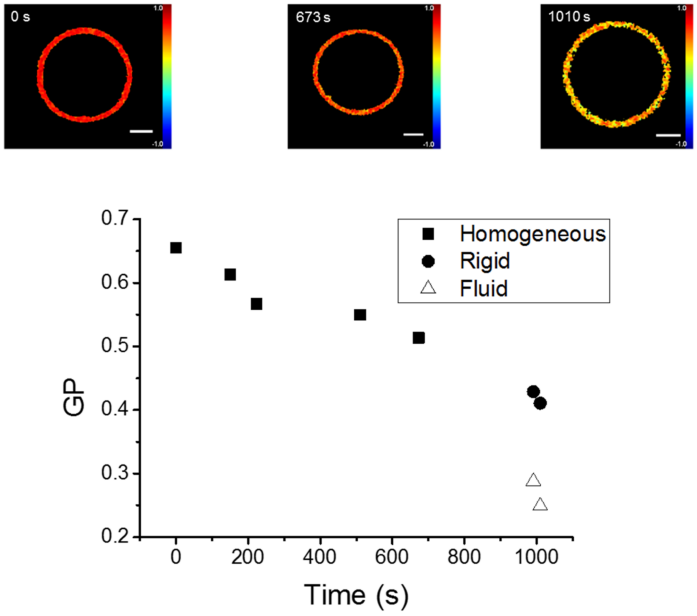

Figure 4.9: Time-evolution of the GP of a single GUV reconstituted from HIV membranes upon treatment with MβCD. An individual HIV-GUV was imaged at different times after addition of MβCD. The average GP decreased steadily due to the effect of MβCD. 15 minutes after adding MβCD the GP pixel-distribution of the GUV was best fit to a bimodal distribution with a rigid (top, circle) and a fluid (bottom, triangle) component. GP color scale: -1 to 1.

alterations undergone by those domains differed in the three samples. Round domains appeared at early times of incubation with MβCD (top panels). These domains disaggregated and mixed with the surrounding membrane at later times, as evidenced in experiments using Rho-DOPE and Topfluor-Chol probes to label the fluid (red) and ordered (green) domains, respectively (Fig. 4.12). The double-label experiments also revealed the appearance of dark patches, consistent with the exclusion and/or extraction from membrane areas of both fluorescent probes. MPER(671-693), on the other hand, induced the formation of a network of ordered domains, disclosing embedded circular patches of disordered lipid regions at the longest times of incubation (middle panels). Finally, AAPH treatment resulted in the appearance of round rigid domains interspersed in the fluid background that remained stable over time (bottom panels).

Higher resolution AFM of fluid and ordered areas provided additional insights into the underlying mechanisms of virucide-induced de-mixing of fluid domains (Figs. 4.13-4.17. The AFM images of MβCD-treated samples revealed depletion of rigid nanodomains from fluid regions, and appearance of large clusters of fluid

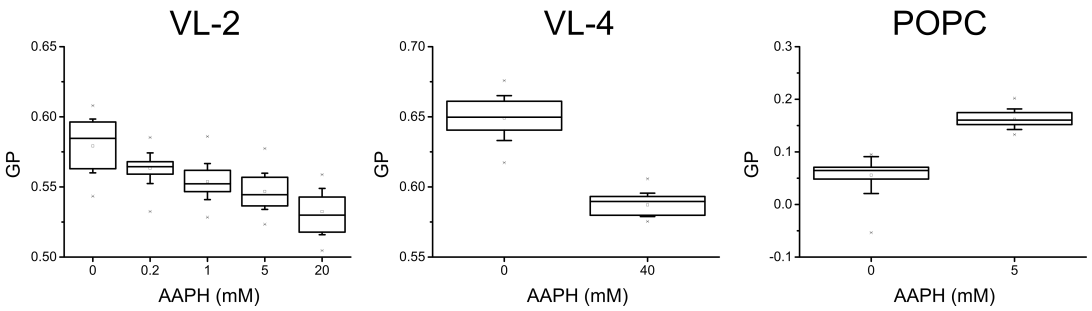

Figure 4.10: Laurdan GP values determined for different model membranes incubated with AAPH.

nanodomains within the ordered regions (Fig. 4.13). In the latter regions nanodomains compacted over time until they started to extrude their contents into the surrounding membrane. The observed effects are consistent with Chol depletion by MβCD, first occurring in the more disordered phase, which becomes more fluid and expands increasing rigid nanodomain propensity to cluster. After equilibration, Chol is also removed from the more ordered regions, which results in domain disaggregation and appearance of gel-like winding domains (Fig. 4.13).

By comparison, the MPER(671-693) peptide seems to disgregate fluid patches within the ordered phase and to generate ordered patches within the fluid phase, fixing the pre-existing rigid domains into a continuous web that becomes more compact over time (Fig. 4.14). The appearance of circular fluid phase domains within these rigid platforms (Fig. 4.11, middle) further suggests that they expand radially (Ryu et al., 2014), concomitant with merger and compaction. This behavior can be explained by the induction of membrane restructuring and lipid packing loosening in the vicinity of the peptide (Apellaniz et al., 2014b), that according to preliminary fluorescence experiments using Quasar-670 labeled MPER(671-693) in VL-4 model monolayers, is located in domain boundaries (Fig 4.15). Rigid domain growth could arise from local perturbations evolving within phase boundaries, thereby affecting membrane organization at a larger scale.

Lastly, fluid areas in AAPH-treated films appeared to be depleted of separated rigid domains. The rigid domains again aggregated into ordered micron-size domains (Fig. 4.16). Based on the effects observed for PC:SM:Chol monolayers (Volinsky et al., 2012), it was argued that oxidized glycerophospholipids stabilize micron-sized domain separation by increasing the hydrophobic mismatch between L_o and L_d phases. The chemical modification is expected to make the L_d phase thinner resulting in augmented line tension at inter-domain boundaries and thus promoting the coalescence of rigid domains into energy-minimizing larger platforms (Volinsky et al., 2012). The oxidized HIV mixture may follow this behavior, as

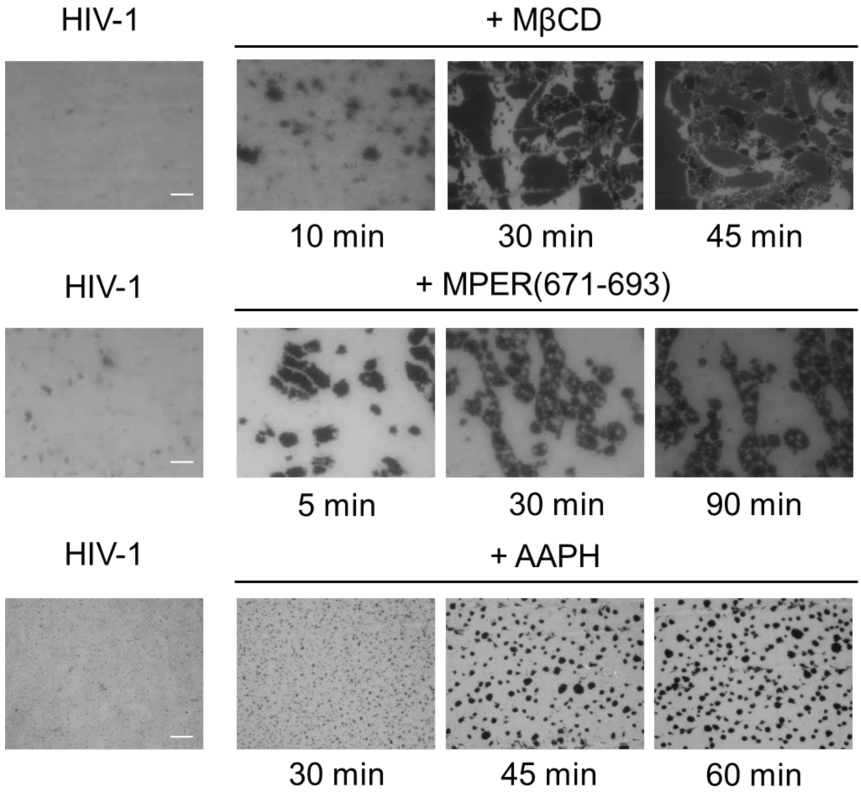

Figure 4.11: Effect of membrane-active compounds on the lipid miscibility of the HIV membrane. Fluorescence images of HIV monolayers showing the effects of MβCD (1 mM), MPER(671-693) (0.1 μM) or AAPH (5 mM) as a function of the incubation time (top, middle and bottom panels, respectively). Conditions otherwise as in the previous Fig. 4.8 B.

inferred from the changes in Δh values observed upon incubation with AAPH (Fig. 4.17). Consistent with L_d phase thinning, the height difference (Δh) increased with time and reached a maximum of ca. 1.1 nm concomitant with the stabilization of the separated domains.

Overall, the monolayer results displayed in Figs. 4.11-4.17 support that, regardless of the mechanism, induction of lateral de-mixing correlates with virucidal activity. This implies that regulation of liquid-liquid immiscibility plays a functional role in the viral entry process.

4.4 Discussion

Cryoelectron microscopy of virions reveals that a lipid membrane covers most of the HIV-1 surface in contact with the external medium (Zhu et al., 2006). Compared

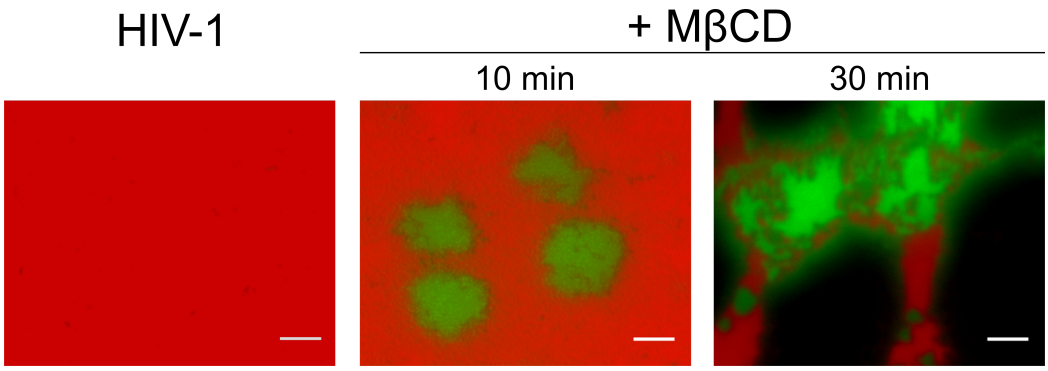

Figure 4.12: Lateral reorganization of the HIV monolayer incubated with MμCD. HIV lipids were doped with 0.1 mole % each of the probes Rho-DOPE (red channel) and Topfluor-Chol (green channel). Fluorescence images were taken for untreated samples (left), and for samples incubated with MβCD (1 mM) for 10 and 30 min (center and right panels, respectively). Conditions otherwise as in Fig. 4.11.

to the plasma membrane of producing cells, this lipid bilayer is enriched in Chol and aminophospholipids PS and PE (Brügger et al., 2006), which all appear to be accessible on the external leaflet (Waheed and Freed, 2010; Callahan et al., 2003; Phoenix et al., 2015). Several findings support that these selective features are of functional relevance: (i) Chol-chelating/depleting compounds inhibit HIV fusion and infectivity (Waheed and Freed, 2010; Liao et al., 2003); (ii) Interaction with T-cell immunoglobulin (Ig) and mucin domain (TIM) proteins tether HIV-1 particles bearing surface-exposed PS to the cell surface as well as to each other, thereby blocking release from infected cells (Badani et al., 2014); (iii) the chimeric antibody, bavituximab, used to identify and target PS exposed at membrane surfaces, suppresses productive HIV infection (Soares et al., 2008); and (iv) cyclotide peptides that associate with membranes through specific binding to PE, exert virucidal activity on HIV virions (Henriques et al., 2012; Phoenix et al., 2015).

In this chapter, to gain insight into the molecular basis underlying the functional organization of the lipid HIV membrane, the properties of membranes made from infectious HIV-1 or from synthetic lipid mixtures have been studied regarding membrane order and domain miscibility. Homogeneous populations of compositionally complex GUVs enriched in Chol have been produced (see previous chapter 3) (Mattila et al., 2015) to accurately quantify membrane lipid packing (Figs. 4.1-4.3). Ratiometric imaging revealed a high level of HIV membrane order (Fig. 4.1 A), which was lower than that observed for the segregated L_o phase in DOPC:SM:Chol GUVs (Fig. 4.1 D). GP measurements on HIV-1 virions confirmed these results (Fig. 4.4). However, due to the subdiffraction size of HIV partiles, this result should be further confirmed using super-resolution compatible polarity sensitive probes (Sezgin et al., 2017b).

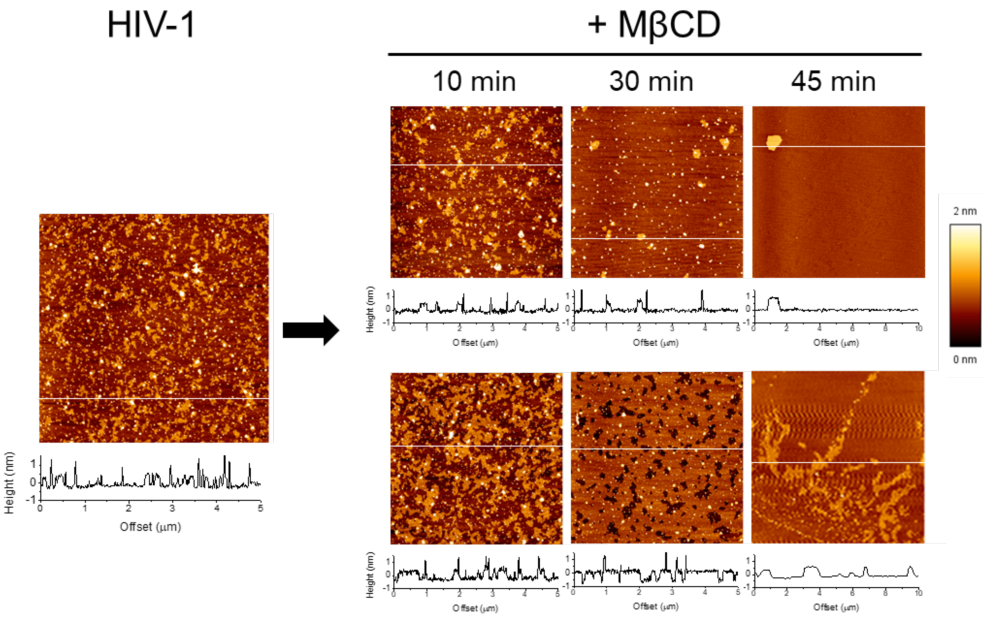

Figure 4.13: Nanoscopic phase organization of MβCD treated HIV-1 monolayers as determined by AFM analyses.

Comparable levels of lipid packing could be attained by increasing SM content in the three-lipid, simplified model VL-0 (Fig. 4.1 B and 4.2). The ordering effect of SM can however be reproduced by incorporating aminophospholipids and saturated acyl chains to render more complex 5- and 7-lipid VL-2, VL-3 and VL-4 surrogates, more faithful to the HIV-1 lipidome (Brügger et al., 2006) (Fig. 4.3). Topographic AFM analyses of HIV membrane monolayers revealed a coarse pattern, including de-mixed rigid nanodomains (Fig. 4.5). Such pattern was not observed in simplified VL-0 and VL-1 models and could be reproduced only with the 7-lipid VL-4 mixture (Fig. 4.7). Thus, the HIV membrane composition appears to be set to optimize high levels of lipid packing and ensure lateral de-mixing. While highly packed membranes can contribute to stabilize the structure of the viral particle in the external medium, lateral separation into rigid nanodomains might be required for the cell entry function (see below).

Taken together, (i) the high membrane order (Figs. 4.1 and 4.4), (ii) the small ΔGP-s between ordered and disordered regions regulated by Chol (Fig. 4.3), (iii) the presence of de-mixed nanoscopic rigid domains (Fig. 4.5) and (iv) the broken line-boundaries separating rigid clusters from the surrounding membrane (Fig. 4.5), strongly suggest that the HIV membrane is actually set at the threshold of fluid phase de-mixing (Honerkamp-Smith et al., 2009). Consistently, small, but significant changes in lipid packing induced by membrane-active compounds

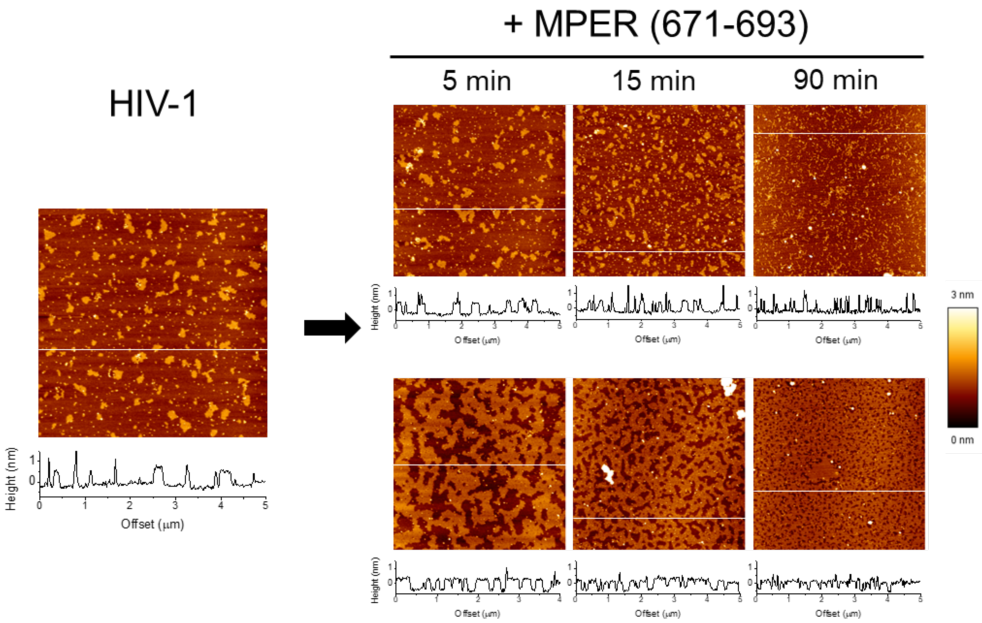

Figure 4.14: Nanoscopic phase organization of MPER(671-693) treated HIV-1 monolayers as determined by AFM analyses.

(Figs. 4.8, 4.9 and 4.10) strongly affected the lateral organization of the HIV membrane as inferred from changes in rigid nanodomain clustering and line tension observed by AFM (Figs. 4.13-4.17). Further underpinning the biological relevance of HIV-1 lipid packing and de-mixing states, the observed structural changes of the virus-derived membrane correlated with functional inhibition of pseudovirus by the membrane-active compounds.

The use of membrane-targeting virucidal compounds, altering the properties of the viral lipid membrane, has been proposed as a viable alternative for the development of broad-spectrum virus entry inhibitors (Vigant et al., 2015; Wolf et al., 2010; St.Vincent et al., 2010). The data reported in this chapter indicate that compounds that perturb the phase state of the HIV membrane by increasing fluidity or inducing ordered domain clustering might encompass effective virucides. Thus, in contrast to previous reports suggesting that virucides act by rigidifying the viral membrane (Vigant et al., 2015), the data reported here indicate that fluidification of the membrane may be detrimental for infectivity. A highly packed fluid phase (i.e., enriched in Chol) may constitute a prerequisite for retaining the nanoscopic sizes and convoluted perimeters of de-mixed rigid domains (Fig. 4.18). Reducing packing of the fluid phase may alter the size and clustering of rigid nanodomains and change the overall lipid miscibility in a way that could be incompatible with its function in viral entry (Fig. 4.18).

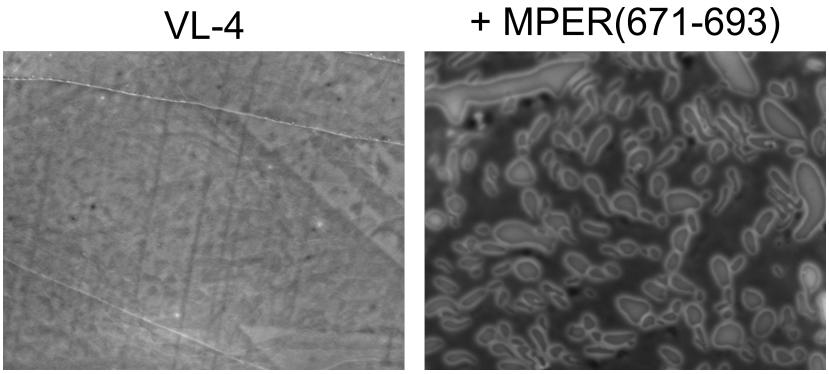

Figure 4.15: VL-4 lipid monolayer compressed at 8 mN/m treated with Quasar labelled MPER(671-693). The fluorescence emission signal corresponds to both Rho-DOPE and Quasar.

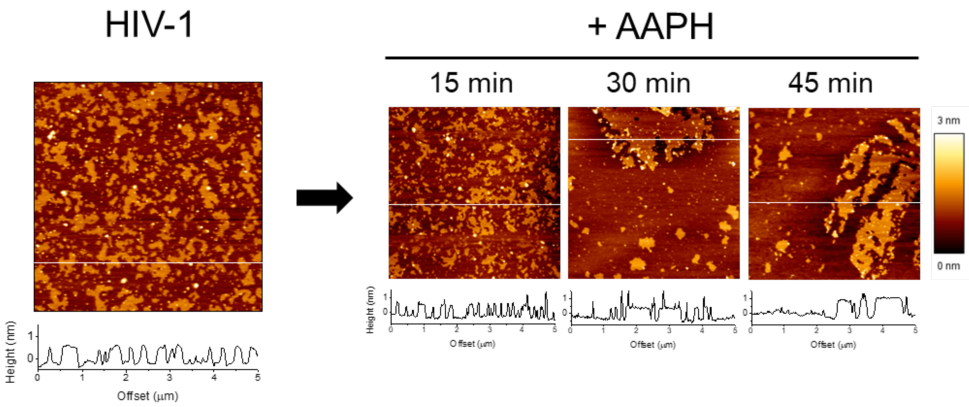

Figure 4.16: Nanoscopic phase organization of AAPH treated HIV-1 monolayers as determined by AFM analyses.

4.5 Conclusions

In its original form the membrane raft hypothesis stated that molecular assemblies of lipids, laterally separated under a variety of physiological conditions, play a functional role in cell compartmentalization of trafficking and signaling (Simons and Ikonen, 1997). A recent model proposes an additional role in HIV fusion, which would occur at boundaries between disordered and ordered domains in both, target cell and viral membrane (Yang et al., 2017; London, 2015). The data presented in this chapter provides evidence for the nanoseparation of the viral lipid envelope, showing that lateral discontinuities may indeed exist in the highly ordered viral membrane, which opposes the view of the HIV lipid envelope as a laterally homogeneous L_o-like membrane. It can be speculated that both fluidification and clustering may affect Env function following two non-exclusive mechanisms: (i) larger rigid clusters may trap functional Env peplomers in distant areas of the

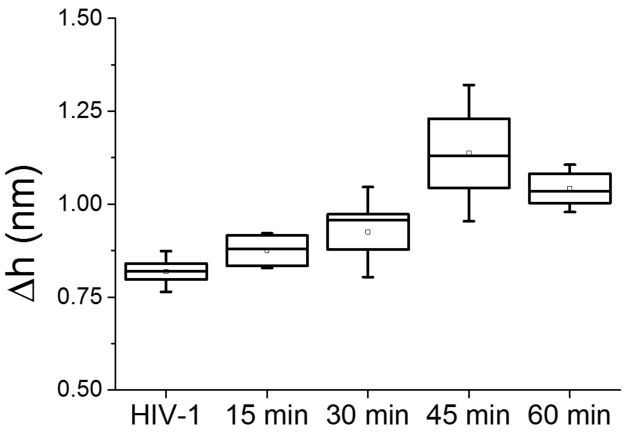

Figure 4.17: Increase in height (Δh) with the surrounding membrane of de-mixed rigid domains in a HIV monolayer incubated with AAPH for different times..

membrane and hinder their lateral diffusion to the sites of fusion (Zhu et al., 2006; Chojnacki et al., 2012; Brandenberg et al., 2015), (ii) merging of small nanodomains into large clusters could reduce the ratio of boundary lipids to total domain lipids, which would diminish the influence of boundaries upon fusion (London, 2015).

The use of HIV-reconstituted membranes has allowed to gain knowledge on the viral membrane at the molecular level. In this sense, the studied biophysical model systems and the reported effects could constitute valuable approaches with biomedical applications such as drug screening. Nonetheless, the complete transfer of these observations to the functional viral particles awaits the future implementation of optical methodologies allowing, precise, nanoscale phase measurements.

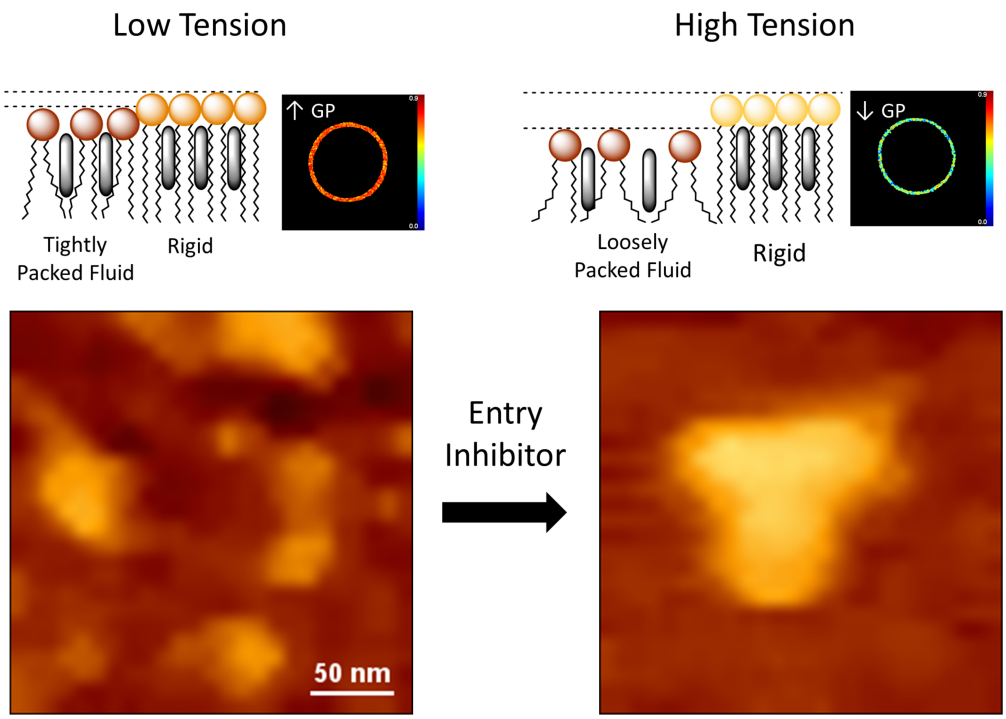

Figure 4.18: Model for the functional organization of the HIV membrane. Left: competence for entry depends on the presence of a highly packed fluid state and low line tension (top), which allows separation of small, convoluted rigid nanodomains (bottom). Membrane fusion would evolve more efficiently at the boundaries between those nanodomains and surrounding membrane (London, 2015). Right: fluidification and/or thinning of the more disordered phase increases line tension (top) and promotes domain clustering (bottom). Coalescence results in a reduction of the separated domain perimeter available for membrane fusion (solid line). Compounds that reduce lipid packing or directly act at domain boundaries could induce the transition between both states, and hence inhibit the entry function. AFM images covering a surface that approximates that of the viral lipid envelope correspond to untreated (left), and AAPH-treated viral lipid mixtures (right). The lighter color of the demixed domain in the latter sample denotes a larger height difference over the surrounding membrane.

Chapter 5

Effects of HIV-1 gp41-derived virucidal peptides on virus-like lipid membranes

Abstract

Membrane fusion induced by the envelope glycoprotein (Env) enables the intracellular replication of the human immunodeficiency virus type 1 (HIV-1); hence, this process constitutes a major target for antiretroviral compounds. It has been proposed that peptides having propensity to interact with membrane interfaces might exert broad antiviral activity against enveloped viruses. In the previous chapter a gp41-derived MPER-TMD peptide was shown to display anti-HIV activity. Based on that result, in this chapter, a collection of MPER-TMD overlapping peptides have been defined and their antiviral activity analyzed. The data support the virucidal activity of a region that combines hydrophobic-at-interface MPER aromatics with hydrophobic residues of the TMD, but not of those domains by themselves. In an attempt to correlate the antiviral activity of these peptides and their effects on the HIV-1 lipid envelope, membrane activity has been measured using a number of biophysical techniques. The data reveal that peptides endowed with virucidal activity are membrane active and induce permeabilization and fusion of virus-like lipid vesicles. In addition, they modulate lipid packing and miscibility of laterally segregated liquid domains. Thus, the overall experimental evidence is consistent with a pattern of HIV-1 inhibition that involves direct alteration of the physical chemistry of the viral membrane. Furthermore, the sequence-dependent effects observed might guide the development of new virucidal peptides.

5.1 Introduction

Among the major drug classes approved for HIV antiretroviral therapy, entry inhibitors are unique at blocking the function of an extracellular target, the envelope glycoprotein (Env) (Wong, 2014; Haqqani and Tilton, 2013; De Clercq and Li, 2016). The Env subunits gp120 (surface) and gp41 (trans-membrane) are responsible for receptor/co-receptor binding and virus-cell fusion, respectively (Checkley et al., 2011; Blumenthal et al., 2012; Melikyan, 2008). Upon activation of the fusion process, gp41 ectodomain trimers refold into low-energy 6-helix bundles (6-HBs) that pull cell and virus membranes into close contact. The conformational transition undergone by gp41 trimers constitutes the target for the clinically approved fusion inhibitor Enfuvirtide (Lalezari et al., 2003), which blocks 6-HB completion and hence membrane merger (Eckert and Kim, 2001).

Development of alternative fusion inhibitors displaying broad and sustained antiretroviral activity against HIV-1 remains a pursued goal to date (Flexner and Saag, 2013; Wisskirchen et al., 2014). It has been recently proposed that membrane-targeting virucidal compounds may comprise broad-spectrum inhibitors of enveloped virus entry (Wisskirchen et al., 2014; Wolf et al., 2010; St.Vincent et al., 2010). Arguably, compounds interfering with fusion by acting on the lipid component of the viral envelope could provide the basis for escape-proof anti-viral therapies (Vigant et al., 2015; Wojcechowskyj and Doms, 2010). In addition, as opposed to host cell membranes that are subject to ongoing synthesis, degradation, and influx and efflux of their components, static viral membranes lacking repairing mechanisms cannot escape the major perturbations induced by virucide activity. In this regard, a series of works support the possibility that peptides derived from hydrophobic-at-interface envelope glycoprotein sequences may comprise new generic antivirals (Giannecchini et al., 2003; Hrobowski et al., 2005; Sainz Jr. et al., 2006; Galdiero et al., 2008; Spence et al., 2014). Along this same line of thinking, in recent reviews it has been contended that these virucidal peptides could block viral entry by changing directly the physical chemistry of the viral membrane upon partitioning (Badani et al., 2014; Galdiero et al., 2015).

In the previous chapter 4, the VL-4 lipid mixture was defined (henceforth just VL), which includes the main 7 lipid species found in the HIV-1 membrane (Brügger et al., 2006) and exhibits the same order degree and phase behavior. In this chapter, to get new insights into the molecular mechanisms governing antiviral activity by membrane-partitioning peptides, the inhibitory potency of several MPER-TMD-derived peptides that possess distinct interfacial hydrophobicity patterns (Badani et al., 2014; Lorizate et al., 2008) are compared and their membrane-restructuring capacities established using the VL mixture as a surrogate of the HIV membrane. The experimental data support a virucide-like activity that alters the physical chemistry of the HIV lipid envelope for peptides combining the hydrophobic-at-

interface C-terminal MPER sequence with the N-terminal hydrophobic section of the TMD. It can be speculated that these sequences may serve as platforms for further development of antiretroviral peptides.

5.2 Experimental Techniques

Materials

1-palmitoyl-2-oleoylphosphatidylcholine (POPC), 1-palmitoyl-2-oleoylphosphatidylethanolamine (POPE), 1-palmitoyl-2-oleoylphosphatidylserine (POPS), cholesterol (Chol), egg sphingomyelin (SM, containing 86% N-palmitoyl SM), dodecanoyl dihydrosphingomyelin (DHSM) and 1-(1Z-octadecenyl)-2-oleoyl-sn-glycero-3-phosphatidylethanolamine (plasmalogen PE, pl-PE) were purchased from Avanti Polar Lipids (Birmingham, AL, USA). The 8-aminonaphtalene-1,3,6-trisulfonic acid sodium salt (ANTS), p-xylenebis(pyridinium)bromide (DPX) N-(7-nitro-benz-2-oxa-1,3-diazol-4-yl)phosphatidylethanolamine (N-NBD-PE), N-(lissamine Rhodamine B sulfonyl)phosphatidylethanolamine (N-Rh-PE) and 6-dodecanoyl-2-dimethylaminonaphthalene (Laurdan) were obtained from Molecular Probes (Eugene, OR, USA). Phospholipid stock concentrations were determined by phosphate assay. The collection of peptides displayed in Fig. 5.2 were synthesized in C-terminal carboxamide form by solid-phase methods using Fmoc chemistry, purified by reverse-phase high-performance liquid chromatography (HPLC), and characterized by matrix-assisted laser desorption ionizationtime-of-flight (MALDI-TOF) mass spectrometry (purity $> 95\%$).

Cell entry assays

Cell-entry assays were performed by measuring GFP gene transduction according to Bobardt et al. (Bobardt et al., 2008), with the modifications described by (Markosyan et al., 2005). In brief, HIV-1 pseudoviruses were produced by transfection of human kidney HEK293T cells with the full-length env clone JR-CSF using calcium phosphate. Cells were co-transfected with vectors pWXLP-GFP and pCMV8.91, encoding a green fluorescent protein and an env-deficient HIV-1 genome, respectively. After 24 h, the medium was replaced with Optimem-Glutamax II (Invitrogen Ltd, Paisley, UK) without serum. Two days after transfection, the pseudovirus particles were harvested, passed through 0.45 μm pore sterile filters (Millex HV, Millipore NV, Brussels, Belgium) and finally concentrated by ultracentrifugation in a sucrose gradient. HIV entry was determined using TZM-bl target cells, a HeLa cell line that stably expresses large amounts of CD4 and CCR5. HIV pseudoviruses diluted to a 10-15% tissue culture infectious dose in PBS were deposited onto Poly-L-Lysine-coated 96-well plates, and incubated at 4 °C for 40

Table 5.1: VL mixtures used in this chapter.

	POPC	CHOL	SM	DHSM	POPE	pl-PE	POPS
VL	14 %	46 %	12 %	5 %	3 %	13 %	7 %
30% Chol	18 %	30 %	16 %	6 %	4 %	17 %	9 %
15% Chol	22 %	15 %	18 %	8 %	5 %	20 %	12 %

minutes. After washing, free polylysine was blocked for 20 minutes by medium addition (90% DMEM, 10% FBS) at 37 °C. Several dilutions of a given peptide in PBS were subsequently applied for 90 min at 37 °C. After three washing steps, 1,1 x 10^4 TZM-bl target cells were layered on top of immobilized virions in the presence of 30 μg/mL DEAE-dextran (Sigma-Aldrich, St-Louis, MO). Infection levels after 72 hours were inferred from the number of GFP-positive cells as determined by flow cytometry using a BD FACSCalibur Flow Cytometer (Becton Dickinson Immunocytometry Systems, Mountain View, CA).

Liposome assays

Large unilamellar vesicles (LUVs) made of the VL lipid mixtures displayed in table 5.1 were produced following the extrusion method. To that end lipid suspensions were subjected to 10 freeze-thaw cycles prior to extrusion 10 times through 2 stacked polycarbonate membranes with a nominal pore-size of 0.1 μm (Nuclepore, Inc., Pleasanton, CA, USA). Vesicle permeability changes and vesicle-vesicle fusion were determined by the standard assays of ANTS/DPX leakage and Rho-PE/NBD-PE-based lipid-mixing, respectively (Huarte et al., 2008).

Giant unilamellar vesicles (GUVs) were produced by spontaneous swelling following the procedure described in Mattila et al. (2015). For preparation of peptide-containing GUVs, lipids (0.125 mg of the VL lipid mixture) and peptides were mixed at the desired peptide-to-lipid molar ratio in $CHCl_3$:CH_3OH (9:1) prior to desiccation for 1 h to remove the organic solvent. Dried silica beads covered with lipid-peptide mixtures were collected and transferred to a 3 g/L sucrose buffer to induce spontaneous swelling of GUVs. Formed vesicles were transferred to the observation dish in an isosmotic 10 mM HEPES, 150 mM KCl (pH 7.4) buffer.

Images were acquired on a Leica TCS SP5 II microscope (Leica Microsystems GmbH, Wetzlar, Germany). Laurdan-stained GUVs were excited at 780 nm using a ×63 water-immersion objective (numerical aperture, NA=1.2) and 512×512 pixel images were acquired at 400 Hz per scanning line. The fluorescence emission was simultaneously imaged at 415-455 nm and at 490-510 nm. Generalized Polarization (GP) images were computed for every pixel in the image (5.1), where I_B is the intensity in the blue channel, and I_R the intensity in the green channel. The G

factor accounts for the relative sensitivity of the two channels, calibrated with a 5 μM Laurdan solution in pure DMSO at 21 °C (Gaus et al., 2003):

$$GP = \frac{I_B - G \times I_R}{I_B + G \times I_R} \tag{5.1}$$

Supported lipid monolayers

To produce planar supported phospholipid monolayers, monolayers were first spread from $CHCl_3$:CH_3OH 9:1 (v/v) solutions onto a 5 mM Tris (pH 7.4), 150 mM NaCl subphase, in a thermostated Langmuir-Blodgett trough (NIMA Technologies, Coventry, United Kingdom), and then transferred onto mica as previously described (Epand et al., 2003, 2005). AFM images were obtained in a JPK Nanowizard II atomic force microscope (JPK Instruments, Germany).

5.3 Results

5.3.1 Virucidal activity of gp41-derived peptides

The plot in Fig. 5.1 displays the distribution of Wimley-White interfacial hydrophobicity (Wimley and White, 1996) along the MPER-TMD region of HIV-1 gp41. At the N-terminus, an amphipathic-at-interface helix (residues 656-671) is followed by a fully hydrophobic-at-interface stretch (residues 672-683). Supporting the biological relevance of these MPER segments, they consecutively span the broadly neutralizing epitopes 2F5 and 4E10 (Huarte et al., 2008; Lorizate et al., 2006; Apellaniz and Nieva, 2015). These interfacial sequences are followed by the TMD (residues 684-704), which is mostly hydrophobic according to Kyte-Doolitle hydropathy index (Kyte and Doolittle, 1982). The TMD is also segmented into two subdomains due to the presence of midway polar residues (Ashkenazi et al., 2013). Interestingly, the MPER C-terminal and the TMD N-terminal subregions are part of a continuous helix (Apellániz et al., 2015; Rujas et al., 2016). Finally, residues ^{679}LWYIK^{683} at the MPER-TMD juncture have been proposed to embody a "cholesterol recognition/interaction amino acid consensus" (CRAC) motif (Epand et al., 2003, 2005; Vincent et al., 2002; Schroeder, 2010; Yang et al., 2016b). This region is absolutely conserved across viral strains and isolates, and would be involved in generating the type of lipid perturbations that prime the rigid viral membrane for fusion (Vishwanathan and Hunter, 2008; Vishwanathan et al., 2008; Chen et al., 2009).

The particular organization of the MPER-TMD region allows on the one hand testing the prediction that CRAC-mediated, Chol-dependent membrane perturbations may sustain antiviral activity of the derived peptides (Epand et al., 2003).

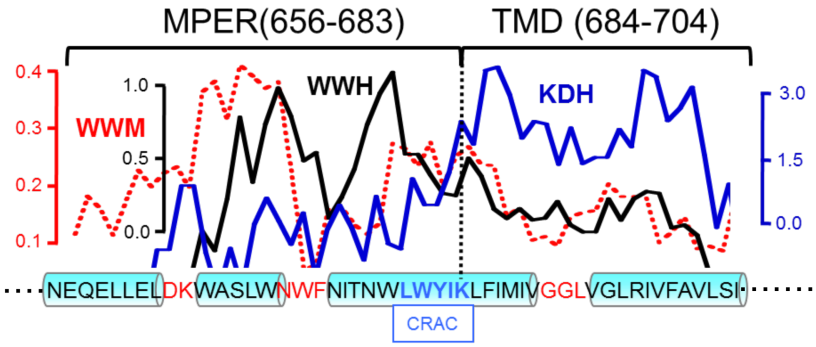

Figure 5.1: Hydrophobicity distribution within the gp41 MPER-TMD region (top) and amino acid sequence (bottom). For calculating mean WW hydrophobicity (black lines, Wimley and White (1996)) and KD hydropathy (blue lines, Kyte and Doolittle (1982)) a window of 5 amino acids was used. The red dotted line represents the WW moment (window of 11 amino acids) calculated for a fixed $\delta = 100°$ (helical periodicity), using the hydrophobicity-at-interface scale (Saez-Cirion et al., 2003). The scale bars follow the same color code. The cylinders on the sequence highlight helical subdomains, which are connected by non-helical joints (residues in red). Position for the postulated CRAC motif (residues in blue) is also indicated.

On the other hand, one can assess the effect of combining distinct hydrophobicity patterns on the inhibitory potency of peptides (Badani et al., 2014). The sequence range covered by each of the peptides displayed in the panels of Fig. 5.2 was thus selected on the basis of the presence of the CRAC motif and the hydrophobicity profiles. The list included a peptide bearing an Ile residue at the position of the absolutely conserved residue Leu-679. The resulting L679I substitution was shown to attenuate interactions of CRAC-representative peptides with Chol and reduce Env fusogenicity (Vishwanathan et al., 2008; Epand et al., 2006).

Fig. 5.2 compares the antiviral activity of the peptides with the effects exerted on VL lipid vesicles (leakage and fusion). Anti-viral activity was evaluated on virions that were first attached to poly-lysine coated plates, and cell infectivity subsequently quantified following procedures described previously (Bobardt et al., 2008). The amphipathic-at-interface peptide MPER(656-671) (Lorizate et al., 2006) did not display significant anti-HIV activity in the 0.1-20 μM range (Fig. 5.2, left panels). Addition of interfacial hydrophobicity and the CRAC motif at the C-terminus to render the peptide MPER(656-683) did not elicit activity. Thus, it appears that bearing high interfacial hydrophobicity was not sufficient to trigger virucidal activity, even if the peptide contained the CRAC sequence. In contrast, the peptide MPER(671-693), which combined the C-terminal hydrophobic-at-interface MPER stretch with the N-terminal section of the TMD, induced robust antiviral activity with a mean IC_{50} value of 1.67 $\pm$ 0.04 μM. Interestingly, the peptide MPER(671-693)L679I with the mutated CRAC motif displayed a comparable virucidal effect

(IC_{50} value of 0.96 ± 0.02 μM). Finally, the TMD(684-704) sequence representing the full-length gp41 TMD as defined by Cohen et al. (Cohen et al., 2010), did not have any apparent effect on pseudovirus cell entry.

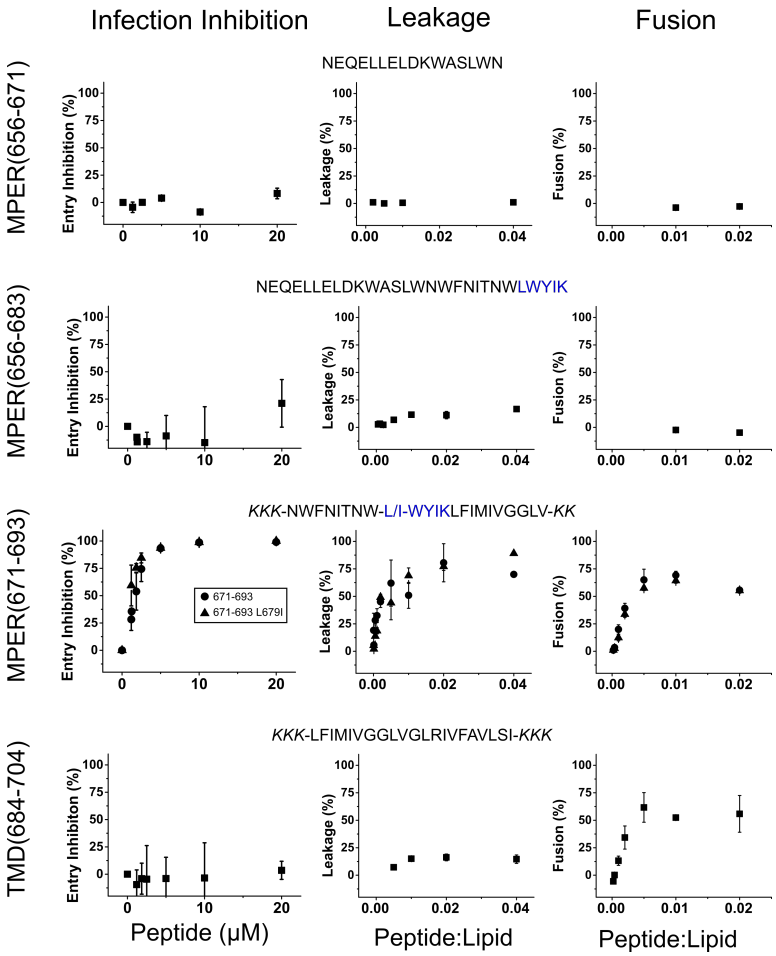

Figure 5.2: Antiviral and membrane-restructuring activities of gp41-derived peptides. Sequences covered by the overlapping peptides used in this study and their effects on pseudovirus infectivity, LUV permeability and LUV-LUV fusion (left, center and right panels, respectively).

To ascertain whether the infection-blocking effect observed in the case of the peptides MPER(671-693) and MPER(671-693)L679I was due to a virucide-type membrane activity, and not a consequence of the specific inhibition of HIV-1 Env-mediated entry/fusion, experiments were also conducted with virions pseudotyped with the VSV G glycoprotein (VSV-G) (Fig. 5.3). Since they are produced from the same env-deficient plasmid, VSV-G virion membrane composition is expected to be the same as that of ther Env+ counterparts. Incubation of VSV-G pseudoviruses with the peptides resulted in comparable levels of infection blocking, thereby

supporting a virucide-like behavior for the inhibitory peptides, rather than an activity dependent on protein sequence-specific mechanisms.

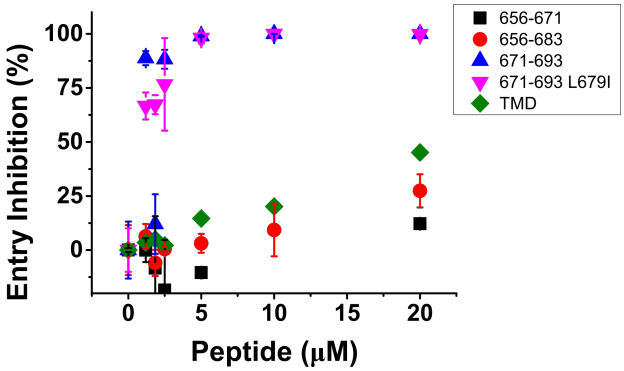

Figure 5.3: Control for sequence specificity. In these assays VSV-G pseudoviruses were used as a control for cell entry mediated by a different viral fusion glycoprotein. Conditions otherwise as in Fig. 5.2.

To determine if the observed virucidal activity correlated with the capacity of the peptides for altering the properties of the viral membrane, the 7-lipid VL mixture was used as an envelope surrogate. Leakage and lipid-mixing induced by the peptides on VL LUVs was first assayed (Fig. 5.2, center and right panels, respectively). Significant leakage of contents and lipid-mixing was observed upon VL LUV incubation with MPER(671-693) or MPER(671-693)L679I peptides. Interestingly, the TMD(684-704) peptide also induced lipid-mixing, an observation consistent with data previously reported in the literature (see for a recent review Klug et al. (2017)). Thus, VL vesicle destabilization correlated with the observed virucidal effects of the peptides MPER(671-693) or MPER(671-693)L679I.

However, peptide-induced perturbations that in the vesicular system (leakage and vesicle-vesicle fusion assays) can relax through vesicle-vesicle aggregation and fusion, must persist in the polylysine immobilized viral particles that are used in the infectivity assays. Control experiments also indicated that lipids were not solubilized or extracted from virions treated with the inhibitory peptides (Fig. 5.4). Thus, it could be hypothesized that the local perturbations leading to LUV leakage and fusion may affect in an interrelated way additional physicochemical properties of the lipid envelope in the immobilized virions.

5.3.2 Role of cholesterol in the membrane activity of virucidal peptides

The HIV particle is enriched in Chol (ca. 50 mole %), which underpins increased membrane order and the potential for liquid phase co-existence (Brügger et al., 2006;

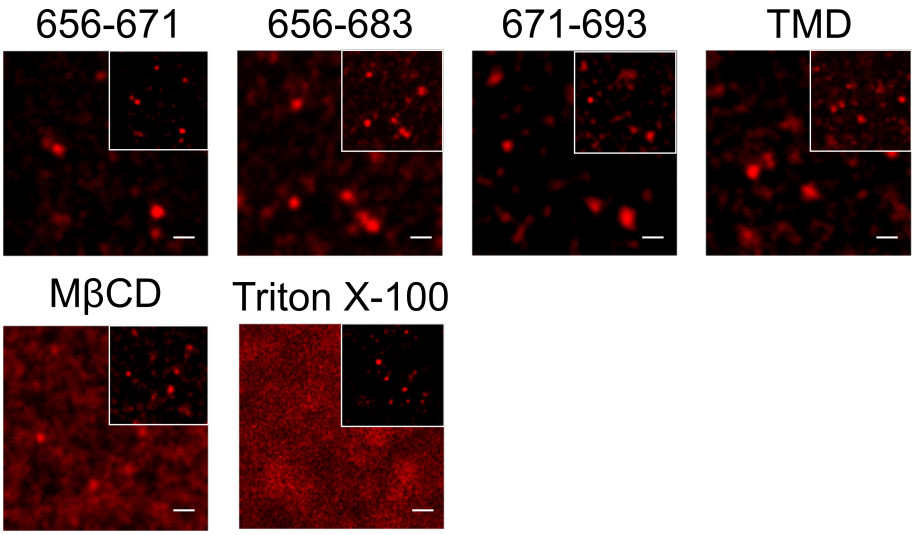

Figure 5.4: Fluorescence imaging of membrane lipids on solid supports containing immobilized viral particles. For fluorescent labeling of membrane lipids, transfected 293T cells were incubated with DiD probe prior to isolation of the pseudoviruses (as described in Padilla-Parra et al. (2013)). Particles were attached to a poly-Lys-coated surface for imaging. Micrographs on top illustrate the effect of the different peptides. Images were taken after 15 min incubation with peptides applied at 20 μM, a concentration that results in full infection inhibition in the case of MPER(671-693) (see Fig. 5.2). Micrographs below display samples treated with Methyl-β-cyclodextrin (10 mM) or Triton X-100 (0.5 %). Insets display micrographs of the samples prior to treatment with the different compounds. Scale bar is 1 m.

Aloia et al., 1993). The lipids extracted from the infectious virus particles and the VL surrogate actually display a high lipid packing level and lateral demixing into nanodomains (see previous chapter 4). Therefore, to identify additional effects that might correlate with virus inactivation in the cell infectivity assays, the changes on the Chol-dependent VL membrane lipid packing and lateral organization induced by the peptides MPER(671-693) and the CRAC mutant MPER(671-693)L679I in VL membranes were evaluated next (Figs. 5.5 and 5.6).

Lipid packing was determined quantitatively by two-photon imaging of Laurdan-stained VL GUVs (Fig. 5.5). Under the assumption that the ^{679}LWYIK^{683} sequence can interact with, and sequester Chol (Epand et al., 2003, 2006), the effect of depleting this compound from the mixtures was assessed in parallel. GP images of the different VL GUV samples displayed a single macroscopic phase (Fig. 5.5 A), which was reflected in a normal, unimodal, distribution of pixel-GP values for every GUV. As expected, decreasing the Chol content resulted in lower mean GP values, consistent with a decrease of the VL membrane order (Fig. 5.5 B, left panel). A more subtle reduction of Laurdan GP values was observed for the GUVs treated with peptides MPER(671-693) and MPER(671-693)L679I (Fig. 5.5

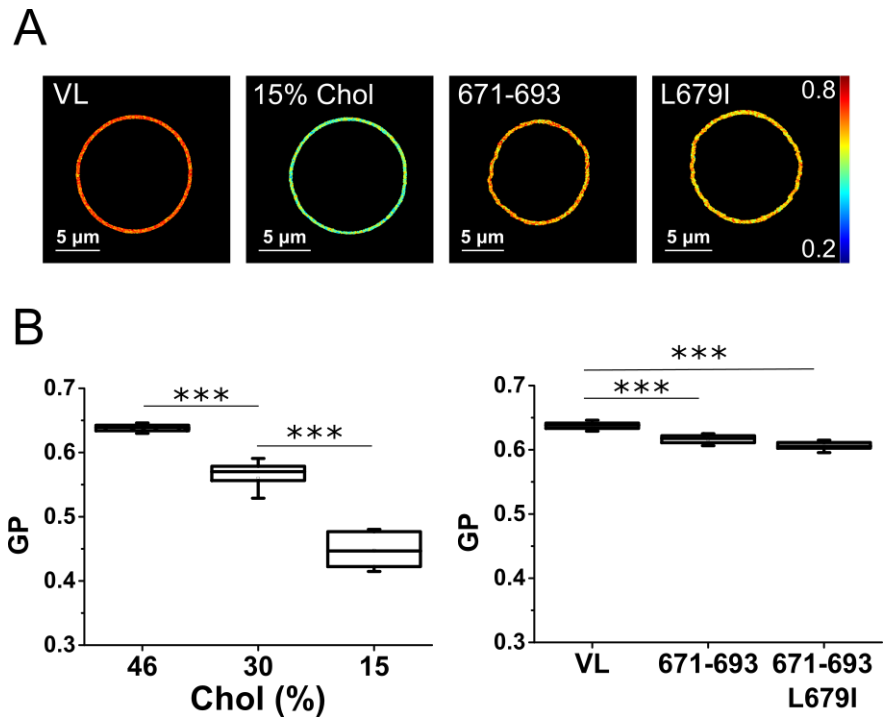

Figure 5.5: Comparison of the effects induced by Chol depletion vs. addition of peptides MPER(671-693) or the CRAC mutant MPER(671-693)L679I on the membrane lateral packing as determined by two-photon excitation GP images of Laurdan-labeled VL GUVs. Laurdan GP imaging of single GUVs (A) and average GP values determined in the different samples (B). GP value distributions were determined for at least 30 single vesicles, and mean values depicted as box-and-whisker plots (the ends of the whiskers represent standard deviations). Peptide concentration was 20 nM. (Mann-Whitney Test: ***$p < 0.001$; **$p < 0.01$, *$p < 0.05$, n.s. ≥ 0.05)

B, right panel). Furthermore, the scored GP reduction was comparable for the two peptides, suggesting that preservation of the CRAC motif was not required for the fluidifying effect.

The capacity of the peptides to alter liquid-liquid miscibility of the VL membrane was analyzed next at the nano-scale (Fig. 5.6). Langmuir-Blodgett films were compressed to 10 mN/m, transferred onto mica and analyzed by AFM. The results displayed in Fig. 5.6 A revealed de-mixed nanoscopic domains in the untreated VL lipid monolayer as expected. Upon reduction of Chol content nanodomains retained rough boundaries and convoluted morphologies. These features were consistent with the low line tension at the domain interfaces under these conditions (23). Inclusion of the peptides MPER(671-693) or MPER(671-693)L679I into the lipid mixture (peptide-to-lipid mole ratio, 1:100) resulted in both cases in segregation of much larger lipid platforms limited by smooth contours, which were not observed

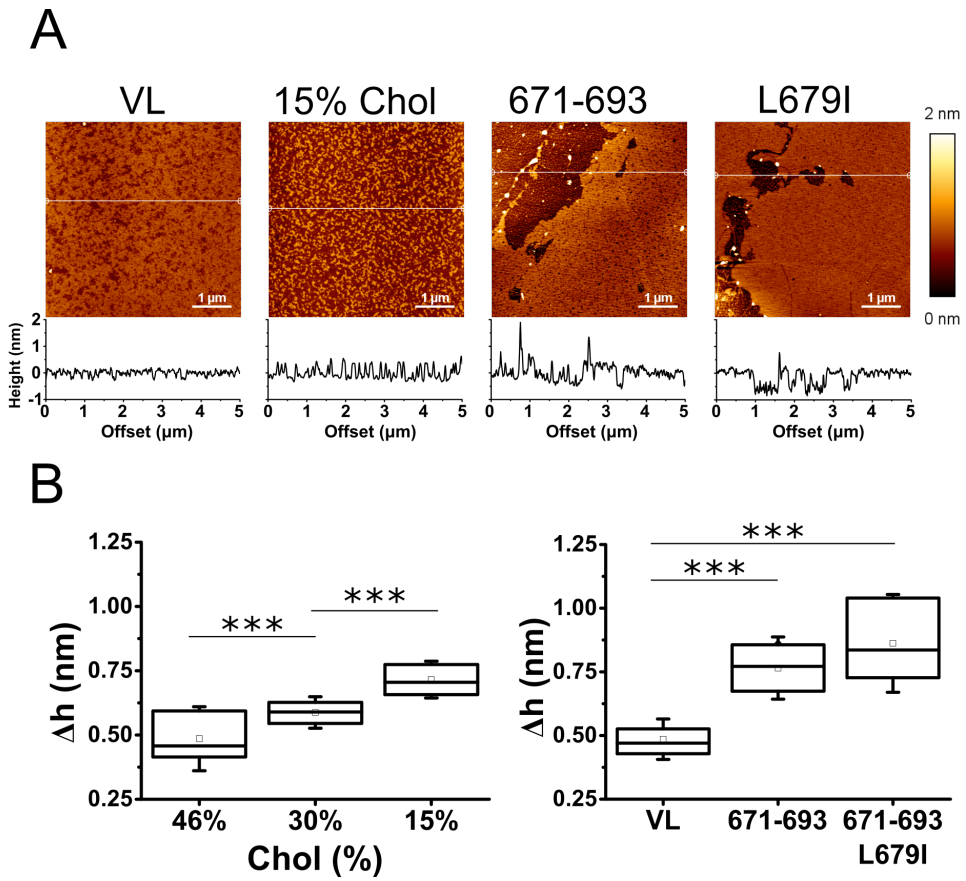

Figure 5.6: Comparison of the effects induced by Chol depletion vs. inclusion of peptides MPER(671-693) or MPER(671-693)L679I on the lateral organization of films made of the VL mixture. (A) AFM images taken from VL mixture films compressed at 10 mN/m. Plots below images display the height profiles for the trajectories indicated by the white lines. (B) Height difference between de-mixed domains and the surrounding lipid surface. (Mann-Whitney Test: ***p $<$ 0.001; **p $<$ 0.01, *p $<$ 0.05, n.s. $\geq$ 0.05)

in lipid monolayers containing lower amounts of Chol.

Line tension at the rims of de-mixing phases intensifies as the height differences between rigid domains and surrounding membrane regions (Δh) increases (Lee et al., 2011). The high interfacial energy can be reduced by coalescence and perimeter minimization of the rigid domains. The value of the Δh parameter increased upon Chol depletion from the mixtures (Fig. 5.6 B, left panel). However, consistently with the smoother contours and larger domain sizes, Δh values were significantly higher in peptide-containing monolayers (Fig. 5.6 B, right panel). Thus, inclusion of 1 mole % of peptide induced a more marked effect on lipid miscibility than reducing the Chol content of the mixture by 30 mole %. Together with the fact that the presence of a functional CRAC was not required for inducing the effect,

these data clearly indicate that the observed alterations were not the consequence of peptide-induced Chol depletion through the formation of equimolar peptide-Chol complexes.

In conclusion, the previous results suggest that the MPER(671-693) peptide does not require the establishment of direct interactions with Chol through the CRAC motif to alter lipid packing and lipid-lipid miscibility.

5.3.3 Membrane activity of gp41-derived peptides

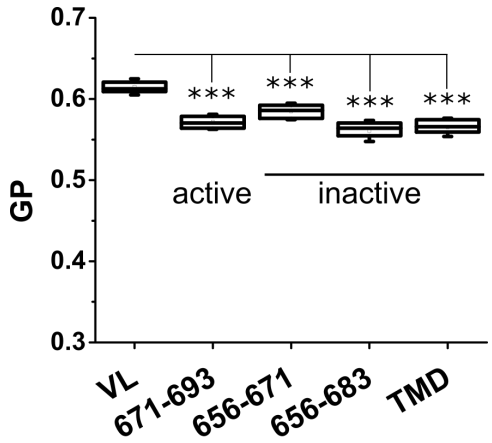

Figure 5.7: Comparison of the effects induced by the different gp41 MPER-TMD-derived peptides on the packing of VL membranes. GP values were determined for VL GUVs that contained peptide (peptide-to-lipid ratio of 1:500). Conditions otherwise as in the previous Figs. 5.5 and 5.6. (Mann-Whitney Test: ***$p < 0.001$; **$p < 0.01$, *$p < 0.05$, n.s. ≥ 0.05)

To gain further insights into the mechanism by which MPER(671-693) exerts its anti-viral activity, its effects were compared next with those produced by the inactive MPER-TMD sequences (Figs. 5.7 and 5.8). Figure 5.7 illustrates the effects of the peptides on lipid packing as inferred from Laurdan GP determinations in single vesicles. In these experiments, peptide and lipids were mixed at defined 1:500 mole ratio prior to desiccation on the silica beads. The data revealed a slight decrease of the mean GP value in GUVs that contained the virucidal peptide MPER(671-693), but comparable decreases in GUVs containing the inactive peptides MPER(656-671), MPER(656-683) or TMD(684-704).

Differences between the active and the inactive sequences became apparent at the nanoscopic level (Fig. 5.8). Besides the segregation of large lipid platforms, AFM measurements disclosed accumulation of material in the fluid areas in the samples containing MPER(671-693), but also at the contacts between condensed and fluid domains (green arrowheads). Lipid monolayers containing the inactive peptides displayed distinct nanostructures. No large segregated platforms, nor

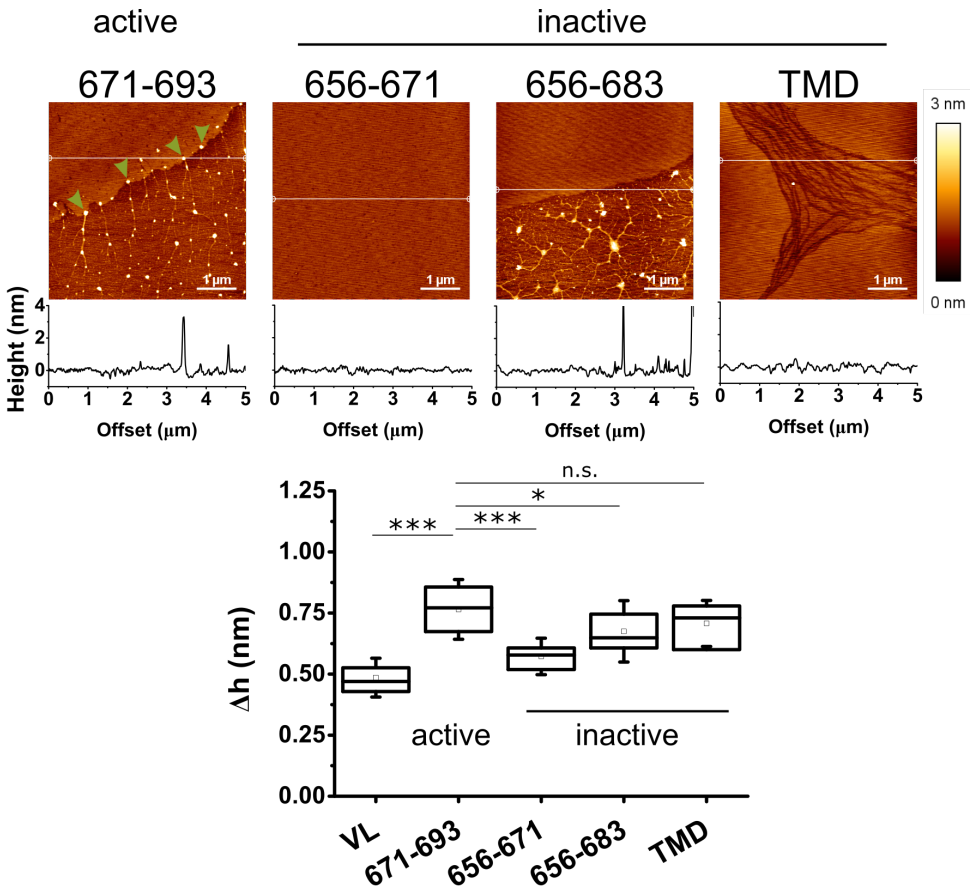

Figure 5.8: Comparison of the effects induced by the different gp41 MPER-TMD-derived peptides on the lateral organization of VL membranes. Nanoscopic structure as determined by AFM analyses of the peptide-containing VL monolayers (top) and height difference between de-mixed domains and the surrounding lipid surface (bottom). Monolayers were supplemented with peptide to a peptide-to-lipid ratio of 1:100. Conditions otherwise as in the previous Figs. 5.5 and 5.6. (Mann-Whitney Test: ***$p < 0.001$; **$p < 0.01$, *$p < 0.05$, n.s. ≥ 0.05)

accumulation of material could be discerned in the samples containing MPER(656-671) peptide. In contrast, segregated domains could be observed in the monolayers containing MPER(656-683) peptide. Although in these samples material was observed to accumulate in the fluid areas, no material was detected at the periphery of the rigid domains. Finally, lipid-lipid immiscibility was also observed in the samples that contained the TMD(684-704) peptide. In this case, the pattern was completely different, with the rigid areas surrounded by streams of fluid lipid. The height differences between domains displayed in the bottom panel further emphasizes that the most substantial effect was induced by the active peptide MPER(671-693), although it was not statistically different from the Δ increase induced by the TMD(684-704) peptide.

Thus, it appears that the capability to accumulate on the edges of the lipid domains and alter line tension is a distinctive property of the active MPER(671-693) sequence. Measurements of the height differences between segregated domains in VL monolayers displayed in Fig. 5.9 support this idea. Consistent with an intrinsic activity of the peptide, the data indicate that MPER(671-693) effect on line tension is dose- and time-dependent (panels A and B, respectively).

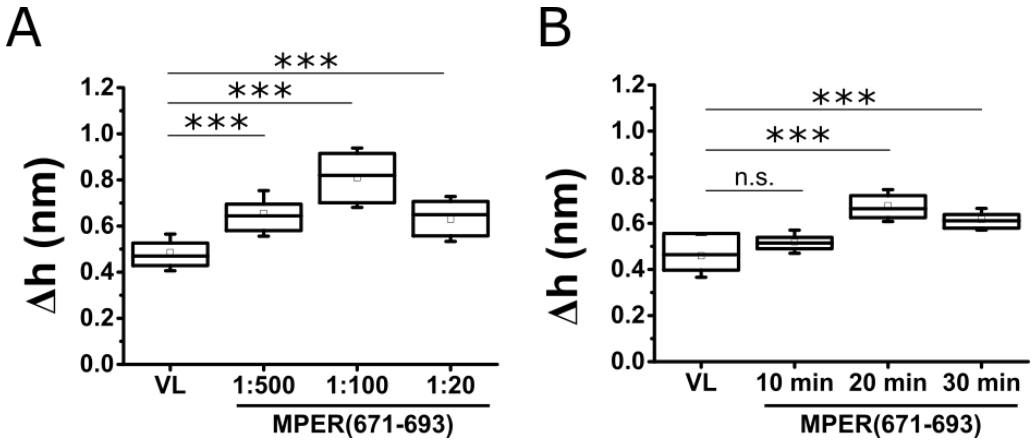

Figure 5.9: Height differences between de-mixed domains and the surrounding lipid surface induced by MPER(671-693) in VL monolayers as function of the peptide-to-lipid mole ratio (A) or time after injection into the subphase (B). (Mann-Whitney Test: ***p < 0.001; **p < 0.01, *p < 0.05, n.s. ≥ 0.05)

5.4 Discussion

The basis for the broad anti-viral activity displayed by some hydrophobic and/or amphipathic peptides is not well understood (Giannecchini et al., 2003; Hrobowski et al., 2005; Sainz Jr. et al., 2006; Galdiero et al., 2008; Spence et al., 2014; Badani et al., 2014; Galdiero et al., 2015). Two factors emphasize the suitability of the HIV envelope as a targetable component for this type of peptides: i) the HIV particle is covered with a solvent-accessible lipid bilayer mostly devoid of protein (Zhu et al., 2006); and ii) preservation of the chemical composition and biophysical properties of that lipid bilayer seems to be critical for the entry function (Wojcechowskyj and Doms, 2010; Brügger et al., 2006; Aloia et al., 1993; Campbell et al., 2002). In addition, the Env subunit gp41 is anchored to the HIV membrane through the MPER-TMD region (Env residues 656 to 704, HXB2c numbering), which encompasses interfacially active sequences enriched in aromatic residues (Lorizate et al., 2008). To map potential virucidal activity within the MPER-TMD region, in this chapter several overlapping peptides that feature different degrees

of interfacial hydrophobicity have been employed (Fig. 5.1). Furthermore, the selected peptides' capacity for altering membrane stability and for modulating the Chol-dependent lipid packing and liquid-liquid miscibility have been assessed using the VL surrogate. In the following summary, these observations are discussed in relation to MPER virucidal activity, providing insights into the mechanism of action of hydrophobic-at-interface antiviral peptides (Badani et al., 2014).

Identification of an MPER-TMD sequence with virucidal activity

The comparative assessment of MPER-TMD-derived peptides identified a sequence, MPER(671-693), which inhibited HIV infection with an IC_{50} of ca. 1 μM (Fig. 5.2). The fact that a similar inhibition pattern was observed for VSV pseudoviruses (Fig. 5.3) supports a virucide-like activity for this peptide. Preservation of interfacial hydrophobicity, although required, was not sufficient to elicit this activity. The peptide MPER(656-683) combining within a single construct amphipatic-at-interface and fully hydrophobic-at-interface sections was not virucidal. Antiviral capacity was not either attained by the fully hydrophobic peptide TMD(684-704). Notably, the peptide MPER(671-693), displaying virucidal efficacy, combined hydrophobic-at-interface aromatic and hydrophobic-aliphatic residues.

The antiviral activity of the peptide MPER(671-693) and the alterations that induced on membranes did not require an intact CRAC motif either (Figs. 5.2, 5.5 and 5.6). This strongly suggests that the virucidal effect was not dependent on a direct interaction of the peptide with Chol. In fact, the observation that 1 mole % peptide induced lipid demixing and augmented line tension more efficiently than reducing Chol content by 30 mole %, excludes the possibility that MPER(671-693) acted by depleting this compound (Fig. 5.6).

Correlation between virucidal activity and VL vesicle destabilization

As compared to the inactive peptides, the MPER(671-693) sequence endowed with antiviral activity destabilized the 7-lipid VL membranes causing significant LUV permeabilization (ANTS leakage) and fusion (lipid mixing) (Fig. 5.2). Thus, the virucidal peptides displayed membrane activity in lipid mixtures that resembled the composition and biophysical properties of the viral envelope.

However, the mechanism relating this membrane activity to infection inhibition is not clear. One plausible mechanism to explain the inhibitory effect of MPER(671-693) could be the general solubilization or disaggregation of the viral envelope by the peptide, either following a detergent-like mechanism, or by extracting lipids, as described for the Chol-depleting compound β-cyclodextrin (Campbell et al., 2002; Guyader et al., 2002). However, control experiments under conditions emulating the infectivity assays (i.e., isolated virions immobilized onto a solid substrate),

indicated that incubation with peptides did not remove membrane lipids (Fig. 5.4, top). In contrast, treatment of the samples with the detergent Triton X-100 or the Chol-depleting -cyclodextrin totally or partially depleted the solid supports of lipid respectively (Fig. 5.4, bottom).

The fact that the immobilized viral particles remained isolated in the cell infectivity experimental set-up, also rules out virion-virion aggregation/fusion induced by peptides as the mechanism underlying their virucidal activity. Thus, it was inferred that perturbations resulting in membrane permeabilization and inter-vesicle lipid mixing might also affect additional biophysical properties of the membranes in the isolated virions, whose preservation might be required to sustain infectivity.

Decrease in Chol-dependent lateral lipid packing

High quantities of Chol incorporate into the viral membrane during HIV assembly (Brügger et al., 2006), while depletion of this compound inactivates the virus (Campbell et al., 2002). It has been argued that the high levels of lipid packing induced by Chol are required to preserve the functionality of the HIV particle (Aloia et al., 1993; Campbell et al., 2002). The virucidal peptides MPER(671-693) and MPER(671-693)L679I slightly, but significantly, decreased lipid packing of the VL mixture (Fig. 5.5). However, a comparable fluidifying effect was observed when inactive sequences MPER(656-683) or TMD were incorporated into VL GUVs (Fig. 5.7). Thus, a general, slight fluidification of the viral membrane does not seem to explain the virucidal activity of MPER(671-693).

Alteration of Chol-dependent lipid miscibility

Chol levels also modulate the liquid-liquid miscibility of the VL mixture (Fig. 5.6). The effects of the MPER-TMD-derived peptides on lateral segregation were approached using lipid monolayers that were compressed to 10 mN/m, which represents a miscibility transition pressure for the HIV lipids and ternary mixtures containing Chol (see previous chapter 4 and Veatch and Keller (2002)). This condition was also selected based on previous observations indicating that increasing lateral pressure to 30 mN/m induces to the collapse of the lipid monolayer made of the viral lipids, whereas its lateral organization, consisting of de-mixed nanodomains, was preserved at the lower values of 20 and 10 mN/m (see previous chapter).

Thus, AFM analysis of VL lipid monolayers allowed scoring at the nanoscopic lengthscale the effect of the different peptides on the de-mixed liquid domain pattern (Figs. 5.6 and 5.8). The topographic information obtained confirmed that the active peptide MPER(671-693) can induce nanodomain clustering. However a similar effect was observed for the inactive peptides MPER(656-683) and TMD(684-704),

Thus, the capacity of the peptides to induce nanodomain clustering does not seem to explain the observed virucidal activity.

Accumulation at edges of lipid domains

The AFM analyses of lipid monolayers also revealed accumulation of material at the rim of rigid domains in VL monolayers containing MPER(671-693) virucidal peptide, a pattern not observed in the case of the inactive peptides (Fig. 5.8). This pattern was also observed for the MPER(671-693) treated HIV-1 lipid monolayers (see Fig. 4.14 in the previous chapter). In addition, the active peptide induced the highest measured domain height difference after nanodomain clustering (Figs. 5.8 and 5.9). This observation suggests that, in comparison with the inactive peptides, MPER(671-693) can alter line tension directly by accumulating at the periphery of the rigid domains.

5.5 Conclusions

The data presented in this chapter provide conclusive evidence to support the virucidal activity of a peptide derived from the HIV-1 MPER-TMD region, and a mechanism of action that involves the change of the physical chemistry of the virus membrane. The comparative analysis identifies the two properties of the virucidal sequence that more robustly correlate with its inhibitory activity: the faculty of permeabilizing VL LUVs and its potential to accumulate at the periphery of rigid domains and modulate line tension. Both effects can be interrelated, since accumulation on the edges of lipid domains might help the assembly of the membrane permeating structures inducing vesicle leakage, as previously shown in the case of some pore-forming toxins (Barlic et al., 2004; Schon et al., 2008). The establishment of correlations between interfacial activity, membrane activity and anti-viral activity as a function of the sequence hydrophobicity pattern, might help future development of virucidal peptides.

Chapter 6

Single virion super-resolution microscopy studies of the mechanistic details of Env glycoprotein recognition by broadly neutralizing hiv-1 antibodies

Abstract

Recognition of the helical MPER epitope in association with the viral membrane by HIV antibodies 4E10 and 10E8 constitutes a new paradigm in molecular immunology, but the underlying mechanism is not totally understood. In particular, the exact contribution to Env glycoprotein binding specificity and viral neutralization of the antibody-lipid interactions that operate at the membrane interface, remains to be determined. Here, to get new insights into those processes, binding of 4E10/10E8 antibodies to native Env on single virions has been visualized using super-resolution STED microscopy. 4E10/10E8 binding patterns have been qualitatively and quantitatively compared to those of antibodies engaging with the surface subunit gp120, and to those of variants endowed with different membrane-interacting capacities. The data reveal that: (i) anti-gp120 and anti-gp41 antibodies engage with the same clusters of native Env on the virion surface; (ii) anti-MPER antibodies do not interact with the bare HIV membrane, nor accumulate within; and (iii) interaction with Env and neutralization potency seem to correlate, and both functions appear to depend similarly on the capacity of the anti-MPER antibodies

for associating with membranes. Thus, the experimental evidence on the whole favor a common Env recognition pattern for HIV-1 broadly neutralizing antibodies, independently of the subunit targeted, which in the case of anti-MPER antibodies evolves with extra contribution of lipid interactions to binding specificity.

6.1 Introduction

To circumvent immune surveillance by the infected host, the human immunodeficiency virus type-1 (HIV-1) puts in practice intricate escape mechanisms, including conformational diversity, sequence variation, N-linked glycosilation and low membrane density of the surface antigen Env glycoprotein (Burton and Hangartner, 2016; Burton and Mascola, 2015). However, individuals suffering from long-term infections may occasionally develop broadly neutralizing responses against the Env complex subunits gp120 and gp41 (Burton and Hangartner, 2016; Burton and Mascola, 2015; Kwong and Mascola, 2012). From structure-function analyses of the isolated broadly neutralizing antibodies (bnAbs), it appears that the strength of specific binding to relatively conserved, recessed sites on each of the Env native subunits, or on the interface between them, generally correlates with neutralization efficacy and breadth of coverage (Burton and Hangartner, 2016; Guttman et al., 2015; Jardine et al., 2016).

Among the isolated bnAbs, 4E10 and 10E8 target the Membrane-Proximal External Region (MPER) vulnerability site on the gp41 subunit (Stiegler et al., 2001; Huang et al., 2012). This domain connects the Env ectodomain to the transmembrane anchor, and its engagement with 4E10/10E8 antibodies results in one of the broadest neutralization levels reported to date (98% of viruses blocked in customary infectivity tests) (Burton and Hangartner, 2016; Kwong and Mascola, 2012). Several functional features appear to differentiate 4E10/10E8 from the rest of anti-HIV bnAbs identified so far, particularly from those raised against the subunit gp120. First, they present the unusual ability to specifically bind the MPER epitope sequence arranged onto the face of a helix (Huang et al., 2012; Cardoso et al., 2005, 2007). Second, this recognition phenomenon takes place in contact with the viral membrane surrounding the virion, precisely at the point where the MPER helix emerges from the lipid bilayer (Irimia et al., 2016; Rujas et al., 2016; Irimia et al., 2017; Lee et al., 2016). Thus, to achieve recognition of the membrane-inserted epitope, these antibodies have evolved distinct structural adaptations (Fig. 6.1) including: (i) a membrane-associated paratope area (MAPA) that can accommodate polar head groups of phospholipids on its surface (Irimia et al., 2016; Rujas et al., 2016; Irimia et al., 2017; Rujas et al., 2017a); and (ii) a long heavy chain complementarity determining region 3 (HCDR3) loop, characterized by a very hydrophobic tip that submerges into the lipid matrix (Burton and Hangartner, 2016; Huang et al., 2012; Rujas et al., 2016; Scherer et al., 2010; Rujas et al., 2015, 2017b).

Some authors argue that self-tolerance mechanisms must be broken to induce

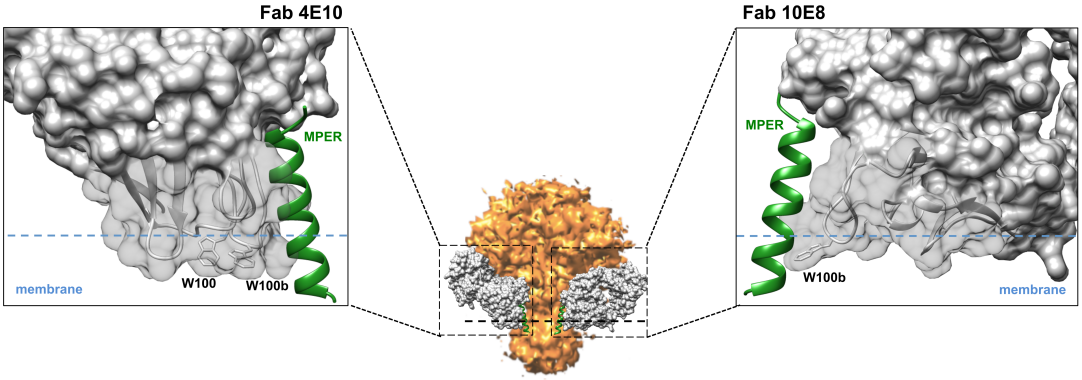

Figure 6.1: Structural view of the modes of binding of anti-MPER antibodies 4E10 and 10E8 to the MPER helical epitope (green ribbon) in the context of the Env glycoprotein (rendered in orange surface). MAPA/HCDR3 regions for interaction with membrane have been highlighted.

HIV antibodies adapted for MPER recognition in membranes, and propose a third distinctive feature for the anti-MPER bnAbs pertaining to their mechanism of antiviral action (Haynes, 2005; Dennison et al., 2009; Verkoczy et al., 2014; Chen et al., 2014, 2013; Alam et al., 2007, 2009). Thus, in contrast to the requirement of native Env engagement for anti-gp120 bnAb-mediated neutralization, it is postulated that anti-MPER bnAbs bind to an epitope sequence that becomes only transiently exposed in the context of the Env fusion intermediate *pre-hairpin* (Burton and Hangartner, 2016; Chen et al., 2014; Alam et al., 2009; Frey et al., 2008, 2010). This theory further proposes that anti-MPER antibodies pre-attach to the viral membrane, where they accumulate until their target epitope becomes fully accessible (two-step model of neutralization) (Rujas et al., 2017a; Chen et al., 2014; Alam et al., 2009; Haynes et al., 2010). However, contrasting those assumptions it remains to be established whether antibody-membrane interactions mediated by the MAPA/HCDR3 tandem occur on intact virions prior or concomitantly to Env specific binding, and which is the exact contribution of this phenomenon to the broad neutralization activity of anti-MPER antibodies. Resolution of this issue bear important implications in the fields of AIDS vaccine and immunotherapy.

In this thesis chapter, that question has been addressed through super-resolution stimulated emission depletion (STED) microscopy (Blom and Widengren, 2017; Sezgin, 2017; Sahl et al., 2017). This optical microscopy technique has made possible sub-diffraction (∼40 nm) observations of Env molecules on individual HIV particles (∼120 nm in diameter) using anti-gp120 antibodies as reporters (Chojnacki et al., 2012, 2017), and therefore constitutes a suitable tool to measure anti-Env antibody binding to viruses. Thus, a qualitative-quantitative description has been carried out by super-resolution STED of the 4E10/10E8 binding phenomenon on intact virions, and compared the observed patterns with those of anti-gp120 antibodies,

or of anti-MPER antibodies with different degrees of affinity for bare membranes. Collectively, the STED data rule out the existence of a membrane-attached, free antibody population, while providing evidence to support a correlation between binding to native Env on intact virions and neutralization. Thus, such functional property appears to be applicable to all anti-HIV bnAbs, independently of the Env subunit targeted. Furthermore, our observations emphasize that the strength of interaction with Env evolves with extra contribution of membrane interactions in the case of the anti-MPER bnAbs.

6.2 Materials and methods

Plasmid and cells

Replication-incompetent HIV-1 particles were produced using pCHIV plasmid, expressing all HIV-$1_{\text{NL4-3}}$ proteins except Nef and lacking the viral long-terminal repeat sequences. Derivatives of this plasmid with a frameshift and premature termination of Env (Env(-)) have been described previously (Lampe et al., 2007). HIV-1 expression plasmid pCHIV and its derivatives were provided by Barbara Müller and Hans-Georg Kräusslich (University Hospital, Heidelberg, Germany). Plasmid expressing eGFP.Vpr was provided by Tom Hop. 293T cells (ATCC CRL-3216) were grown in Dulbecco's modified Eagle's medium (Sigma), supplemented with 10% fetal calf serum, 100 U/mL penicillin-streptomycin and 20 mM HEPES pH 7.4. Cells were maintained at 37 °C, 5% CO2.

Antibodies and dyes

Human anti-gp120 monoclonal antibody 2G12 and b12 were purchased from Polymun Scientific. Fab fragments were generated using the Fab Micro Preparation kit (Pierce) according to the manufacturer's instructions. Anti-human IgG Fab fragments (Jackson ImmunoResearch) were coupled to the Abberior STAR 600 dye (Abberior GmbH, Gttingen, Germany) via NHS-ester chemistry according to the dye manufacturer's instructions. Anti-Env antibodies PG9, PGT145, VRC01, b13 and F240 were kindly provided by Jean-Philippe Julien (The Hospital for Sick Children, Ontario, Canada).

The sequences of 4E10 or 10E8 were cloned in the plasmid pColaDuet and expressed in Escherichia coli T7-shuffle strain. Recombinant expression was induced at 18 °C overnight with 0.4 mM isopropyl-D-thiogalactopyranoside when the culture reached an optical density of 0.8. Cells were harvested and centrifuged at 8,000 g, after which they were resuspended in a buffer containing 50 mM HEPES (pH 7.5), 500 mM NaCl, 35 mM imidazole, DNase (Sigma-Aldrich, St. Louis, MO) and an EDTA-free protease inhibitor mixture (Roche, Spain). Cell lysis was

performed using an Avestin Emulsiflex C5 homogenizer. Cell debris was removed by centrifugation, and the supernatant loaded onto a nickel-nitrilotriacetic acid (Ni-NTA) affinity column (GE Healthcare). Elution was performed with 500 mM imidazole, and the fractions containing the His-tagged proteins were pooled, concentrated and dialyzed against 50 mM sodium phosphate (pH 8.0), 300 mM NaCl, 1 mM DTT, and 0.3 mM EDTA in the presence of purified protease Tobacco etch virus. Fabs were separated from the cleaved peptides containing the His6× tag by an additional step in a Ni-nitrilotriacetic column. The flow-through fraction containing the antibody was dialyzed overnight at 4 °C against sodium acetate (pH 5.6) supplemented with 10% glycerol and subsequently loaded onto a MonoS ion exchange chromatography (IEC) column (GE Healthcare). Elution was carried out with a gradient of potassium chloride and the fractions containing the purified Fab concentrated and dialyzed against a buffer containing 10 mM sodium phosphate (pH 7.5), 150 mM NaCl, and 10% glycerol. For the preparation of mutant Fabs, the KOD-Plus mutagenesis kit (Toyobo, Osaka, Japan) was employed following the instructions of the manufacturer. Anti-MPER Fab labeling with the Abberior STAR RED (KK114) (Abberior GmbH, Gttingen, Germany) in vitro at position C216HC was performed as previously described (Shepard et al., 1998; Heuck et al., 2000).

Virus particle preparation and purification

Virus particles were prepared from the tissue culture supernatant of 293T cells co-transfected using polyethyleneimine with 14 μg pCHIV or pCHIV Env(-) and 1 μg peGFP. For pseudotyped particles, 15 μg of pCHIV Env(-), 1 μg of peGFP.Vpr and 2.5 μg of the indicated $\mathrm{Env}_{\mathrm{JR\text{-}CSF}}$ expression plasmid were used. Tissue culture supernatants were harvested 48 h after transfection, cleared by filtration through a 0.45 μm nitrocellulose filter, and particles were purified by ultracentrifugation through 20% (w/w) sucrose cushion at 70,000 g (avg.) for 2 h at 4 °C. Particles were resuspended in ice-cold 20 mM HEPES/PBS pH 7.4, snap frozen and stored in aliquots at -80 °C. All ultracentrifugation steps were performed in SW 41 Ti rotor.

Microscopy sample preparation

Purified virus particles were adhered to poly-Llysine (Sigma) coated glass coverslips for 15 min. Coverslips were blocked using 2% fatty acid free bovine serum albumin (BSA) (Sigma)/PBS for 15 min. Abberior STAR RED (KK114) conjugated anti-MPER Fabs (20-100 ng/μL) were incubated for 1 h in blocking buffer. Annexin V was incubated in 10 mM $CaCl_2$/HBS. Immunostained particles were washed and mounted in PBS, followed by STED analysis. All steps were carried out at

room temperature. For colocalization experiments, before adding labeled anti-MPER Fabs (100 ng/μL), unlabeled anti-Env Fabs and anti-human Abberior STAR 600 conjugated Fab fragments were incubated for 1 h in blocking buffer (100 ng/μL). Three very gentle 5-minute PBS washing steps were performed before and after adding the secondary Fabs. Control experiments without anti-Env primary antibodies show no Abberior STAR 600 signal, indicating that washing steps successfully removed free anti-human secondary Fabs from the sample.

STED microscopy measurements

Imaging was performed on a STED microscope based on a modified Abberior Instrument RESOLFT QUAD-P super-resolution microscope (Abberior Instruments GmbH) installed in a biosafety level 3 environment. The microscpe was equipped with three pulsed excitation lasers (640, 594, and 485 nm; LDH-D-C-640P and LDH-D-C- 485P; Picoquant, Berlin, Germany, and PDL 594; Abberior Instruments) with 80 ps pulse width and a pulsed STED laser (Titanium:Sapphire laser system, MaiTai; Newport Spectra-Physics Ltd, Didcot, UK) operating at 780 nm and 80 MHz repetition rate. STED laser pulses were stretched to a pulse width of ∼250350 ps using two 20 cm SF6 optical glass rods and a 120 m-long single-mode polarization maintaining optical fibre (OZ Optics/AMS Technologies Ltd, Lutterworth, UK). Shuttering and power adjustment of the STED laser were controlled with an acousto-optical modulator (MT110-B50A1.5-IRHK, AAA/Photon Lines Ltd, Banbury, UK). Control over the circular polarization and generation of a doughnut shaped focal intensity distribution was achieved by incorporation of half-wave/quarter-wave plates (B. Halle, Berlin, Germany) and a phase-modifying vortex plate (VPP-1a, RPC Photonics, Rochester, NY), respectively, into the optical path of the STED laser beam. STED and excitation laser beams were spatially superimposed and the fluorescence light was separated using appropriate dichroic filters (ZT740SPRDC, AHF Analysentechnik, Tbingen, Germany). The temporal synchronization of laser pulses was achieved by triggering the excitation lasers by the STED laser using a photodiode (APS-100-01, Becker & Hickl, Berlin, Germany). An on-board FPGA card (Abberior Instruments) was used for time alignment control between the laser pulses. Positioning and scanning of laser foci was realised using the QUAD beam scanner unit of the Abberior system for lateral directions, and an objective lens positioning system (MIPOS 100PL, Piezosystem Jena, Jena, Germany) for the axial direction. The fluorescence excitation and collection was performed using a 100×/1.40 NA UPlanSApo oil immersion objective (Olympus Industrial, Southend-on-Sea, UK). The fluorescence signal was descanned, passed through an adjustable pinhole (Thorlabs Limited, Ely, UK) and detected by a single photon counting avalanche photo diode (SPCM-AQRH-13, Excelitas Techologies) with appropriate fluorescence filters (AHF Analysentechnik). All acquisition operations

were controlled by Imspector software (Abberior Instruments).

Image analysis

Images analysis was performed using Python scripting language and custom written functions based on the program developed for Galiani et al. (2016). Individual viral particles were identified from the GFP.Vpr channel using the Fiji/ImageJ *Find Maxima* algorithm on a Gaussian smoothed image ($\sigma = 2.0$). Detection of maxima was kept consistent throughout using a noise tolerance parameter of 10. A circular region (diameter, 20 pixels; 400 nm) was then superimposed on each detected location, and all of the regions were saved for subsequent analysis. For every detected region, a random location was also generated to sample areas where Vpr.GFP staining and thus HIV-1 virions were not likely to be present. This was achieved by randomly translating each of the detected regions to a different point within a 180-pixel radius of the original location but constrained so as not to pick an existing region, which might contain another fragment of Vpr.GFP fluorescence. This method was effective at finding random regions that were close to virions but not overlapping and so ensured accurate comparisons between virion-containing and non-virion regions. These randomly perturbed regions were saved and used for subsequent comparisons as with the original set.

Correlation analysis was performed on the raw pixel data in each of the previously detected regions (Fig. 6.4). The intensity contained within each region was first integrated, in the Vpr.GFP confocal and in the STED channel under comparison, to form each measurement pair (g_i, r_i), and then the Pearson's correlation coefficient was calculated from all the measurements (I) in each cell.

$$\rho = \frac{\sum_{i=1}^{I}(g_i - \mu_g)(r_i - \mu_r)}{\sum_{i=1}^{I}(g_i - \mu_g)^2 \sum_{i=1}^{I}(r_i - \mu_r)^2} \tag{6.1}$$

where μ_g and μ_r are equal to the mean intensity of all the summed patches in the cell. To compare the mean values of correlation from each condition, one-way analysis of variance was performed with Tukey's pairwise comparison to test for a statistical difference between the comparisons.

Cell entry inhibition

HIV-1 pseudoviruses were first produced by transfection of human kidney HEK293T cells with the full-length env clones HXB2 or JR-CSF (kindly provided by Jamie K. Scott and Naveed Gulzar, Simon Fraser University, Burnaby, Canada) using calcium phosphate. The cells were co-transfected with vectors pWXLP-GFP and pCMV8.91, encoding a green fluorescent protein and an env-deficient HIV-1 genome, respectively (generously provided by Patricia Villace, CSIC, Madrid, Spain). After

24 h, the medium was replaced with Optimem-GlutaMAX II (Invitrogen) without serum. Three days after transfection, the pseudovirus particles were harvested, passed through 0.45 μm pore sterile filters (Millex HV; Millipore NV, Brussels, Belgium), and finally concentrated by ultracentrifugation in a sucrose gradient. Neutralization was determined using TZM-bl target cells (AIDS Research and Reference Reagent Program, Division of AIDS, NIAID, NIH, contributed by J. Kappes). Samples were set up in duplicate in 96-well plates and incubated for 1.5 h at 37 °C with a 1015% tissue culture infectious dose of pseudovirus. After antibody-pseudovirus coincubation, 11,000 target cells were added in the presence of 30 μg/ml DEAE-dextran (Sigma-Aldrich). Neutralization levels after 72 h were inferred from the reduction in the number of GFP-positive cells as determined by flow cytometry using a BD-FACSCalibur flow cytometer (Becton Dickinson).

Liposome flotation assays

LUVs were prepared following the extrusion method. Lipids were mixed in chloroform and dried under a N_2 stream. Traces of organic solvent were removed by overnight vacuum pumping. Subsequently, the dried lipid films were dispersed in buffer and subjected to 10 freeze-thaw cycles prior to extrusion 10 times through 2 stacked polycarbonate membranes with a nominal pore size of 100 nm (Nuclepore, Inc., Pleasanton, CA). Phospholipid concentration of liposome suspensions was determined by phosphate analysis. Vesicle flotation experiments in sucrose gradients were subsequently performed. In brief, 100 μL of a sample containing rhodamine-labeled liposomes and Fab (1.5 mM lipid and 1.5 μM Fab) was adjusted to a sucrose concentration of 1.4 M in a final volume of 300 μL and subsequently overlaid with 400 μL and 300 μL layers of 0.8 M and 0.5 M sucrose, respectively. The gradient was centrifuged at 436,000 g for 3 h in a TLA 120.2 rotor (Beckman Coulter, Brea, CA). After centrifugation, four 250 μL fractions were collected. The material adhered to the tubes was collected into a fifth fraction by washing with 250 μL of hot (100 °C) 1% (w/v) SDS. The different fractions were run on SDS-PAGE, and the presence of Fab was probed by Western blotting using a sandwich comprising a goat (anti-human Fab) antibody (Sigma) and a mouse (anti-goat) antibody-HRP conjugate (Santa Cruz). The results displayed in the figures are representative of at least two replicates.

Preparation of giant unilamellar vesicles

Giant unilamellar vesicles (GUVs) were produced by spontaneous swelling of lipid films deposited on 40 μm silica beads as described (Mattila et al., 2015). Briefly, lipid-Laurdan mixtures (0.125 mg total lipid) in $CHCl_3$:CH_3OH (9:1) were dried in a vacuum desiccator for 1 h to remove the organic solvent. The desiccated lipid was

hydrated for 1 h at temperatures above the transition temperature of the mixture (typically 55 °C) and subsequently subjected to 30 cycles of extrusion through two 0.4 μm pore size polycarbonate filters in an Avanti Mini Extruder at 65 °C. Five microliters of silica beads was then mixed with 20 μL of the MLV suspension, separated in $\approx$ 3 μL drops on a teflon film, and vacuum-dried for 45 min. Dried beads covered with lipid were collected and transferred to a 3 g/L sucrose buffer to induce spontaneous swelling of GUVs. Finally vesicles were transferred to the observation dish in an isosmotic 10 mM HEPES, 150 mM KCl (pH 7.4) buffer.

Fluorescence correlation spectroscopy

4E10 mobility in solution was measured after acquiring the emission signal in a single point, calculating the autocorrelation function and fitting it to a 3D diffusion model (equation 1.7). For membrane diffusion calculations, GUVs were incubated with KK114-labeled 4E10 Fabs (10-50 nM) for 15 minutes and measured by scanning FCS using 15× zoom and 64 pixels in the x axis direction, which resulted in a pixel size of 260 nm. The emission signal was acquired for 3-5 minutes and in the membrane pixels the autocorrelation function calculated and fitted to a 2D diffusion autocorrelation function (equation 1.10) to calculate the diffusion coefficient (D) according to equation 1.8.

6.3 Results

To visualize binding of anti-MPER antibodies to Env on intact HIV viruses using super-resolution STED microscopy, 4E10 and 10E8 Fabs were conjugated with the fluorescent probe Abberior STAR RED (also known as and henceforth KK114). Fig. 6.2 A displays confocal images of eGFP-labeled viral particles incubated with KK114-labeled Fabs, the latters visualized in STED mode. In samples incubated with the functional 4E10 or 10E8 WT specimens, the antibodies colocalized with the viral particles (red signal in the left-side micrographs). To confirm dependence of this phenomenon on specific Fab binding, virions were also incubated with non-neutralizing HCDR3 loop tip-ablated versions: 4E10-Δloop or 10E8-W100bG (henceforth 10E8-WG) (Table 6.1) (Rujas et al., 2016, 2015). In contrast to the WT Fab samples, particles incubated with the inactive mutants were mostly devoid of the antibody signal (micrographs on the right).

Direct Fab labeling further allowed an estimation of the number of emitted photons by the KK114 fluorophore in eGFP-associated regions. Mean KK114 intensity was therefore assumed to reflect quantitatively the amount of antibody bound in the viral particle population (Fig. 6.2 B). Again, quantitation of emitted photons revealed a strong reduction of binding in the samples incubated with

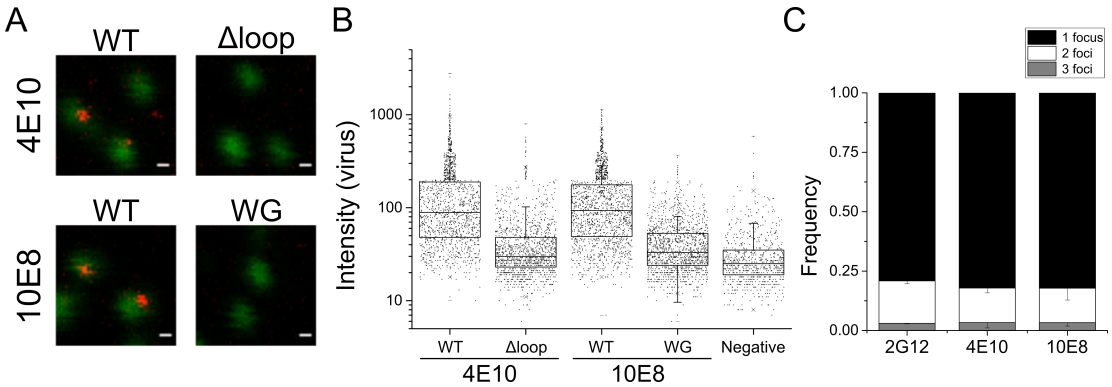

Figure 6.2: Qualitative and quantitative aspects of anti-MPER bnAb binding to Env (NL4-3) on intact virions visualized by super-resolution STED microscopy. (A) Representative images of anti-MPER Fabs (KK114, red, STED) bound to HIV-1 virions (green, Vpr.eGFP, confocal). Scale bars are 100 nm. (B) Quantification of HIV-1 bound Fab-KK114 intensity. Each point represents the intensity sum in a single viral particle. End of whiskers represents SD. Note the logarithmic scale. (C) Distribution analysis of Fab STED foci number detected on HIV-1 virions.

Table 6.1: Neutralization (IC_{50}, μg/mL) of JR-CSF (tier-2) and pIIIenv (tier-1) viruses by 4E10 and 10E8 WT and mutant Fabs as measured in cell entry assays.

Fab 4E10	JRCSF	pIIIenv	Fab 10E8	JRCSF	pIIIenv
WT	4.70 ± 0.51	0.15 ± 0.03	**WT**	0.40 ± 0.08	0.13 ±0.02
Δloop	>100	>100	**WG**	>30	>30
3R Δloop	>100	>50	**3R WG**	6.38 ± 0.71	3.31 ± 0.20
3R	2.06 ± 0.31	0.42 ± 0.08	**3R**	0.04 ± 0.01	0.05 ± 0.01
R73E	13.2 ± 3.5	5.3 ± 0.4			
R73E Δloop	>100	>100			

the non-neutralizing versions KK114-4E10-Δloop or KK114-10E8-W100bG, which displayed antibody emission levels close to the background (*Negative* samples measured in the absence of labeled antibody). These results emphasize the suitability of the STED measurements to characterize anti-MPER antibody binding to intact virions, and allow establishing a first quantitative relationship between biological function (neutralization) and binding to the viral particle.

The punctuate staining of the virions by 4E10/10E8 observed through STED further reflected clustering of native Env proteins, and followed the pattern described for mature particles incubated with the anti-gp120 antibody 2G12, which was revealed with an anti-human Abberior KK114 conjugated secondary antibody (Fig. 6.2 C, see also references by Chojnacki et al. (2012, 2017)). Thus, similarly to 2G12, directly labeled anti-MPER antibodies in association with individual eGFP-labeled particles distributed predominantly into single foci (ca. 80% of the particles), and

less frequently into two, or more than two foci. The same pattern was reproduced by a set of anti-gp120 antibodies and by anti-gp41 antibodies when revealed by a secondary antibody (Fig. 6.3). These observations support the engagement of anti-gp120 and anti-gp41 with the same type of Env clusters on the viral particles.

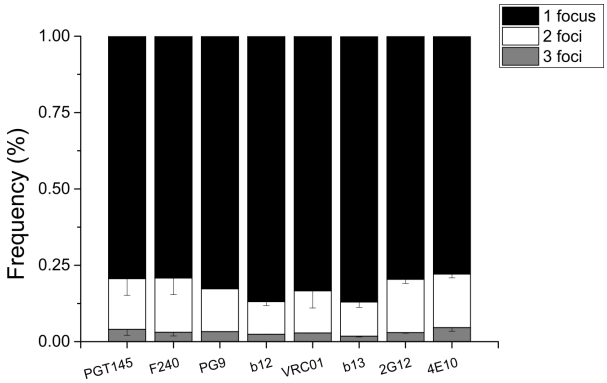

Figure 6.3: Distribution of Fab foci on the viral membrane of NL4-3 virions revealed by secondary staining (anti-human Fab-KK114). Bars are SD of at least three independent experiments.

Having demonstrated that distribution was comparable for antibodies that were either directly labeled, or revealed by a secondary antibody, next the colocalization of anti-MPER and anti-gp120 antibodies was established quantitatively using dual color STED microscopy colocalization analysis (Galiani et al., 2016) (Figs. 6.4 and 6.5). Thus, HIV-1 virions were incubated with anti-gp120 antibodies, which were revealed using a secondary anti-human Fab antibody conjugated with the Abberior STAR 600 dye. After washing, these samples were subsequently treated with Abberior KK114 labeled anti-MPER 4E10 and 10E8 antibodies. Both STED signals were recorded line by line and Vpr.eGFP was next imaged in confocal mode to determine the location of HIV-1 virions. The STED resolution was below 60 nm in both channels. To ensure that the colocalization signals were not underestimated, only virions presenting a minimum of one focus in both STED channels were selected for the analysis (i.e., virions positive for both antibodies). Then, a pixel-wise Pearson's correlation test was run to calculate quantitatively degrees of colocalization, according to which values of 1, 0, and -1 corresponded to maximal-colocalization, no-colocalization and opposing-colocalization, respectively.

Fig. 6.4 A shows a representative image of a dual color STED experiment, where colocalization of the STED signals of VRC01 (blue) and 10E8 (red) antibodies can be observed in virus particles (green). As illustrated by the diagrams in Fig. 6.4 B (top), to establish the significance of the correlation values determined in these samples, measurements were done in (i) Vpr.eGFP positive areas (i.e. HIV-1 virions); (ii) the same area after flipping one of the STED channels as a control for coincidental colocalization (i.e., colocalization that may arise from the restricted

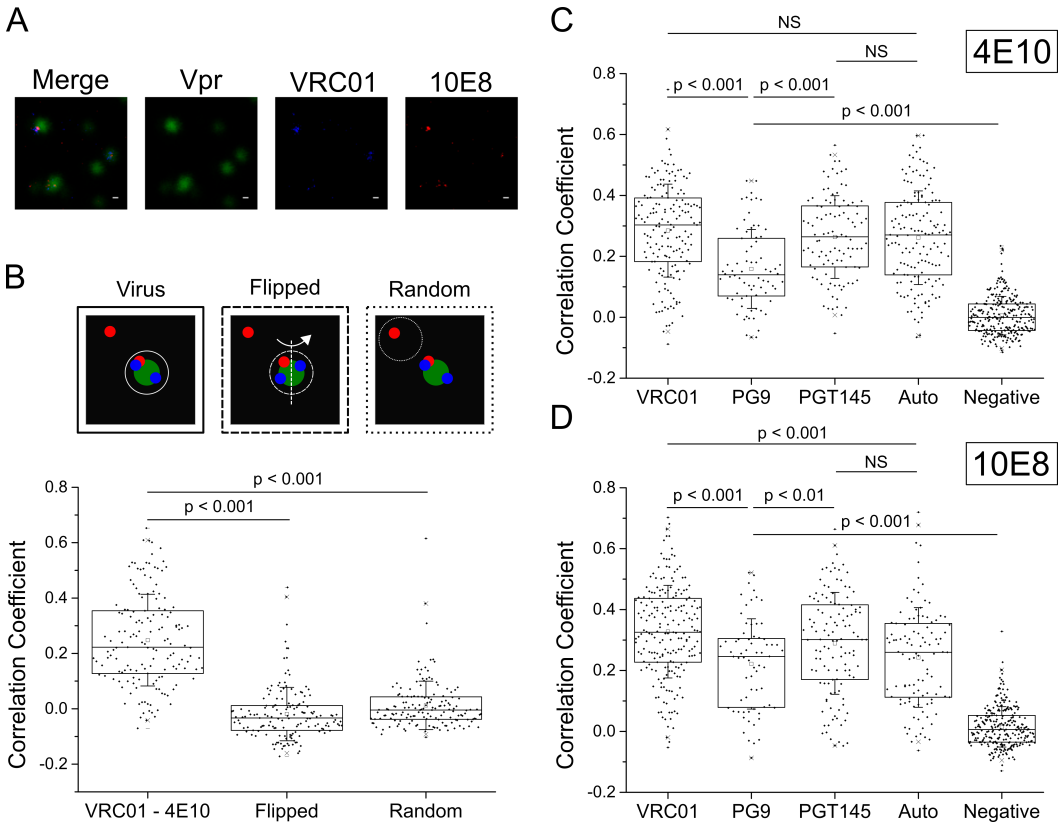

Figure 6.4: Dual color STED colocalization analysis of anti-gp120 and anti-gp41 antibodies bound to Env (NL4-3) in HIV-1 virions. (A) Representative images of a colocalization experiment. Vpr.GFP (green), VRC01 (STAR 600, blue, secondary labeling), 10E8 (KK114, red, direct labeling). Scale bars are 100 nm. (B) Example of colocalization analysis. Pearsons correlation coefficient for VRC01 and 4E10. Flipped: mirror image of one of the channels. Random: correlation in random ROIs negative for Vpr.GFP. (C) 4E10 and VRC01, PG9, PGT145 and 4E10 (Auto) Pearson's colocalization coefficients. (D) 10E8 and VRC01, PG9, PGT145 and 10E8 (Auto) Pearson's colocalization coefficients. Mean difference significance was tested using Tukey's test.

size of the analyzed area) and (iii) a random Vpr.eGFP-negative area (non-virus). Both, flipped and random controls showed correlation values close to 0, consistent with no-colocalization, which were significantly lower than those measured for the VRC01-4E10 sample (Fig. 6.4 B, bottom). Correlation values close to 0 of the flipped and random control measurements were obtained for all antibody combinations described in the following experiments (not shown).

Figs. 6.4 C and D display colocalization data of three different anti-gp120 antibodies with 4E10 or 10E8, respectively. The broadly neutralizing VRC01 antibody recognizes the CD4 binding site (CD4bs) on gp120, whereas PG9 and PGT145 bind to the V1/V2 site (Burton and Hangartner, 2016). Specifically, PGT145 is extremely trimer-specific and thus, thought to associate exclusively with properly folded Env oligomers. To establish maximal self-correlation values under our experimental conditions, dual color STED measurements of anti-MPER antibodies were performed (i.e., colocalization analysis of KK114-Fabs, also stained with a secondary anti-Fab fluorescent STAR 600 conjugated antibody), which yielded median Pearson's coefficients of 0.27 and 0.26 for 4E10 and 10E8, respectively (*Auto* samples in Figs. 6.4 C and D). In addition, samples incubated with fluorescently labeled secondary antibody in the absence of primary anti-gp120 antibody, were used as a negative control for colocalization with KK114-labeled anti-MPER antibodies (*Negative* in 6.4 C and D). These samples, showing median Pearson's values of 0.00 and 0.01 for 4E10 and 10E8, respectively, also confirmed the absence of cross-talk between the STED channels.

As judged from the calculated correlation coefficients, both, 4E10 and 10E8 colocalized with anti-gp120 antibodies (Figs. 6.4 C and D, respectively). The higher and lower values for both anti-MPER antibodies were calculated in mixtures with VRC01 or PG9 respectively. Other anti-gp120 control antibodies were also tested (Fig. 6.5). The b12 antibody, which also binds the CD4bs, was previously demonstrated to preferentially recognize and fix Env in a relaxed conformation, in which MPER is thought to be more accessible (Guttman et al., 2015; Lee et al., 2016). Interestingly, the correlation coefficient for b12 was significantly lower than those calculated for other anti-gp120 antibodies known to fix Env in the closed conformation (e.g. VRC01 and PGT145) (Munro et al., 2014). Controls for antibodies recognizing non-properly folded Env conformations were also tested. F240, which recognizes gp41 stumps, and b13, a non-neutralizing antibody that binds to the CD4bs, also colocalize with 4E10 and 10E8. These results suggest that anti-MPER antibodies are able to bind their epitopes in properly folded (functional) and misfolded (non-functional) Env molecules. Note that the resolution offered by STED may not be sufficient to resolve antibodies bound to individual Env molecules in clusters. However, maximal colocalization being attained with two of the most potent anti-gp120 antibodies described, i.e.

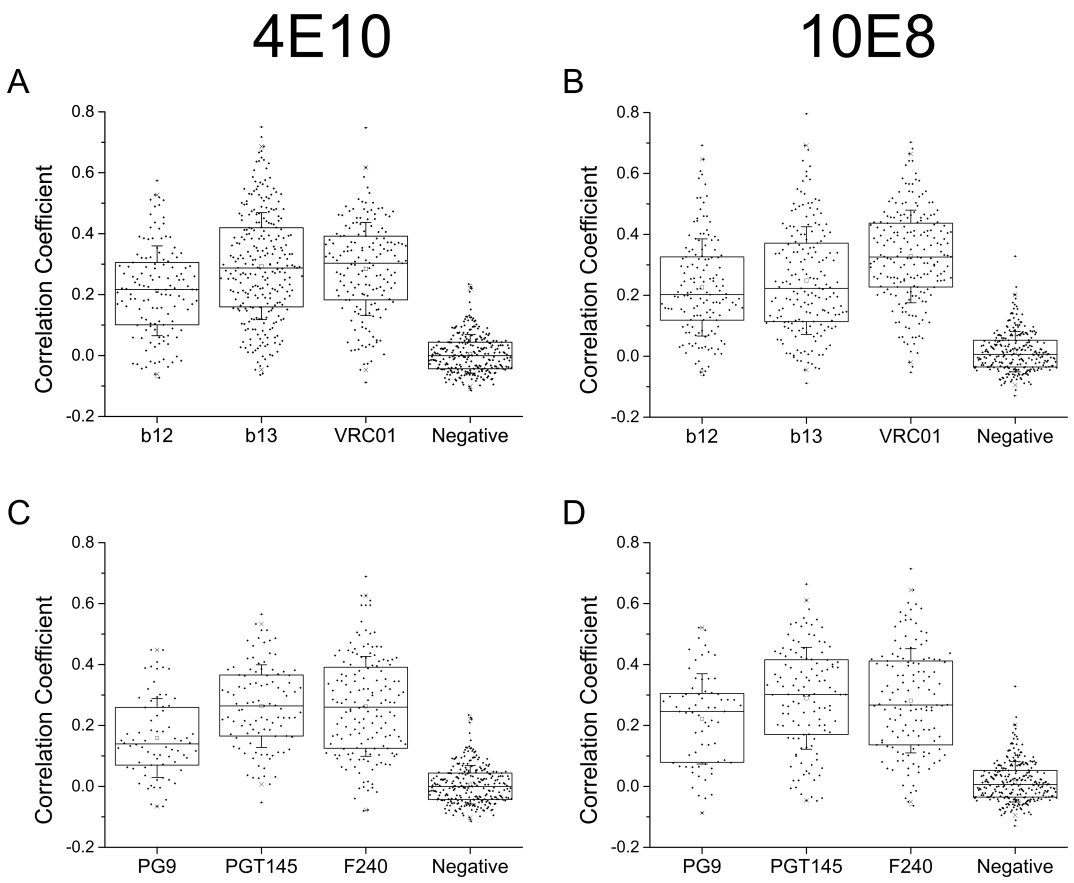

Figure 6.5: Colocalization of anti-gp120 and anti-gp41 antibodies through dual color STED microscopy. 4E10 (A) and 10E8 (B) show positive colocalization with anti-gp120 CD4bs-targeting Fabs. 4E10 (C) and 10E8 (D) also colocalize with trimer specific (PG9 and PGT145) or gp41 stump-binding (F240) antibodies. Conditions as in Fig. 6.4.

VRC01 and the extremely trimer specific PGT145, in the most likely scenario anti-MPER antibodies are recognizing functional Env conformations relevant to HIV-1 infectivity. Thus, overall, colocalization studies using the two-color STED microscopy support engagement of anti-gp120 and anti-gp41 antibodies with the same Env complexes on the intact virions.

Subsequent quantitative analyses helped unveiling more details of the antibody-virion association phenomenon (Fig. 6.6). First 4E10/10E8 binding to viral particles lacking the Env glycoprotein was determined (Fig. 6.6 A, Env(-) samples). Consistent with absence of binding, incubation of Env(-) particles with labeled antibodies resulted in background-like KK114 emission levels. Further evidence for antibody binding dependence on Env came from quantitative experiments using particles containing gp41 mutated in the MPER epitope (Fig. 6.6 B). Single F673A or double W672A/F673A mutations of MPER residues critical for

4E10/10E8 binding (Huang et al., 2012; Zwick et al., 2005), severely limited, or totally inhibited antibody binding to the viral particles, respectively. Finally, to rule out that antibody engagement with the viral membrane may occur in regions devoid of Env molecules, the viral particle staining patterns induced by K114-labeled antibodies were compared with those of phosphatidylserine (PS)-binding Annexin V-ATTO 647 (Fig 6.6 C). Metabolically inert virions lose the aminophospholipid asymmetric distribution existing at the plasma membrane of producing cells, resulting in exposure of the PS at the viral membrane external leaflet (Callahan et al., 2003; Li et al., 2014). Thus, whereas staining by the anti-MPER antibodies occurred in defined foci that occupied less than 10 % of the viral area, the PS-binding protein Annexin V-ATTO 647 STED signal distributed over the complete surface of eGFP emission, consistently with its binding to the lipid component of the viral membrane.

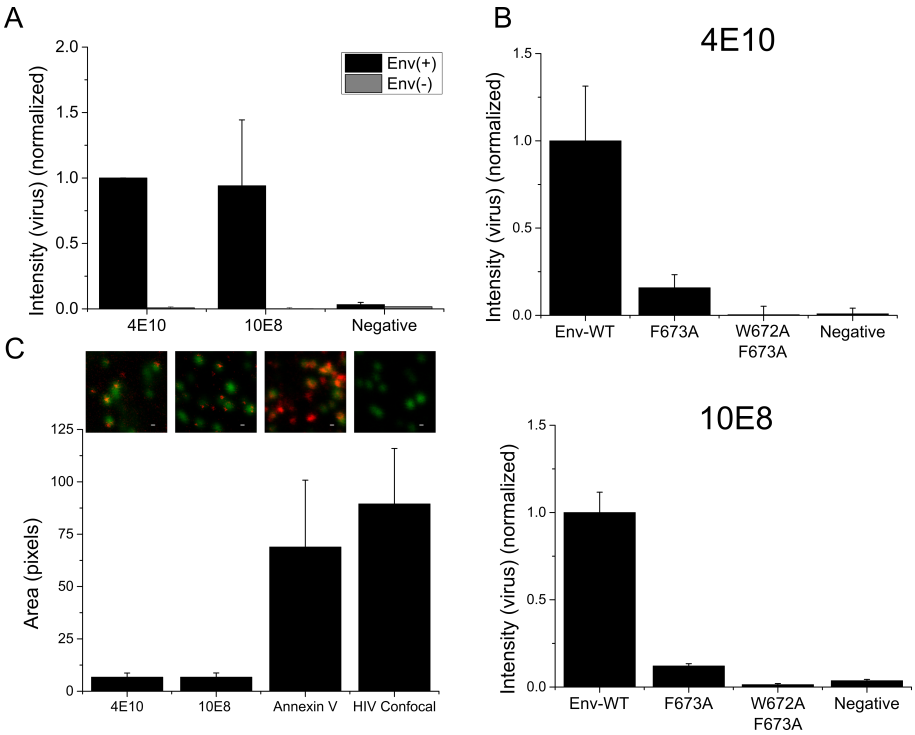

Figure 6.6: Dependence of anti-MPER antibody binding on Env glycoprotein. (A) 4E10 and 10E8 STED signal (normalized to 4E10-Env(+) signal after background subtraction) in Env_{NL4-3}-positive and negative HIV-1 virions. Bars are the SD of at least 3 independent experiments. (B) 4E10 (top) and 10E8 (bottom) STED intensity signal (after background subtraction and normalization) in HIV-1 virions pseudotyped with WT and mutant Env_{JR-CSF} versions. (C) (Top) Micrographs of 4E10-KK114, 10E8-KK114 and Annexin V-ATTO 647 (STED, red) bound to HIV-1 virions (confocal, green, Vpr.GFP). Scale bars are 100 nm. (Bottom) Mean pixel area (20×20 nm^2) and SD of STED (4E10, 10E8 and Annexin V) and confocal (Vpr.GFP) signals.

Altogether, the previous results support that 4E10/10E8 anti-gp41 antibody association with intact virions mainly depends on the Env glycoprotein. Even though, as mentioned above, cumulative structural evidence suggests that anti-gp41 bnAbs can interact with the lipid bilayer through the MAPA/HCDR3 elements to boost MPER epitope recognition (Fig. 6.1). To evaluate the contribution of antibody-membrane interactions to the process, a series of 4E10 and 10E8 variants mutated on the MAPA/HCDR3 regions were generated (Figs. 6.7 and 6.8), and quantitative STED imaging was applied to analyze Env binding to intact virions (Figs. 6.9 and 6.10).

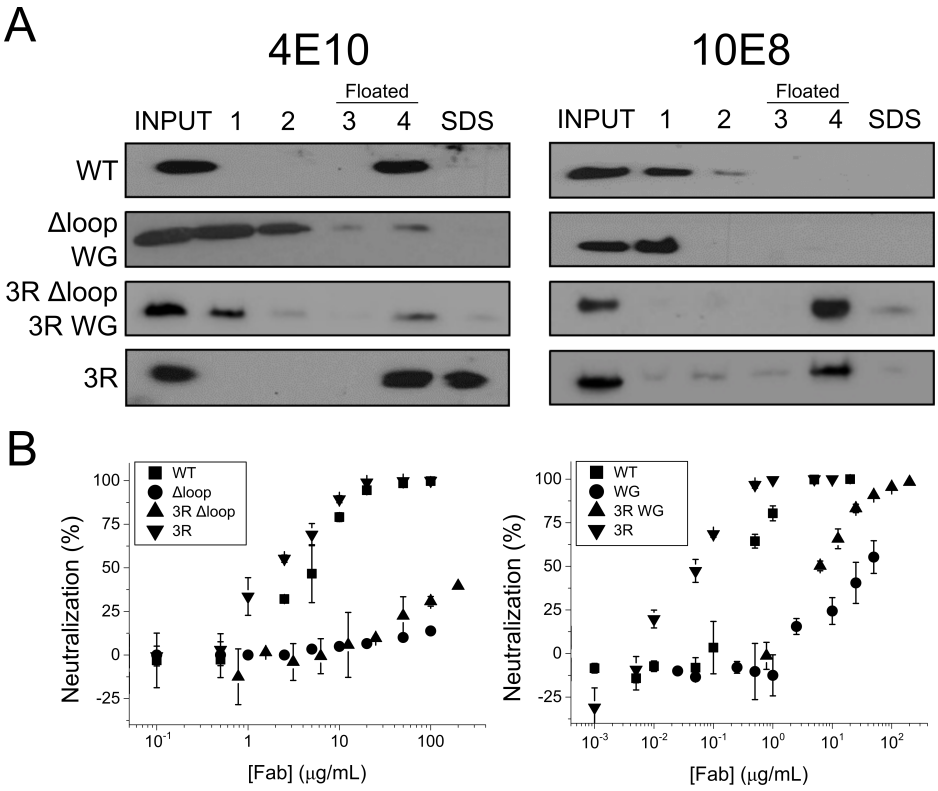

Figure 6.7: Membrane-interacting (A) and virus neutralizing (B) capacities of anti-MPER bnAbs mutated in the MAPA/HCDR3 region. (A) Membrane interaction or 4E10 (left) and 10E8 (right) WT and mutant variants measured by LUV flotation assay. Floated vesicles are found in fractions 3 and 4. SDS is used to extract the Fab fraction unspecifically bound to the tube. Membrane composition was DOPC:DOPS (1:1). (B) Neutralizing activity of 4E10 (left) and 10E8 (right) of JR-CSF HIV-1 pseudovirions measured by cell entry assay.

Antibody modifications affecting the MAPA/HCDR3 elements of 4E10 and 10E8 combined the previously described deletions at the tip of the HCDR3 loop (Δloop and WG mutants) with substitutions of solvent-exposed MAPA residues by Arg to augment electrostatic attraction to the negatively charged membrane

surface (3R mutants). Lipid vesicle flotations assays were employed to reveal distinct degrees of antibody-membrane interactions induced by these modifications (Fig. 6.7 A). All input 4E10 WT antibody was found co-floating with vesicles containing high levels of PS (PC:PS 1:1, mole ratio) that favor MAPA-mediated electrostatic interaction (Rujas et al., 2017a). Ablation of the hydrophobic HCDR3 tip interfered with 4E10-membrane interaction as inferred from the absence of the Δloop mutant in the vesicle-floating fractions. The capacity of this antibody to interact with vesicles was however recovered upon inclusion of the 3R residues to the MAPA surface to render the 3R/Δloop mutant. Finally, the 4E10 3R mutant with HCDR3 tip intact also co-floated with the vesicles.

The vesicle interaction trend was somehow different in the case of 10E8. Consistent with previous reports indicating its incapacity for spontaneous partitioning into membranes (Rujas et al., 2016, 2017a), the WT version of 10E8 was no present in the floating fractions containing the vesicles. This pattern was reproduced by the WG mutant, which interestingly gained the capacity for associating with membranes upon inclusion of the 3R mutation (3R/WG mutant). Accordingly, the 3R mutant with an intact HCDR3, also showed full capacity for partitioning into membranes. These results suggest that the lack of membrane interaction caused by the reduced HCDR3 hydrophobicity can be partially complemented by strengthening electrostastic interactions through the MAPA.

To establish a correlation between the biological function and membrane interactions, the potency of the antibody variants were subsequently evaluated in neutralization assays (Fig. 6.7 B and Table 6.1). Consistent with previously reported results (Huang et al., 2012; Rujas et al., 2016; Scherer et al., 2010; Rujas et al., 2015), mutations reducing hydrophobicity of the HCDR3 loop (4E10 Δloop and 10E8 WG), greatly inhibited the neutralization activity of 4E10 and 10E8 antibodies (Fig 6.7 B, left and right panels, respectively). Following the trend for membrane interaction recovery observed in the flotation experiments, 4E10 3R/Δloop and 10E8 3R/WG variants, displayed enhanced neutralizing capacity, albeit much lower than their WT counterparts. The 3R mutants with intact HCDR3 displayed higher neutralization potency than the parental Fabs, the effect being more conspicuous in the case of the 10E8 antibody. Surprisingly, these effects were not observed when the 4E10 WT and 3R antibodies were assayed in tier-1-based neutralization assays (Table 6.1). Viral isolates are classified depending on the sensitivity to to antibody-mediated neutralization; tier-1 and tier-2 isolates display high and moderate sensitivity, respectively (Seaman et al., 2010).

The previous data support that mutations that enhanced membrane interactions had a positive effect on the neutralization potency of the anti-MPER antibodies. It must be noted however that the conditions favoring antibody partitioning into vesicles were merely used in this study to establish membrane-interacting differences

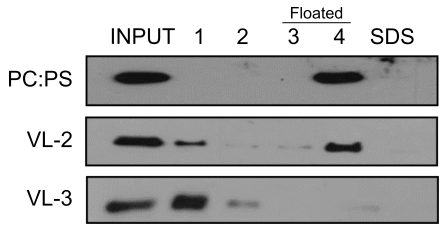

Figure 6.8: Lipid composition dependence of 4E10 antibody interaction with membranes as measured by vesicle flotation assay. Conditions as in Fig. 6.7 A. See table 4.1 for membrane compositions.

among the mutants, and that those conditions unlikely reflected the more restrictive conditions for partitioning imposed by the highly ordered viral membrane (Huarte et al., 2016). This point is further illustrated by the results obtained for the Fab 4E10 using mixtures of lipids that emulate more closely the viral membrane (Fig. 6.8). Thus, consistently with the results displayed in Fig. 6.6 C, the 4E10 antibody was unable to interact directly with vesicles made of the virus-like VL-3 mixture, which displays lipid packing levels comparable to those of the viral membrane (see chapter 4, Fig. 4.1 B).

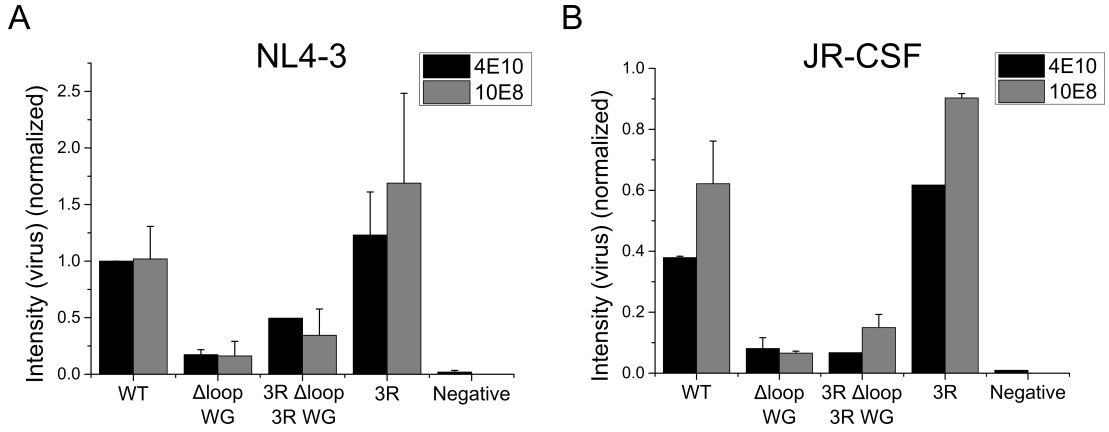

Figure 6.9: Effects of MAPA/HCDR3 mutation on anti-MPER antibody binding to Env (NL4-3, left or JR-CSF, right) on intact virions. The intensity signal after background subtraction was normalized to the 4E10 WT-NL4-3 signal. Bars represent SD of at least three different experiments.

The levels of binding of the anti-MPER Fab variants to NL4-3 (tier-1) and JR-CSF (tier-2) intact virions were next quantitatively compared through STED microscopy (Fig. 6.9). As shown in Fig. 6.2, ablation of the hydrophobic HCDR3 tip severely reduced binding of 4E10/10E8 antibodies to $Env_{NL4\text{-}3}$ (Δloop and WG mutants in Fig. 6.9 A). In accordance with the PC:PS flotation experiments and the neutralization data (Fig. 6.7 and Table 6.1), partial recovery of Fab binding was

observed for the 3R/Δloop and 3R/WG mutants exposing basic Arg residues on the MAPA. Finally, 3R mutants with intact HCDR3s displayed levels of binding that were even higher than that of the WT Fabs, the difference being more significant in the case of the Fab 10E8 (see also Fig. 6.10 A). Effects of the mutations in the MAPA/HCDR3 regions were almost similar in the case of tier-2 JR-CSF, although the antibody binding process occurred with certain variations (Fig. 6.9 B). First, binding levels were overall lower than in the tier-1 samples (note the y-axis range), which followed the trend of the neutralization potency (Table 6.1). Second, except for the NL4-3 WT and HCDR3 loop mutant samples, binding measured for the 10E8 variants was higher than that of the 4E10 variants, which again paralleled the neutralization potency of these antibodies.

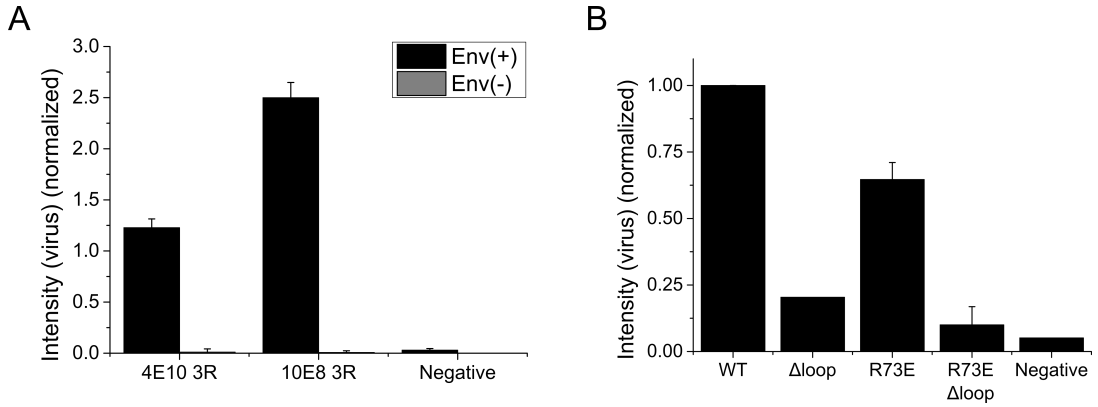

Figure 6.10: (A) 4E10 3R and 10E8 3R STED intensity signal in HIV-1 (Vpr.GFP positive) particles (normalized to 4E10 WT - NL4-3 intensity and after background subtraction) in HIV-1 virions (NL4-3 (Vpr.GFP positive regions). Error bars are the standard error of the mean of a single experiment. (B) STED intensity signal of 4E10 WT and MAPA mutants in HIV-1 particles. Bars are SD of at least three independent experiments.

Thus, the previous results put forward the role of electrostatic interactions with membranes in modulating anti-MPER antibody binding to Env on intact virions. Further evidence sustaining this hypothesis was provided by the experiments in Fig. 6.10 B, showing that negative charge addition to the otherwise positive MAPA surface of the Fab 4E10 (mutant R73E) resulted in lower levels of binding, which, in the case of the R73E-Δloop double mutant, reached levels comparable to background (*Negative*). The neutralization IC_{50} value determined for the mutant R73E was reduced by approximately one order of magnitude with respect to WT, whereas the R73E-Δloop was devoid of activity (Table 6.1). These data demonstrated that mutations reducing the electrostatic charge in the vicinity of the paratope have a negative impact not only in the binding to Env on virions, but also in the biological function of the antibody.

To gain insights into the distinctive features of the binding mechanism of

4E10 to lipids in model membranes that is not reproduced in the case of intact virions devoid of Env (Fig. 6.6 A), the mobility of the 4E10 Fab was studied by means of fluorescence correlation spectroscopy (FCS, see section 1.2.4). The diffusion coefficient for the Fab in solution (98.1 μm/s^2) was reduced more than one order of magnitude (7.86 μm/s^2) when measured interacting with lipids by scanning FCS in giant unilamellar vesicles (GUVs) made of a virus-like lipid mixture (VL-2) (Figs. 6.11 A and B). Mobility was further reduced (2.57 μm/s^2) upon incorporation of the MPER(671-693) peptide that contains the 4E10 epitope sequence. Interestingly, diffusion of the Δloop mutant bound to membrane inserted peptides increased to 7.15 μm/s^2 (Figs. 6.11 C and D). These results suggest that antibody-epitope interactions in a lipid environment differ depending on the presence of the hydrophobic HCDR3 loop tip.

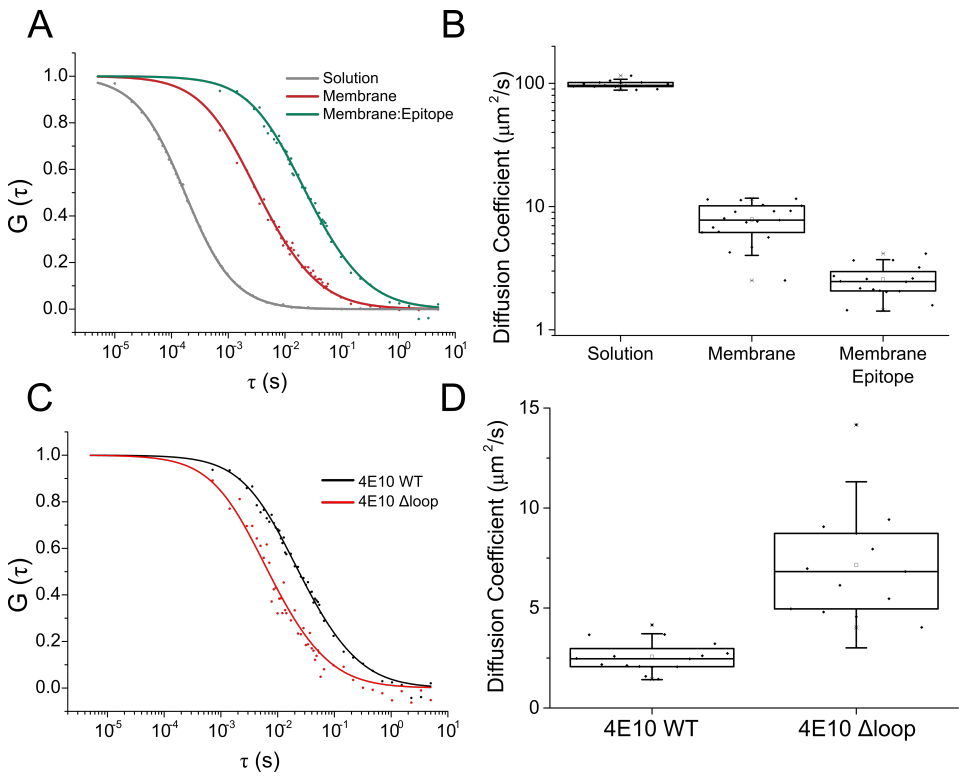

Figure 6.11: 4E10 diffusion studied by FCS. (A) Autocorrelation curves and (B) diffusion coefficients of the 4E10 Fab in solution, bound to VL-2 GUVs (*Membrane*) and interacting with the MPER(671-693) peptide in VL-2 GUVs (1:1000 peptide:lipid ratio). Ablation of the HCDR3 loop in VL-2:MPER (*Membrane Epitope*) GUVs resulted in autocorrelation curves shifted to shorter lag times (τ) (C), i.e. higher diffusion coefficients(D).

The different antibody versions may recognize peptides in different oligomeric states, which would explain the observed differences. However, attempts to measure

peptide mobility in GUVs failed due to the poor photostability of the fluorescent dye used (Quasar 670). Future trials with FCS-compatible fluorophores will for sure provide interesting information of peptide behavior in virus-like membrane environments.

Other possibility is that the hydrophobic residues ablated from the HCDR3 loop provide the antibody with the capacity to insert deeper into the membrane, so 4E10 Δloop mobility would be faster due to a more superficial interaction with the lipid bilayer. To study this putative scenario, the diffusion of 4E10 WT was measured upon increase of PS content, i.e. the mean negative surface potential of the membrane. Interestingly, higher PS concentrations yielded slower diffusion coefficient for 4E10 (Fig. 6.12 A). This results suggests that the antibody inserts deeper in membranes presenting stronger surface potential and contrasts with the view of 4E10 binding a single lipid molecule that would constitute an integral part of the epitope (Irimia et al., 2016).

Annexin V, that recognizes PS molecules specifically, was used in control experiments for specific lipid recognition. Annexin V diffusion remained unaltered even after a 50% increase of membrane PS content (Fig. 6.12 B). Moreover, Annexin V (38 kDa) diffused significantly slower than 4E10 (48 kDa), even if the Chol content was 20% lower (35% vs 15%) in the Annexin V experiments and the molecule is smaller, further suggesting that the 4E10 antibody-lipid interaction stoichiometry is not 1:1. Moreover, increasing the Chol content of the membrane decreased the diffusion coefficient of the antibody to a lesser extent that increasing PS (Fig. 6.12 C).

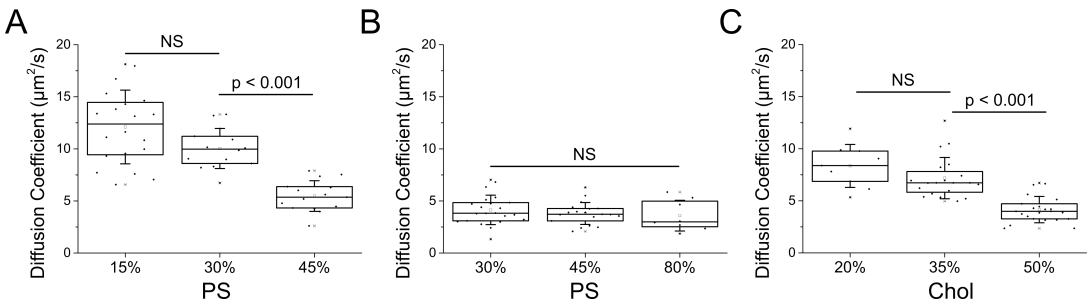

Figure 6.12: 4E10 mobility on membranes depends on electrostatic forces and membrane dynamics. (A) Increasing the PS content of membranes decreased 4E10 WT Fab mobility (Chol concentration was fixed to 35% and PC decreased as a function of PS). (B) This behavior was not observed for Annexin V (Chol concentration fixed to 15%). (C) Chol increase at fixed 30% PS concentrations also slowed down the antibody.

Altogether the mobility experiments suggest that membrane potential and, to a lesser extent, membrane dynamics, rule antibody diffusion on the membrane and that the 4E10 interaction with PS is unspecific.

6.4 Discussion

Induction of antibodies functional in viral inactivation and clearance appears to be required for attaining effective prophylaxis by a preventive HIV vaccine. In this regard, identification within these antibodies of structural adaptations required for function, and their distinction from accessory elements merely arising from prolonged contact with antigen, are critical in the fields of HIV-1 vaccine design and immunotherapy (Burton and Hangartner, 2016; Stephenson and Barouch, 2016). Particularly the potential requirement of unusually long HCDR3 loops poses a challenge to the recovery of similar antibodies through vaccination given the low frequency of these elements in naïve B cells (Haynes and Mascola, 2017; Burton, 2017).

Demonstration that the hydrophobic and aromatic residues existing at apex of the HCDR3s of anti-MPER bnAbs are essential for viral neutralization (Huang et al., 2012; Rujas et al., 2016; Scherer et al., 2010), has supported the proposal that these elements constitute membrane anchors conferring the anti-MPER antibodies with properties of integral membrane proteins (Scherer et al., 2010). It has been argued that, in contrast to the most efficient anti-gp120 bnAbs, 4E10/10E8 appear to bind only weakly to the native Env. Moreover, experimental evidence obtained in gp41 proteins engineered to emulate structurally the Env fusion intermediate *pre-hairpin*, has put forward the possibility that anti-MPER antibodies bind to fusion-activated Env intermediates, rather than to native pre-fusion Env complexes on virions (Frey et al., 2008, 2010). Together, these assumptions sustain the hypothesis that 4E10/10E8 antibodies attach first to the viral membrane, where they reside as integral membrane proteins until engagement with their MPER epitope that becomes transiently accessible on the pre-hairpin fusion intermediate of Env. If true, this two-step mechanism of action would have important implications on the applicability of anti-MPER antibodies as templates to vaccine and immunotherapy developments. Most importantly, potency would be directly dependent on the capacity for pre-insertion into the bare membrane, a faculty whose development would be limited by self-tolerance mechanisms, specifically lipid auto-reactivity.

Contrasting this general assumption, 10E8, the most potent of both antibodies studied in this chapter, presents, if any, little polyreactivity with lipids and other autoantigens, and shows no propensity for spontaneous insertion into membranes (Huang et al., 2012; Rujas et al., 2016, 2017a). Emphasizing its applicability in vivo, this antibody has been included as a component of recently engineered bi-specific and tri-specific anti-HIV antibodies ((Huang et al., 2016; Xu et al., 2017)). Moreover, a relatively new view proposes that anti-MPER antibody engagement with the membrane surface also occurs through the flat MAPA, mediated by electrostatic forces (Irimia et al., 2016; Rujas et al., 2016; Irimia et al., 2017; Rujas et al., 2017a). According to this view, accessibility to MPER epitopes 4E10/10E8 is limited by a

molecular surface that conforms to both the membrane plane and the Env complex ectodomain (Fig. 6.1) (Lee et al., 2016). In addition and similarly to what stands for antibodies targeting gp120, it is postulated that the long-hydrophobic HCDR3 loop is required to stabilize an antibody-epitope complex, which in the case of anti-MPER antibodies will be formed at the membrane interface (Irimia et al., 2016; Rujas et al., 2016; Irimia et al., 2017; Scherer et al., 2010; Rujas et al., 2015, 2017b). Thus, the maturation processes undergone by 4E10 and 10E8 antibodies that led to MAPA/HCDR3 development could hypothetically be interpreted in terms of steric adaptations to the Env/membrane surface.

The work presented in this chapter is based on the use of nanoscopy techniques, and intends to clarify the role of antibody-membrane interactions mediated by the MAPA/HCDR3 elements in the antiviral efficacy of the anti-HIV bnAbs 4E10 and 10E8. Definition of the MAPA/HCDR3 function at the molecular level is particularly important to infer whether their molecular properties, i.e., the electrostatic interaction of the flat MAPA with the membrane-interface, and the membrane insertion of the unusually long and hydrophobic HCDR3, comprise strict functional requirements that must be preserved within effective anti-MPER bnAbs.

Taking the advantage of HIV-neutralizing antibody binding in isolated virions occurring in segregated foci containing Env glycoprotein clusters (Figs. 6.2 and 6.3), the co-localization of anti-MPER and anti-gp120 antibodies could be established using dual color STED imaging (Figs. 6.4 and 6.5). Furthermore, imaging directly labeled anti-MPER antibodies through STED microscopy provided a quantitative means to study the interaction of 4E10 and 10E8 with the viral membrane (Fig. 6.6) and to compare binding by different 4E10/10E8 variants, which interacted with membranes to different degrees (Figs. 6.7-6.10). sFCS single molecule mobility measurements also allowed for studying the behavior of antibody-epitope and antibody-lipid interactions in a membrane environment (Figs. 6.11 and 6.12). Together, these approaches have provided unprecedented insights into the anti-MPER bnAb binding process at the molecular level.

The experimental data reveal that broadly neutralizing anti-gp120 and antigp41 antibodies engage with the same Env clusters. Moreover, they rule out the putative association of the anti-MPER antibodies to viral membrane areas devoid of Env glycoprotein. They also establish a correlation between stronger antibody-membrane interaction, enhanced neutralization and increase of the amount of antibody bound to intact virions. Therefore, the unprecedented STED microscopy approach gives full support to the hypotheses (i) that anti-MPER antibodies bind to native Env to exert neutralization, (ii) that the strength of this interaction conditions potency, and (iii) that the antibody-membrane interaction adds to the antibody-antigen interactions sustaining Env binding. *In vitro* experiments using model membranes (flotation and FCS) further suggest that the nature of 4E10-membrane interac-

tions is electrostatic, hydrophobic and unspecific and that these interactions are impaired in virions due to the high molecular packing off the viral lipid envelope. These observations will inform new approaches to vaccine design, and clarify what elements of anti-MPER antibodies can be subject of optimization when used as templates for immunotherapeutic agent development.

6.5 Conclusions

Structure-function analyses of bnAbs have overall established a correlation between strength of binding to native Env and efficiency for blocking HIV infection (neutralization). Anti-MPER bnAbs targeting the transmembrane subunit gp41 are of special interest in the field because they consistently display broad coverage and high efficacy *in vivo*. However, for these antibodies a distinct mechanism of antiviral action has been postulated involving pre-attachment to and accumulation within the viral membrane. Results in this chapter support that 4E10 and 10E8 anti-MPER antibodies do not bind to the viral membrane in the absence of Env or upon mutations in their epitope. Moreover, these bnAbs are able to recognize the same set of Env clusters than anti-gp120 neutralizing and non-neutralizing antibodies. 4E10 and 10E8 show a neutralization strength that correlates with their tendency to bind to virions, that further depends on their ability to interact with lipid membranes. Furthermore, the interaction between 4E10 and lipid bilayers, which is both hydrophobic and electrostatic, seems to be unspecific and superficial. The data presented in this chapter might be relevant for vaccine and immunotherapeutic agent development.

Chapter 7

Conclusions

- DOPC:cholesterol:SM ternary lipid mixtures organize in a single liquid phase at sphingomyelin:cholesterol ratios lower than 1 according to two-photon Laurdan microscopy studies. Two photon excitation prevents lipid photooxidation that can induce microscopic phase separation. Lateral packing of this mixture is governed largely by SM:cholesterol interactions.
- Lipids extracted from HIV-1 particles form membranes nearly as packed as SM:Chol raft like model membranes and organize in lipid nanodomains. Membrane active compounds displaying virucidal activity are able to interfere with the phase behavior of the HIV-1 envelope lipids.
- Faithful virus-like lipid mixtures have to include the most abundant species of the HIV-1 lipidome.
- The $MPER_{671-693}$ peptide, including the MPER and N-terminal sequence of the TMD domains inhibits HIV-1 infectivity upon interaction with the membrane. Its function is correlated with the ability to permeabilize virus-like membranes and to accumulate at the boundaries of lipid domains.
- 4E10 and 10E8 anti-MPER broadly neutralizing antibodies bind to Env in HIV-1 virions, but no direct interaction with the viral membrane has been detected. Their neutralizing potency is correlated to their ability to bind Env on the viral surface, that further depends on antibody-lipid interactions.

Bibliography

Aeffner, S., Reusch, T., Weinhausen, B., and Salditt, T. Energetics of stalk intermediates in membrane fusion are controlled by lipid composition. *Proceedings of the National Academy of Sciences of the United States of America*, 109(25): 1609–1618, 2012.

Alam, S. M., McAdams, M., Boren, D., Rak, M., Scearce, R. M., Gao, F., Camacho, Z. T., Gewirth, D., Kelsoe, G., Chen, P., and Haynes, B. F. The role of antibody polyspecificity and lipid reactivity in binding of broadly neutralizing anti-HIV-1 envelope human monoclonal antibodies 2F5 and 4E10 to glycoprotein 41 membrane proximal envelope epitopes. *Journal of Immunology*, 178(7):4424–35, apr 2007.

Alam, S. M., Morelli, M., Dennison, S. M., Liao, H. X., Zhang, R., Xia, S. M., Rits-Volloch, S., Sun, L., Harrison, S. C., Haynes, B. F., and Chen, B. Role of HIV membrane in neutralization by two broadly neutralizing antibodies. *Proceedings of the National Academy of Sciences of the United States of America*, 106(48): 20234–20239, 2009.

Almeida, P. F. Thermodynamics of lipid interactions in complex bilayers, 2009.

Almeida, P. F. The many faces of lipid rafts. *Biophysical Journal*, 106(9):1841–1843, 2014.

Aloia, R. C., Jensen, F. C., Curtain, C. C., Mobley, P. W., and Gordon, L. M. Lipid composition and fluidity of the human immunodeficiency virus. *Proceedings of the National Academy of Sciences of the United States of America*, 85(3):900–4, 1988.

Aloia, R. C., Tian, H., and Jensen, F. C. Lipid composition and fluidity of the human immunodeficiency virus envelope and host cell plasma membranes. *Proceedings of the National Academy of Sciences of the United States of America*, 90(11):5181–5185, 1993.

Amaro, M., Reina, F., Hof, M., Eggeling, C., and Sezgin, E. Laurdan and Di-4-ANEPPDHQ probe different properties of the membrane. *Journal of Physics D: Applied Physics*, 50(13):134004, 2017.

Apellaniz, B. and Nieva, J. L. The Use of Liposomes to Shape Epitope Structure and Modulate Immunogenic Responses of Peptide Vaccines Against HIV MPER. *Advances in Protein Chemistry and Structural Biology*, 99:15–54, 2015.

Apellaniz, B., Ivankin, A., Nir, S., Gidalevitz, D., Nieva, J. L., Apellániz, B., Ivankin, A., Nir, S., Gidalevitz, D., and Nieva, J. L. Membrane-proximal external HIV-1 gp41 motif adapted for destabilizing the highly rigid viral envelope. *Biophysical Journal*, 101(10):2426–2435, 2011.

Apellaniz, B., Huarte, N., Largo, E., and Nieva, J. L. The three lives of viral fusion peptides. *Chemistry and Physics of Lipids*, 181:40–55, 2014a.

Apellaniz, B., Rujas, E., Carravilla, P., Requejo-Isidro, J., Huarte, N., Domene, C., and Nieva, J. L. Cholesterol-Dependent Membrane Fusion Induced by the gp41 Membrane-Proximal External Region-Transmembrane Domain Connection Suggests a Mechanism for Broad HIV-1 Neutralization. *Journal of Virology*, 88 (22):13367–13377, 2014b.

Apellániz, B., Rujas, E., Serrano, S., Morante, K., Tsumoto, K., Caaveiro, J. M. M., Jiménez, M. Á., and Nieva, J. L. The Atomic Structure of the HIV-1 gp41 Transmembrane Domain and Its Connection to the Immunogenic Membrane-proximal External Region. *Journal of Biological Chemistry*, 290(21):12999–13015, may 2015.

Ariola, F. S., Li, Z., Cornejo, C., Bittman, R., and Heikal, A. A. Membrane fluidity and lipid order in ternary giant unilamellar vesicles using a new bodipy-cholesterol derivative. *Biophysical Journal*, 96(7):2696–2708, 2009.

Ashkenazi, A., Faingold, O., and Shai, Y. HIV-1 fusion protein exerts complex immunosuppressive effects. *Trends in Biochemical Sciences*, 38(7):345–349, 2013.

Aussenac, F., Tavares, M., and Dufourc, E. J. Cholesterol dynamics in membranes of raft composition: A molecular point of view from 2H and 31P solid-state NMR. *Biochemistry*, 42(6):1383–1390, 2003.

Ayuyan, A. G. and Cohen, F. S. Lipid Peroxides Promote Large Rafts: Effects of Excitation of Probes in Fluorescence Microscopy and Electrochemical Reactions during Vesicle Formation. *Biophysical Journal*, 91(6):2172–2183, 2006.

Badani, H., Garry, R. F., and Wimley, W. C. Peptide entry inhibitors of enveloped viruses: The importance of interfacial hydrophobicity. *Biochimica et Biophysica Acta - Biomembranes*, 1838(9):2180–2197, sep 2014.

Bagatolli, L. A. To see or not to see: lateral organization of biological membranes and fluorescence microscopy. *Biochimica et Biophysica Acta - Biomembranes*, 1758(10):1541–1556, 2006.

Bagatolli, L. a. and Gratton, E. Two photon fluorescence microscopy of coexisting lipid domains in giant unilamellar vesicles of binary phospholipid mixtures. *Biophysical Journal*, 78(1):290–305, 2000.

Bakht, O., Pathak, P., and London, E. Effect of the structure of lipids favoring disordered domain formation on the stability of cholesterol-containing ordered domains (lipid rafts): identification of multiple raft-stabilization mechanisms. *Biophysical Journal*, 93(12):4307–4318, 2007.

Barlic, A., Gutierrez-Aguirre, I., Caaveiro, J. M., Cruz, A., Ruiz-Arguello, M. B., Perez-Gil, J., and Gonzalez-Manas, J. M. Lipid phase coexistence favors membrane insertion of equinatoxin-II, a pore-forming toxin from Actinia equina. *Journal of Biological Chemistry*, 279(33):34209–34216, 2004.

Barre-Sinoussi, F., Chermann, J., Rey, F., Nugeyre, M., Chamaret, S., Gruest, J., Dauguet, C., Axler-Blin, C., Vezinet-Brun, F., Rouzioux, C., Rozenbaum, W., and Montagnier, L. Isolation of a T-lymphotropic retrovirus from a patient at risk for acquired immune deficiency syndrome (AIDS). *Science*, 220:868–871, 1983.

Bezlyepkina, N., Gracià, R. S., Shchelokovskyy, P., Lipowsky, R., and Dimova, R. Phase diagram and tie-line determination for the ternary mixture DOPC/eSM/Cholesterol. *Biophysical Journal*, 104(7):1456–1464, 2013.

Blom, H. and Widengren, J. Stimulated Emission Depletion Microscopy. *Chemical Reviews*, 117(11):7377–7427, 2017.

Blumenthal, R., Durell, S., and Viard, M. HIV entry and envelope glycoprotein-mediated fusion. *Journal of Biological Chemistry*, 287(49):40841–40849, 2012.

Bobardt, M. D., Cheng, G., de Witte, L., Selvarajah, S., Chatterji, U., Sanders-Beer, B. E., Geijtenbeek, T. B. H., Chisari, F. V., and Gallay, P. A. Hepatitis C virus NS5A anchor peptide disrupts human immunodeficiency virus. *Proceedings of the National Academy of Sciences of the United States of America*, 105(14): 5525–5530, 2008.

Brandenberg, O. F., Magnus, C., Regoes, R. R., and Trkola, A. The HIV-1 Entry Process: A Stoichiometric View. *Trends in Microbiology*, 23(12):763–774, 2015.

Brügger, B., Glass, B., Haberkant, P., Leibrecht, I., Wieland, F. T., and Kräusslich, H.-G. G. The HIV lipidome: a raft with an unusual composition. *Proceedings of the National Academy of Sciences of the United States of America*, 103(8): 2641–2646, 2006.

Burton, D. R. What Are the Most Powerful Immunogen Design Vaccine Strategies? Reverse Vaccinology 2.0 Shows Great Promise. *Cold Spring Harbor Perspectives in Biology*, 9(11):a029470, nov 2017.

Burton, D. R. and Hangartner, L. Broadly Neutralizing Antibodies to HIV and Their Role in Vaccine Design. *Annual Review of Immunology*, 34(1):635–659, may 2016.

Burton, D. R. and Mascola, J. R. Antibody responses to envelope glycoproteins in HIV-1 infection. *Nature Immunology*, 16(6):571–576, may 2015.

Callahan, M. K., Popernack, P. M., Tsutsui, S., Truong, L., Schlegel, R. A., and Henderson, A. J. Phosphatidylserine on HIV Envelope Is a Cofactor for Infection of Monocytic Cells. *The Journal of Immunology*, 170(9):4840–4845, 2003.

Campbell, S. M., Crowe, S. M., and Mak, J. Virion-associated cholesterol is critical for the maintenance of HIV-1 structure and infectivity. *AIDS*, 16(17):2253–2261, 2002.

Cardoso, R. M., Zwick, M. B., Stanfield, R. L., Kunert, R., Binley, J. M., Katinger, H., Burton, D. R., and Wilson, I. A. Broadly Neutralizing Anti-HIV Antibody 4E10 Recognizes a Helical Conformation of a Highly Conserved Fusion-Associated Motif in gp41. *Immunity*, 22(2):163–173, feb 2005.

Cardoso, R. M., Brunel, F. M., Ferguson, S., Zwick, M., Burton, D. R., Dawson, P. E., and Wilson, I. A. Structural Basis of Enhanced Binding of Extended and Helically Constrained Peptide Epitopes of the Broadly Neutralizing HIV-1 Antibody 4E10. *Journal of Molecular Biology*, 365(5):1533–1544, feb 2007.

Cavacini, L. A., Emes, C. L., Wisnewski, A. V., Power, J., Lewis, G., Montefiori, D., and Posner, M. R. Functional and molecular characterization of human monoclonal antibody reactive with the immunodominant region of HIV type 1 glycoprotein 41. *AIDS Research and Human Retroviruses*, 14(14):1271–80, sep 1998.

Chachaty, C., Rainteau, D., Tessier, C., Quinn, P. J., and Wolf, C. Building up of the liquid-ordered phase formed by sphingomyelin and cholesterol. *Biophysical Journal*, 88(June):4032–4044, 2005.

Chamoun-Emanuelli, A. M., Pecheur, E. I., Simeon, R. L., Huang, D., Cremer, P. S., Chena, Z., Chen, Z., and Chena, Z. Phenothiazines inhibit hepatitis C virus entry, likely by increasing the fluidity of cholesterol-rich membranes. *Antimicrobial Agents and Chemotherapy*, 57(6):2571–2581, 2013.

Chan, R., Uchil, P. D., Jin, J., Shui, G., Ott, D. E., Mothes, W., and Wenk, M. R. Retroviruses Human Immunodeficiency Virus and Murine Leukemia Virus Are Enriched in Phosphoinositides. *Journal of Virology*, 82(22):11228–11238, 2008.

Checkley, M. A., Luttge, B. G., and Freed, E. O. HIV-1 envelope glycoprotein biosynthesis, trafficking, and incorporation. *Journal of Molecular Biology*, 410 (4):582–608, 2011.

Chen, J., Frey, G., Peng, H., Rits-Volloch, S., Garrity, J., Seaman, M. S., and Chen, B. Mechanism of HIV-1 Neutralization by Antibodies Targeting a Membrane-Proximal Region of gp41. *Journal of Virology*, 88(2):1249–1258, jan 2014.

Chen, S. S.-L., Yang, P., Ke, P.-Y. Y., Li, H.-F. F., Chan, W.-E. E., Chang, D.-K. K., Chuang, C.-K. K., Tsai, Y., and Huang, S.-C. C. Identification of the LWYIK motif located in the human immunodeficiency virus type 1 transmembrane gp41 protein as a distinct determinant for viral infection. *Journal of Virology*, 83(2): 870–883, 2009.

Chen, Y., Zhang, J., Hwang, K.-K., Bouton-Verville, H., Xia, S.-M., Newman, A., Ouyang, Y.-B., Haynes, B. F., and Verkoczy, L. Common Tolerance Mechanisms, but Distinct Cross-Reactivities Associated with gp41 and Lipids, Limit Production of HIV-1 Broad Neutralizing Antibodies 2F5 and 4E10. *The Journal of Immunology*, 191(3):1260–1275, aug 2013.

Chernomordik, L. V. and Kozlov, M. M. Mechanics of membrane fusion. *Nature Structural & Molecular Biology*, 15(7):675–683, 2008.

Chojnacki, J., Staudt, T., Glass, B., Bingen, P., Engelhardt, J., Anders, M., Schneider, J., Muller, B., Hell, S. W., Krausslich, H. G., Müller, B., Hell, S. W., and Kräusslich, H.-G. Maturation-dependent HIV-1 surface protein redistribution revealed by fluorescence nanoscopy. *Science*, 338(6106):524–528, 2012.

Chojnacki, J., Waithe, D., Carravilla, P., Huarte, N., Galiani, S., Enderlein, J., and Eggeling, C. Envelope glycoprotein mobility on HIV-1 particles depends on the virus maturation state. *Nature Communications*, 8(1):545, 2017.

Cohen, T., Cohen, S. J., Antonovsky, N., Cohen, I. R., and Shai, Y. HIV-1 gp41 and TCRalpha trans-membrane domains share a motif exploited by the HIV virus to modulate T-cell proliferation. *PLoS Pathog*, 6(9):e1001085, 2010.

Colpitts, C. C., Ustinov, A. V., Epand, R. F., Epand, R. M., Korshun, V. A., and Schang, L. M. 5-(Perylen-3-yl)ethynyl-arabino-uridine (aUY11), an arabino-based rigid amphipathic fusion inhibitor, targets virion envelope lipids to inhibit fusion of influenza virus, hepatitis C virus, and other enveloped viruses. *Journal of Virology*, 87(7):3640–3654, 2013.

Connell, S. D. and Smith, D. A. The atomic force microscope as a tool for studying phase separation in lipid membranes. *Molecular Membrane Biology*, 23(1):17–28, 2006.

Cruz, A. and Pérez-Gil, J. Langmuir Films to Determine Lateral Surface Pressure on Lipid Segregation. In Dopico, A., editor, *Methods in Membrane Lipids*, volume 400, chapter 29, pages 439–457. Humana Press, 2007.

de Almeida, R. F., Fedorov, A., and Prieto, M. Sphingomyelin/Phosphatidylcholine/Cholesterol Phase Diagram: Boundaries and Composition of Lipid Rafts. *Biophysical Journal*, 85(4):2406–2416, 2003.

de Almeida, R. F., Borst, J., Fedorov, A., Prieto, M., and Visser, A. J. Complexity of Lipid Domains and Rafts in Giant Unilamellar Vesicles Revealed by Combining Imaging and Microscopic and Macroscopic Time-Resolved Fluorescence. *Biophysical Journal*, 93(2):539–553, 2007.

De Almeida, R. F. M., Loura, L. M. S., Fedorov, A., and Prieto, M. Lipid rafts have different sizes depending on membrane composition: A time-resolved fluorescence resonance energy transfer study. *Journal of Molecular Biology*, 346(4):1109–1120, 2005.

De Clercq, E. and Li, G. Approved Antiviral Drugs over the Past 50 Years. *Clinical Microbiology Reviews*, 29(3):695–747, 2016.

Dean, J. M. and Lodhi, I. J. Structural and functional roles of ether lipids. *Protein & Cell*, in press, 2017.

Demirkhanyan, L. H., Marin, M., Padilla-Parra, S., Zhan, C., Miyauchi, K., Jean-Baptiste, M., Novitskiy, G., Lu, W., and Melikyan, G. B. Multifaceted mechanisms of HIV-1 entry inhibition by human α-defensin. *Journal of Biological Chemistry*, 287(34):28821–28838, 2012.

Dennison, S. M., Stewart, S. M., Stempel, K. C., Liao, H.-X., Haynes, B. F., and Alam, S. M. Stable Docking of Neutralizing Human Immunodeficiency Virus Type 1 gp41 Membrane-Proximal External Region Monoclonal Antibodies 2F5 and 4E10 Is Dependent on the Membrane Immersion Depth of Their Epitope Regions. *Journal of Virology*, 83(19):10211–10223, oct 2009.

Dittrich, P. S. and Schwille, P. Photobleaching and stabilization of fluorophores used for single-molecule analysis with one- and two-photon excitation. *Applied Physics B: Lasers and Optics*, 73(8):829–837, 2001.

Dodes Traian, M. M., Flecha, F. L. G., and Levi, V. Imaging lipid lateral organization in membranes with C-laurdan in a confocal microscope. *Journal of Lipid Research*, 53(3):609–616, 2012.

Domanska, M. K., Wrona, D., and Kasson, P. M. Multiphasic effects of cholesterol on influenza fusion kinetics reflect multiple mechanistic roles. *Biophysical Journal*, 105(6):1383–1387, 2013.

Domanska, M. K., Dunning, R. A., Dryden, K. A., Zawada, K. E., Yeager, M., and Kasson, P. M. Hemagglutinin Spatial Distribution Shifts in Response to Cholesterol in the Influenza Viral Envelope. *Biophysical Journal*, 109(9): 1917–1924, 2015.

Donnert, G., Eggeling, C., and Hell, S. W. Major signal increase in fluorescence microscopy through dark-state relaxation. *Nature Methods*, 4(1):81–86, 2007.

Doria-Rose, N. A., Klein, R. M., Manion, M. M., O'Dell, S., Phogat, A., Chakrabarti, B., Hallahan, C. W., Migueles, S. A., Wrammert, J., Ahmed, R., Nason, M., Wyatt, R. T., Mascola, J. R., and Connors, M. Frequency and Phenotype of Human Immunodeficiency Virus Envelope-Specific B Cells from Patients with Broadly Cross-Neutralizing Antibodies. *Journal of Virology*, 83(1): 188–199, jan 2009.

Dowall, S. D., Graham, V. A., Corbin-Lickfett, K., Empig, C., Schlunegger, K., Bruce, C. B., Easterbrook, L., and Hewson, R. Effective binding of a phosphatidylserine-targeting antibody to ebola virus infected cells and purified virions. *Journal of Immunology Research*, 2015, 2015.

Eckert, D. M. and Kim, P. S. Mechanisms of Viral Membrane Fusion and Its Inhibition. *Annual Review of Biochemistry*, 70(1):777–810, 2001.

Eggeling, C., Volkmer, A., and Seidel, C. A. M. Molecular photobleaching kinetics of Rhodamine 6G by one- and two-photon induced confocal fluorescence microscopy. *ChemPhysChem*, 6(5):791–804, 2005.

Eggeling, C., Ringemann, C., Medda, R., Schwarzmann, G., Sandhoff, K., Polyakova, S., Belov, V. N., Hein, B., von Middendorff, C., Schönle, A., and Hell, S. W. Direct observation of the nanoscale dynamics of membrane lipids in a living cell. *Nature*, 457(7233):1159–1162, feb 2009.

Epand, R. F., Sayer, B. G., and Epand, R. M. The Tryptophan-Rich Region of HIV gp41 and the Promotion of Cholesterol-Rich Domains . *Biochemistry*, 44 (14):5525–5531, apr 2005.

Epand, R. F., Thomas, A., Brasseur, R., Vishwanathan, S. A., Hunter, E., and Epand, R. M. Juxtamembrane protein segments that contribute to recruitment of cholesterol into domains. *Biochemistry*, 45(19):6105–14, may 2006.

Epand, R. M., Sayer, B. G., and Epand, R. F. Peptide-Induced Formation of Cholesterol-Rich Domains. *Biochemistry*, 42(49):14677–14689, 2003.

Feigenson, G. W. Phase boundaries and biological membranes. *Annual Review of Biophysics and Biomolecular Structure*, 36:63–77, 2007.

Filippov, A., Orädd, G., and Lindblom, G. Lipid lateral diffusion in ordered and disordered phases in raft mixtures. *Biophysical Journal*, 86(February):891–896, 2004.

Flexner, C. and Saag, M. The antiretroviral drug pipeline: prospects and implications for future treatment research. *Current Opinion in HIV and AIDS*, 8(6): 572–578, 2013.

Frazier, M. L., Wright, J. R., Pokorny, A., and Almeida, P. F. Investigation of domain formation in sphingomyelin/cholesterol/POPC mixtures by fluorescence resonance energy transfer and Monte Carlo simulations. *Biophysical Journal*, 92 (7):2422–2433, 2007.

Freed, E. O. HIV-1 assembly, release and maturation. *Nature Reviews Microbiology*, 13(8):484–496, 2015.

Frey, G., Peng, H., Rits-Volloch, S., Morelli, M., Cheng, Y., and Chen, B. A fusion-intermediate state of HIV-1 gp41 targeted by broadly neutralizing antibodies. *Proceedings of the National Academy of Sciences of the United States of America*, 105(10):3739–3744, mar 2008.

Frey, G., Chen, J., Rits-Volloch, S., Freeman, M. M., Zolla-Pazner, S., and Chen, B. Distinct conformational states of HIV-1 gp41 are recognized by neutralizing and non-neutralizing antibodies. *Nature Structural & Molecular Biology*, 17(12): 1486–1491, dec 2010.

Galdiero, S., Falanga, A., Vitiello, M., D'Isanto, M., Cantisani, M., Kampanaraki, A., Benedetti, E., Browne, H., and Galdiero, M. Peptides containing membrane-interacting motifs inhibit herpes simplex virus type 1 infectivity. *Peptides*, 29(9):1461–1471, 2008.

Galdiero, S., Falanga, A., Morelli, G., and Galdiero, M. GH625: A milestone in understanding the many roles of membranotropic peptides. *Biochimica et Biophysica Acta - Biomembranes*, 1848(Part A):16–25, 2015.

Galiani, S., Waithe, D., Reglinski, K., Cruz-Zaragoza, L. D., Garcia, E., Clausen, M. P., Schliebs, W., Erdmann, R., and Eggeling, C. Super-resolution microscopy reveals compartmentalization of peroxisomal membrane proteins. *Journal of Biological Chemistry*, 291(33):16948–16962, 2016.

Gallo, R., Sarin, P., Gelmann, E., Robert-Guroff, M., Richardson, E., Kalyanaraman, V., Mann, D., Sidhu, G., Stahl, R., Zolla-Pazner, S., Leibowitch, J., and Popovic, M. Isolation of human T-cell leukemia virus in acquired immune deficiency syndrome (AIDS). *Science*, 220(4599):250–867, 1983.

Gaschen, B. Diversity Considerations in HIV-1 Vaccine Selection. *Science*, 296 (5577):2354–2360, jun 2002.

Gaus, K., Gratton, E., Kable, E. P. W., Jones, A. S., Gelissen, I., Kritharides, L., and Jessup, W. Visualizing lipid structure and raft domains in living cells with two-photon microscopy. *Proceedings of the National Academy of Sciences of the United States of America*, 100(26):15554–15559, 2003.

Gaus, K., Zech, T., and Harder, T. Visualizing membrane microdomains by Laurdan 2-photon microscopy, 2006.

Gerl, M. J., Sampaio, J. L., Urban, S., Kalvodova, L., Verbavatz, J. M., Binnington, B., Lindemann, D., Lingwood, C. A., Shevchenko, A., Schroeder, C., and Simons, K. Quantitative analysis of the lipidomes of the influenza virus envelope and MDCK cell apical membrane. *Journal of Cell Biology*, 196(2):213–221, 2012.

Giannecchini, S., Di Fenza, A., D'Ursi, A. M., Matteucci, D., Rovero, P., and Bendinelli, M. Antiviral activity and conformational features of an octapeptide derived from the membrane-proximal ectodomain of the feline immunodeficiency virus transmembrane glycoprotein. *Journal of Virology*, 77(6):3724–3733, 2003.

Girotti, a. W. Photodynamic lipid peroxidation in biological systems. *Photochemistry and Photobiology*, 51(4):497–509, 1990.

Gohain, N., Tolbert, W. D., Orlandi, C., Richard, J., Ding, S., Chen, X., Bonsor, D. A., Sundberg, E. J., Lu, W., Ray, K., Finzi, A., Lewis, G. K., and Pazgier, M. Molecular basis for epitope recognition by non-neutralizing anti-gp41 antibody F240. *Scientific Reports*, 6(1):36685, dec 2016.

Goñi, F. M., Alonso, A., Bagatolli, L. A., Brown, R. E., Marsh, D., Prieto, M., Thewalt, J. L., Goñi, F. M., Alonso, A., Bagatolli, L. A., Brown, R. E., Marsh, D., Prieto, M., and Thewalt, J. L. Phase diagrams of lipid mixtures relevant to the study of membrane rafts. *Biochimica et Biophysica Acta - Molecular and Cell Biology of Lipids*, 1781(11-12):665–684, 2008.

Güther-Ausborn, S., Praetor, A., and Stegmann, T. Inhibition of membrane fusion by lysophosphatidylcholine. *Biochemistry*, 270(49):29279–29285, 1995.

Guttman, M., Cupo, A., Julien, J.-P., Sanders, R. W., Wilson, I. A., Moore, J. P., and Lee, K. K. Antibody potency relates to the ability to recognize the closed, pre-fusion form of HIV Env. *Nature Communications*, 6:6144, feb 2015.

Guyader, M., Kiyokawa, E., Abrami, L., Turelli, P., and Trono, D. Role for Human Immunodeficiency Virus Type 1 Membrane Cholesterol in Viral Internalization. *Journal of Virology*, 76(20):10356–10364, 2002.

Haqqani, A. A. and Tilton, J. C. Entry inhibitors and their use in the treatment of HIV-1 infection. *Antiviral Research*, 98(2):158–170, 2013.

Haynes, B. F. Cardiolipin Polyspecific Autoreactivity in Two Broadly Neutralizing HIV-1 Antibodies. *Science*, 308(5730):1906–1908, jun 2005.

Haynes, B. F. and Mascola, J. R. The quest for an antibody-based HIV vaccine. *Immunological Reviews*, 275(1):5–10, jan 2017.

Haynes, B. F., Nicely, N. I., and Alam, S. M. HIV-1 autoreactive antibodies: are they good or bad for HIV-1 prevention? *Nature Structural & Molecular Biology*, 17(5):543–545, may 2010.

He, J., Yin, Y., Luster, T. A., Watkins, L., and Thorpe, P. E. Antiphosphatidylserine Antibody Combined with Irradiation Damages Tumor Blood Vessels and Induces Tumor Immunity in a Rat Model of Glioblastoma. *Clinical Cancer Research*, 15(22):6871–6880, 2009.

Henriques, S. T., Huang, Y. H., Rosengren, K. J., Franquelim, H. G., Carvalho, F. A., Johnson, A., Sonza, S., Tachedjian, G., Castanho, M. A. R. B., Daly, N. L., and Craik, D. J. Decoding the membrane activity of the cyclotide kalata B1: The importance of phosphatidylethanolamine phospholipids and lipid organization

on hemolytic and anti-HIV activities. *Journal of Biological Chemistry*, 286(27): 24231–24241, 2011.

Henriques, S. T., Huang, Y. H., Castanho, M. A. R. B., Bagatolli, L. A., Sonza, S., Tachedjian, G., Daly, N. L., and Craik, D. J. Phosphatidylethanolamine binding is a conserved feature of cyclotide-membrane interactions. *Journal of Biological Chemistry*, 287(40):33629–33643, 2012.

Heuck, A. P., Hotze, E. M., Tweten, R. K., and Johnson, A. E. Mechanism of Membrane Insertion of a Multimeric β-Barrel Protein. *Molecular Cell*, 6(5): 1233–1242, nov 2000.

Hoffmann, P. R., Kench, J. A., Vondracek, A., Kruk, E., Daleke, D. L., Jordan, M., Marrack, P., Henson, P. M., and Fadok, V. A. Interaction between Phosphatidylserine and the Phosphatidylserine Receptor Inhibits Immune Responses In Vivo. *The Journal of Immunology*, 174(3):1393–1404, 2005.

Hollmann, A., Castanho, M. A. R. B. a. R. B., Lee, B., and Santos, N. C. C. Singlet oxygen effects on lipid membranes: implications for the mechanism of action of broad-spectrum viral fusion inhibitors. *The Biochemical Journal*, 459(1):161–70, 2014.

Hollmann, A., Gonçalves, S., Augusto, M. T., Castanho, M. A. R. B., Lee, B., and Santos, N. C. Effects of singlet oxygen generated by a broad-spectrum viral fusion inhibitor on membrane nanoarchitecture. *Nanomedicine*, 11(5):1163–7, 2015.

Holopainen, J. M., Metso, A. J., Mattila, J.-P., Jutila, A., and Kinnunen, P. K. J. Evidence for the lack of a specific interaction between cholesterol and sphingomyelin. *Biophysical Journal*, 86(3):1510–1520, 2004.

Honerkamp-Smith, A. R., Veatch, S. L., and Keller, S. L. An introduction to critical points for biophysicists; observations of compositional heterogeneity in lipid membranes. *Biochimica et Biophysica Acta - Biomembranes*, 1788(1):53–63, 2009.

Hrobowski, Y. M., Garry, R. F., and Michael, S. F. Peptide inhibitors of dengue virus and West Nile virus infectivity. *Virology journal*, 2(1):49, 2005.

Huang, J., Ofek, G., Laub, L., Louder, M. K., Doria-Rose, N. A., Longo, N. S., Imamichi, H., Bailer, R. T., Chakrabarti, B., Sharma, S. K., Alam, S. M., Wang, T., Yang, Y., Zhang, B., Migueles, S. A., Wyatt, R., Haynes, B. F., Kwong, P. D., Mascola, J. R., and Connors, M. Broad and potent neutralization of HIV-1 by a gp41-specific human antibody. *Nature*, 491(7424):406–412, sep 2012.

Huang, Y., Yu, J., Lanzi, A., Yao, X., Andrews, C. D., Tsai, L., Gajjar, M. R., Sun, M., Seaman, M. S., Padte, N. N., and Ho, D. D. Engineered Bispecific Antibodies with Exquisite HIV-1-Neutralizing Activity. *Cell*, 165(7):1621–1631, jun 2016.

Huarte, N., Lorizate, M., Maeso, R., Kunert, R., Arranz, R., Valpuesta, J. M., and Nieva, J. L. The broadly neutralizing anti-human immunodeficiency virus type 1 4E10 monoclonal antibody is better adapted to membrane-bound epitope recognition and blocking than 2F5. *Journal of Virology*, 82(18):8986–8996, 2008.

Huarte, N., Carravilla, P., Cruz, A., Lorizate, M., Nieto-Garai, J. A., Kräusslich, H.-g., Pérez-gil, J., Requejo-isidro, J., Nieva, J. L., Krausslich, H. G., Perez-Gil, J., Requejo-isidro, J., and Nieva, J. L. Functional organization of the HIV lipid envelope. *Scientific Reports*, 6:34190, 2016.

Ionova, I. V., Livshits, V. A., and Marsh, D. Phase diagram of ternary cholesterol/palmitoylsphingomyelin/ palmitoyloleoyl-phosphatidylcholine mixtures: Spin-label EPR study of lipid-raft formation. *Biophysical Journal*, 102(8):1856–1865, 2012.

Irimia, A., Sarkar, A., Stanfield, R. L., and Wilson, I. A. Crystallographic Identification of Lipid as an Integral Component of the Epitope of HIV Broadly Neutralizing Antibody 4E10. *Immunity*, 44(1):21–31, 2016.

Irimia, A., Serra, A. M., Sarkar, A., Jacak, R., Kalyuzhniy, O., Sok, D., Saye-Francisco, K. L., Schiffner, T., Tingle, R., Kubitz, M., Adachi, Y., Stanfield, R. L., Deller, M. C., Burton, D. R., Schief, W. R., and Wilson, I. A. Lipid interactions and angle of approach to the HIV-1 viral membrane of broadly neutralizing antibody 10E8: Insights for vaccine and therapeutic design. *PLOS Pathogens*, 13(2):1–20, 2017.

Jacob, R. F. and Mason, R. P. Lipid peroxidation induces cholesterol domain formation in model membranes. *Journal of Biological Chemistry*, 280(47):39380–7, 2005.

Jardine, J. G., Sok, D., Julien, J.-P., Briney, B., Sarkar, A., Liang, C.-H., Scherer, E. A., Henry Dunand, C. J., Adachi, Y., Diwanji, D., Hsueh, J., Jones, M., Kalyuzhniy, O., Kubitz, M., Spencer, S., Pauthner, M., Saye-Francisco, K. L., Sesterhenn, F., Wilson, P. C., Galloway, D. M., Stanfield, R. L., Wilson, I. A., Burton, D. R., and Schief, W. R. Minimally Mutated HIV-1 Broadly Neutralizing Antibodies to Guide Reductionist Vaccine Design. *PLOS Pathogens*, 12(8): e1005815, aug 2016.

Kahya, N., Scherfeld, D., Bacia, K., Poolman, B., and Schwille, P. Probing lipid mobility of raft-exhibiting model membranes by fluorescence correlation spectroscopy. *Journal of Biological Chemistry*, 278(30):28109–28115, 2003.

Kaiser, H.-J., Lingwood, D., Levental, I., Sampaio, J. L., Kalvodova, L., Rajendran, L., and Simons, K. Order of lipid phases in model and plasma membranes. *Proceedings of the National Academy of Sciences of the United States of America*, 106(39):16645–16650, 2009.

Katz, G., Benkarroum, Y., Wei, H., Rice, W. J., Bucher, D., Alimova, A., Katz, A., Klukowska, J., Herman, G. T., and Gottlieb, P. Morphology of influenza B/lee/40 determined by cryo-electron microscopy. *PLOS ONE*, 9(2):e88288, 2014.

Keller, S. L., Pitcher, W. H., Huestis, W. H., and McConnell, H. M. Red Blood Cell Lipids Form Immiscible Liquids. *Physical Review Letters*, 81(22):5019–5022, 1998.

Khaselev, N. and Murphy, R. C. Structural characterization of oxidized phospholipid products derived from arachidonate-containing plasmenyl glycerophosphocholine. *The Journal of Lipid Research*, 41(4):564–572, 2000.

Klar, T. A., Jakobs, S., Dyba, M., Egner, A., and Hell, S. W. Fluorescence microscopy with diffraction resolution barrier broken by stimulated emission. *Proceedings of the National Academy of Sciences of the United States of America*, 97(15):8206–8210, 2000.

Klein, F., Mouquet, H., Dosenovic, P., Scheid, J. F., Scharf, L., and Nussenzweig, M. C. Antibodies in HIV-1 Vaccine Development and Therapy. *Science*, 341 (6151):1199–1204, sep 2013.

Klug, Y. A., Rotem, E., Schwarzer, R., and Shai, Y. Mapping out the intricate relationship of the HIV envelope protein and the membrane environment. *Biochimica et Biophysica Acta - Biomembranes*, 1859(4):550–560, 2017.

Kozlov, M. M., McMahon, H. T., and Chernomordik, L. V. Protein-driven membrane stresses in fusion and fission. *Trends in Biochemical Sciences*, 35(12): 699–706, 2010.

Krasnowska, E. K., Gratton, E., and Parasassi, T. Prodan as a membrane surface fluorescence probe: partitioning between water and phospholipid phases. *Biophysical Journal*, 74(4):1984–1993, 1998.

Kwon, Y. D., Georgiev, I. S., Ofek, G., Zhang, B., Asokan, M., Bailer, R. T., Bao, A., Caruso, W., Chen, X., Choe, M., Druz, A., Ko, S.-Y., Louder, M. K., McKee, K., O'Dell, S., Pegu, A., Rudicell, R. S., Shi, W., Wang, K., Yang, Y., Alger, M., Bender, M. F., Carlton, K., Cooper, J. W., Blinn, J., Eudailey, J., Lloyd, K., Parks, R., Alam, S. M., Haynes, B. F., Padte, N. N., Yu, J., Ho, D. D., Huang, J., Connors, M., Schwartz, R. M., Mascola, J. R., and Kwong, P. D. Optimization of the Solubility of HIV-1-Neutralizing Antibody 10E8 through Somatic Variation and Structure-Based Design. *Journal of Virology*, 90(13):5899–5914, 2016.

Kwong, P. D. and Mascola, J. R. Human Antibodies that Neutralize HIV-1: Identification, Structures, and B Cell Ontogenies. *Immunity*, 37(3):412–425, sep 2012.

Kyte, J. and Doolittle, R. F. A simple method for displaying the hydropathic character of a protein. *Journal of Molecular Biology*, 157(1):105–132, 1982.

Lalezari, J. P., Henry, K., O'Hearn, M., Montaner, J. S., Piliero, P. J., Trottier, B., Walmsley, S., Cohen, C., Kuritzkes, D. R., Eron, J. J., Chung, J., DeMasi, R., Donatacci, L., Drobnes, C., Delehanty, J., and Salgo, M. Enfuvirtide, an HIV-1 Fusion Inhibitor, for Drug-Resistant HIV Infection in North and South America. *New England Journal of Medicine*, 348(22):2175–2185, 2003.

Lampe, M., Briggs, J. A., Endress, T., Glass, B., Riegelsberger, S., Kräusslich, H.-G., Lamb, D. C., Bräuchle, C., and Müller, B. Double-labelled HIV-1 particles for study of viruscell interaction. *Virology*, 360(1):92–104, mar 2007.

Lee, D. W., Min, Y., Dhar, P., Ramachandran, A., Israelachvili, J. N., and Zasadzinski, J. A. Relating domain size distribution to line tension and molecular dipole density in model cytoplasmic myelin lipid monolayers. *Proceedings of the National Academy of Sciences of the United States of America*, 108(23): 9425–9430, 2011.

Lee, J. H., Ozorowski, G., and Ward, A. B. Cryo-EM structure of a native, fully glycosylated, cleaved HIV-1 envelope trimer. *Science*, 351(6277):1043–1048, mar 2016.

Lenard, J., Rabson, A., and Vanderoef, R. Photodynamic inactivation of infectivity of human immunodeficiency virus and other enveloped viruses using hypericin and rose bengal: inhibition of fusion and syncytia formation. *Proceedings of the National Academy of Sciences of the United States of America*, 90(1):158–162, 1993.

Levental, I., Grzybek, M., and Simons, K. Raft domains of variable properties and compositions in plasma membrane vesicles. *Proceedings of the National Academy of Sciences of the United States of America*, 108(28):11411–11416, 2011.

Li, M., Ablan, S. D., Miao, C., Zheng, Y.-M., Fuller, M. S., Rennert, P. D., Maury, W., Johnson, M. C., Freed, E. O., and Liu, S.-L. S.-L. TIM-family proteins inhibit HIV-1 release. *Proceedings of the National Academy of Sciences of the United States of America*, 111(35):E3699–E3707, 2014.

Liao, Z., Cimakasky, L. M., Hampton, R., Nguyen, D. H., and Hildreth, J. E. Lipid rafts and HIV pathogenesis: host membrane cholesterol is required for infection by HIV type 1. *AIDS Research and Human Retroviruses*, 17(11):1009–1019, 2001.

Liao, Z., Graham, D. R., and Hildreth, J. E. K. Lipid Rafts and HIV Pathogenesis: Virion-Associated Cholesterol Is Required for Fusion and Infection of Susceptible Cells. *AIDS Research and Human Retroviruses*, 19(8):675–687, 2003.

Lindblom, G., Orädd, G., and Filippov, A. Lipid lateral diffusion in bilayers with phosphatidylcholine, sphingomyelin and cholesterol. An NMR study of dynamics and lateral phase separation. *Chemistry and Physics of Lipids*, 141(1-2):179–184, 2006.

Lingwood, D. and Simons, K. Lipid Rafts As a Membrane-Organizing Principle. *Science*, 327(5961):46–50, 2010.

London, E. Membrane fusion: A new role for lipid domains? *Nature Chemical Biology*, 11(6):383–384, 2015.

Lorizate, M., De La Arada, I., Huarte, N., Sánchez-Martínez, S., De La Torre, B. G., Andreu, D., Arrondo, J. L. R., and Nieva, J. L. Structural analysis and assembly of the HIV-1 Gp41 amino-terminal fusion peptide and the pretransmembrane amphipathic-At-interface sequence. *Biochemistry*, 45(48):14337–14346, 2006.

Lorizate, M., Huarte, N., Sáez-Cirión, A., and Nieva, J. L. Interfacial pre-transmembrane domains in viral proteins promoting membrane fusion and fission. *Biochimica et Biophysica Acta - Biomembranes*, 1778(7-8):1624–1639, 2008.

Lorizate, M., Brügger, B., Akiyama, H., Glass, B., Müller, B., Anderluh, G., Wieland, F. T., and Kräusslich, H. G. Probing HIV-1 membrane liquid order by Laurdan staining reveals producer cell-dependent differences. *Journal of Biological Chemistry*, 284(33):22238–22247, 2009.

Lorizate, M., Kra, H.-g., and Krausslich, H. G. Role of lipids in virus replication. *Cold Spring Harbor Perspectives in Biology*, 3(10):a004820, 2011.

Lorizate, M., Sachsenheimer, T., Glass, B., Habermann, A., Gerl, M. J., Kräusslich, H.-G. G., and Brügger, B. Comparative lipidomics analysis of HIV-1 particles and their producer cell membrane in different cell lines. *Cellular Microbiology*, 15(2):292–304, 2013.

Mannock, D. A., McIntosh, T. J., Jiang, X., Covey, D. F., and McElhaney, R. N. Effects of natural and enantiomeric cholesterol on the thermotropic phase behavior and structure of egg sphingomyelin bilayer membranes. *Biophysical journal*, 84 (2 Pt 1):1038–1046, 2003.

Markosyan, R. M., Cohen, F. S., and Melikyan, G. B. Time-resolved Imaging of HIV-1 Env-mediated Lipid and Content Mixing between a Single Virion and Cell Membrane. *Molecular Biology of the Cell*, 16(12):5502–5513, 2005.

Martin, I. and Ruysschaert, J. Lysophosphatidylcholine inhibits vesicles fusion induced by the NH z-terminal extremity of SIV/HIV fusogenic proteins. *Biochimica et Biophysica Acta*, 1240:95–100, 1995.

Mattila, J.-P., Shnyrova, A. V., Sundborger, A. C., Hortelano, E. R., Fuhrmans, M., Neumann, S., Muller, M., Hinshaw, J. E., Schmid, S. L., and Frolov, V. A. A hemi-fission intermediate links two mechanistically distinct stages of membrane fission. *Nature*, 524(7563):109–113, 2015.

Melikyan, G. B. Common principles and intermediates of viral protein-mediated fusion: the HIV-1 paradigm. *Retrovirology*, 5:111, 2008.

Mills, T. T., Tristram-Nagle, S., Heberle, F. A., Morales, N. F., Zhao, J., Wu, J., Toombes, G. E., Nagle, J. F., and Feigenson, G. W. Liquid-Liquid Domains in Bilayers Detected by Wide Angle X-Ray Scattering. *Biophysical Journal*, 95(2): 682–690, 2008.

Miyauchi, K., Komano, J., Yokomaku, Y., Sugiura, W., Yamamoto, N., and Matsuda, Z. Role of the specific amino acid sequence of the membrane-spanning domain of human immunodeficiency virus type 1 in membrane fusion. *Journal of Virology*, 79(8):4720–9, 2005.

Moon, S., Yan, R., Kenny, S. J., Shyu, Y., Xiang, L., Li, W., and Xu, K. Spectrally Resolved, Functional Super-Resolution Microscopy Reveals Nanoscale Compositional Heterogeneity in Live-Cell Membranes. *Journal of the American Chemical Society*, 139(32):10944–10947, 2017.

Moore, P. L., Crooks, E. T., Porter, L., Zhu, P., Cayanan, C. S., Grise, H., Corcoran, P., Zwick, M. B., Franti, M., Morris, L., Roux, K. H., Burton, D. R., and Binley, J. M. Nature of nonfunctional envelope proteins on the surface of human immunodeficiency virus type 1. *Journal of Virology*, 80(5):2515–28, mar 2006.

Morizono, K. and Chen, I. S. Y. Role of Phosphatidylserine Receptors in Enveloped Virus Infection. *Journal of Virology*, 88(8):4275–4290, 2014.

Munro, J. B., Gorman, J., Ma, X., Zhou, Z., Arthos, J., Burton, D. R., Koff, W. C., Courter, J. R., Smith, A. B., Kwong, P. D., Blanchard, S. C., and Mothes, W. Conformational dynamics of single HIV-1 envelope trimers on the surface of native virions. *Science*, 346(6210):759–763, nov 2014.

Mütze, J., Iyer, V., MacKlin, J. J., Colonell, J., Karsh, B., Petrášek, Z., Schwille, P., Looger, L. L., Lavis, L. D., Harris, T. D., Mutze, J., Iyer, V., MacKlin, J. J., Colonell, J., Karsh, B., Petrasek, Z., Schwille, P., Looger, L. L., Lavis, L. D., and Harris, T. D. Excitation spectra and brightness optimization of two-photon excited probes. *Biophysical Journal*, 102(4):934–944, 2012.

Nehete, P. N., Vela, E. M., Hossain, M. M., Sarkar, A. K., Yahi, N., Fantini, J., and Sastry, K. J. A post-CD4-binding step involving interaction of the V3 region of viral gp120 with host cell surface glycosphingolipids is common to entry and infection by diverse HIV-1 strains. *Antiviral Research*, 56(3):233–51, dec 2002.

Nguyen, D. H. and Hildreth, J. E. K. Evidence for Budding of Human Immunodeficiency Virus Type 1 Selectively from Glycolipid-Enriched Membrane Lipid Rafts. *Journal of Virology*, 74(7):3264–3272, 2000.

Nieva, J. L., Apellaniz, B., Huarte, N., and Lorizate, M. A new paradigm in molecular recognition? Specific antibody binding to membrane-inserted HIV-1 epitopes., 2011.

Nyholm, T. K. M., Nylund, M., and Slotte, J. P. A calorimetric study of binary mixtures of dihydrosphingomyelin and sterols, sphingomyelin, or phosphatidylcholine. *Biophysical Journal*, 84(5):3138–3146, 2003.

Nyholm, T. K. M., Lindroos, D., Westerlund, B., and Slotte, J. P. Construction of a DOPC/PSM/cholesterol phase diagram based on the fluorescence properties of trans-parinaric acid. *Langmuir*, 27(13):8339–50, 2011.

Obaid, A. L., Loew, L. M., Wuskell, J. P., and Salzberg, B. M. Novel naphthylstyrylpyridinium potentiometric dyes offer advantages for neural network analysis. *Journal of Neuroscience Methods*, 134(2):179–190, 2004.

Ono, a. and Freed, E. O. Plasma membrane rafts play a critical role in HIV-1 assembly and release. *Proceedings of the National Academy of Sciences of the United States of America*, 98(24):13925–30, 2001.

Oradd, G., Lindblom, G., and Westerman, P. W. Lateral diffusion of cholesterol and dimyristoylphosphatidylcholine in a lipid bilayer measured by pulsed field gradient NMR spectroscopy. *Biophysical Journal*, 83(5):2702–2704, 2002.

Owen, D. M., Rentero, C., Magenau, A., Abu-Siniyeh, A., and Gaus, K. Quantitative imaging of membrane lipid order in cells and organisms. *Nature Protocols*, 7 (1):24–35, 2011.

Owen, D. M., Williamson, D. J., Magenau, A., and Gaus, K. Sub-resolution lipid domains exist in the plasma membrane and regulate protein diffusion and distribution. *Nature Communications*, 3:1256, 2012.

Padilla-Parra, S., Marin, M., Gahlaut, N., Suter, R., Kondo, N., and Melikyan, G. B. Fusion of Mature HIV-1 Particles Leads to Complete Release of a Gag-GFP-Based Content Marker and Raises the Intraviral pH. *PLoS ONE*, 8(8), 2013.

Parasassi, T., De Stasio, G., Ravagnan, G., Rusch, R. M., and Gratton, E. Quantitation of lipid phases in phospholipid vesicles by the generalized polarization of Laurdan fluorescence. *Biophysical Journal*, 60(1):179–189, 1991.

Parasassi, T., Krasnowska, E. K., Bagatolli, L., and Gratton, E. Laurdan and Prodan as polarity-sensitive fluorescent membrane probes. *Journal of fluorescence*, 8(4):365–373, 1998.

Patra, S. K., Alonso, A., Arrondo, J. L. R., and Goiii, F. M. Liposomes Containing Sphingomyelin and Cholesterol: Detergent Solubilisation and Infrared Spectroscopic Studies. *Journal of Liposome Research*, 9(2):247–260, 1999.

Patterson, G. H. and Piston, D. W. Photobleaching in Two-Photon Excitation Microscopy. *Biophysical Journal*, 78(4):2159–2162, 2000.

Phoenix, D. A., Harris, F., Mura, M., and Dennison, S. R. The increasing role of phosphatidylethanolamine as a lipid receptor in the action of host defence peptides. *Progress in Lipid Research*, 59:26–37, 2015.

Pinto, S. N., Fernandes, F., Fedorov, A., Futerman, A. H., Silva, L. C., and Prieto, M. A combined fluorescence spectroscopy, confocal and 2-photon microscopy approach to re-evaluate the properties of sphingolipid domains. *Biochimica et Biophysica Acta - Biomembranes*, 1828(9):2099–2110, 2013.

Pokorny, A., Yandek, L. E., Elegbede, A. I., Hinderliter, A., and Almeida, P. F. F. Temperature and composition dependence of the interaction of delta-lysin with ternary mixtures of sphingomyelin/cholesterol/POPC. *Biophysical Journal*, 91 (6):2184–2197, 2006.

Pollock, S., Nichita, N. B., Böhmer, A., Radulescu, C., Dwek, R. a., and Zitzmann, N. Polyunsaturated liposomes are antiviral against hepatitis B and C viruses and HIV by decreasing cholesterol levels in infected cells. *Proceedings of the National Academy of Sciences of the United States of America*, 107(40):17176–81, 2010.

Quinn, P. J. Structure of sphingomyelin bilayers and complexes with cholesterol forming membrane rafts. *Langmuir*, 29(30):9447–9456, 2013.

Ray, K., Mengistu, M., Lewis, G. K., Lakowicz, J. R., and DeVico, A. L. Antigenic Properties of the HIV Envelope on Virions in Solution. *Journal of Virology*, 88 (3):1795–1808, 2014.

Requejo-Isidro, J. Fluorescence nanoscopy. Methods and applications, 2013.

Rinia, H. A., Snel, M. M., Van Der Eerden, J. P., and De Kruijff, B. Visualizing detergent resistant domains in model membranes with atomic force microscopy. *FEBS Letters*, 501(1):92–96, 2001.

Roberts, J., Bebenek, K., and Kunkel, T. The accuracy of reverse transcriptase from HIV-1. *Science*, 242(4882):1171–1173, nov 1988.

Rujas, E., Gulzar, N., Morante, K., Tsumoto, K., Scott, J. K., Nieva, J. L., and Caaveiro, J. M. M. Structural and Thermodynamic Basis of Epitope Binding by Neutralizing and Nonneutralizing Forms of the Anti-HIV-1 Antibody 4E10. *Journal of Virology*, 89(23):11975–11989, dec 2015.

Rujas, E., Caaveiro, J. M. M., Partida-Hanon, A., Gulzar, N., Morante, K., Apellániz, B., García-Porras, M., Bruix, M., Tsumoto, K., Scott, J. K., Jiménez, M. Á., and Nieva, J. L. Structural basis for broad neutralization of HIV-1 through the molecular recognition of 10E8 helical epitope at the membrane interface. *Scientific Reports*, 6(1):38177, 2016.

Rujas, E., Caaveiro, J. M. M., Insausti, S., García-Porras, M., Tsumoto, K., and Nieva, J. L. Peripheral Membrane Interactions Boost the Engagement by an Anti-HIV-1 Broadly Neutralizing Antibody. *Journal of Biological Chemistry*, 292(13):5571–5583, mar 2017a.

Rujas, E., Insausti, S., García-Porras, M., Sánchez-Eugenia, R., Tsumoto, K., Nieva, J. L., and Caaveiro, J. M. Functional Contacts between MPER and the

Anti-HIV-1 Broadly Neutralizing Antibody 4E10 Extend into the Core of the Membrane. *Journal of Molecular Biology*, 429(8):1213–1226, apr 2017b.

Ryu, Y.-S., Lee, I.-H., Suh, J.-H., Park, S. C., Oh, S., Jordan, L. R., Wittenberg, N. J., Oh, S.-H., Jeon, N. L., Lee, B., Parikh, A. N., and Lee, S.-D. Reconstituting ring-rafts in bud-mimicking topography of model membranes. *Nature Communications*, 5, 2014.

Saez-Cirion, A., Arrondo, J. L., Gomara, M. J., Lorizate, M., Iloro, I., Melikyan, G., and Nieva, J. L. Structural and functional roles of HIV-1 gp41 pretransmembrane sequence segmentation. *Biophysical Journal*, 85(6):3769–3780, 2003.

Sahl, S. J., Hell, S. W., and Jakobs, S. Fluorescence nanoscopy in cell biology. *Nature Reviews Molecular Cell Biology*, 2017.

Sainz Jr., B., Mossel, E. C., Gallaher, W. R., Wimley, W. C., Peters, C. J., Wilson, R. B., Garry, R. F., Sainz, B., Mossel, E. C., Gallaher, W. R., Wimley, W. C., Peters, C. J., Wilson, R. B., Garry, R. F., Sainz Jr., B., Mossel, E. C., Gallaher, W. R., Wimley, W. C., Peters, C. J., Wilson, R. B., and Garry, R. F. Inhibition of severe acute respiratory syndrome-associated coronavirus (SARS-CoV) infectivity by peptides analogous to the viral spike protein. *Virus Research*, 120(1-2):146–155, 2006.

Sánchez, E. J., Novotny, L., Holtom, G. R., Xie, X. S., Sa, E. J., Novotny, L., Holtom, G. R., Xie, X. S., Sanchez, E. J., Novotny, L., Holtom, G. R., and Xie, X. S. Room-temperature fluorescence imaging and spectroscopy of single molecules by two-photon excitation. *Journal of Physical Chemistry A*, 101(38):4, 1997.

Sando, L., Henriques, S. T., Foley, F., Simonsen, S. M., Daly, N. L., Hall, K. N., Gustafson, K. R., Aguilar, M. I., and Craik, D. J. A synthetic mirror image of kalata B1 reveals that cyclotide activity is independent of a protein receptor. *ChemBioChem*, 12(16):2456–2462, 2011.

Sankaram, M. B. and Thompson, T. E. Modulation of Phospholipid Acyl Chain Order by Cholesterol. A Solid-State 2H Nuclear Magnetic Resonance Study. *Biochemistry*, 29(47):10676–10684, 1990.

Schaffner, C. P., Plescia, O. J., Pontani, D., Sun, D., Thornton, A., Pandey, R. C., and Sarin, P. S. Anti-viral activity of amphotericin B methyl ester: inhibition of HTLV-III replication in cell culture. *Biochemical Pharmacology*, 35 (22):4110–4113, nov 1986.

Scherer, E. M., Leaman, D. P., Zwick, M. B., McMichael, A. J., and Burton, D. R. Aromatic residues at the edge of the antibody combining site facilitate viral glycoprotein recognition through membrane interactions. *Proceedings of the National Academy of Sciences of the United States of America*, 107(4):1529–1534, 2010.

Schon, P., Garcia-Saez, A. J., Malovrh, P., Bacia, K., Anderluh, G., and Schwille, P. Equinatoxin II permeabilizing activity depends on the presence of sphingomyelin and lipid phase coexistence. *Biophysical Journal*, 95(2):691–698, 2008.

Schroeder, C. Cholesterol-binding viral proteins in virus entry and morphogenesis. *Subcellular Biochemistry*, 51:77–108, 2010.

Seaman, M. S., Janes, H., Hawkins, N., Grandpre, L. E., Devoy, C., Giri, A., Coffey, R. T., Harris, L., Wood, B., Daniels, M. G., Bhattacharya, T., Lapedes, A., Polonis, V. R., McCutchan, F. E., Gilbert, P. B., Self, S. G., Korber, B. T., Montefiori, D. C., and Mascola, J. R. Tiered Categorization of a Diverse Panel of HIV-1 Env Pseudoviruses for Assessment of Neutralizing Antibodies. *Journal of Virology*, 84(3):1439–1452, feb 2010.

Sezgin, E. Super-resolution optical microscopy for studying membrane structure and dynamics. *Journal of Physics: Condensed Matter*, 29(27):273001, 2017.

Sezgin, E., Levental, I., Grzybek, M., Schwarzmann, G., Mueller, V., Honigmann, A., Belov, V. N., Eggeling, C., Coskun, Ü., Simons, K., and Schwille, P. Partitioning, diffusion, and ligand binding of raft lipid analogs in model and cellular plasma membranes. *Biochimica et Biophysica Acta - Biomembranes*, 1818(7): 1777–1784, 2012.

Sezgin, E., Chwastek, G., Aydogan, G., Levental, I., Simons, K., and Schwille, P. Photoconversion of Bodipy-Labeled Lipid Analogues. *ChemBioChem*, 14(6): 695–698, 2013.

Sezgin, E., Sadowski, T., and Simons, K. Measuring lipid packing of model and cellular membranes with environment sensitive probes. *Langmuir*, 30(27): 8160–8166, 2014.

Sezgin, E., Gutmann, T., Buhl, T., Dirkx, R., Grzybek, M., Coskun, Ü., Solimena, M., Simons, K., Levental, I., and Schwille, P. Adaptive Lipid Packing and Bioactivity in Membrane Domains. *PLoS One*, 10(4):e0123930, 2015a.

Sezgin, E., Waithe, D., Bernardino De La Serna, J., and Eggeling, C. Spectral imaging to measure heterogeneity in membrane lipid packing. *ChemPhysChem*, 16(7):1387–1394, 2015b.

Sezgin, E., Levental, I., Mayor, S., and Eggeling, C. The mystery of membrane organization: composition, regulation and roles of lipid rafts. *Nature Reviews Molecular Cell Biology*, 18(6):361–374, 2017a.

Sezgin, E., Schneider, F., Zilles, V., Urbančič, I., Garcia, E., Waithe, D., Klymchenko, A. S., and Eggeling, C. Polarity-Sensitive Probes for Superresolution Stimulated Emission Depletion Microscopy. *Biophysical Journal*, pages 1321–1330, 2017b.

Shepard, L. A., Heuck, A. P., Hamman, B. D., Rossjohn, J., Parker, M. W., Ryan, K. R., Johnson, A. E., and Tweten, R. K. Identification of a Membrane-Spanning Domain of the Thiol-Activated Pore-Forming Toxin Clostridium perfringens Perfringolysin O: An α-Helical to β-Sheet Transition Identified by Fluorescence Spectroscopy . *Biochemistry*, 37(41):14563–14574, oct 1998.

Shlomovitz, R., Maibaum, L., and Schick, M. Macroscopic phase separation, modulated phases, and microemulsions: A unified picture of rafts. *Biophysical Journal*, 106(9):1979–1985, 2014.

Shnyrova, A. V., Bashkirov, P. V., Akimov, S. A., Pucadyil, T. J., Zimmerberg, J., Schmid, S. L., and Frolov, V. A. Geometric Catalysis of Membrane Fission Driven by Flexible Dynamin Rings. *Science*, 339(6126):1433–1436, 2013.

Simek, M. D., Rida, W., Priddy, F. H., Pung, P., Carrow, E., Laufer, D. S., Lehrman, J. K., Boaz, M., Tarragona-Fiol, T., Miiro, G., Birungi, J., Pozniak, A., McPhee, D. A., Manigart, O., Karita, E., Inwoley, A., Jaoko, W., DeHovitz, J., Bekker, L.-G., Pitisuttithum, P., Paris, R., Walker, L. M., Poignard, P., Wrin, T., Fast, P. E., Burton, D. R., and Koff, W. C. Human Immunodeficiency Virus Type 1 Elite Neutralizers: Individuals with Broad and Potent Neutralizing Activity Identified by Using a High-Throughput Neutralization Assay together with an Analytical Selection Algorithm. *Journal of Virology*, 83(14):7337–7348, jul 2009.

Simons, K. and Ikonen, E. Functional rafts in cell membranes. *Nature*, 387(6633): 569–72, 1997.

Slotte, J. P. The importance of hydrogen bonding in sphingomyelin's membrane interactions with co-lipids. *Biochimica et Biophysica Acta - Biomembranes*, 1858 (2):304–310, 2016.

Smaby, J. M., Brockman, H. L., and Brown, R. E. Cholesterol's Interfacial Interactions with Sphingomyelins and Phosphatidylcholines: Hydrocarbon Chain Structure Determines the Magnitude of Condensation. *Biochemistry*, 33(31): 9135–9142, 1994.

Smith, A. K. and Freed, J. H. Determination of tie-line fields for coexisting lipid phases: An ESR study. *Journal of Physical Chemistry B*, 113(12):3957–3971, 2009.

Soares, M. M., King, S. W., and Thorpe, P. E. Targeting inside-out phosphatidylserine as a therapeutic strategy for viral diseases. *Nature Medicine*, 14(12):1357–1362, 2008.

Spence, J. S., Melnik, L. I., Badani, H., Wimley, W. C., and Garry, R. F. Inhibition of Arenavirus Infection by a Glycoprotein-Derived Peptide with a Novel Mechanism. *Journal of Virology*, 88(15):8556–8564, 2014.

Stamatatos, L., Morris, L., Burton, D. R., and Mascola, J. R. Neutralizing antibodies generated during natural HIV-1 infection: good news for an HIV-1 vaccine? *Nature Medicine*, jun 2009.

Stephenson, K. E. and Barouch, D. H. Broadly Neutralizing Antibodies for HIV Eradication. *Current HIV/AIDS Reports*, 13(1):31–37, feb 2016.

Stiegler, G., Kunert, R., Purtscher, M., Wolbank, S., Voglauer, R., Steindl, F., and Katinger, H. A Potent Cross-Clade Neutralizing Human Monoclonal Antibody against a Novel Epitope on gp41 of Human Immunodeficiency Virus Type 1. *AIDS Research and Human Retroviruses*, 17(18):1757–1765, dec 2001.

St.Vincent, M. R., Colpitts, C. C., Ustinov, A. V., Muqadas, M., Joyce, M. a., Barsby, N. L., Epand, R. F., Epand, R. M., Khramyshev, S. A., Valueva, O. a., Korshun, V. A., Tyrrell, D. L. J., and Schang, L. M. Rigid amphipathic fusion inhibitors, small molecule antiviral compounds against enveloped viruses. *Proceedings of the National Academy of Sciences of the United States of America*, 107(40):17339–17344, 2010.

Sun, X. and Whittaker, G. R. Role for In uenza Virus Envelope Cholesterol in Virus Entry and Infection. *Journal of Virology*, 77(23):12543–12551, 2003.

Sundquist, W. I. and Kräusslich, H.-G. G. HIV-1 assembly, budding, and maturation. *Cold Spring Harbor Perspectives in Medicine*, 2(7), 2012.

Thewalt, J. L. and Bloom, M. Phosphatidylcholine: cholesterol phase diagrams. *Biophysical Journal*, 63(4):1176–1181, 1992.

Tian, A., Johnson, C., Wang, W., and Baumgart, T. Line tension at fluid membrane domain boundaries measured by micropipette aspiration. *Physical Review Letters*, 98(20), 2007.

Vancompernolle, S. E., Taylor, R. J., Oswald-richter, K., Jiang, J., Youree, B. E., Bowie, J. H., Tyler, M. J., Conlon, J. M., Wade, D., Aiken, C., Dermody, T. S., Kewalramani, V. N., Kewalramani, V. N., Rollins-smith, L. A., and Unutmaz, D. Antimicrobial Peptides from Amphibian Skin Potently Inhibit Human Immunode ciency Virus Infection and Transfer of Virus from Dendritic Cells to T Cells. *Journal of Virology*, 79(18):11598–11606, 2005.

Vasiljevic, S., Beale, E. V., Bonomelli, C., Easthope, I. S., Pritchard, L. K., Seabright, G. E., Caputo, A. T., Scanlan, C. N., Dalziel, M., and Crispin, M. Redirecting adenoviruses to tumour cells using therapeutic antibodies: Generation of a versatile human bispecific adaptor. *Molecular Immunology*, 68(2): 234–243, 2015.

Veatch, S. L. and Keller, S. L. Organization in Lipid Membranes Containing Cholesterol. *Physical Review Letters*, 89(26):268101, 2002.

Veatch, S. L. and Keller, S. L. Separation of Liquid Phases in Giant Vesicles of Ternary Mixtures of Phospholipids and Cholesterol. *Biophysical Journal*, 85(5): 3074–3083, 2003a.

Veatch, S. L. and Keller, S. L. A closer look at the canonical 'Raft Mixture' in model membrane studies. *Biophysical Journal*, 84(1):725–726, 2003b.

Veatch, S. L. and Keller, S. L. Miscibility phase diagrams of giant vesicles containing sphingomyelin. *Physical Review Letters*, 94(14), 2005a.

Veatch, S. L. and Keller, S. L. Seeing spots: Complex phase behavior in simple membranes, 2005b.

Veatch, S. L., Leung, S. S. W., Hancock, R. E. W., and Thewalt, J. L. Fluorescent probes alter miscibility phase boundaries in ternary vesicles. *Journal of Physical Chemistry B*, 111(3):502–504, 2007.

Verkoczy, L., Kelsoe, G., and Haynes, B. F. HIV-1 Envelope gp41 Broadly Neutralizing Antibodies: Hurdles for Vaccine Development. *PLOS Pathogens*, 10 (5):e1004073, may 2014.

Vigant, F., Lee, J., Hollmann, A., Tanner, L. B., Akyol Ataman, Z., Yun, T., Shui, G., Aguilar, H. C., Zhang, D., Meriwether, D., Roman-Sosa, G., Robinson, L. R., Juelich, T. L., Buczkowski, H., Chou, S., Castanho, M. A. R. B., Wolf, M. C., Smith, J. K., Banyard, A., Kielian, M., Reddy, S., Wenk, M. R., Selke, M., Santos, N. C., Freiberg, A. N., Jung, M. E., and Lee, B. A Mechanistic Paradigm for Broad-Spectrum Antivirals that Target Virus-Cell Fusion. *PLOS Pathog*, 9(4):e1003297, 2013.

Vigant, F., Hollmann, A., Lee, J., Santos, N. C., Jung, M. E., and Lee, B. The rigid amphipathic fusion inhibitor dUY11 acts through photosensitization of viruses. *Journal of Virology*, 88(3):1849–53, 2014.

Vigant, F., Santos, N. C., and Lee, B. Broad-spectrum antivirals against viral fusion. *Nature Reviews Microbiology*, 13(7):426–437, 2015.

Vincent, N., Genin, C., and Malvoisin, E. Identification of a conserved domain of the HIV-1 transmembrane protein gp41 which interacts with cholesteryl groups. *Biochimica et Biophysica Acta - Biomembranes*, 1567(1-2):157–164, 2002.

Vishwanathan, S. A. and Hunter, E. Importance of the membrane-perturbing properties of the membrane-proximal external region of human immunodeficiency virus type 1 gp41 to viral fusion. *Journal of Virology*, 82(11):5118–5126, 2008.

Vishwanathan, S. A., Thomas, A., Brasseur, R., Epand, R. F., Hunter, E., and Epand, R. M. Hydrophobic substitutions in the first residue of the CRAC segment of the gp41 protein of HIV. *Biochemistry*, 47(1):124–130, 2008.

Volinsky, R., Paananen, R., and Kinnunen, P. K. J. Oxidized Phosphatidylcholines Promote Phase Separation of Cholesterol-Sphingomyelin Domains. *Biophysical Journal*, 103(2):247–254, 2012.

Waheed, A. A. and Freed, E. O. The Role of Lipids in Retrovirus Replication. *Viruses*, 2(5):1146, 2010.

Waheed, A. A., Ablan, S. D., Mankowski, M. K., Cummins, J. E., Ptak, R. G., Schaffner, C. P., and Freed, E. O. Inhibition of HIV-1 replication by amphotericin B methyl ester: Selection for resistant variants. *Journal of Biological Chemistry*, 281(39):28699–28711, 2006.

Waheed, A. A., Ablan, S. D., Roser, J. D., Sowder, R. C., Schaffner, C. P., Chertova, E., and Freed, E. O. HIV-1 escape from the entry-inhibiting effects of a cholesterol-binding compound via cleavage of gp41 by the viral protease. *Proceedings of the National Academy of Sciences of the United States of America*, 104(20):8467–8471, 2007.

Waheed, A. A., Ablan, S. D., Soheilian, F., Nagashima, K., Ono, A., Schaffner, C. P., and Freed, E. O. Inhibition of human immunodeficiency virus type 1 assembly and release by the cholesterol-binding compound amphotericin B methyl ester: evidence for Vpu dependence. *Journal of Virology*, 82(19):9776–81, 2008.

Wang, G., Watson, K. M., Peterkofsky, A., and Buckheit, R. W. Identification of novel human immunodeficiency virus type 1-inhibitory peptides based on the

antimicrobial peptide database. *Antimicrobial Agents and Chemotherapy*, 54(3): 1343–1346, 2010.

Ward, A. B. and Wilson, I. A. Insights into the trimeric HIV-1 envelope glycoprotein structure. *Trends in Biochemical Sciences*, 40(2):101–107, 2015.

Weber, G. and Farris, F. J. Synthesis and Spectral Properties of a Hydrophobic Fluorescent Probe: 6-Propionyl-2-(dimethylamino)naphthalene. *Biochemistry*, 18(14):3075–3078, 1979.

White, J. M., Delos, S. E., Brecher, M., and Schornberg, K. Structures and mechanisms of viral membrane fusion proteins: Multiple variations on a common theme, 2008.

Wilen, C. B., Tilton, J. C., and Doms, R. W. HIV: Cell binding and entry. *Cold Spring Harbor Perspectives in Medicine*, 2(8), 2012.

Wimley, W. C. and White, S. H. Experimentally determined hydrophobicity scale for proteins at membrane interfaces. *Nature Structural & Molecular Biology*, 3 (10):842–848, 1996.

Wisskirchen, K., Lucifora, J., Michler, T., and Protzer, U. New pharmacological strategies to fight enveloped viruses. *Trends in Pharmacological Sciences*, 35(9), 2014.

Wojcechowskyj, J. A. and Doms, R. W. A potent, broad-spectrum antiviral agent that targets viral membranes. *Viruses*, 2(5):1106–1109, 2010.

Wolf, M. C., Freiberg, A. N., Zhang, T., Akyol-Ataman, Z., Grock, A., Hong, P. W., Li, J., Watson, N. F., Fang, A. Q., Aguilar, H. C., Porotto, M., Honko, A. N., Damoiseaux, R., Miller, J. P., Woodson, S. E., Chantasirivisal, S., Fontanes, V., Negrete, O. a., Krogstad, P., Dasgupta, A., Moscona, A., Hensley, L. E., Whelan, S. P., Faull, K. F., Holbrook, M. R., Jung, M. E., and Lee, B. A broad-spectrum antiviral targeting entry of enveloped viruses. *Proceedings of the National Academy of Sciences of the United States of America*, 107(7):3157–3162, 2010.

Wong, A. The HIV pipeline. *Nature Reviews Drug Discovery*, 13(9):649–650, 2014.

Xu, K., Babcock, H. P., and Zhuang, X. Dual-objective STORM reveals three-dimensional filament organization in the actin cytoskeleton. *Nature Methods*, 9 (2):185–188, 2012.

Xu, L., Pegu, A., Rao, E., Doria-Rose, N., Beninga, J., McKee, K., Lord, D. M., Wei, R. R., Deng, G., Louder, M., Schmidt, S. D., Mankoff, Z., Wu, L., Asokan, M., Beil, C., Lange, C., Leuschner, W. D., Kruip, J., Sendak, R., Do Kwon, Y., Zhou, T., Chen, X., Bailer, R. T., Wang, K., Choe, M., Tartaglia, L. J., Barouch, D. H., O'Dell, S., Todd, J.-P., Burton, D. R., Roederer, M., Connors, M., Koup, R. A., Kwong, P. D., Yang, Z.-y., Mascola, J. R., and Nabel, G. J. Trispecific broadly neutralizing HIV antibodies mediate potent SHIV protection in macaques. *Science*, 358(6359):85–90, oct 2017.

Yang, S.-T., Kiessling, V., Simmons, J. a., White, J. M., and Tamm, L. K. HIV gp41-mediated membrane fusion occurs at edges of cholesterol-rich lipid domains. *Nature Chemical Biology*, 11(6):1–10, 2015.

Yang, S.-T., Kiessling, V., and Tamm, L. K. Line tension at lipid phase boundaries as driving force for HIV fusion peptide-mediated fusion. *Nature Communications*, 7:11401, 2016a.

Yang, S.-T., Kreutzberger, A. J., Lee, J., Kiessling, V., and Tamm, L. K. The role of cholesterol in membrane fusion. *Chemistry and Physics of Lipids*, 199: 136–143, 2016b.

Yang, S.-T., Kreutzberger, A. J. B., Kiessling, V., Ganser-Pornillos, B. K., White, J. M., and Tamm, L. K. HIV virions sense plasma membrane heterogeneity for cell entry. *Science Advances*, 3(6):e1700338, 2017.

Zaitseva, E., Zaitsev, E., Melikov, K., Arakelyan, A., Marin, M., Villasmil, R., Margolis, L. B., Melikyan, G. B., and Chernomordik, L. V. Fusion Stage of HIV-1 Entry Depends on Virus-Induced Cell Surface Exposure of Phosphatidylserine. *Cell Host & Microbe*, 22(1):99–110.e7, jul 2017.

Zanetti, G., Briggs, J. A. G., Grünewald, K., Sattentau, Q. J., and Fuller, S. D. Cryo-Electron Tomographic Structure of an Immunodeficiency Virus Envelope Complex In Situ. *PLOS Pathogens*, 2(8):e83, 2006.

Zhang, L., Yu, W., He, T., Yu, J., Caffrey, R. E., Dalmasso, E. A., Fu, S., Pham, T., Mei, J., Ho, J. J., Zhang, W., Lopez, P., and Ho, D. D. Contribution of Human -Defensin 1, 2, and 3 to the Anti-HIV-1 Activity of CD8 Antiviral Factor. *Science*, 298(5595):995–1000, 2002.

Zhao, J., Wu, J., Shao, H. L., Kong, F., Jain, N., Hunt, G., and Feigenson, G. Phase studies of model biomembranes: Macroscopic coexistence of L alpha plus L beta, with light-induced coexistence of L alpha plus Lo Phases. *Biochim Biophys Acta, Biomembr*, 1768(11):2777–2786, 2007.

Zhu, P., Liu, J., Bess, J., Chertova, E., Lifson, J. D., Grisé, H., Ofek, G. A., Taylor, K. A., and Roux, K. H. Distribution and three-dimensional structure of AIDS virus envelope spikes. *Nature*, 441(7095):847–852, 2006.

Zwaal, R. F., Comfurius, P., and Bevers, E. M. Surface exposure of phosphatidylserine in pathological cells. *Cellular and Molecular Life Sciences*, 62(9):971–988, 2005.

Zwick, M. B., Jensen, R., Church, S., Wang, M., Stiegler, G., Kunert, R., Katinger, H., and Burton, D. R. Anti-Human Immunodeficiency Virus Type 1 (HIV-1) Antibodies 2F5 and 4E10 Require Surprisingly Few Crucial Residues in the Membrane-Proximal External Region of Glycoprotein gp41 To Neutralize HIV-1. *Journal of Virology*, 79(2):1252–1261, jan 2005.